LEABHARLANN CHOLÁISTE NA TRÍONÓIDE, BAILE ÁTHA CLIATH | TRINITY COLLEGE LIBRARY DUBLIN
Ollscoil Átha Cliath | The University of Dublin

Terms and Conditions of Use of Digitised Theses from Trinity College Library Dublin

Copyright statement

All material supplied by Trinity College Library is protected by copyright (under the Copyright and Related Rights Act, 2000 as amended) and other relevant Intellectual Property Rights. By accessing and using a Digitised Thesis from Trinity College Library you acknowledge that all Intellectual Property Rights in any Works supplied are the sole and exclusive property of the copyright and/or other IPR holder. Specific copyright holders may not be explicitly identified. Use of materials from other sources within a thesis should not be construed as a claim over them.

A non-exclusive, non-transferable licence is hereby granted to those using or reproducing, in whole or in part, the material for valid purposes, providing the copyright owners are acknowledged using the normal conventions. Where specific permission to use material is required, this is identified and such permission must be sought from the copyright holder or agency cited.

Liability statement

By using a Digitised Thesis, I accept that Trinity College Dublin bears no legal responsibility for the accuracy, legality or comprehensiveness of materials contained within the thesis, and that Trinity College Dublin accepts no liability for indirect, consequential, or incidental, damages or losses arising from use of the thesis for whatever reason. Information located in a thesis may be subject to specific use constraints, details of which may not be explicitly described. It is the responsibility of potential and actual users to be aware of such constraints and to abide by them. By making use of material from a digitised thesis, you accept these copyright and disclaimer provisions. Where it is brought to the attention of Trinity College Library that there may be a breach of copyright or other restraint, it is the policy to withdraw or take down access to a thesis while the issue is being resolved.

Access Agreement

By using a Digitised Thesis from Trinity College Library you are bound by the following Terms & Conditions. Please read them carefully.

I have read and I understand the following statement: All material supplied via a Digitised Thesis from Trinity College Library is protected by copyright and other intellectual property rights, and duplication or sale of all or part of any of a thesis is not permitted, except that material may be duplicated by you for your research use or for educational purposes in electronic or print form providing the copyright owners are acknowledged using the normal conventions. You must obtain permission for any other use. Electronic or print copies may not be offered, whether for sale or otherwise to anyone. This copy has been supplied on the understanding that it is copyright material and that no quotation from the thesis may be published without proper acknowledgement.

The development of a computational model of an osteochondral defect

Adam O'Reilly

Trinity College Dublin

PhD 2016

TRINITY LIBRARY
27 JUL 2016
DUBLIN
Thesis 11021

Declaration

I declare that this thesis has not been submitted as an exercise for a degree for this or any other university and it is entirely my own work.

I agree to deposit this thesis in the University's open access institutional repository or allow the library to do so on my behalf, subject to Irish Copyright Legislation and Trinity College Library conditions of use and acknowledgement.

Summary

Osteochondral defects arise in the knee after structural damage penetrates through the hyaline cartilage and into the underlying subchondral bone. The current surgical options used to treat this condition have limited success in the long term because they fail to successfully regenerate the damaged tissues. While currently not in widespread clinical use, tissue engineering has the potential to reconstruct the native tissue and therefore provide long term relief to the patient. A promising variant of this approach is to insert scaffolds seeded with mesenchymal stem cells (MSCs) into the defect site. The basis of this is that the scaffold will provide the correct mechanical and biological cues to promote the seeded cell population to reconstruct the native tissue. One of the difficulties associated with this treatment option, however, is that the *in vivo* environment is complex and as a result it is difficult to understand how it will affect cell behaviour within the osteochondral defect. To address this problem, the objective of this thesis was to develop a computational model of MSC differentiation and tissue formation within an osteochondral defect. This model was then used to help improve tissue engineering strategies under development for the treatment of osteochondral defects.

To achieve this objective, this thesis first sought to improve a previously developed tissue differentiation algorithm in which it was assumed that MSC fate was directed by the local oxygen tension and the stiffness of the surrounding substrate. The model was updated to include a series of rules which hypothesised that the local oxygen tension directs the course of chondrocyte hypertrophy and endochondral ossification during bone regeneration. In order to test this hypothesis, this thesis examined if the updated model could simulate the time course of tissue formation during both normal and ischemic fracture healing within a murine tibia. The model was able to predict temporal changes in the levels of hypertrophic cartilage within the fracture callus. In addition to providing support for the updated algorithm, this study also highlighted the relationship between angiogenesis and bone formation during fracture healing.

In the second study of this thesis, the efficacy of the updated tissue differentiation algorithm was further evaluated by attempting to simulate the spontaneous repair process within an osteochondral defect. Following the development of this model, a sensitivity analysis and a parametric study were performed in order to explore the extent to which angiogenesis, and the subsequent oxygen environment, affects the spontaneous repair process. The results from this study highlighted the key role played by angiogenesis in

regulating MSC fate during osteochondral defect repair. In addition to this, it also led us to hypothesise that osteochondral defect repair can be enhanced by interventions where angiogenesis is promoted but confined to within the subchondral region of the defect.

In the third study of this thesis, the tissue differentiation algorithm was further updated to consider the effect of mechanical loading on the fate of cartilage within an osteochondral defect. In particular, additional rules were developed based on the hypotheses that chondrocyte hypertrophy and endochondral ossification are inhibited in regions of high strain, while excessively large magnitudes of strain result in the formation of mechanically inferior fibrocartilage. These rules were first developed by simulating stem cell differentiation within an *in vitro* bioreactor system which was capable of controlling the levels of oxygen and the mechanical cues within MSC laden hydrogels. Following this, the updated model was used to simulate the experimentally observed course of the spontaneous repair process within an osteochondral defect. As well as correctly predicting the spatial patterns of bone formation, the updated model also provided insights into the role which the mechanical environment plays on the spontaneous repair process; namely that oxygen regulates endochondral ossification during the early phases of repair while mechanics plays a key role in directing this process during the latter stages of regeneration.

In the final study of this thesis the developed framework was used to better understand how tissue engineering strategies can be used to regenerate osteochondral defects. In the first part of this study, a series of rules were implemented to take into account the fact that hyaline cartilage secretes factors which are known to inhibit the progression of angiogenesis. These rules were again tested by using them to model the spontaneous repair process. The updated model was then used to simulate how the implementation of different cell-free and cell-laden scaffolds influence osteochondral defect regeneration. By comparing the results of these different simulations, this thesis was able to identify potential mechanisms to explain the success of the specific scaffolds in regenerating damaged joints. Such computational models are expected to become integral to the optimizing the design of next generation scaffolds for tissue engineering and regenerative medicine.

Acknowledgements

First and foremost, I must thank my supervisor Professor Daniel Kelly, without whom this thesis would have never gotten off the ground. Additional thanks have to be given to him for his constant guidance and the long hours he had to spend proof-reading the drafts of studies that I sent him over the previous four years.

There were some very dark days when writing this thesis, and so I have to thank my family and friends for putting up with a considerable amount of moaning. In particular I have to thanks my mother for providing me with numerous care packages and my father for taking time out of his busy days of retirement to proof-read the final thesis. I also have to thank my brothers, Dan, Evin and Nathan for their support over the last few years. Special thanks must also be paid to my housemates Jim and Niall, whose suggestions that I finish this thesis with the statement 'In conclusion, the knee did it', while not helpful, was certainly entertaining. I also must thank Emmet O'Neill for providing a constant source of entertainment with his attempts to make me acknowledge that crypto-zoology is a legitimate scientific field, it's not. Finally, I have to acknowledge Maria Browne for the weekly lunches in which we both lamented our terrible decision to undertake a PhD.

I must also acknowledge all of my colleagues from the past four years. Special attention must be paid to my predecessors Dr. Thomas Nagel and Dr. Darren Burke who laid much of the groundwork for the computational models used in this thesis. Finally, I have to thank everyone in TBSI; for the chats beside the coffee machine; the tag rugby every summer; and all of the Team Danny events.

Finally, as with all things PhD related, I have to thank the funding, because there was no way I was going to do this for free.

Table of Contents

Declaration i

Summary iii

Acknowledgements v

Table of Contents vii

List of Figures xiii

List of Tables xxi

Nomenclature xxiii

Publications and Conference Contributions xxv

Publications xxv

Conference Contributions xxvi

Chapter 1 Introduction 1

1.1 Osteochondral Defect Repair 1

1.2 Computational Mechanobiology 2

1.3 Objectives 4

Chapter 2 Literature Review 7

2.1 Mesenchymal Stem Cells 8

2.2 Environmental Factors Regulating Stem Cell Differentiation 9

2.2.1 Mechanical Regulation 9

2.2.2 Cell Shape 17

2.2.3 Substrate Stiffness 19

2.2.4 Oxygen Tension 25

2.2.5 Biochemical Cues 28

2.3 Tissue Differentiation *In Vivo* 31

2.3.1 Fracture Healing 31

2.3.2 Osteochondral Defects 40

2.4 Computational Mechanobiology 54

2.5 Conclusion 59

Chapter 3 A computational model to explore the role of angiogenic impairment on endochondral ossification during fracture healing 62

3.1 Introduction 63

3.2 Method 65

3.2.1 Experimental Models of Fracture Healing to be Simulated 65

3.2.2 Iterative Procedure 65

3.2.3 Finite Element Model 66

3.2.4 Angiogenesis 68

3.2.5 Cell Migration, Cell Proliferation & Cell Death 70

3.2.6 Oxygen Transport 71

3.2.7 MSC Differentiation 73

3.2.8 Chondrocyte Hypertrophy and Endochondral Ossification 74

3.2.9 Simulations 75

3.3 Results 77

3.3.1 Normal Fracture Healing 77

3.3.2 Fracture Healing with Impaired Angiogenesis 81

3.4 Discussion 84

Chapter 4 The role of oxygen as a regulator of stem cell fate during the spontaneous repair of osteochondral defects 91

4.1 Introduction 92

4.2 Method 93

4.2.1 Iterative Procedure 93

4.2.2 Finite Element Model 94

4.2.3 Angiogenesis 95

4.2.4 Cell Migration, Cell Proliferation and Cell Death 96

4.2.5 Oxygen Transport 97

4.2.6 MSC Differentiation 98

4.2.7 Simulations 99
4.3 Results 99
4.3.1 Untreated Osteochondral Defect 99
4.3.2 Sensitivity Analysis 101
4.3.3 Influence of angiogenesis on osteochondral defect repair 103
4.4 Discussion 106
Chapter 5 An exploration of the role that functional loading of an osteochondral defect plays on tissue formation during the spontaneous repair process 114
5.1 Introduction 115
5.2 Method 117
5.2.1 *In Vitro* Experiment to be Simulated 117
5.2.2 Iterative Procedure 117
5.2.3 Finite Element Models 118
5.2.4 Angiogenesis 120
5.2.5 Cell Migration, Cell Proliferation and Cell Death 121
5.2.6 Oxygen Transport 122
5.2.7 MSC Differentiation and Chondrocyte Hypertrophy 123
5.2.8 Role of Strain in Cell Differentiation 124
5.2.9 Study design 124
5.3 Results 126
5.3.1 Simulation of In Vitro Models 126
5.3.2 Simulation of spontaneous repair; inhibition of chondrocyte hypertrophy in response to tissue strain 128
5.3.3 Simulation of spontaneous repair; formation of fibrocartilage in response to tissue strain 130
5.4 Discussion 131
Chapter 6 A Computational Model of Osteochondral Defect Repair Using a Tissue Engineered Scaffold 139

6.1 Introduction 140
6.2 Method 142
6.2.1 Iterative Procedure 142
6.2.2 Finite Element Models 142
6.2.3 Finite Element Models of Scaffold Treated Defects 144
6.2.4 Angiogenesis 145
6.2.5 Cell Migration, Cell Proliferation and Cell Death 146
6.2.6 Oxygen Transport 146
6.2.7 MSC Differentiation and Chondrocyte Hypertrophy 147
6.2.8 Bilayer and Trilayer Models 148
6.2.9 Study Design 149
6.3 Results 150
6.3.1 Spontaneous repair within an empty osteochondral defect 150
6.3.2 Osteochondral defect treated with a bilayer scaffold 152
6.3.3 Osteochondral defect treated with a trilayer scaffold 154
6.3.4 Osteochondral defects treated with cell-free scaffolds 156
6.4 Discussion 158
Chapter 7 Discussion 165
7.1 Main Findings of this Thesis 165
7.2 Updated Tissue Differentiation Algorithm 169
7.3 General Limitations 170
7.4 Summary 171
Chapter 8 Conclusions and Future Directions 173
8.1 Conclusions 173
8.2 Future Directions 174
Bibliography 177
Appendices 195

Appendix I: Parametric Study: Load Supported by Pin (Chapter 3) 195

Appendix II: Analysis of Random Variation in the Baseline Models (Chapter 4) 197

Appendix III: Comparison of Angiogenesis Models (Chapter 5) 199

Appendix IV: Alternative Rules for Strain Regulation of Hypertrophy (Chapter 5) 201

Appendix V: Alternative Rules for Strain Regulation of Fibrocartilage (Chapter 5) 207

Appendix VI: Model Parameters 209

List of Figures

Figure 2-1: The mesengenic process. The hypothesised scheme by which mesenchymal stem cells form mesenchymal tissues [77]. 9

Figure 2-2: (A) Exposure to fluid flow activates the RhoA/ROCK II signalling pathway which regulates MSC differentiation by generating tension within the actin cytoskeleton. (B) ROCK II is required alongside an intact cytoskeleton for Runx2 expression. 11

Figure 2-3: Mediators of mechanotransduction [105]. 15

Figure 2-4: Model of mechanically mediated lineage commitment to an adipogenic or osteogenic fate [68]. 19

Figure 2-5: Effect of substrate stiffness on the lineage commitment of MSCs [123]. 20

Figure 2-6: Effect of dynamically altering substrate stiffness on MSC morphology [67]. (a) Change in traction force with time for soft, stiff and dynamically stiffening (soft to stiff) hydrogels. (b) Colour traction maps (of spatial traction forces) for representative cells from the soft and stiff hydrogels (scale bar is 25 μm). (c) Change in cell shape with accompanying traction maps of a cell exposed to the dynamically stiffening hydrogel. 22

Figure 2-7: The relationship between cytoskeletal tension and cell shape [105]. 24

Figure 2-8: A low oxygen tension during expansion and differentiation promotes collagen and sGAG synthesis in MSCs cultured in (A & B) pellets and (C & D) hydrogels. Alcian blue (sGAG) and picrosirius red (collagen) staining for MSCs differentiated at either 5 % O2 or 20 % O2 following expansion at 5 % O2 in (E) pellets and (F) hydrogels [37]. 26

Figure 2-9: The mechanism by which the TGF-β superfamily triggers a response through the SMAD signalling pathway [137]. 29

Figure 2-10: Schematic depiction of the cross section of a long bone undergoing the stages of fracture healing. The stages include formation of the primary haematoma, soft and hard callus formation, internal and external bony bridging and finally bone remodelling [153]. 32

Figure 2-11: Progression of bone during fracture healing in long bones [23]. 35

Figure 2-12: Depiction of axial compression and translational shear as used in the models of fracture healing developed by Steiner et al [167]. 36

Figure 2-13: The formation of bone within an ovine fracture callus under axial compression (left) and a mixture of axial compression and transverse shear loading (right) at 2-, 3-, 6- and 9- week time points [171]. 38

Figure 2-14: Oxygen tension and temperature versus time within the periosteal callus of an ovine fractured tibia [184]. 40

Figure 2-15: Pattern of tissue formation during osteochondral defect repair within an untreated lapine model as reported by Orth *et al.* [4]. The schematics (A – E) display the (A) cylindrical, (B) infundibuliform, (C) plane, (D) concave and (E) convex geometrical subchondral bone reconstitution patterns. Images (F – K) show histological sections stained by Goldner's trichrome method to highlight bone while images (L – U) are histological sections stained with safranin-O to highlight sGAG (cartilage). Images (V – F) depict sections taken under polarized light microscopy in order to show the collagen architecture. 43

Figure 2-16: Progression of the repair tissue in an osteochondral defect within a minipig model at (a) week 6, (b) week 12 and (c) week 52 [8]. At weeks 6 and 12 the defect was filled with a mixture of fibrous tissue and fibrocartilage. At one year the repair tissue was composed mainly of fibrous tissue while within the subchondral region there was strong disruption as well as cyst formation. 45

Figure 2-17: General overview of the steps involved in tissue engineering based osteochondral defect repair [11]. 48

Figure 2-18: Results of a bioreactor study conducted by Pei et al [201]. Goat osteochondral defects treated with scaffolds cultured with mechanically- and biochemically- stimulated MSCs (Group A) at (a) 12 weeks and (b) 24 weeks. Goat osteochondral defects treated with scaffolds cultured with biochemically seeded MSCs (Group B) at (c) 12 weeks and (d) 24 weeks. Goat osteochondral defects left untreated (Group C) at (e) 12 weeks and (f) 24 weeks. 51

Figure 2-19: An overview of the computational mechanobiological modelling approach [17]. 55

Figure 2-20: Mechano-regulatory tissue differentiation algorithms developed by (A) Carter *et al.* [26] and (B) Claes *et al.* [163] 56

Figure 2-21: Mechano regulatory tissue differentiation algorithm developed by (A) Prendergast et al [22] and (B) Burke et al [44]. 57

Figure 2-22: Predictions of the course of ovine fracture healing using the tissue differentiation algorithm developed by Burke *et al.* [44] (Case A) and using the algorithm developed by Prendergast *et al.* [22] (Case B). These are compared with experimental observations obtained by Vetter et al [220]. 59

Figure 3-1: Iterative procedure used for the tissue differentiation model. 66

Figure 3-2: (A) FE Model of the fracture callus. Loading is applied at the top of the cortical bone. Displacement and fluid velocity boundary conditions are shown as u and v^f

respectively. (B) A 3-dimensional finite element with corresponding lattice. Each lattice point represents a potential location for a cell. 68
Figure 3-3: (A) Tissue differentiation regulated by substrate stiffness and oxygen availability. The oxygen availability axis extends radially from the centre of the circle with low oxygen in the centre which increases towards the periphery. The substrate stiffness axis extends circumferentially in a clockwise direction from the right side of the dotted line at the top of the circle. (B) Geometry and boundary conditions of the fracture callus 74
Figure 3-4: Results of parametric study. (A) Equation and values used to determine the parameters which best fit the experimental results of normal fracture healing at 10 dpf. The parameters chosen were the ones which produced the minimum value for d. (B) Calculated values for d where $O_2^{hypertrophy} = 30 \times 10^{-12}$ mol mm^{-3}, $O_2^{endochondral} = 50 \times 10^{-12}$ mol mm^{-3} and $V^{density,\ max}$ and V^{growth} were varied. (C) Calculated values for d where $O_2^{hypertrophy} = 30 \times 10^{-12}$ mol mm^{-3}, $O_2^{endochondral} = 70 \times 10^{-12}$ mol mm^{-3} and $V^{density,\ max}$ and V^{growth} were varied. (B) Calculated values for d where $O_2^{hypertrophy} = 50 \times 10^{-12}$ mol mm^{-3}, $O_2^{endochondral} = 70 \times 10^{-12}$ mol mm^{-3} and $V^{density,\ max}$ and V^{growth} were varied. The parameters which produced the smallest value for d were $O_2^{hypertrophy} = 30 \times 10^{-12}$ mol mm^{-3}, $O_2^{endochondral} = 50 \times 10^{-12}$ mol mm^{-3}, $V^{density,\ max} = 8$ % and $V^{growth} = 0.06$ mm day^{-1}. 78
Figure 3-5: (A) Experimental vs. Predicted percentages of callus area made up by cartilage and bone during normal fracture healing. (B) Safranin-O staining 10 days post fracture for normal fracture healing compared to model predictions for cartilage and bone formation. Both cartilage and hypertrophic cartilage are treated as the same material. (C) Experimental vs. Predicted percentage of cartilage tissue area which is hypertrophic in the normal fracture healing model at day 10. 79
Figure 3-6: Results from normal fracture healing at various time points: (A) Angiogenesis; (B) Oxygen Diffusion; (C) Cell Differentiation; (D) Tissue Phenotypes 80
Figure 3-7: Predicted tissue phenotypes from the impaired angiogenic fracture healing models: (A) Fracture healing during mild vascular impairment conditions (B) Fracture healing during moderate vascular impairment conditions (C) Fracture healing during severe vascular impairment conditions. 82
Figure 3-8: (A) Percentages of callus area made up by cartilage and bone observed experimentally by Miedel *et al.* [181] at day 10 in the ischemic fracture healing model compared to the percentages predicted in the computational model of fracture healing during mild vascular impairment. (B) Percentages of callus area made up by cartilage and bone observed experimentally at day 20 by Miedel *et al.* [181] in the ischemic fracture healing model compared

to the percentages predicted in the computational model of fracture healing during mild vascular impairment. (C) Percentages of cartilage tissue area which is hypertrophic observed experimentally by Miedel *et al.* [181] in the model of ischemic fracture healing compared to the predicted percentages obtained from the computational model of fracture healing during mild vascular impairment.....83
Figure 3-9: Predicted quantity of (A) cartilage and (B) bone at different time points in the simulations of fracture healing under normal, mild angiogenic impairment, moderate angiogenic impairment and severe angiogenic impairment.....84
Figure 4-1: Finite Element Model of the knee with an osteochondral defect including boundary conditions.....95
Figure 4-2: (A) Tissue differentiation algorithm as directed by the local oxygen tension and substrate stiffness. (B) A 3-dimensional finite element with corresponding lattice. Each lattice point represents a potential location for a cell.....98
Figure 4-3: Predicted pattern of (A) angiogenesis, (B) oxygen tension, (C) cell differentiation and (D) tissue type during the spontaneous repair of an osteochondral defect at day 28, 56 and 84.....101
Figure 4-4: Results of the parametric study where V^{growth} and L^{min} & L^{max} are varied with respect to their respective baseline values ($V^{growth,\ baseline}$ = 0.1 mm day^{-1}; $L^{min,\ baseline}$ = 0.2 mm & $L^{max,\ baseline}$ = 0.5 mm). The predicted angiogenesis and cell phenotype within the defect are shown for (A, B) day 28, (C, D) day 56 and (E, F) day 84.....105
Figure 4-5: Assessment of the effect that the different elements of the mechanically regulated model of angiogenesis had on the predicted vasculature at different time points during the predictions of spontaneous repair within an osteochondral defect. The angiogenesis model was split into two components; inhibition of vessel growth in regions of high octahedral shear strain (shear inhibition), and bias of blood vessel growth in the direction of the minimum principal strain (strain direction). The effects of these components were assessed by running the simulation where: (A) both shear inhibition and strain direction were active (B) shear inhibition was active and strain direction was inactive (C) shear inhibition was inactive and strain direction was active, and (D) shear inhibition and strain direction were inactive.....109
Figure 4-6: Assessment of the effect that the different elements of the mechanically regulated model of angiogenesis had on the predicted pattern of cell differentiation at different time points during the simulation of the spontaneous repair process within an osteochondral defect. The angiogenesis model was split into two components; inhibition of vessel growth

in regions of high octahedral shear strain (shear inhibition), and; bias of blood vessel growth towards the direction of the minimum principal strain (strain direction). The effect of these components were assessed by running the simulation where: (A) both shear inhibition and strain direction were active (B) shear inhibition was active and strain direction was inactive (C) shear inhibition was inactive and strain direction was active, and (D) shear inhibition and strain direction were inactive. 112
Figure 5-1: FE Model and boundary conditions for the (A) Unconfined and (B) Confined in-vitro simulations. Displacement in the x and z directions, fluid velocity and fluid pressure are shown as u^x, u^z, v^f and P respectively. 119
Figure 5-2: FE model and boundary conditions for the osteochondral defect simulations. 120
Figure 5-3: (A) A 3-dimensional finite element with corresponding lattice. Each lattice point represents a potential location for a cell. (B) Tissue differentiation algorithm as directed by the local oxygen tension and substrate stiffness. 123
Figure 5-4: Experimental and simulation results for the In vitro FS groups. Alcian red staining was used to determine the spatial arrangement of calcific deposition (and chondrocyte hypertrophy) in the unconfined and confined groups following 21 days of FS culture. These were compared to the predicted spatial distribution of chondrocyte hypertrophy and oxygen tension from the unconfined and confined in silico models of the FS groups. 126
Figure 5-5: Experimental and simulation results for the in vitro DC groups where chondrocyte hypertrophy was inhibited by the octahedral shear strain. (A; D) The spatial arrangement of calcific deposition (and chondrocyte hypertrophy) determined for the unconfined and confined groups after 21 days of DC. (B; E) The octahedral shear strain predicted by the unconfined and confined FE models at the onset of DC. (C; F) The predicted spatial arrangement of chondrocyte hypertrophy for the unconfined and confined in silico models after 21 days of DC for different values of $\varepsilon^{hypertrophy}$. 127
Figure 5-6: Model predictions of cell differentiation at different times during the spontaneous repair of an osteochondral defect using: (A) our previous tissue differentiation algorithm where chondrocyte hypertrophy was regulated solely by the oxygen tension (B – D) an updated algorithm where chondrocyte hypertrophy was regulated by the oxygen tension and the octahedral shear strain. The parameter $\varepsilon^{hypertrophy}$ was varied between (B) 5 %, (C) 7.5 % and (D) 10 %: 129

Figure 5-7: Model predictions of cell differentiation at different times during the spontaneous repair of an osteochondral defect using the updated algorithm where chondrocyte hypertrophy was regulated by the oxygen tension and the octahedral shear strain ($\varepsilon^{hypertrophy}$= 5 %) and fibrocartilage could form based on the local octahedral shear strain. The parameter $\varepsilon^{fibrocartilage}$ was varied between (E) 10 %, (F) 12.5 % and (G) 15 %. 131
Figure 5-8: Model Predictions vs experimental observations for the simulations where $\varepsilon^{hypertrophy}$ = 5 % and $\varepsilon^{fibrocartilage}$ = 12.5 %. (A – D) The model predictions of the spatial pattern of (A) blood vessel growth, (B) oxygen tension, (C) cell differentiation and (D) tissue formation at different stages of the spontaneous repair process within an osteochondral defect. (E) The spatial pattern of bone formation within an osteochondral defect observed at different stages of the spontaneous repair process by Orth et al. [4]. 135
Figure 5-9: Tissue differentiation algorithm where (A) MSC fate is governed by a combination of the substrate stiffness and local oxygen tension and (B) chondrocyte fate is governed by the octahedral shear strain and the local oxygen tension. 138
Figure 6-1: FE model and boundary conditions of an osteochondral defect for the simulations of (A) the spontaneous repair process and tissue formation following the implantation of the (B) bilayer scaffold and (C) trilayer scaffold , similar to that developed by Da et al. [58]...143
Figure 6-2: Tissue differentiation algorithm where (A) MSC fate is governed by a combination of the substrate stiffness and local oxygen tension and (B) chondrocyte fate is governed by the octahedral shear strain and the local oxygen tension. 148
Figure 6-3: Model predictions of cell differentiation at different times during the spontaneous repair of an osteochondral defect using: (A) our previous tissue differentiation algorithm where angiogenesis was independent of the tissue phenotype and (B - G) the updated model where the parameter T^{stable} was varied between (B) 2 weeks (C) 4 weeks (D) 6 weeks (E) 8 weeks (F) 10 weeks and (G) 12 weeks. 151
Figure 6-4: The relative volume of the different tissue phenotypes predicted within the chondral phase of the osteochondral defect at the (A) 12 week and (B) 24 week time points for different values of T^{stable}. 152
Figure 6-5: Results of the simulations of an osteochondral defect treated with the bilayer scaffold developed by Da et al. [58]. (A) Model predictions of cell differentiation for different values of the parameter T^{stable}. (B; C)The relative volume of the different tissue phenotypes predicted within the chondral phase of an empty defect (T^{stable} = 10 weeks) and a defect treated with the bilayer scaffold at the (B) 12 week and (C) 24 week time points for different values of T^{stable}. 154

Figure 6-6: Results of the simulations of an osteochondral defect treated with the trilayer scaffold developed by Da et al. [58]. (A) Model predictions of cell differentiation for different values of the parameter $T^{degrade}$. (B; C)The relative volume of the different tissue phenotypes predicted within the chondral phase of an empty defect (T^{stable} = 10 weeks) and a defect treated with the trilayer scaffold at the (B) 12 week and (C) 24 week time points for different values of $T^{degrade}$. 155
Figure 6-7: Comparison of the predicted spatial pattern of blood vessel formation at different time points between: (A) the model of the spontaneous repair process (B) the model of a defect treated with the bilayer scaffold and (C) the model of the defect treated with the trilayer scaffold. In all simulations T^{stable} = 10 weeks and for the trilayer simulation $T^{degrade}$ = 10 weeks. 156
Figure 6-8: Model predictions of the spatial and temporal pattern of (A) angiogenesis and (B) cell differentiation in the simulation of an osteochondral defect treated with a cell-free bilayer scaffold developed by Da et al.[58] 157
Figure 6-9: Model predictions of the spatial and temporal pattern of (A) angiogenesis and (B) cell differentiation in the simulation of an osteochondral defect treated with a cell-free trilayer scaffold developed by Da et al.[58] 158

List of Tables

Table 3-1: Dimensions of Finite Element Model [45] 67
Table 3-2: Material Properties 67
Table 3-3: Tissue Differentiation Model Parameters 70
Table 3-4: Cell Model Parameters 71
Table 3-5: Oxygen consumption parameters of each cell phenotype 72
Table 4-1: Material Properties 94
Table 4-2: Angiogenesis and MSC Differentiation Model Parameters 96
Table 4-3: Cell Model Parameters 97
Table 4-4: Oxygen parameters for each cell phenotype 98
Table 4-5: Results of the sensitivity analysis. The percentage of each tissue type is measured at day 84 and the standard condition is indicated in bold. Each parameter is varied between 50 % and 150 % of its respective baseline value. 102
Table 5-1: Material Parameters 118
Table 5-2: Angiogenesis and MSC Differentiation Model Parameters 121
Table 5-3: Cell Model Parameters 122
Table 5-4: Michealas-Menten parameters for each cell phenotype 123
Table 6-1: Material Parameters 143
Table 6-2: Angiogenesis and MSC Differentiation Model Parameters 145
Table 6-3: Cell Model Parameters 146
Table 6-4: Michealas-Menten parameters for each cell phenotype 147

Nomenclature

This section contains some of the abbreviations used in this thesis. It is not a full list of all abbreviations and symbols used – these will be explained in the text whenever used.

AB	adipocyte
ACI	autologous chondrocyte implantation
BMP	bone morphogenic protein
CC	chondrocyte
dpf	days post fracture
ECM	extra cellular matrix
FB	fibroblast
FC	fibrochondrocyte
FE	finite element
GIT1	GPCR kinase 2 interacting protein – 1
HC	hypertrophic chondrocyte
HIF-1	hypoxia induction factor
hMSC	human mesenchymal stem cell
IFM	interfragmentary movement
MACI	matrix assisted autologous chondrocyte implantation
MSC	mesenchymal stem cell
NMM	non muscle myosin
OB	osteoblast
OFF	oscillatory fluid flow
Rock	rho-kinase
TAZ	transcriptional coactivator with PDZ binding motif

TGF-β	transforming growth factor – β
TNF-α	tumour necrosis factor – α
VEGF	vascular endothelial growth factor
YAP	yes-associated protein

Publications and Conference Contributions

Publications

O'Reilly, A. R., Hankenson, K. D., Kelly, D. J., *A computational model to explore the role of angiogenic impairment on endochondral ossification during fracture healing.* Biomechanics and Modelling in Mechanobiology, Accepted February 2016. doi:10.1007/s10237-016-0759-4.

O'Reilly, A. R. and Kelly D. J., *The role of oxygen as a regulator of stem cell fate during the spontaneous repair of osteochondral defects.* Journal of Orthopaedic Research. Accepted, Nov 2015. doi: 10.1002/jor.23110.

Conference Contributions

O'Reilly, A.R., Kelly, D.J., 2012, *The potential of FEBio for modelling articular cartilage with a view to examining the influence of micro scale matrix distribution on macro scale tissue properties*, Proceedings of Bioengineering in Ireland, the Annual 18th Conference of the Section of Bioengineering of the Royal Academy of Medicine in Ireland. Queens University, Belfast, Northern Ireland. (Poster and Presentation).

O'Reilly, A.R., Kelly, D.J., 2013, *A finite element model of oxygen and glucose transport and consumption in agarose hydrogels seeded with mesenchymal stem cells*, Proceedings of Bioengineering in Ireland, the Annual 19th Conference of the Section of Bioengineering of the Royal Academy of Medicine in Ireland. Trinity College Dublin, Dublin, Ireland. (Presentation).

O'Reilly, A.R., Kelly, D.J., 2014, *The development of a mechanoregulation model of vascularisation during ischemic fracture repair*, Proceedings of Bioengineering in Ireland, the Annual 20th Conference of the Section of Bioengineering of the Royal Academy of Medicine in Ireland. University of Limerick, Limerick, Ireland (Presentation).

O'Reilly, A.R., Kelly, D.J., 2014, *The development of a mechanoregulation model of vascularisation during ischemic fracture repair,* 22nd Annual Symposium on Computation Methods in Orthopaedic Biomechanics (pre-ORS), Tulane University, New Orleans, Louisiana, USA. (Presentation).

O'Reilly, A.R., Kelly, D.J., 2014, *Integrating histological and biochemical analyses with computational models to determine the role of spatial ECM distribution on the mechanical properties of tissue engineered cartilage*. 60th Annual Meeting of the Orthopaedic Research Society 2014, Hyatt Regency New Orleans, Louisiana, USA. (Poster).

O'Reilly, A.R., Kelly, D.J., 2014, *Integrating histological and biochemical analyses with computational models to determine the role of spatial ECM distribution on the mechanical properties of tissue engineered cartilage*, 17th Annual Sir Bernard Crossland Symposium, NUI Galway, Galway. Ireland. (Poster and Presentation representing Trinity College Dublin).

O'Reilly, A. R., Kelly, D.J., 2015, *A computational model to explore the role of angiogenic impairment on endochondral ossification during fracture healing*, Proceedings of Bioengineering in Ireland, the Annual 21st Conference of the Section of Bioengineering of the Royal Academy of Medicine in Ireland. University College Dublin, Ireland. *Shortlisted for the Engineers Ireland Biomedical Research Medal*. (Presentation).

Chapter 1 Introduction

1.1 Osteochondral Defect Repair

Trauma to the knee often results in structural damage to the cartilaginous tissues of the joint [1]. When this damage penetrates through the hyaline cartilage and into the underlying subchondral bone, the resulting pathology is known as an osteochondral defect [2]. Osteochondral defects have a limited capacity for self-repair. In cases where the defect is below a specific size (deemed the 'critical size') a spontaneous repair process is initiated which leads to the partial regeneration of the damaged tissue. This 'critical size' varies depending on the animal model [3] (in rabbits the critical size is approximately less than φ 3 - 4 mm [4], while in in goats it is less than φ 6 mm [5]), however the general stages of the spontaneous repair process are the same. Initially, mesenchymal stem cells (MSCs) from the underlying bone marrow invade the defect and replace the damaged tissues [2,6–9]. This relief is generally short lived, however, as the repair tissue is structurally inferior to the native tissues [6,9]. This mechanical instability leads to a cascade of events which eventually results in the degradation of the repair tissue as well as further damage to the joint [6,9]. To address this inability to self-repair, several treatment solutions have been developed. Despite numerous advances however, all of the current available surgical options fail to regenerate the damaged tissue [10].

While currently not in widespread clinical use as a treatment for osteochondral defects, tissue engineering has the potential to provide long term relief to patients by reconstructing the damaged tissue. The general methodology involved in this process is to insert scaffolds seeded with cells into the defect site [11]. The basis of this is that the scaffold will provide the correct mechanical and biological cues to promote the seeded cell population to reconstruct the native tissue [11]. Due to their abundance, ease of expansion and ability to

differentiate into a number of tissue phenotypes, recent studies have explored the possibility of using MSCs for this application [12]. One of the main issues with using such cells however is that, while their behaviour *in vitro* has been well documented, the mechanisms by which they respond to their *in vivo* environment remain unclear.

The *in vivo* environment is complex and as such it is often difficult to isolate the effects of specific cues on MSC lineage commitment. In the context of osteochondral defect repair, there is emerging evidence to suggest that the extent of regeneration depends on the local mechanical environment. For example, continuous passive motion of the injured limb during the spontaneous osteochondral defect repair process has been shown to result in a more robust repair tissue compared to when subjects are subjected to active loading regimes or complete immobilisation [13,14]. Appropriate regulation of angiogenesis may also be central to osteochondral defect regeneration. For example, limiting the ingress of blood vessels into the defect site has also been shown to assist in the spontaneous repair process by promoting the formation of hyaline cartilage within the chondral phase [15,16]. While these studies have provided clues as to the global factors which influence repair, the exact mechanisms by which these interventions enhance repair remain unknown. A better understanding of factors regulating cell fate during such regenerative processes should lead to improved tissue engineering strategies for osteochondral defect repair.

1.2 Computational Mechanobiology

Van Der Meulen proposed that the aim of computational mechanobiology was 'to determine the quantitative rules that govern the effects of mechanical loading on tissue differentiation, growth, adaptation and maintenance by trial-and-error' [17]. This field utilises computer models to simulate the *in vivo* environment and in turn provide a means with which to better understand how environmental cues direct cell behaviour. Computational mechanobiology has been used to explore, among other features, the factors which direct

embryonic limb development [18], muscle adaptation [19], cell migration and proliferation [20], and blood vessel growth [21]. In the case of this thesis, computational mechanobiology may also be used to explore how environmental factors affect stem cell differentiation and tissue formation during regenerative processes such as the spontaneous repair process within an osteochondral defect. The basic premise of this is that a finite element (FE) model is used to simulate the mechanical environment *in vivo*. The predictions of the model (i.e. strain, fluid flow, stress, etc.) are then used as input parameters for a tissue differentiation algorithm which predicts MSC fate based on an underlying hypothesis. As MSCs are predicted to differentiate and produce new tissue, the material parameters in the FE model are updated. The overall process is run iteratively to simulate the time course of the regenerative process. At the end of this, the underlying model hypotheses are tested by comparing the predicted results with experimental observations.

In recent years a number of advances have been made within the field of computational mechanobiology. Improvements in computing power have allowed for more detailed simulations, while more complex material models of biological tissues have led to the development of more accurate FE models. In conjunction with these improvements, new tissue differentiation algorithms have been developed. While many of these models have hypothesised that stem cell fate is governed solely by the mechanical environment [22–27], more recent *in silico* studies have highlighted the importance of angiogenesis and/or the nutrient supply in directing stem cell differentiation [26,28–32]. One such algorithm was developed by Burke *et al.* [33], and was based on the findings of *in vitro* studies which have shown that substrate stiffness [34–36] and oxygen availability [37–40], play a key role in regulating MSC fate. Based on studies which have shown that angiogenesis is regulated by tissue strain [41–43], Burke *et al.* [33] further hypothesised that biophysical cues act indirectly on MSC fate by determining blood vessel progression and hence oxygen availability. Using their tissue

differentiation algorithm, the authors were able to accurately predict the progression of fracture healing within an ovine tibia [44], the acceleration of fracture healing in mice deficient in the angiogenic inhibiting factor Thrombospondin-2 [45], and the temporal and spatial pattern of tissue formation in a mechanically loaded bone chamber [46].

This algorithm has yet to be applied to an osteochondral defect. Before this can be achieved, a number of deficiencies associated with the model must first be addressed. Firstly, Burke *et al.* [33] did not propose a specific hypothesis to describe how environmental factors regulate the initiation and progression of chondrocyte hypertrophy and endochondral ossification; rather it was assumed that cartilage is converted directly to bone at the interface between the two tissues. Regarding these processes, *in vitro* studies have shown that they are affected by the local oxygen tension [37,47–50] as well as by mechanical loading of the cells [51,52]. Furthermore, in the developed algorithm the authors did not differentiate between hyaline cartilage and mechanically inferior fibrocartilage. Finally, in the models developed by Burke *et al.* [33], it was assumed that blood vessel growth was directed solely by the mechanical environment. However it has been hypothesised that angiogenesis within an osteochondral defect is affected by growth factors released by the differentiated cells [53,54]. Implementing these features into the current tissue differentiation algorithm will not only improve its predictive capacity, but also provide useful insights into how the environment of the osteochondral defect directs regeneration of the damaged tissues.

1.3 Objectives

The overall objective of this thesis is to develop a computational model of MSC differentiation and tissue formation within an osteochondral defect. This model will then be used to help improve tissue engineering strategies under development for the treatment of osteochondral defects.

In order to achieve this objective, the model of tissue differentiation developed by Burke *et al.* [44] will first be improved upon. Additional rules which were absent in the original algorithm will be developed to account for the process of chondrocyte hypertrophy and endochondral ossification. This is necessary as these are key features which dictate the pattern of healing observed within an osteochondral defect. This thesis will test the hypothesis that it is the local oxygen tension which directs the process of chondrocyte hypertrophy and endochondral ossification during skeletal tissue regeneration. In order to test this, the predictions of a model incorporating the hypothesised rules will be compared to the results of in vivo studies where angiogenesis, and hence oxygen availability, is altered within a regenerating tissue. Such a situation arises during ischemic fracture healing. In such a scenario, severe disruption of the local blood supply results in a pattern of healing which differs to the one observed during non-ischemic fracture healing. To this end, the updated computational mechanobiological model will first be used to simulate the time-course of healing within both normal and ischemic fracture healing.

In the next phase of this thesis the efficacy of the updated tissue differentiation algorithm will be examined by using it to model the spontaneous repair process within an osteochondral defect. The model will be used to explore the extent to which angiogenesis, and the subsequent oxygen environment, affects the spontaneous repair process. This will be achieved by varying the parameters controlling blood vessel growth within the developed models. The validity of the model will again be tested by comparing the simulation predictions to the spatial patterns of tissue differentiation observed *in vivo* within osteochondral defects treated with factors known to inhibit angiogenesis [15,16].

Following this, the tissue differentiation algorithm will be updated to account for the findings of *in vitro* studies which have shown that dynamic compressive loading inhibits hypertrophy of chondrocytes [51,52], while dynamic tensile loading promotes the formation of

fibrocartilage [55,56]. The developed rules will again be tested by using them to model the spontaneous repair process within an osteochondral defect, the results of which will be compared to experimental observations [4,57].

In the final study of this thesis the developed framework will be used to model the observed course of healing in an osteochondral defect treated with a multiphasic, tissue engineered scaffold [58]. As part of this study, a series of rules whereby functional cartilage inhibits the progression of angiogenesis will be tested within the model. This model will then be used to better understand the mechanisms by which MSC laden scaffolds can facilitate osteochondral defect regeneration.

Chapter 2 Literature Review

In this chapter a background to this work is provided through a review of the applicable scientific literature. Firstly, the potential of mesenchymal stem cells (MSCs) for use in tissue engineering strategies is introduced. The *in vitro* studies examining the factors affecting the lineage commitment of these progenitor cells is then reviewed. Following this, the difficulty in isolating these factors within the *in-vivo* environment is presented through a description of the stages of, and the factors affecting, both fracture healing of long bones and the spontaneous repair of osteochondral defects. Finally, the concept of computational mechanobiology is outlined as a potential means of determining the factors which influence MSC fate *in vivo*.

2.1 Mesenchymal Stem Cells

Mesenchymal stem cells (MSCs) are non-hematopoietic stromal cells which were first discovered in bone marrow by Friedenstein *et al.* [59]. They have subsequently been isolated from almost every other form of connective tissue [60]. MSCs possess a number of abilities and features which make them viable candidates for use in tissue engineering strategies [61]. The first is their ability to differentiate into a variety of mesenchymal phenotypes. Pittenger *et al.*[12] showed that, when cultured in suitable conditions *in-vitro*, MSCs could be induced to differentiate exclusively down chondrogenic, osteogenic or adipogenic lineages. They also found that this multilineage potential was unaffected even after multiple expansions within culture. This feature is necessary as MSCs represent approximately 1 in every 10,000 nucleated cells within bone marrow and thus must be expanded before use in tissue engineering strategies [62]. Finally, MSCs have been shown to be non-immunogenic and therefore have the potential to be transplanted into an allogeneic host without the need for immunosuppression [62].

For these reasons, numerous studies have examined MSCs as a treatment strategy in musculoskeletal repair. Although many of these have reported varying degrees of success, there are only a limited number of published clinical studies exploring MSC- based approaches to tissue repair [63]. In order to improve upon this and develop more accurate tissue engineering treatment strategies, a better understanding of how the local environment affects the lineage commitment of MSCs is required.

Caplan *et al.*[64] proposed that lineage commitment is one of the five stages by which MSCs form mesengenic tissues (Figure 2-1). While it has emerged that this overall process is more complex than initially postulated (for example, mature cells can dedifferentiate into MSCs [65]), the general five stage hypothesis is still considered to be accurate. Prior to the lineage commitment phase MSCs proliferate extensively by mitosis. Following lineage

commitment, the cells differentiate before maturing and eventually producing mesenchymal tissue [64]. It is known that the lineage commitment stage is dictated by environmental cues. *In vitro* studies have examined the roles played by substrate stiffness [34,66,67], cell shape [68,69], mechanical forces [70,71], oxygen tension [37,72,73] and biochemical cues [74–76] on cell fate. The details of these studies are discussed later in this review. Although these mechanisms are well understood *in vitro*, the specific conditions which drive differentiation *in vivo* are less well understood [62]. A better understanding of how these factors regulate MSCs within the *in vivo* environment will greatly improve many aspects within the field of regenerative medicine.

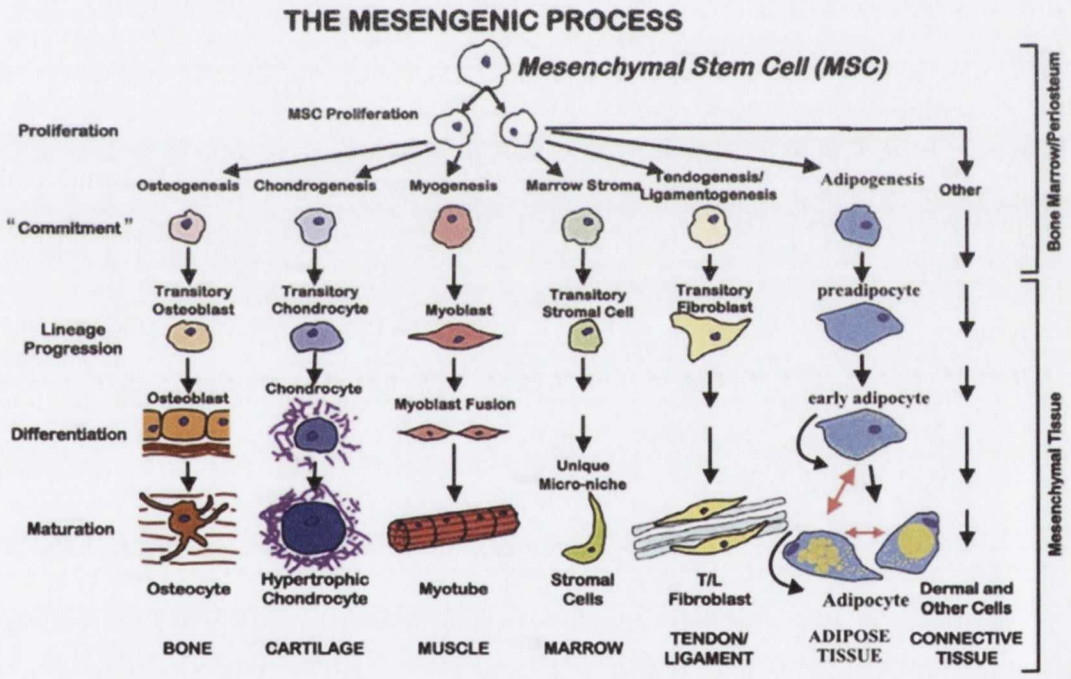

Figure 2-1: The mesengenic process. The hypothesised scheme by which mesenchymal stem cells form mesenchymal tissues [77].

2.2 Environmental Factors Regulating Stem Cell Differentiation

2.2.1 Mechanical Regulation

As early as the late nineteenth century it was hypothesised that mechanics play a role in guiding tissue differentiation in developing or regenerating limbs [70]. Since then, a number of mechano-regulation theories have been proposed to explain how the local mechanical

environment determines the lineage commitment of MSCs [70]. One of the earliest theories was proposed by Pauwels *et al.* [78,79] who suggested that stress and strain guide the tissue differentiation pathways of stem cells. In this model, hydrostatic pressure results in cartilage and distortional strain which favours fibrous tissue formation. Similar mechano-regulation algorithms have been suggested since then (Section 2.4). While extensive work has examined these potential mechanisms, the exact processes with which stem cells sense and respond to mechanical cues from their external environment remains largely unknown [70]. Despite this, results from *in vitro* studies have reported distinct lineage responses of MSCs to specific mechanical cues, namely: oscillatory fluid flow (OFF); dynamic and static compressive loading regimes; dynamic tensile loading and; hydrostatic pressure.

2.2.1.1 Oscillatory Fluid Flow (OFF)

Based on the results of studies which have shown that mechanical loading of long bones induces an internal fluid flow, Li *et al.*[80] proposed that OFF plays a role in the commitment of MSCs towards an osteoblastic lineage. In their study they found that hMSCs which were exposed to OFF exhibited an increase in the expression of osteoblastic markers as well as cell proliferation and intracellular Ca^{2+} activity. Later work went on to show that, as well as upregulating Runx2 (an osteogenic transcription factor), OFF also led to an increase in the expression of Sox9 (a chondrogenic marker) and PPARγ (an adipogenic marker) [81]. In this study, Arnsdorff *et al.*[81] examined the mechanism controlling this by showing that OFF activated the RhoA and Rho-kinase II (ROCK II) signalling pathways. These results led them to hypothesise that cytoskeletal tension plays a role in this particular mechanism (Figure 2-2; discussed in greater detail in Section 2.2.3). The authors validated this hypothesis by inhibiting ROCK II with Y27632 treatment which resulted in a decrease in Runx2 expression as well as an increase in Sox9 expression (a marker of chondrogenesis). Furthermore, activation of RhoA with lysophosphatidic acid sodium salt (LPA) resulted in

a twofold increase in Runx2 which in turn was further upregulated with OFF. In a separate study Arnsdorff *et al.*[82] also reported that OFF regulates Wnt β-catenin activity, a signalling pathway which has been shown to be involved in both osteogenesis and chondrogenesis of MSCs [83]. Briefly, β-catenin is involved in signalling for osteogenesis. In the absence of Wnt ligands with which to bond to, it is tagged for degradation inside the cytoplasm of the cell. When Wnt ligands are present however, β-catenin is able to translocate to the nucleus where it increases the expression of osteogenic genes [83]. Arnsdorff *et al.*[82] reported an increase in Wnt and β-catenin signalling in response to OFF.

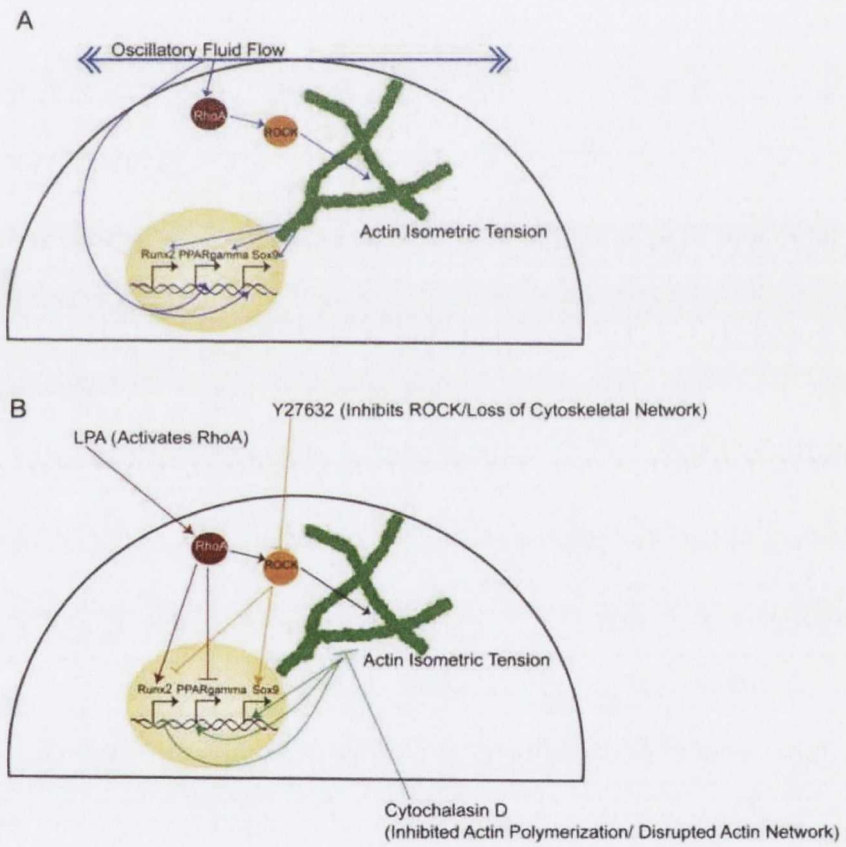

Figure 2-2: (A) Exposure to fluid flow activates the RhoA/ROCK II signalling pathway which regulates MSC differentiation by generating tension within the actin cytoskeleton. (B) ROCK II is required alongside an intact cytoskeleton for Runx2 expression.

2.2.1.2 Tensile and Compressive Loading

Other forms of mechanical stimulation include tensile and compressive loading. Both of these loading regimes have been shown to promote different lineage commitments in MSCs. Firstly, dynamic tensile loading has been reported to promote osteogenic and

fibrogenic gene expression while inhibiting the genetic marker of hyaline cartilage in MSCs [55,84–89]. Sumanasinghe *et al.*[85] reported that uniaxial tensile loading promoted an upregulation in the mRNA expression of bone morphogenic protein 2 (BMP-2) in hMSCs which were seeded in 3D collagen matrices and cultured in the absence of osteogenic induction factors. BMP-2 has previously been found to promote osteogenesis [90]. Similarly Sen *et al.*[88] reported that biaxial tensile loading of MSCs cultured in adipogenic media inhibited adipogenesis and promoted osteogenesis. In all of these studies an upregulation of β-catenin signalling was implicated in promoting osteogenic differentiation of MSCs [84,88]. In the case of fibrogenesis, dynamic tensile loading was found to promote this lineage commitment when applied to MSCs seeded within collagen fibre scaffolds which mimicked the mechanical properties of tendons and ligaments [87]. The mechanisms controlling this lineage commitment are however, not as well defined as they are in the case of osteogenesis [87]. The magnitude of the loading environment has been shown to affect whether MSCs commit to an osteogenic or a fibrogenic lineage [91,92]. In this case, low magnitude tensile strains (< 5 %) have been found to upregulate the expression of osteogenic genetic markers (Cbfa1, ALP and OCN) while higher magnitudes of tensile strain (> 10 %) upregulate the genetic markers indicative of fibrogenesis (type I collagen, type III collagen and tenascin-C) [91,92].

Dynamic tensile loading has also been implicated in the synthesis of the fibrous components of fibrocartilage [55,56]. This was observed by both Thomopoulis *et al.*[55] and Connelly *et al.*[56] who exposed MSCs to dynamic tensile strain. Both studies observed an increase in the genetic markers for the fibrous elements of fibrocartilage (upregulation of scleraxis and type I collagen) in response to dynamic tensile strain [55,56]. Conversely, tensile loading had little to no effect on the expression of the cartilaginous elements (Sox 9 and aggrecan) of fibrocartilage without the presence of the chondrogenic factor transforming growth factor β-3 (TGF-β3) [55,56]. Based on these findings both studies concluded that the

fibrous components of fibrocartilage could be generated using mechanical cues while both mechanical and biochemical cues were required to generate the cartilage components of the tissue [55,56].

While tensile loading promotes osteogenesis and fibrogenesis, there is an extensive body of research which reports that compressive loading increases the expression of chondrogenic markers [93]. Static compressive loading has been shown to promote chondrogenesis of mice embryonic limb bud MSCs [94]. Similarly, Huang *et al.*[95] found that dynamic compressive strain induced chondrogenesis in bone marrow derived MSCs as effectively as the biochemical cue transforming growth factor β-1 (TGF-β1)[96]. It was later shown that dynamic compression of the matrix was required in all three principle directions to induce a chondrogenic response from hMSCs [97]. Zahedmanesh *et al.*[97] demonstrated this using finite element analysis of dynamically compressed fibrin-polyurethane composite scaffolds seeded with hMSCs. The time at which dynamic compression is applied has also been demonstrated to be important in initiating chondrogenesis in MSCs [89]. Mouw *et al.*[89] showed that when dynamic compression was applied at day 8, it failed to upregulate chondrogenic gene expression in bovine bone marrow derived MSCs. When loading was applied at day 16 however, MSCs increased their chondrogenic gene expression. These results suggest that the mechanisms by which MSCs respond to compressive mechanical cues are dependent upon the stage of chondrogenesis within the cell and also potentially dependent on the stage of development of the pericellular matrix. Finally, Li *et al.*[98] showed that dynamic compression of hMSCs promoted chondrogenesis by inducing the cells to produce the chondrogenic promoters TGF-β1 and TGF-β3.

2.2.1.3 Hydrostatic Pressure

Hydrostatic pressure is another mechanical cue which has been shown to initiate MSC commitment towards a chondrogenic lineage [70]. One such study, conducted by Wagner

et al.[99], examined MSCs which were cultured in both osteogenic and chondrogenic media and were subjected to cyclic hydrostatic pressure with a magnitude of 1 MPa. The author reported that hydrostatic pressure resulted in a marked increase in proteoglycan staining (a marker of chondrogenesis) as well as an upregulation in the mRNA expression of chondrogenic genes such as aggrecan, type II collagen and Sox9. In a similar study, Carroll *et al.*[100] examined the response of porcine MSCs to cyclic hydrostatic pressure of a magnitude of 10 MPa. The authors found that the application of hydrostatic pressure led to an increase in the development of functional cartilage tissues as well as a suppression of tissue calcification. These findings conformed with earlier results from the study conducted by Wong *et al.* [101] where chondrocytes were exposed to a hydrostatic pressure of 5 MPa over a period of 3 days. In this case the gene MMP-13, which is one of the dominant genes in the endochondral ossification process, was downregulated. The exact mechanisms controlling the response of MSCs to hydrostatic pressure are unknown, although Steward *et al.*[102] showed that they are linked to cell-matrix interactions. The understanding of these mechanisms is further complicated by the fact that MSCs appear to exhibit a donor dependency in their response to hydrostatic pressure [103]. This was reported by Meyer *et al.*[103] who found that, while porcine MSCs taken from one particular donor showed no response to hydrostatic pressure, porcine MSCs taken from a separate donor responded with an increased expression of chondrogenic genes.

The exact cellular mechanisms with which the cell senses and initiates a response to each of the mechanical regulators discussed in this section are largely unknown [70]. Despite this, there are a number of mechano-sensory mechanisms which have been extensively studied and are hypothesised to be involved in these processes [104]. These are discussed in the next section.

2.2.1.4 Mechanosensation

Mechano-sensing is the process by which cells probe and detect external forces within their environment [105]. Following mechano-sensation, cells convert the mechanical signals into biochemical responses through a process known as mechano-transduction [105]. Mechano-sensing and mechano-transduction have been shown to involve a number of elements of the cell. These include; cell to extra cellular matrix adhesions; cell-cell adhesions; surface processes; membrane components and; cytoskeletal filaments (Figure 2-3) [105].

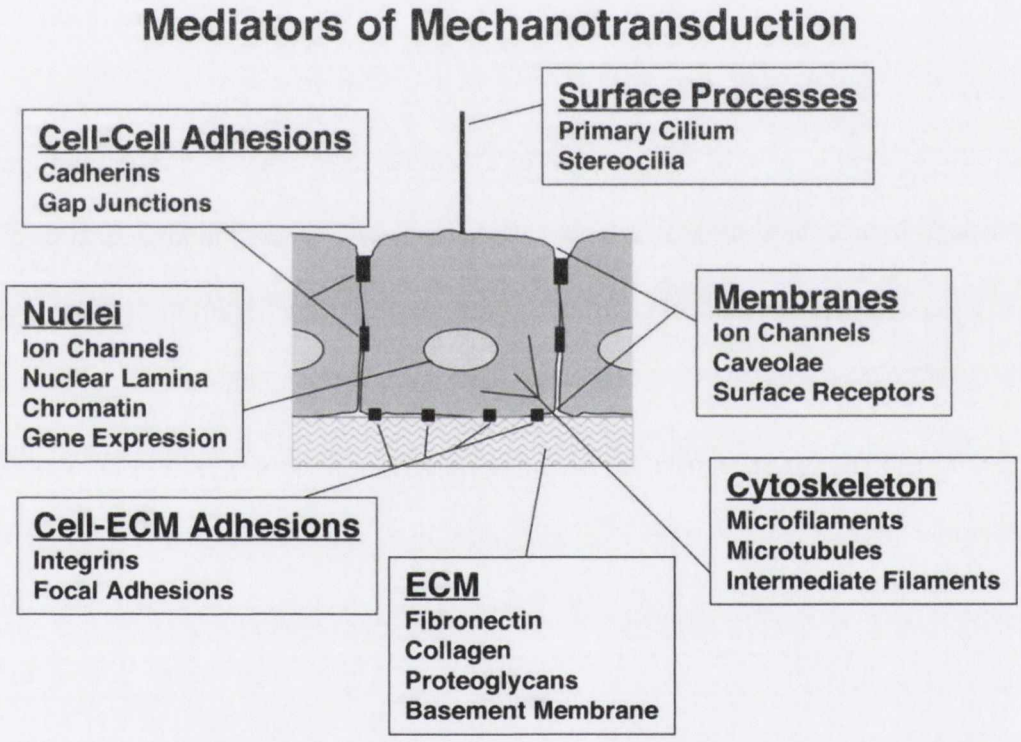

Figure 2-3: Mediators of mechanotransduction [105].

Among the most studied mechano-sensory mechanisms are the adhesion structures which connect the cellular cytoskeleton to the surrounding matrix [71]. Known as focal adhesions, these are composed of integrins, as well as a multitude of adaptor and signalling proteins [71]. Through these adhesion structures, the cell is able to probe and generate biochemical signals in response to the local environment [106]. One such response which has been studied involves focal adhesion structures changing their shape, size and composition

when exposed to external forces [106]. As well as this, focal adhesion structures have been shown to play a role in the lineage commitment of MSCs in response to the stiffness of the surrounding substrate (Section 2.2.3) [106].

Cell-Cell adhesion mechano-sensation mechanisms have been proposed to operate through gap junctions [107]. Gap junctions are channels which span the membrane of cells and allow the passage of hormones, neurotransmitters and ions to pass between neighbouring cells [107]. It has been hypothesised that in osteoblasts, the application of physical stimuli such as fluid flow or cell deformation serves to physically stretch the gap junction and thus promote intercellular communication [107]. This mechanism has been found in all bone-forming cells [108].

The primary cilium is one of the main surface processes which is thought to function as a dual sensory organelle capable of both mechano-sensation and chemo-sensation [109]. It is a microtubule based structure which projects out into the extracellular matrix from the cell body and has been linked to MSC lineage commitment [110]. It is believed to act as a flow meter which responds to oscillatory fluid flow [110]. Hoey *et al.* [110] demonstrated that in hMSCs, the mechanics of the primary cilium change in response to oscillatory fluid flow. In addition to this they also showed that it plays a role in the mechano-regulated induction of osteogenesis. Furthermore, in cartilage the primary cilium has been linked to the compression based upregulation of chondrogenic gene expression and matrix synthesis through the ATP modulated release of the intracellular messenger Ca^{2+} [111].

The term 'membrane components' refers to the large number of cell-surface receptors which exist on the cell membrane. It has been postulated that many of these surface receptors are able to respond to both mechanical strains and biochemical cues [71]. It is because of these multiple receptor roles that it is very difficult to isolate the receptors which respond to mechanical cues [71]. Despite this, a small number of the surface receptors have been found

which have the capacity to modify cell fate in response to mechanical cues [71]. One example of this is the mechanical force activation of the Notch-signalling pathway [112]. Fundamentally the Notch pathway allows for short range signalling between adjacent cells and has a role in promoting cell fate and specific cell differentiation lineages [112]. It has been hypothesised that the Notch pathway is initiated by external mechanical forces which uncovers the Notch activation site on the cell membrane [112].

The cytoskeleton works in parallel with many of the other mechano-sensory mechanisms outlined in this section. The term 'cytoskeleton' refers to the network of fibres which are contained within the cytoplasm [104]. These fibres support compressive forces by means of structures known as microtubules and tensile forces through actin microfilaments and actin intermediate filaments [104]. One of the main mechanisms with which the cytoskeleton is involved in mechano-sensation and mechano-transduction is through the remodelling of the actin fibres [71]. The signalling pathway involved in this process is the Rho-family GTPases, namely RhoA [113]. RhoA activates its effector Rho-kinase (ROCK) which in turn induces contraction of the cytoskeleton [105]. This is one of the main processes with which cells sense and respond to cell shape and substrate stiffness. These mechanisms are outlined in sections 2.2.2 and 2.2.3.

2.2.2 Cell Shape

Cell shape plays an important role in the functions of specific cell phenotypes. A rounded morphology is beneficial for adipocytes as it assists in lipid storage, while in osteoblasts a spread morphology promotes matrix deposition during bone morphology [114]. Cell morphology has also been isolated as a key factor in the commitment of MSCs to a specific lineage [68,115]. McBeath *et al.* [68] used a micro-patterning technique which controlled cell shape to examine its effect on MSC differentiation. The authors reported that MSCs which adopted a rounded morphology expressed markers for adipogenesis while MSCs

which adopted a spread morphology expressed markers for osteogenesis. Other studies have also concluded that a round cell morphology facilitates chondrogenesis of MSCs [69,115–117] while the induction of an aligned, spindle-shaped morphology through the use of topographical cues has been shown to promote tenogenesis in MSCs [118].

McBeath *et al.* [68] also explored the mechanisms governing the process by which lineage commitment is dictated by cell shape. Mesenchymal stem cells with a spread morphology tend to have more cytoskeletal stress fibres than their round counterparts, and the authors postulate that the process is controlled by cytoskeletal tension, namely through the RhoA and ROCK signalling pathways. Both RhoA and ROCK have been shown to be upregulated in cells with a spread morphology, indicating that both proteins are involved in the process [68,113].

The mechanism by which RhoA affects lineage commitment was examined using MSCs which were modified to have either an overexpression or an inhibition of RhoA [68]. Firstly, when cell morphology was not induced through their micro-patterning technique, the former group expressed osteogenic markers and the latter expressed adipogenic markers. When the RhoA overexpression group was cultured with a round morphology however, contrary to expectations, they exhibited markers for adipogenesis. Similarly, when MSCs which had an inhibition of RhoA were induced to have a spread morphology, they expressed markers for osteogenesis. These results imply that, while RhoA has a dependency on cell shape and MSC fate, it does not act downstream to cell shape in determining MSC lineage commitment (Figure 2-4). The role of ROCK in the process was then examined by either inhibiting or overexpressing it in MSC groups which had either a round or spread morphology. In contrast to RhoA, when ROCK was inhibited, both round and spread cells expressed adipogenic markers. Similarly, when ROCK was upregulated, both round and spread cells exhibited markers for osteogenesis. These results imply that cell shape-

mediated lineage commitment was regulated by ROCK- induced cytoskeletal tension (Figure 2-4).

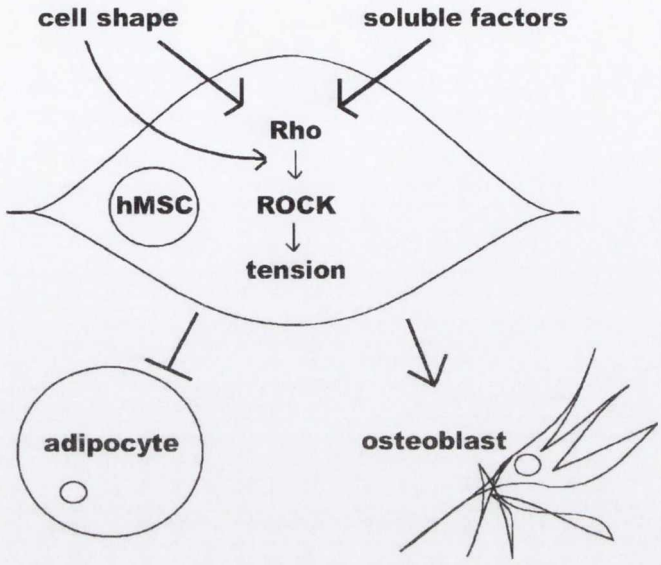

Figure 2-4: Model of mechanically mediated lineage commitment to an adipogenic or osteogenic fate [68].

It is clear that MSC shape (and its contribution to MSC lineage commitment) is determined by changes to the cell's actin cytoskeleton. A number of studies have validated this by culturing MSCs with the actin disrupting agent cytochalasin-D [34,68,119]. All of these studies reported that disrupting the actin cytoskeleton resulted in a rounded morphology which in turn led to either adipogenesis or chondrogenesis [34,68,119]. It has been hypothesised that the cellular shape and cytoskeletal tension are related by means of a complex force balance relationship between the microfilaments, microtubules and the extra cellular matrix [105]. The details of this relationship are discussed in the following section in which the role played by substrate stiffness on MSC fate is examined.

2.2.3 Substrate Stiffness

The effect of substrate stiffness on the determination of MSC lineage commitment was first proposed by Engler *et al.* [34]. Their hypothesis was based on the fact that many of the tissues which MSCs migrate to (such as bone, smooth muscle and neurological tissue) are synthesised by cells which have an anchorage dependency [34]. Earlier studies had shown

that, for a wide range of differentiated cell types, the focal adhesion structures and the cytoskeleton were affected by the stiffness of the local substrate [120–122]. Engler *et al.* [34] proposed that in MSCs these features were also governed by the stiffness of the local substrate. As these elements contribute to the lineage commitment of naïve MSCs, the authors further hypothesised that MSC fate was affected by the stiffness of the local substrate [34].

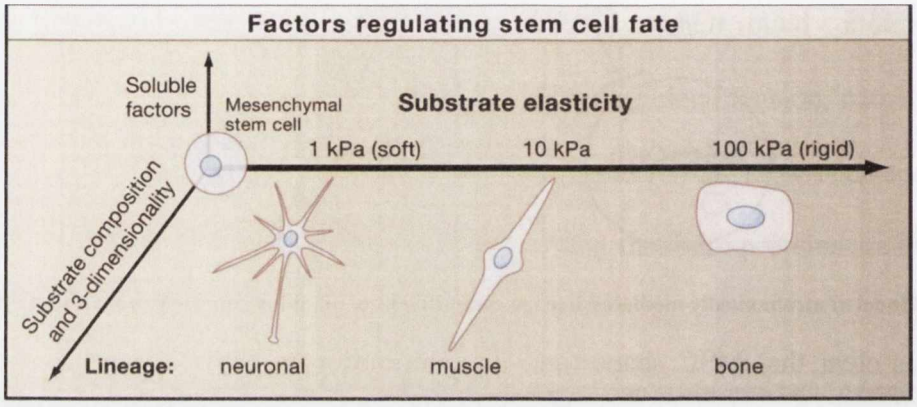

Figure 2-5: Effect of substrate stiffness on the lineage commitment of MSCs [123].

To test this hypothesis, human mesenchymal stem cells (hMSCs) were cultured in 2D on variably compliant polyacrylamide gels coated with collagen I [34]. It was found that a soft substrate which mimicked the stiffness of brain tissue (0.1 – 1 kPa) promoted the expression of genetic markers, as well as a dendritic morphology, indicative of a neurological lineage [34]. Similarly, gels which had a stiffness representative of smooth muscle (8 – 17 kPa) promoted myogenesis and a spindle shaped morphology [34]. It was also found that stiff gels mimicking the elasticity of osteoid (25 – 50 kPa) promoted the polygonal osteoblastic morphology and an increase in osteogenic markers (Figure 2-5) [34].

Later work expanded upon the findings of Engler *et al.* [34]. Firstly, Pek *et al.* [124] reported the same results when they repeated the study within 3D hydrogels. Park *et al.* [35] then showed that hMSCs cultured on polyacrylamide gels with a stiffness of 1 kPa expressed markers for both chondrogenesis and adipogenesis. Guvendiran & Burdick [67] then examined the role of dynamic substrate stiffening in a bid to better understand how the changing local

mechanical environments within the body affects MSC differentiation. In the first part of this study hMSCs were cultured on either soft or stiff substrates in bipotenial media which could promote both adipogenesis and osteogenesis. Similar to previous studies, it was found that a soft substrate promoted a rounded cell morphology and an upregulation in the markers of adipogenesis. Furthermore, stiff gels produced spread cell morphologies which stained positive for osteogenic markers (Figure 2-6). When the authors examined the effect of dynamically stiffening gels it was found that when stiffening was induced at an early time point, more of the cells were rounded and had committed to an adipogenic lineage. When stiffening was induced at a later time point, however, it was found that more of the cells were spread and had committed to an osteogenic lineage. Finally, when stiffening was induced midway through the culturing time the authors reported that the ratio of osteogenic to adipogenic cells approached 1:1.

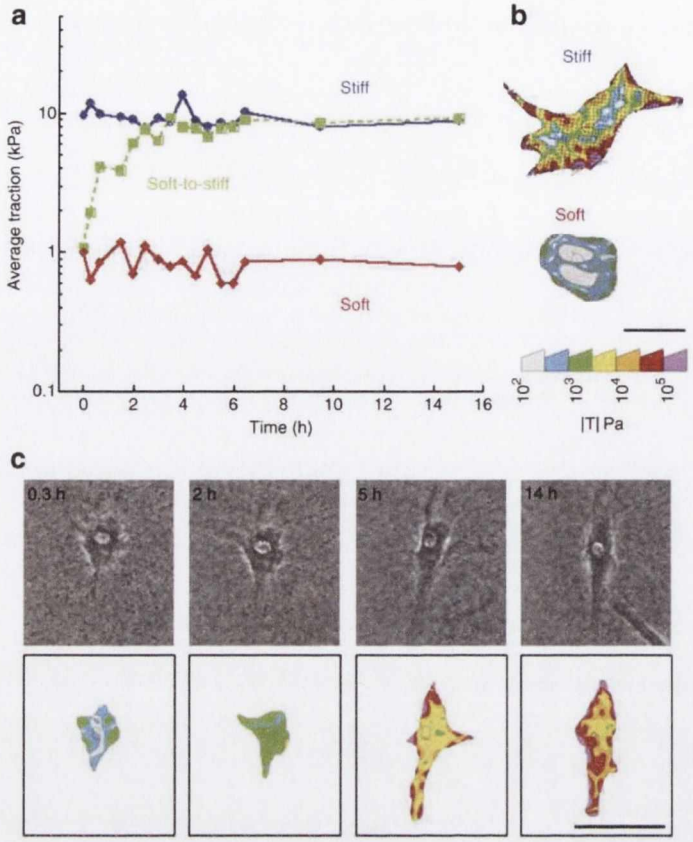

Figure 2-6: Effect of dynamically altering substrate stiffness on MSC morphology [67]. (a) Change in traction force with time for soft, stiff and dynamically stiffening (soft to stiff) hydrogels. (b) Colour traction maps (of spatial traction forces) for representative cells from the soft and stiff hydrogels (scale bar is 25 μm). (c) Change in cell shape with accompanying traction maps of a cell exposed to the dynamically stiffening hydrogel.

The studies presented in this section also examined the mechanisms by which substrate stiffness directs the lineage commitment of MSCs. Engler *et al.* [34] hypothesised that this involved two processes. In the first process, MSCs 'sense' their environment by deforming it on a molecular level. This involves forming actin structures which adhere to the surrounding substrate. These focal adhesion structures manipulate the local matrix by contracting in response to the cytoskeletal motor non-muscle myosin (NMM). The cells respond to stiffer substrates by producing stiffer focal adhesions and greater quantities of NMM. To test this hypothesis Engler *et al.* [34] blocked NMM II using the inhibitor blebbistatin. The result of this was that the cells retained their round morphology independently of the substrate stiffness. Pek *et al.* [124] further validated this hypothesis by examining the effect of adding RGD receptors to the hydrogel. RGD receptors provide further adhesion sites and thus lead to the formation of additional focal adhesions [124]. The

result of this was that in the stiff gel group, it was reported that the addition of RGD led to a greater degree of cell spreading. Park *et al.* [35] then examined the role played by adhesion strength by first comparing the number of focal adhesions between gels of varying stiffness and then by directly measuring the focal adhesion strength between the gel groups. It was found that both of these parameters increased in response to increasing substrate stiffness. Finally, Guvendiran & Burdick [67] disrupted the formation of the actin structures by culturing the cells in the inhibitor cytochalasin-D. This led the cells to retain their round morphology and to commit to an adipogenic lineage independent of stiffness. They also reported the same results as Engler *et al.* [34] when they cultured cells in blebbistatin.

The second process in the regulation of MSC fate by substrate stiffness describes the mechanism by which cells respond to their local environment after sensing its stiffness [34]. Engler *et al.* [34] hypothesised that this involved the release of mechano-transducers which generate signals to the cell based on the magnitude of the force experienced by the actin structures. This molecular mechanism was isolated by Dupont *et al.* [125]. The nuclear relays of the mechanical signals were reported as Yorkie-homologues Yes-associated protein (YAP) and transcriptional coactivator with PDZ-binding motif (TAZ) [125]. The authors showed that YAP/TAZ transcriptional activity was regulated by ECM rigidity. Cells cultured on a stiff substrate (40 kPa) showed increased YAP/TAZ activity as well as increased translocation of YAP/TAZ from the cytoplasm to the nucleus when compared to cells cultured on a soft substrate (0.7 kPa). Dupont *et al.* [125] also induced adipogenesis on a stiff substrate by inhibiting YAP/TAZ activity and osteogenesis on a soft substrate by overexpression of YAP/TAZ activity.

An interesting feature of the studies outlined in this section is that there appears to be a potential coupling between the determination of cell fate by both substrate stiffness and cell shape. All of the literature reviewed in this section reported that stiff substrates produce

spread cells while soft substrates produce rounded cells. Furthermore, Dupont *et al.* [125] reported that cell shape was also a regulator of YAP/TAZ activity with greater activity occurring in spread cells. A mechanism has been proposed by Ingber *et al.* [105] to explain how the cell shape and cytoskeletal tension are related via a complex force balance relationship between the microfilaments, microtubules and substrate stiffness. As outlined above, the intracellular tension on a rigid substrate is high as the cell produces stiffer stress fibres and an increase in the expression of NMM II. It has also been found that when cultured on a stiff substrate, bovine endothelial cells responded by upregulating ROCK and myosin activity [113]. These factors serve to increase the cytoskeletal tension which results in cell flattening, bundling of the actin filaments and enhanced buckling of the microtubules. This in turn results in a spread cell morphology (Figure 2-7). Conversely, when the stiffness of the surrounding substrate is so low that it is not able to bear the cell traction forces, the forces transfer to the internal microtubules. These respond by buckling and bending, which in turn leads to disassembly of the stress fibres and eventually rounding of the cell (Figure 2-7).

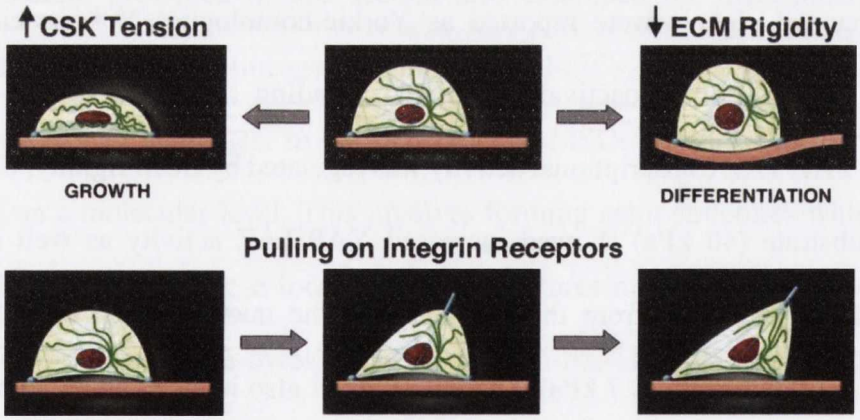

Figure 2-7: The relationship between cytoskeletal tension and cell shape [105].

It is important to note that one of the major flaws with all of the studies discussed in this section is that each one examined the effect of substrate stiffness on MSC differentiation using an elastic material rather than a viscoelastic material. Elastic materials have an elastic modulus which is independent of time and, as such, they exert a constant traction force on

the cell. Conversely, viscoelastic materials have a time dependent elastic modulus and, as such, experience stress relaxation. This property is hypothesised to reduce the resistance to cellular traction forces over time and to limit the amount of cell spreading [126]. As the majority of ECM components within the in-vivo environment are viscoelastic, Chaudhuri *et al.* [126] examined how varying the stiffness of viscoelastic materials affects the degree of cell spreading. In this study the authors observed that, contrary to expectations, spreading on soft substrates (~ 1 kPa) which exhibited stress relaxation was greater than cell spreading on elastic substrates of the same modulus. Furthermore, cell spreading on the soft viscoelastic material was similar to cell spreading on stiffer (~ 9 kPa) elastic substrates. In addition to this, the experimental behaviour was also observed in computational models. It is important to note, however, that the authors still observed a relationship between the degree of cellular spreading and the stiffness of the viscoelastic material. This study therefore raises questions regarding the previously observed stiffness ranges which induce specific lineage commitments in MSCs, rather than contradicting the overall hypothesis that substrate stiffness regulates MSC lineage commitment.

The studies reviewed in this section also indicate that while substrate stiffness can direct stem cell fate, it is not specific to particular phenotypes. This is most apparent in the finding of Park *et al.* [35] who reported both adipogenic and chondrogenic markers in response to a soft substrate (1 kPa). This implies that in some cases, matrix stiffness alone is not sufficient to determine cell fate and that other factors must therefore be considered.

2.2.4 Oxygen Tension

Different cell phenotypes of mesenchymal origin reside in various tissues around the body. The oxygen tension differs between these tissue types; for example, bone is highly vascularised and is known to have an oxygen tension which ranges between 5 % and 12.5 % [37] while articular cartilage is avascular and been shown to support an oxygen tension as low

as 1 % [72,73]. For this reason it has been postulated that oxygen tension plays a crucial role in the determination of lineage commitment in MSCs. *In vitro* studies have examined the effect of oxygen tension on MSCs during both the expansion phase and the differentiation phase. In the case of the former, Sheehy *et al.* [37] showed that bone marrow derived porcine MSCs which were expanded in a low oxygen environment (5 % O_2 tension) showed greater potential for osteogenic and chondrogenic differentiation (Figure 2-8). Similarly, Valorani *et al.* [127] reported that adipose derived hMSCs exhibited increased proliferation and viability when cultured in 2 % oxygen tension. The low oxygen tension also enhanced the ability of MSCs to undergo adipogenesis and osteogenesis when compared to MSCs which were expanded in a normoxic oxygen tension (21 % O_2 tension).

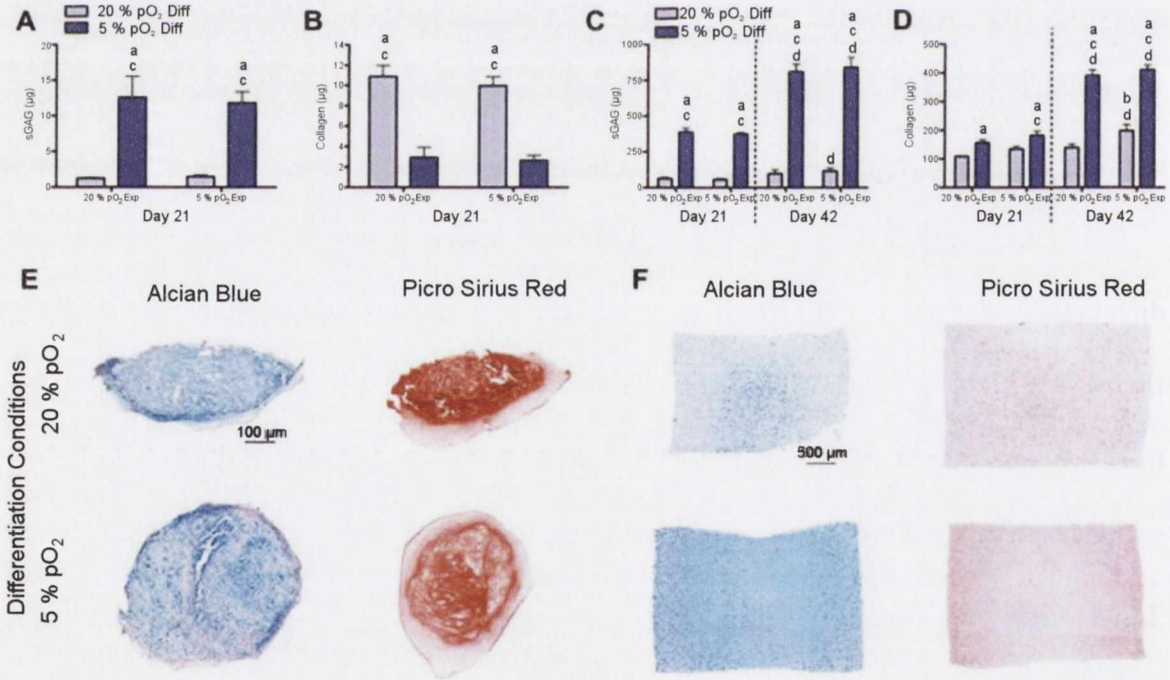

Figure 2-8: A low oxygen tension during expansion and differentiation promotes collagen and sGAG synthesis in MSCs cultured in (A & B) pellets and (C & D) hydrogels. Alcian blue (sGAG) and picrosirius red (collagen) staining for MSCs differentiated at either 5 % O2 or 20 % O2 following expansion at 5 % O2 in (E) pellets and (F) hydrogels [37].

Oxygen tension has also been shown to play a role in the determination of MSC lineage commitment. Firstly, there is extensive literature which reports that a hypoxic

environment supports chondrogenesis of MSCs [37–39,50,103]. Munir *et al.* [38] examined the effect of differentiating human adipose derived MSCs at low oxygen tension (5 % O_2 tension) in the presence of transforming growth factor-β3 (TGF-β3). The authors demonstrated that the hypoxic conditions led to a higher expression of chondrogenic genes (Sox9; aggrecan; collagen II) and a decreased expression for markers of hypertrophy (collagen X). Similarly Markway *et al.* [39] reported that an oxygen tension of less than 2 %, in conjunction with TGF-β3, promoted chondrogenic gene expression in human bone marrow derived MSCs. Finally, Meyer *et al.*[128] found that a low oxygen environment (5% O2) was a better promoter of chondrogenesis than dynamic compression. Conversely, hypoxic environments have been shown to inhibit adipogenic and fibrogenic lineage commitment in MSCs [40,129]. Holzwarth *et al.*[129] reported that, when cultured at 1% oxygen tension, adipogenesis in human bone marrow derived MSCs was impaired. Similarly, Sheehy *et al.* [37] found that hypoxia reduced the expression of type I collagen, which is a marker for fibrogenesis, in MSCs.

The relationship between oxygen tension and osteogenesis of MSCs appears more complex. Holzwarth *et al.* [129] reported that 1 % oxygen tension decreased osteogenic differentiation in bone marrow derived MSCs; however this potential was restored at 3 % oxygen tension. In a more recent study, Wagegg *et al.* [40] showed that an oxygen tension of less than 2 % promoted the expression of the osteogenic transcription factor Runx2 in human bone marrow derived MSCs. Similarly, Sheehy *et al.* [37] reported that 5 % oxygen tension enhanced osteogenesis of bone marrow derived MSCs compared to normoxic conditions (20 % O_2 tension). In contrast it has been shown that the same oxygen tension (5 % O_2 tension) inhibits osteogenesis of human adipose derived MSCs [130]. Furthermore, an oxygen tension of 2 % was reported to inhibit osteogenic differentiation of murine adipose derived MSCs cultured in osteogenic media when compared to cells cultured at 21 % [131]. These results may

suggest that MSCs taken from different locations respond differentially to altered levels of oxygen tension.

The mechanism through which hypoxia initiates specific responses in MSCs is mediated through the transcriptional regulator Hypoxia-Induction Factor (HIF-1) [132]. HIF-1 is composed of an oxygen sensitive α subunit and a constitutively expressed β subunit [40]. In hypoxic conditions HIF-1α is stabilised and activates a number of genes, one of which promotes the transcription of Sox9 and aggrecan (both of which are markers of chondrogenesis) [133]. Kanichai *et al.* [134] demonstrated that an siRNA knockdown of HIF-1α eliminated the pro-chondrogenic effect of low oxygen tension. HIF-1α has also been reported to inhibit both an adipogenic and fibrogenic lineage commitment [40,133]. Duval *et al.* [133] showed that a promotion of HIF-1α inhibited the expression of the fibrogenic markers COL1A1, COL1A2 and COL3A1. Similarly, Wagegg *et al.* [40] found that hypoxia-induced expression (< 2 % O_2 tension) of HIF-1α suppressed the adipogenic PPARG gene expression in human bone marrow derived MSCs. A shRNA mediated knockdown of HIF-1α then led to an upregulation of these adipogenic markers in both hypoxic and normoxic oxygen tension. These findings indicate that hypoxia promotes a chondrogenic lineage commitment in MSCs while normoxia promotes either adipogenic or fibrogenic differentiation.

2.2.5 Biochemical Cues

The roles played by biochemical cues on stem cell function and fate have been recognised and studied extensively [135]. One of the main groups of growth factors involved in stem cell differentiation is the Transforming Growth Factor β (TGF-β) superfamily [74]. These factors are released by cells and are known to feature prominently in a wide range of cellular functions including embryonic development and tissue regeneration [74]. Cells are able to sense and respond to these chemical signals through transmembrane proteins which act as chemoreceptors [74]. These serve to bind signalling molecules from outside the cell and

transmit information through sequences of molecular switches and signal transduction cascades to the nucleus [74]. In the case of the TGF-β superfamily the signal passes to the nucleus through the SMAD pathway (Figure 2-9) [136]. The response of specific growth factors has been studied extensively both *in vitro* and *in vivo.* In the case of the latter, this has involved examining human genetic disorders as well as animal models whereby the expression of these molecules has been suppressed or promoted through genetic manipulation [75]. Through these models a number of TGF-β subfamilies have emerged which play prominent roles in the differentiation of MSCs; these include TGF-β1 and TGF-β3, as well as the bone morphogenetic protein (BMP) group.

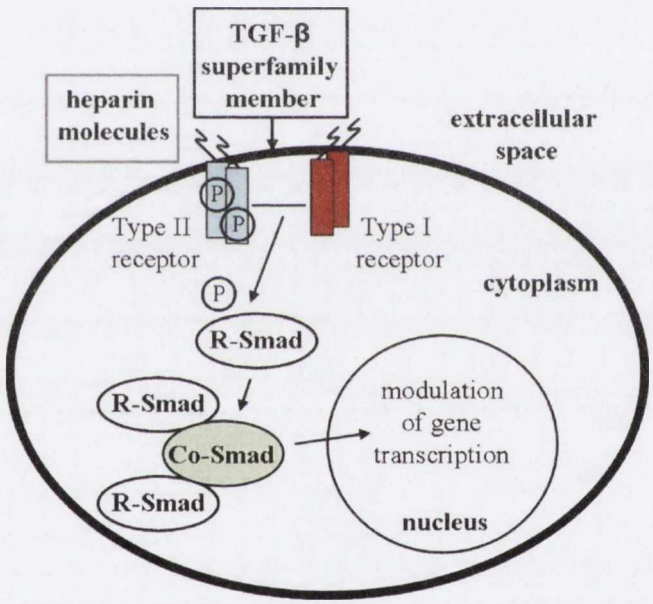

Figure 2-9: The mechanism by which the TGF-β superfamily triggers a response through the SMAD signalling pathway [137].

TGF-β1 and TGF- β3 are closely related isoforms which direct a number of functions within the body [76]. TGF- β1 is associated with regulating the proliferation and differentiation of osteoprogenitor cells *in vivo* [138]. It is released from the bone matrix by osteoclasts during the process of bone remodelling where it then serves to recruit MSCs to the remodelling site [76]. This function is apparent through studies conducted on the genetic disorder Camurati-Engelman disease (CED) which manifests itself in fusiform thickening of the diaphysis of the long bone and skull [138]. Tang *et al.* [138] showed that this was caused by high levels of TGF-

β1 in the bone marrow which in turn resulted in an uncoupling of the osteoclast-osteoblast bone resorption-formation relationship during remodelling. *In vitro* studies have also shown that TGF-β1 promotes MSC proliferation as well an upregulation of chondrogenic markers [136,139,140]. Similar studies have shown this to be the case with MSCs cultured with TGF-β3 [141,142]. It was also reported that TGF-β3 promotes a more chondrogenic phenotype in MSCs compared to TGF-β1 [143].

BMPs are multifunctional growth factors which play important roles in heart, neural and cartilage development as well as postnatal bone development [144]. Three of these proteins which have been studied extensively are BMP-2, BMP-4 and BMP-7 [144]. Mice which are deficient for either BMP-2 or BMP-4 have been shown to die at an early stage of embryotic development [145,146]. In the case of BMP-2 this was due to defects in cardiac development [146] while BMP-4 mutant embryos showed little to no mesodermal development [145]. Similarly, BMP-7 has been shown to be synthesised by chondrocytes and to play a role in the regeneration of articular cartilage [137]. *In-vitro* studies have also found that these factors induce chondrogenic differentiation of MSCs [137]. When cultured with BMP-2, MSCs present an increase in cartilaginous extra cellular matrix production as well a decrease in gene expression for the fibrogenic marker collagen type I [137]. BMP-4 has been reported to produce similar results as well as to reduce gene expression for type X collagen, which is a marker for hypertrophy [137]. Similarly, BMP-7 stimulates the expression of cartilaginous extra cellular matrix components. This factor however also negatively affects the proliferation activity of MSCs [137].

The role played by BMPs *in vivo* is complex. For example BMP-2 has also been shown to affect osteoblast differentiation and proliferation [144]. Overexpressing this protein in mice has promotes an increase in bone size and bone formation rates [147]. This osteoinductive ability has in turn been examined in a number of animal models which have

explored its impact on the healing of critical sized defects in long bones [144]. Chang *et al.* [148] reported that bone defects healed with the implantation of a bioresorbable polymer mixed with bone marrow derived MSCs to which adenoviral BMP-2 was added.

There are many other growth factors which influence MSC differentiation. Further discussion of these would, however, exceed the scope of this review.

2.3 Tissue Differentiation *In Vivo*

Although MSC behaviour has been studied extensively *in vitro*, the mechanisms controlling their behaviour *in vivo* remains less well understood [62]. In order to provide insights into how MSCs respond to their environment *in vivo*, studies have examined spontaneous tissue repair events. Two of these events which are detailed in this review are fracture healing of long bones and osteochondral defect repair.

2.3.1 Fracture Healing

A fracture arises when the upper limit of bone strain is exceeded, often through physical trauma [149]. Following fracture a series of generalised specific and systematic tissue responses are set in motion which conclude with the restoration of the biomechanical competence of the tissue [149]. There are two different overall responses by which a fracture is repaired; direct and indirect healing. Direct fracture healing (also known as primary fracture healing) rarely occurs naturally as it requires absolute stability as well as anatomical reduction of the fracture ends with no gap formation between the cortical surfaces [150,151]. In this case, the interrupted cortex is re-established through intramembranous ossification (whereby osteoprogenitor cells differentiate directly into osteoblasts which then mineralise the surrounding tissue) [150,151]. Indirect (or secondary fracture healing) is a more complex mechanism which arises from inadequate stabilisation of the fracture site [149–151]. This results in the formation of an external callus which is eventually vascularised and mineralised to

form new bone [149–151]. This new bone is formed through a mixture of intramembranous and endochondral ossification (the process by which cartilage is mineralised and remodelled to form lamellar bone) [149–151]. Secondary healing is the dominant healing mechanism *in vivo* and as such is detailed in this section.

Indirect healing can be broken up into three overlapping phases which serve the function of firstly removing any damaged tissue before re-establishing the vascular supply and eventually producing new skeletal matrix [149]. The first stage in this process is the inflammation phase whereby a haematoma forms around the fracture site and stabilises the fracture gap [152]. As this stage ends the reparative stage begins and new tissue is formed within the callus [152]. The final process is the remodelling phase in which the tissue which was formed during the reparative phase is remodelled in order to restore the biomechanical properties of normal bone to the site [152].

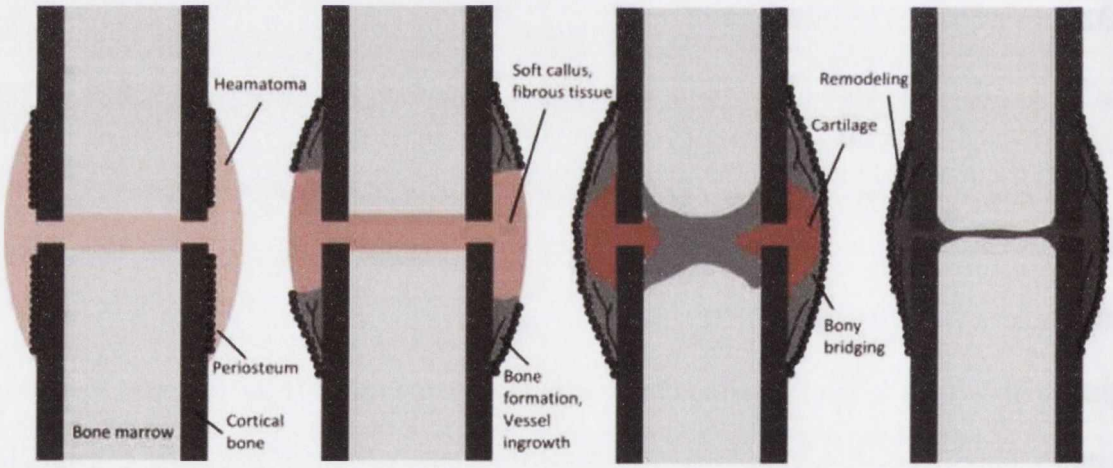

Figure 2-10: Schematic depiction of the cross section of a long bone undergoing the stages of fracture healing. The stages include formation of the primary haematoma, soft and hard callus formation, internal and external bony bridging and finally bone remodelling [153].

2.3.1.1 The Inflammation Phase

The inflammation phase is initiated immediately following fracture of the bone and lasts for approximately 5 days in weight-bearing bones in humans [149]. The fracture impact results in a disruption of the local blood supply which in turn causes haemorrhage, anoxia, cell death and an aseptic inflammatory response (Figure 2-10) [150]. The damaged blood

vessels at the bone-ends and the associated soft tissue bleed into the fracture site and a clot known as the primary haematoma forms between the bone fragments [152]. The region is invaded with growth factors, cytokines, fibroblasts, stem cells and inflammatory cells (macrophages, monocytes, lymphocytes and polymorphonuclear cells) [154]. The inflammatory cells perform a number of functions including the removal of debris and necrotic tissue from the fracture site as well as the secretion of additional growth factors [149]. One factor involved in this process is vascular endothelial growth factor (VEGF) which initiates the ingrowth of vascular tissue [154].

The released growth factors also promote the migration of stem cells into the haematoma [150]. These factors include BMPs such as BMP-7 as well as tumour necrosis factor-α (TNF-α) [90,155]. Hypoxic gradients also regulate MSC trafficking through the factor HIF-1α [156]. It remains unclear, however, from which tissue these cells migrate [150]. Studies have suggested that potential sources of these cells are the periosteum [157,158], the marrow space within the medullary cavity [149,158] and the surrounding soft tissue [158]. As well as this, it has been demonstrated that there is a systematic recruitment of circulating MSCs to the injured site [159,160]. Within the haematoma these invading stem cells rapidly proliferate immediately after the fracture is initiated and reach a maximum rate after 24 hours [152]. The invading and proliferating stem cells, in conjunction with the aforementioned inflammatory cells, vessel cells and fibroblasts then replace the haematoma with a fibrin rich granulation tissue which provides a degree of stability to the fracture [161].

2.3.1.2 The Reparative Phase

The reparative phase begins in weight bearing bones in humans at approximately day 4 and continues until approximately day 40 [149]. One of the first features of this phase occurs when the periosteum 'lifts' off the bone surface due to intramembranous ossification which stems from the cambial layer of the periosteum (Figure 2-10) [162]. Einhorn *et al.* [162]

hypothesised that this is one of the most important events of fracture healing as it leads to the release of osteoprogenitor cells into the fracture site. A bone front persists from the periosteal and endosteal cortices towards the fracture gap through intramembranous ossification (Figure 2-10) [163]. Simultaneously, when the callus is not sufficiently stabilised (as is the case in most animal models), the MSCs within the core differentiate into chondrocytes [150] and the granulation tissue is replaced with cartilaginous tissue to form the soft callus [151]. This can be split into two regions; the external callus which forms on the outside of the fractured bone and; the internal callus which is the region within the medullary cavity [151]. At this point the bone front progresses via endochondral ossification [151]. During this process chondrocytes become hypertrophic [164]. In general these are more prominent in close proximity to bone [164]. The hypertrophic chondrocytes direct the mineralisation of their surrounding matrix and secrete factors such as VEGF which promotes vascularisation of the tissue [164]. The result of this is that as the bone front progresses through the callus it is preceded by blood capillaries which invade the mineralised cartilage [165]. Through this process a bony bridge forms in the external callus distal to the bone (Figure 2-11) [151]. This forms a bony union between the two fractured surfaces [151]. Alternatively, or in conjunction with this, a bony bridge forms in the internal callus [151]. In any of these cases the bridge provides additional stability to the fracture by creating a load transfer path distal to the damaged cortical bone [163]. As the strain within the fracture gap decreases, bone continues to form within this region until the callus is almost completely ossified [163]. At this point the entire region is referred to as the hard callus [151].

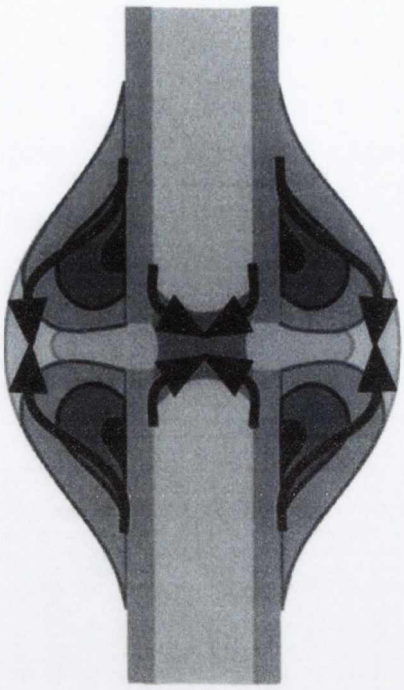

Figure 2-11: Progression of bone during fracture healing in long bones [23].

2.3.1.3 The Remodelling Phase

The remodelling phase begins following bony union and can take years to complete [150]. Although the newly formed hard callus provides stability, it does not restore the biomechanical properties of cortical bone [150]. One of the main processes during this phase involves remodelling any woven bone (formed by intramembranous ossification) with the mechanically superior lamellar bone [150]. The newly formed bone in the distal regions of both the internal and external calluses are exposed to very little strain during loading [149,151]. According to Wolff's Law, these 'low strain' regions are thus resorbed [149,151]. In the internal callus a medullarization process occurs whereby the unloaded bone is resorbed and replaced by marrow [149,151]. Similarly, in the external callus, the bone regions which are distal to the cortical bone are resorbed, which serves to restore the shape of the bone (Figure 2-10) [149,151].

2.3.1.4 Factors Affecting Fracture Healing

There are a large number of factors which influence the outcomes of fracture healing, many of which interact to form complex pathways which direct the progression of bone

healing [166]. Three of these factors which have been studied extensively are mechanics, angiogenesis and oxygen tension.

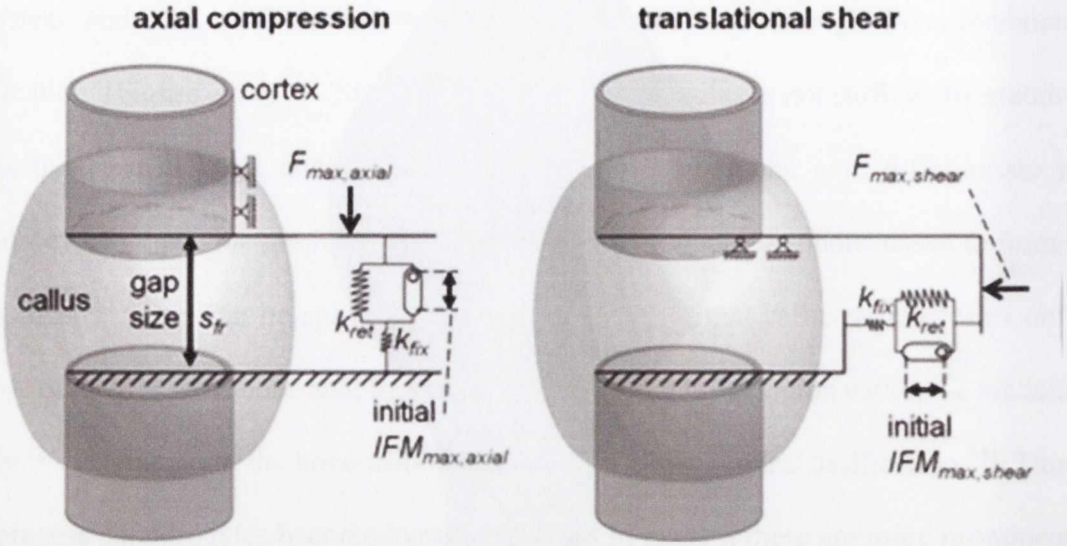

Figure 2-12: Depiction of axial compression and translational shear as used in the models of fracture healing developed by Steiner et al [167].

Within the area of mechanics, interfragmentary movement (IFM) has been isolated as the most important parameter influencing the fracture healing process [168]. Two different types of IFM which have been shown to affect healing are axial compression [169,170] and translational shear [171–173] (Figure 2-12). With regards to the former category, it has been shown that axial compression can lead to decreased healing times as well as a lower probability of delayed union [169–171]. This was reported by Goodship *et al.* [169] who found that micro-movement within the axial direction promoted healing in ovine tibias. Later work by Claes *et al.* [170] showed that this was dependent upon the amplitude of compression whereby high magnitude strains led to the production of more fibrocartilage and less bone when compared to low magnitude strains. While the effect of axial compression is well documented, the role played by translational shear is more complex. In their study, Epari *et al.* [171] examined the effect of two different external fixation devices on fracture healing in an ovine tibia. The first, deemed rigid, allowed movement only within the axial plane while the second, referred to as semi rigid, allowed for both axial compression and translational

shear. The latter group resulted in slower healing due to the persistence of cartilage tissue within the fracture callus (Figure 2-13). A similar finding was reported by Augat *et al.* [172] who examined the effects of translational shear and axial compression on fracture healing within an ovine tibia. The authors reported that translational shear resulted in severely delayed healing and delayed bone formation, as well as to a reduction in the mechanical stability of the callus. In contrast to this, Park *et al.* [173] found that shear stimulation not only led to the formation of a larger fracture callus and greater cartilage differentiation, but also that it did not inhibit bony union. In order to address these contradictory results, Steiner *et al.* [167] used numerical simulations to compare the response of fracture healing in ovine tibias to different loading conditions. By comparing the healing outcomes of different loading directions under normalized mechanical conditions the authors concluded that axial compression was more beneficial to the fracture healing process than translational shear. In accordance with these results it was also hypothesised by Augat *et al.* [172] and Epari *et al.* [174] that the findings obtained by Park *et al.* [173] were inadvertently caused by the induction of an axially compressive loading environment which was generated within their model of fracture healing.

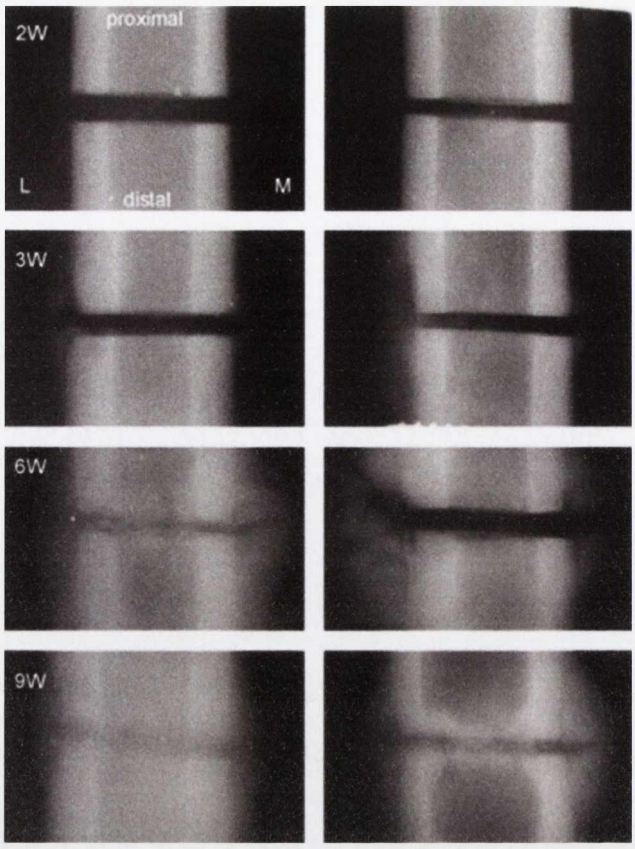

Figure 2-13: The formation of bone within an ovine fracture callus under axial compression (left) and a mixture of axial compression and transverse shear loading (right) at 2-, 3-, 6- and 9- week time points [171].

Despite extensive experimental investigations, the mechanisms with which mechanical stimulation affects fracture healing remains relatively unclear. It has been hypothesised that mechanical stimulation directly affects the lineage commitment of MSCs [22] (Section 2.2.1 and Section 2.4). However, it has also been shown that mechanical stimulation affects vascularisation of the fracture callus [23,175]. This feature has also been studied extensively and has been isolated as one of the most important factors in promoting successful fracture healing [166].

Blood vessels transport oxygen, nutrients and other biological factors necessary for bone formation [176]. As such the relationship between successful bone healing and an adequate blood supply has been recognised for a considerable amount of time [177]. Previous studies have explored this relationship by either inhibiting [82,175,178,179] or promoting [180–182] vascularisation of the fracture callus. In the case of the former; Hausman *et al.* [178] showed that treatment of a fracture with the angiogenic inhibitor TNP-470 completely prevented

healing. Similar results were reported by Yin *et al.* [179] who studied fracture healing in mice which had a genetic knockout of the protein GIT1. GIT1 plays an important role in angiogenesis among other processes [179]. The GIT1 KO mice presented a persistence of cartilage which led to delayed healing. Finally, devascularisation of the periosteum in sheep has been shown to lead to reduced bone formation as well as delayed union [183]. Conversely, studies in which vascularisation has been upregulated have shown an improvement in fracture healing [180–182]. By inhibiting the expression of thrombospondin-2 (a negative regulator of angiogenesis), Taylor *et al.* [182] showed that fractured murine tibias healed faster via enhanced intramembranous ossification. Murata *et al.* [180] reported similar results following the inhibition of miR-92a which is also a negative regulator of angiogenesis. These results demonstrate the importance of angiogenesis to the fracture healing process.

The local oxygen tension is closely linked to vascularisation of the fracture callus and has been shown to be an important regulator of MSC differentiation *in vitro* (see section 2.2.4). The local oxygen environment changes during the course of fracture healing and it has been hypothesised that this contributes to the spatial distribution of tissue phenotypes observed at various times within the fracture callus [45]. This changing environment is apparent in the results of the study conducted by Epari *et al.* [184] in which the oxygen tension within the external callus of a fractured ovine tibia was measured at various time points (Figure 2-14). During the first few days the oxygen tension decreased dramatically towards hypoxic levels (0 – 2 %) due to the severe disruption experienced by the vasculature. However, as neovasculature invaded the callus during the early stages of repair, the decrease in the oxygen concentration began to level off before eventually returning to the pre-fracture levels. The effect of oxygen on the fracture healing process was further explored by Lu *et al.* [185]. In this study the progression of fracture healing was examined within mice which breathed in either hypoxic (13 %), normoxic (21 %) or hyperoxic (50 %) conditions. It was

found that hyperoxia led to increased tissue vascularity as well as improved bone synthesis and reduced healing. The hypoxic group, on the other hand, presented decreased tissue vascularity and a reduction in bone generation which in turn led to an increased healing time.

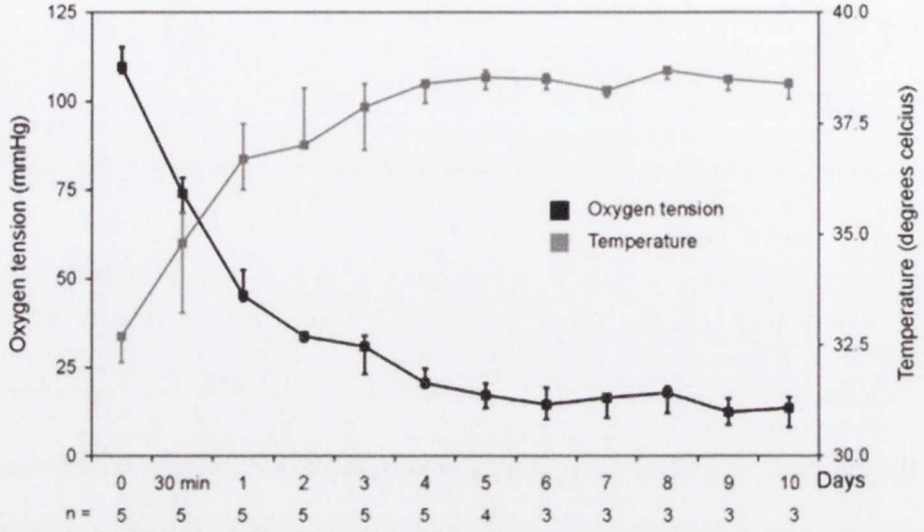

Figure 2-14: Oxygen tension and temperature versus time within the periosteal callus of an ovine fractured tibia [184].

In order to better understand the interaction between each of these factors a number of computational models have been developed which attempt to predict the course of fracture healing under different conditions. These are discussed in section 2.4.

2.3.2 Osteochondral Defects

Osteochondral defects arise following structural damage to both the articular cartilage and the underlying subchondral bone in a joint [2]. They can occur anywhere in the body, but due to the high loading conditions experienced by the knee, they are commonly found in the contact regions where the femur meets the tibia [1]. Osteochondral defects are associated with trauma or other causes of avascular necrosis of the bone and, as a result, they usually affect children or young adults [1].

In the initial weeks following the formation of an osteochondral defect, the subchondral bone exhibits healing while the exposed cartilage region is replaced with fibrocartilaginous tissue [2,6,7,186]. This is because the damaged subchondral bone provides a source of MSCs in osteochondral defects, whereas only the articular cartilage is affected in

chondral defects. As time progresses however, the newly formed repair tissue begins to break down and eventually degrades completely [6,8,9,186,187]. Despite this inevitable break down of the tissue, the spontaneous repair response within osteochondral defects forms the basis of a number of surgical interventions which aim to induce the healing of articular cartilage lesions [186]. For this reason, osteochondral defects have been studied extensively within animal models in order to better understand, as well as develop, methods with which to repair the damaged joint.

2.3.2.1 Spontaneous Repair of Osteochondral Defects

Osteochondral defects which are of a specific size or less (termed the 'critical defect size') undergo a process spontaneous repair whereby new tissue forms in the defect and eventually breaks down over time [8]. The first feature of this process is the formation of a blood clot [2]. Following this, MSCs invade the defect site and differentiate to form new tissues. The progression of the spontaneous repair process within critical sized defects has been studied extensively in a number of different animal models [4,6,9,57,187–189]. While a number of differences exist regarding the design of each model (animal, defect size and defect location) the pattern of observed tissue formation tends to follow the same general discrete pattern.

In the first 2 to 3 days, the developed haematoma rapidly becomes organised into a rich fibrin clot [6]. As in the inflammation phase of fracture healing, the haematoma is invaded by MSCs from the exposed bone marrow [6]. This blood clot adheres well to the surfaces of the bony tissue, although in most cases it fails to adhere to the articular cartilage [186]. In the bottom of the tissue, woven bone is formed by intramembranous ossification, although at the early stages the genetic markers for osteogenesis (mRNA expression of type I collagen and osteonectin) remain low [9]. In a similar study which examined osteochondral defects

within canine models, DePalma *et al.* [187] observed increased cell proliferation in the bone marrow but not in the defect by day 2.

By day 7, the blood clot is completely removed and replaced by a fibrous granulation tissue which in turn is filled with undifferentiated MSCs [6]. This fibrous tissue is oriented in parallel to the articular surface which in turn serves to align the cells in that direction [6]. At this point the native articular cartilage immediately adjacent to the defect site becomes necrotic and the local chondrocytes die [6]. The genetic markers of osteogenesis (type I collagen) increase dramatically from days 3 to 7 and remain high until day 14 [9]. Conversely the genetic markers for cartilage (type II collagen mRNA) are at lower levels than those observed in healthy articular cartilage [9]. In their study, DePalma *et al.* [187] reported the first signs of cell proliferation within the defect at day 7. The rate of proliferation increased with respect to the distance from the articular surface [187].

By day 14 distinct zones of different tissue phenotypes are apparent [6]. Bone formed by intramembranous ossification is found at the base of the defect while at the surface a layer of fibrous tissue forms [6]. Shapiro *et al.*[6] showed that this uppermost region stained negative for safranin-O, a marker of chondrogenesis. Cartilaginous tissue also forms between the two layers [6]. This was apparent through safranin-O staining as well as the expression of small amounts of collagen type II [6,9]. Despite this, the cartilaginous region fails to generate either the Benninghoff fibre organisation or the zonal structure found in native articular cartilage and is, in fact, more akin to fibrous rather than hyaline cartilage [186]. For this reason it is mechanically inferior to the native articular cartilage [186]. As well as this, in most cases the repair tissue fails to integrate with the surrounding tissue [6,186].

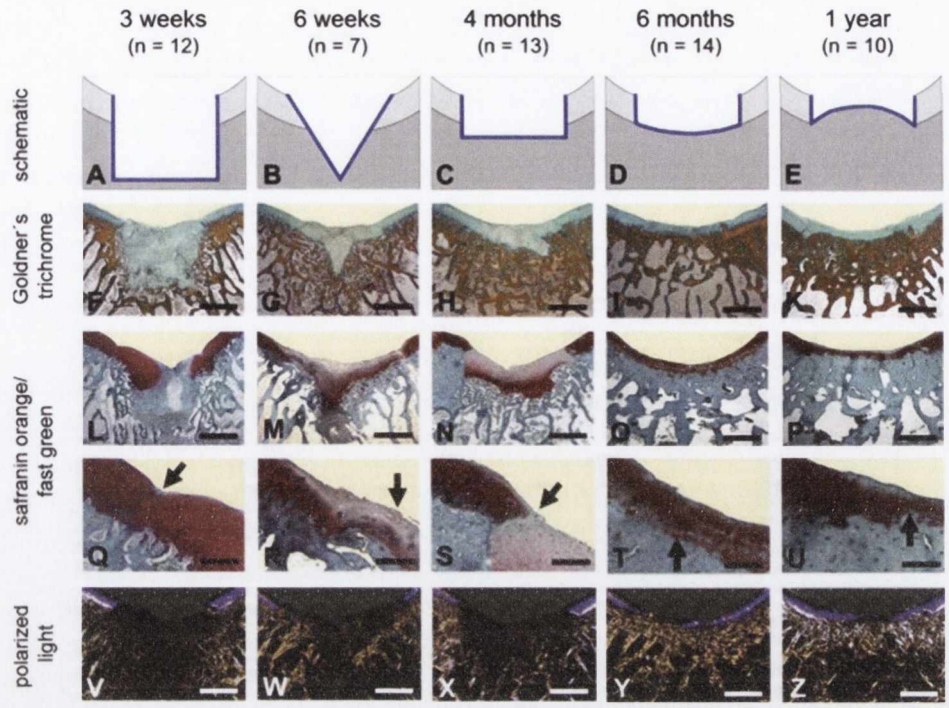

Figure 2-15: Pattern of tissue formation during osteochondral defect repair within an untreated lapine model as reported by Orth *et al.* [4]. The schematics (A – E) display the (A) cylindrical, (B) infundibuliform, (C) plane, (D) concave and (E) convex geometrical subchondral bone reconstitution patterns. Images (F – K) show histological sections stained by Goldner's trichrome method to highlight bone while images (L – U) are histological sections stained with safranin-O to highlight sGAG (cartilage). Images (V – F) depict sections taken under polarized light microscopy in order to show the collagen architecture.

From week 2 onwards the osseous region spreads upwards through a mixture of intramembranous and endochondral ossification [6]. Orth *et al.* [4] observed that bone formation in the base of the defect first adopts a cylindrical shape by day 21 before transforming into an infundibuliform shape by the start of week 6. As this osseous front progresses towards the native tidemark it becomes plane with the native bone (6 months) before advancing beyond it in a convex arrangement (1 year) (Figure 2-15). This thinning out was also observed by Qui *et al.* [57] who reported that the newly formed subchondral plate progresses beyond the native tidemark by week 16. The advance of the osseous plate results in a 'thinning' of the newly formed cartilaginous zone which continues to express collagen type II mRNA from within the centre of the defect [9]. At the same time as this, the well-developed fibrous tissue at the articular surface persists and can in turn penetrate downwards into the defect which leads to further thinning of the cartilage region [6]. By week 6 this fibrous region can be twice as thick as the superficial layer in the native articular cartilage [6].

By week 8 the repair tissue is structurally inferior to normal articular cartilage [57]. Furthermore, between weeks 8 and 10 the early signs of degeneration first appear. Fibrillation and tearing of the surface tissue was observed by Shapiro *et al.* [6], while in their study, DePalma *et al.* [187] noted that cellular proliferation within the defect region began to decrease from week 8. This degeneration continues and by week 12 Shapiro *et al.* [6] reported a reduction in safranin-O staining indicating the breakdown of the cartilaginous tissue. The deterioration of the repair tissue is most severe at the articular surface as indicated by more intense safranin-O staining in the deeper regions [4,6]. By week 16, as the subchondral plate progresses beyond the native tidemark, Qui *et al.* [57] reported that no hyaline cartilage remains in the repair tissue. Finally by week 36 extensive acellular regions were present in the repair cartilage of many defects (Figure 2-16) [6]. The degeneration process continues and eventually progresses into the surrounding tissues [6]. Orth *et al.* [4] reported a similar pattern of healing, although this did not begin to happen until after 6 months in their study.

While this section outlines the general stages of the spontaneous repair process, it is important to note that a number of contradictions exist between the different studies. This is most apparent regarding the times at which certain features occur (for example, Orth *et al.* [4] reported that the cartilage repair tissue began to degrade after 6 months while Qui *et al.* [57] reported that it had completely degraded by month 4). Based on the differences observed between the various animal models it is possible to deduce a number of factors which affect the spontaneous repair process within osteochondral defects.

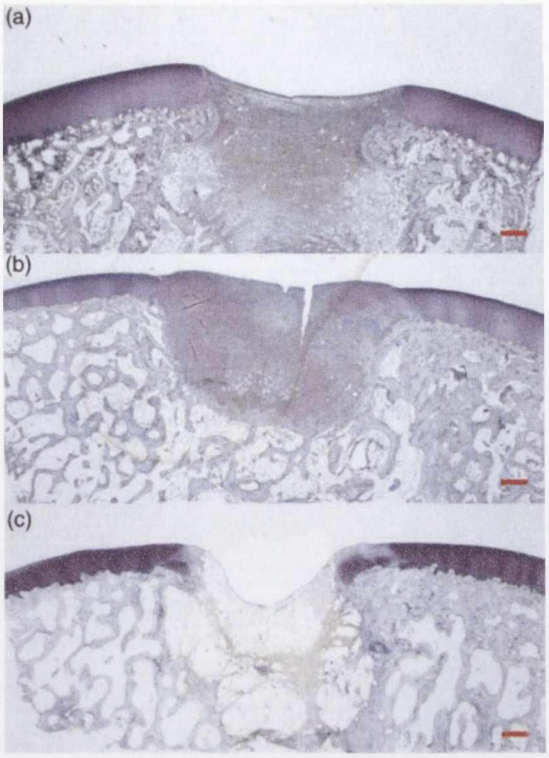

Figure 2-16: Progression of the repair tissue in an osteochondral defect within a minipig model at (a) week 6, (b) week 12 and (c) week 52 [8]. At weeks 6 and 12 the defect was filled with a mixture of fibrous tissue and fibrocartilage. At one year the repair tissue was composed mainly of fibrous tissue while within the subchondral region there was strong disruption as well as cyst formation.

2.3.2.2 Factors Affecting Osteochondral Defect Repair

Two of the main factors which affect the spontaneous healing process of osteochondral defect are the size and the location of the defect. Firstly, the size of the defect plays an important role as, in defects which are larger than the critical size, the haematoma fails to successfully fill the gap and the repair process is thus unable to commence [5,8,186,190]. This was shown in a horse model by Convery *et al.* [190] who reported healing of small defects (φ 3 mm) after 3 months whereas larger defects (φ 9mm x 9 mm) showed incomplete repair at 9 months. Similar findings were presented by Jackson *et al.* [5] who, instead of spontaneous repair within a goat model, found the following: progressive resorption of the osseous walls of the defect; the formation of a large cavity region and finally; the collapse of the surrounding articular cartilage and subchondral bone [5]. It is important to note that although there appears to be a relationship between the animal model and the critical defect size, this

does not appear to be linear. This is apparent when one considers that in rabbit models, defects of size φ 3.2 mm x 5 mm have been shown to undergo spontaneous healing [4] while in the larger goat model examined by Jackson *et al.* [5], it was reported that defects of size φ 6 mm x 6 mm failed to undergo spontaneous healing.

The location of the defect has also been shown to influence spontaneous repair through mechanical loading of the repair tissue. In this case, in defects which arise in non-weight bearing areas, cartilage formation has been observed to form at a slower and quantitatively inferior rate compared to that which arises in defects in weight bearing areas [187]. Based on these findings, postoperative loading has been isolated as a key factor affecting the spontaneous repair process. Salter *et al.* [13] reported that, following the creation of an osteochondral defect in rabbit models, continuous passive motion led to a significant increase in the amount of defects healed by hyaline cartilage (52 %) compared to those healed using intermittent passive motion (9 %) or complete immobilization (8 %). Similar results were reported by Kim *et al.* [14] who found that osteochondral defects in a rabbit model treated with continuous passive motion for two weeks postoperatively had mature, hyaline-like cartilage as the predominant repair tissue at 12 weeks. Mechanical loading has also been shown to affect bone formation during the spontaneous repair process. This was reported by Harada *et al.* [188] who created osteochondral defects in rats which were exposed to normal gait, low-load-bearing or low-load-bearing with complete immobilisation. After 4 weeks the authors reported that subchondral bone formation was worst in the immobilised group.

A final factor which has recently been shown to affect the outcome of the spontaneous repair process is the degree of blood vessel formation within the defect site. In this case, it has been hypothesised that limiting angiogenesis improves the quality of the repair tissue formed, particularly in the chondral phase of the defect. Klinger *et al.* [16] examined this by inhibiting angiogenesis within a porcine model of cartilage repair by

microfracture. In this study angiogenesis was inhibited using cells which were genetically altered to synthesise the anti-angiogenic factor chondromodulin 1. In this case, compared to the control group, treated defects presented less vascular invasion, an inhibition of chondrocyte hypertrophy and endochondral ossification, as well as more robust hyaline cartilage at later time points. Similar results were observed by Nagai *et al.* [15] within a rabbit model examining spontaneous osteochondral defect repair. In this case the anti-VEGF antibody bevacizumab was used to inhibit angiogenesis. Similar to Klinger *et al.* [16], the authors reported more robust hyaline cartilage at later time points as well as less chondrocyte hypertrophy and endochondral ossification compared to the control group [15].

Based on the findings outlined in this section, current treatment options for osteochondral defect repair aim to create conditions which promote the formation of robust repair tissue. These current treatments are outlined in the following section.

2.3.2.3 Articular Cartilage and Osteochondral Tissue Engineering

The current surgical options available for osteochondral defect repair include arthroscopic debridement, abrasion arthroplasty, chondroplasty and microfracture [10,11]. These treatments are deemed as either palliative, in which case the aim is to simply remove the damaged tissue, or 'reparative', where the goal is to replace the defect with biological matter [11]. Although all of these treatments provide relief to the patient in the short term, their success in the long term is limited [10]. Tissue engineering, however, offers a 'restorative' treatment option where the overall goal is to reconstruct the natural tissue and thus provide long term relief to the patient [11]. Currently the only tissue engineering option which is in use for the treatment of cartilage defects clinically is autologous chondrocyte implantation (ACI) [11]. This process involves isolating autologous chondrocytes from the patient which are then expanded *in vitro* before being inserted into the defect site [191]. The final stage involves covering the area with a flap of periosteal tissue. The most recent generation of ACI is known

as matrix-assisted autologous chondrocyte implantation (MACI) [192]. This involves seeding the expanded chondrocytes into a biodegradable synthetic matrix which is press-fitted into the defect site [192]. The benefit of this is that it removes the need for the periosteal flap [192]. As both ACI and MACI are only used as a treatment option for chondral defects they are not discussed any further in this review.

The general process of tissue engineering is similar to the MACI approach. This is outlined in Figure 2-17. In some cases a cell free scaffold which alleviates the necessity for cell isolation and expansion is used [10,11]. The overall goal of the tissue engineering approach to osteochondral defect repair is to insert a scaffold into the defect site which mimics the environment of the native extra cellular matrix, provides structural support to the regenerating and neighbouring tissues, and provides a suitable environment for cellular migration, adhesion and differentiation [193]. In order to achieve this, considerable research has been conducted in the areas of scaffold design, growth factor supplementation regimes, bioreactor design and potential sources of cartilage and bone forming cells.

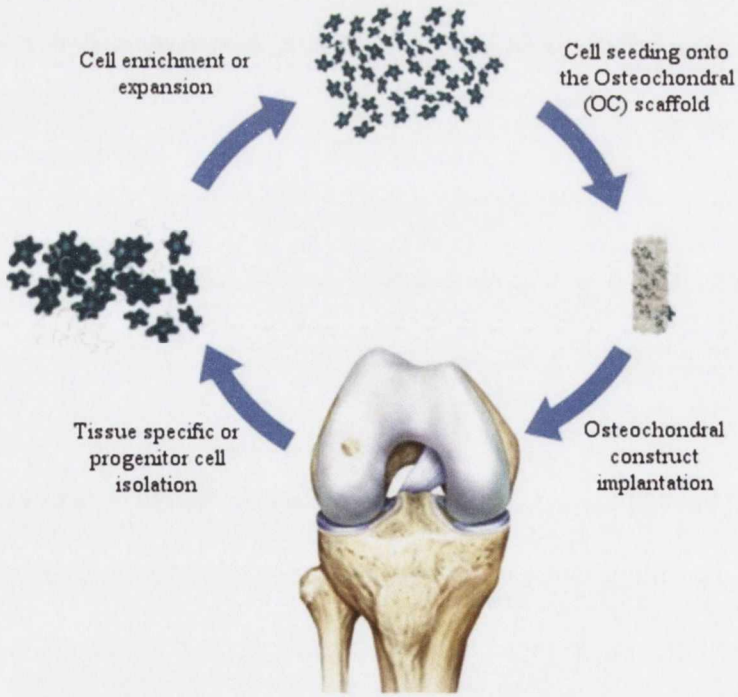

Figure 2-17: General overview of the steps involved in tissue engineering based osteochondral defect repair [11].

The general requirements of the tissue engineering approach to osteochondral defect repair is that the scaffold used is biodegradable, biocompatible, must present suitable fixation to the defect site, facilitate cell attachment, regulate cell expression and promote the supply of nutrients and growth factors [194]. The first types of scaffolds developed were composed of a single phase material. This approach has yielded some positive results. For example, Coburn *et al.* [195] used electro-spinning to develop a low density, nanofibre, single-phase scaffold which had an architecture similar to that of hyaline cartilage. In addition to the cues from the scaffold, chondroitin-sulphate methacrylate was used as a biological cue to promote chondrogenic differentiation. The scaffolds were tested *in vivo* whereby the cell-free scaffolds were inserted into rat osteochondral defects. They were found to support enhanced chondrogenesis (as indicated by increased sGAG production) when compared to empty defects.

Despite these results, it has been suggested that single-phase scaffolds lack the structural complexity required to support either chondrogenesis or osteogenesis within appropriate regions of the osteochondral defect [196]. In general, in order to produce bone a mechanically stiff biomaterial which supports vascularisation is required [10]. Conversely, for cartilage, softer materials (for example hydrogels) which inhibit vascularisation are commonly used [10]. For this reason biphasic and multiphasic scaffolds have been developed which are composed of more than one distinct region [58,197,198]. One such scaffold which was developed by Deng *et al.* [197] was composed of two distinct but integrated layers. The upper layer (or cartilage region) was formed from gelatin, chondroitin sulphate and sodium hyaluronate while the lower layer (the bone region) comprised gelatin and ceramic bovine bone. The scaffold was tested *in vivo* in a large osteochondral defect which was created within a rabbit model. Three groups were tested. In the first group the scaffold was seeded with a mixture of chondrocytes and bone marrow derived MSCs. In the second group the

scaffold remained cell-free and in the third group the defect was left unfilled. At weeks 6 and 12 the first group had developed hyaline-like cartilage in the upper region and new bone in the lower region. By week 36 a visible tidemark could be observed within specific areas of the scaffold. In contrast, the other two groups showed the formation of fibrous tissue as opposed to cartilage while very little bone was observed.

More complicated scaffolds have included additional phases in order to mimic the complexity of the native tissue. One such example was developed by Da *et al.* [58] who built upon previous findings by creating a scaffold which contained a third phase which they classified as the 'compact layer'. This was a thin layer composed of PLGA/β-TCP which resided between a chondral phase (formed using a bovine cartilage extra cellular matrix scaffold and seeded with chondrogenically-primed MSCs) and a bone phase (formed from PLGA/TCP and seeded with osteogenically-primed MSCs). The purpose of this compact layer was to mimic the behaviour of calcified cartilage and act as a barrier between the two regions. The aim of this barrier was to prevent the flow of nutrients and biochemical signals between the two phases as well as generating a mechanical environment throughout the scaffold which was representative of the native tissue. This scaffold was tested *in vivo* within a rabbit model and the results were compared to those obtained using a biphasic scaffold which did not contain the compact layer. At both 3 months and 6 months the compact layer scaffold outperformed the biphasic scaffold with regards to histological score, the quantity of subchondral bone which was formed and both the quality and quantity of neo-cartilage which was formed. In addition to this, at 6 months in the compact layer scaffold groups, a visible tidemark was observed where the neo-cartilage and newly formed bone fused together at the subchondral interface. This feature was not apparent in the biphasic group.

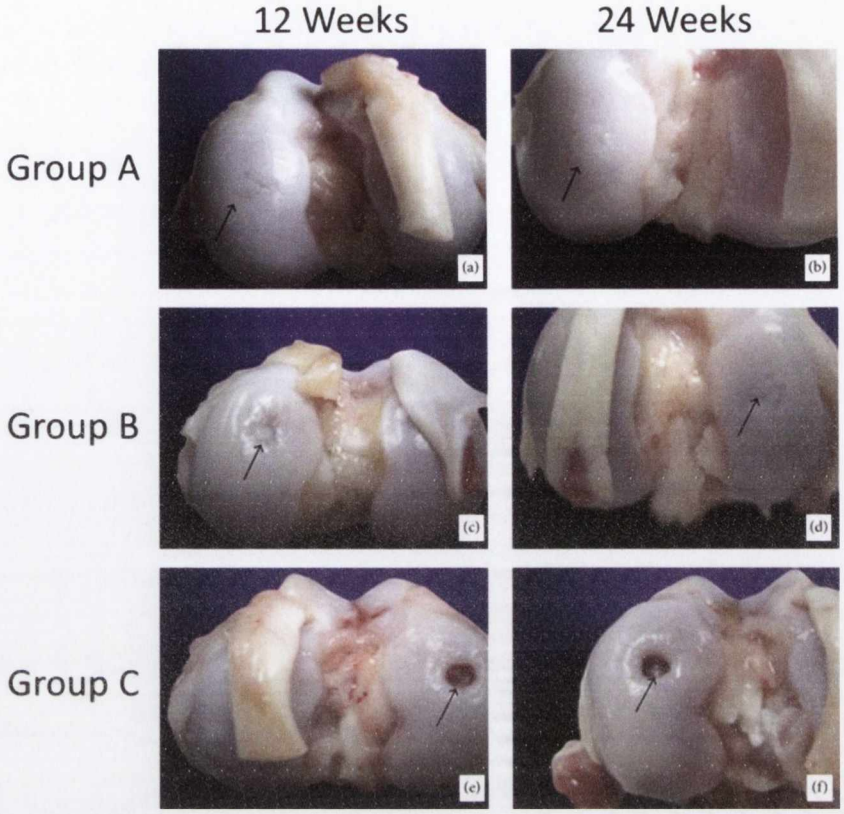

Figure 2-18: Results of a bioreactor study conducted by Pei et al [201]. Goat osteochondral defects treated with scaffolds cultured with mechanically- and biochemically- stimulated MSCs (Group A) at (a) 12 weeks and (b) 24 weeks. Goat osteochondral defects treated with scaffolds cultured with biochemically seeded MSCs (Group B) at (c) 12 weeks and (d) 24 weeks. Goat osteochondral defects left untreated (Group C) at (e) 12 weeks and (f) 24 weeks.

It often happens that the scaffold materials alone are not sufficient to promote the regeneration of the osteochondral tissues. For this reason biological cues may be used to promote cell migration, proliferation and appropriate lineage commitment. Different methods may be used to incorporate these growth factors within osteochondral scaffolds. In some cases, cells are pre-cultured in specific growth factors before being seeded onto scaffolds [58]. Alternatively the cells are seeded onto the scaffolds before the entire construct is cultured *in vitro* within growth factor containing media [199]. Another option is to use the scaffold itself as a mechanism with which growth factors are delivered to the seeded cells [200]. Using microspheres it is possible to synthesise scaffolds with growth factor gradients [200]. This was achieved by Wang *et al.* [200] who used PGLA and silk microspheres containing either osteogenic or chondrogenic growth factors to implement reverse gradients of either

factor. The scaffolds were then seeded with MSCs and cultured for 5 weeks *in-vitro* after which histological analysis confirmed gradients of bone and cartilage throughout the construct.

In conjunction with the combination of scaffold materials and growth factors, additional cues can be applied to the seeded cells *in vitro* through pre-culture within bioreactors [11]. These bioreactor systems assist in replicating the essential site-specific properties of the native tissue by inducing uniform concentrations of cells within the scaffold, facilitating the mass transfer between the cells and their local environment, and applying external physical and biochemical cues to the cells [202] (many of these external cues are discussed in section 2.2). An example of the utilisation of these cues within a bioreactor design is outlined in the study conducted by Pei et al [201]. The authors developed a double chamber bioreactor which allowed chondrogenic and osteogenic stimulation to be applied at either end of a cell-seeded scaffold. Chondrogenic stimulation was applied via a mixture of chondrogenic media and mechanical stirring of the media while osteogenic stimulation was applied by a combination of osteogenic media and mechanical stirring of the media. A single-phase scaffold was seeded with goat bone marrow-derived MSCs before being inserted into the bioreactor for 5 weeks. The efficacy of the method was then tested by inserting a cultured scaffold into a goat osteochondral defect model. The pattern of healing was then compared to that seen in osteochondral defects treated with scaffolds seeded with MSC and cultured without stirring and osteochondral defects which were left untreated. At weeks 12 and 24, through the use of histological staining, the mechanically stimulated scaffold showed more robust cartilage and bone formation compared to the other groups. As well as this, although the scaffolds cultured without mechanical stimulation showed signs of cartilage and bone formation, the mechanically stimulated scaffolds showed better integration with the surrounding cartilage and bone tissue (Figure 2-18).

A final feature of tissue engineered osteochondral defect repair which has been studied extensively is whether or not to seed and culture autologous cells onto the scaffold [10,11,203]. Studies have explored the possibility of using cell free scaffolds for the reason that it removes the problem of donor variability as well as allowing for an easier regulatory pathway [203,204]. The basis of this method is that the scaffold provides the cues not only recruit progenitor cells to the defect site, but also provides the correct 'regenerative' signals to promote the appropriate differentiation response [203]. One of the major difficulties with this approach, however, is that it requires the surrounding tissue to be healthy and contain a sufficient number of tissue-forming cells [10]. As this is not often the case, alternative approaches have employed seeding autologous cells onto the scaffolds [58,197,198]. Two cell types which are commonly used in osteochondral repair are tissue-specific cells or progenitor cells [11]. Tissue-specific cells refers to the use of cells found in the native host tissue, namely chondrocytes, for the purpose of cartilage reconstruction and osteoblasts for bone reconstruction [205]. Although tissue-specific cells, particularly chondrocytes, have been observed to produce more functional tissue *in vivo* than their progenitor counterparts [206], there are a number of features which make them less desirable for osteochondral repair. These include their small number *in vivo* as well as the fact that they very easily lose their phenotype during the culture and expansion process [207]. In contrast to this, progenitor cells, namely MSCs, are relatively abundant and retain their ability to differentiate even after multiple population doublings [207]. For this reason many of the current focus involves the use of MSCs as part of osteochondral repair [11].

One of the main issues with using MSCs for osteochondral defect repair is their tendency to undergo endochondral ossification after differentiating into chondrocytes [207]. For this reason, one of the main areas of research within the field of tissue engineering is the examination of how to prevent MSCs from dedifferentiating *in vivo* [207]. This has been

attempted through scaffold design, the use of growth factors, as well as bioreactor development [11]. Computational models have also been used to better understand the cues which control this process *in vivo* [208,209], these are discussed in the next section.

2.4 Computational Mechanobiology

While it is known that certain conditions improve *in-vivo* healing processes (Section 2.3.1.4 and Section 2.3.2.2), the exact mechanisms which are activated by these conditions remain largely unknown [17]. A better understanding of the specific mechanisms involved in these processes will allow for more accurate strategies in initiating and promoting repair [17]. Many of these processes are very complex however and in many cases it is either too difficult, too expensive or considered impossible to determine these experimentally [17]. Computer modelling provides a method of simulating these complex environments and it provides a potential means of elucidating these pathways [210]. One of the main aims of computer modelling in the areas of fracture healing and osteochondral defect repair is to determine the mechanisms by which the local environment regulates the differentiation of MSCs *in vivo* [17]. Mechanics has often been shown to affect MSC differentiation both *in vitro* and *in vivo*, and many computer modelling approaches have been developed, based on the assumption that mechanics is the main factor in determining MSC lineage commitment [211]. This field, termed 'computational mechanobiology', aims to determine the quantitative rules which govern the effects of mechanical loading on such features as tissue differentiation, growth, adaptation and maintenance [211]. The overall process involves simulating the local environment using a finite element (FE) model. The results are then used as inputs to a tissue differentiation algorithm which in turn is used to update the parameters (e.g. geometry, material parameters) of a new FE model (Figure 2-19) [17]. The process is then run iteratively in order to simulate the progression of tissue differentiation over a period of time [17]. One of the main elements of this approach is the differentiation algorithm which dictates how the

simulated environment affects MSC fate and the progression of repair. Various algorithms have been developed over the years and these are discussed in this section.

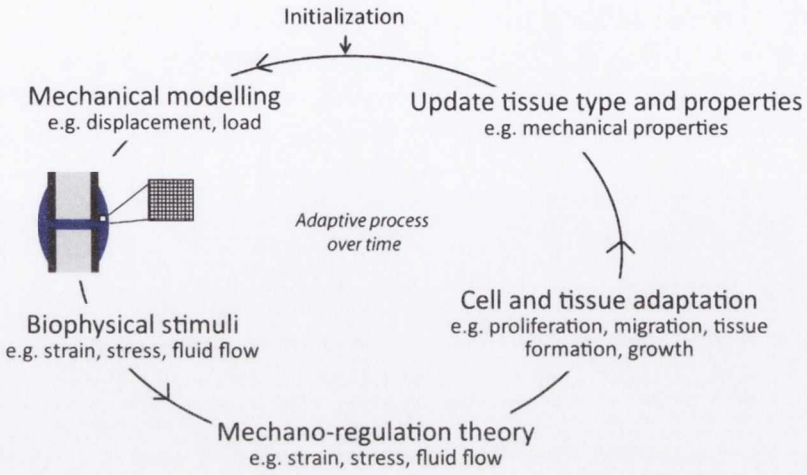

Figure 2-19: An overview of the computational mechanobiological modelling approach [17].

One of the earliest mechanobiological tissue differentiation algorithms was developed by Carter *et al.* [26] and was based on a previous concept proposed by Pauwel *et al.* [79]. In their algorithm, Carter *et al.* [26] proposed that high tensile strain leads to the formation of fibrous tissue, that high pressure leads to cartilaginous tissue and that a combination of low tensile strain and low pressure induces bone formation (Figure 2-20a). This algorithm was able to predict the main stages of bone formation within a fractured tibia [26] as well as the pattern of tissue formation which was observed histologically around an orthopaedic implant [212]. More recent models have applied this algorithm to the study of asymmetric fractures [213] and distraction osteogenesis [214]. In both of these cases, although the model was able to predict the initial pattern of healing, it was unable to predict the adaptive changes in tissue differentiation over time [213,214]. One of the major issues with the algorithm developed by Carter *et al.* [26] is that it does not set specific threshold values by which tension regulates fibrogenesis and pressure regulates chondrogenesis. For this reason, Claes *et al.* [163] developed upon the work conducted by Carter *et al.* [26] by quantifying these thresholds (Figure 2-20b). This algorithm was developed by comparing FE predictions of the local strain environment with histological observations taken from animal studies examining the

effect of gap size and interfragmentary strain on bone healing. The Claes algorithm has been used in conjunction with other rules developed for bone healing to form a 'fuzzy logic' algorithm which has been used to investigate trabecular bone healing [32].

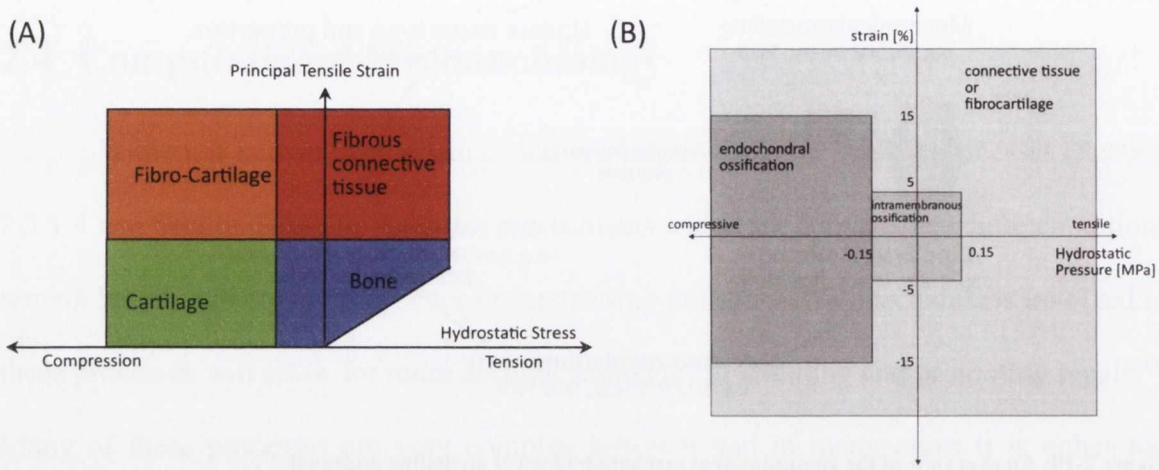

Figure 2-20: Mechano-regulatory tissue differentiation algorithms developed by (A) Carter *et al.* [26] and (B) Claes *et al.* [163]

The evolution of more advanced material models for use in FE analysis allowed for the development of alternative tissue differentiation algorithms. The algorithms developed by Claes *et al.* [163] and Carter *et al.* [26] were achieved using single phase material models in which both the solid and fluid phases of biological tissues are treated as a single component. In biphasic analysis however, the solid and fluid phases are treated as separate components [215]. This new method enabled researchers to consider the role played by the interstitial fluid and was first explored by Prendergast *et al.* [22]. In their tissue differentiation algorithm it was assumed that MSC lineage commitment was determined by a combination of two biophysical stimuli; the shear (deviatoric) strain and the interstitial fluid velocity. In this case, high magnitudes of both stimuli promoted fibrous tissue while low magnitudes led to bone formation (Figure 2-21a). The authors validated their approach by using it to predict the pattern of healing observed during bone fracture healing [216,217]. In this case the model was able to simulate the main stages including intramembranous bone formation originating at the periosteum, endochondral ossification within the external callus and finally resorption of the external callus [216]. The model was also able to predict the experimentally observed

delay in healing caused by increased gap size and the upregulation of connective tissue production as a result of higher magnitudes of interfragmentary strain [217]. In a separate study the algorithm was used to successfully predict the spatial pattern of healing observed during the spontaneous repair of osteochondral defects [209]. Based on the results from this, the authors were able to suggest possible mechanisms which cause the bone front to advance from the base of the defect and result in a thinning of the cartilage region [209].

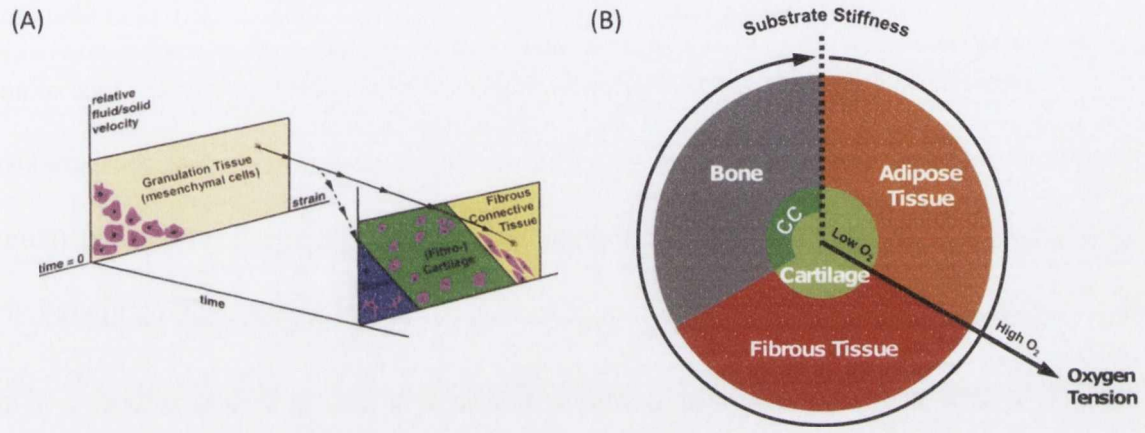

Figure 2-21: Mechano regulatory tissue differentiation algorithm developed by (A) Prendergast et al [22] and (B) Burke et al [44].

The efficacies of each of the tissue differentiation algorithms discussed in this section were examined in the study conducted by Isaksson *et al.* [218]. The authors used the different algorithms to predict the course of fracture healing under either axial or torsional loading conditions. The predictions were then compared to experimentally observed results. Of the three algorithms examined, the model predictions obtained using the Prendergast model were the most representative of the experimentally observed behaviour; however, like the Carter and Claes models it was unable to fully predict the spatial and temporal distributions of tissues observed at every single time point [218].

In order to address these shortcomings, an alternative tissue differentiation algorithm has recently been proposed by Burke *et al.* [44] (Figure 2-21b). This was based on the hypothesis that, rather than acting directly on MSC lineage commitment, the mechanical environment affects differentiation by directing angiogenesis and thus altering the local

oxygen concentration. A second stimulus was incorporated into the model whereby MSC differentiation was governed by the substrate stiffness. The basis of this model was that both the local oxygen tension and substrate stiffness have been shown to affect MSC fate (Section 2.2.3 and 2.2.4) while the local mechanical environment has also been implicated in directing blood vessel growth [219]. The premise of the algorithm is that chondrogenesis is promoted by hypoxia while in normoxic conditions, depending on the local substrate stiffness, MSCs can either undergo adipogenesis, fibrogenesis or osteogenesis. High substrate stiffness leads to osteogenesis while soft substrate promotes adipogenesis. Alternatively, in the presence of an intermediate substrate stiffness cells undergo fibrogenesis. This algorithm was compared to the Prendergast model by using the two approaches to model fracture healing of an ovine tibia [44]. The predicted patterns of healing from each model were then compared to experimental results obtained by Vetter *et al.* [220]. While both models were able to predict the main events of fracture healing, there were notable differences between the two sets of results (Figure 2-22). Firstly, in the Prendergast model, at the early stages of fracture healing cartilage formed within the medullary cavity region of the fracture callus contrary to experimental results. Furthermore this model also predicted that bone initially formed from within the centre of the medullary cavity. In reality, however, it usually begins at the endosteal cortex and progresses into the centre of the cavity [220]. Both of these features were predicted by the algorithm developed by Burke *et al.* [44].

Further support was provided for this algorithm by using it to simulate fracture healing in Thrombospondin-2 Null mice [45]. Thrombospondin-2 is a negative regulator of angiogenesis and as such, mice which do not have this gene show accelerated fracture healing by means of increased intramembranous ossification [45]. Using their model, Burke *et al.*[45] were able to predict this behaviour. Furthermore, in a separate study the authors predicted the pattern of tissue formation observed within a mechanically loaded bone

chamber inserted into a rat tibia [46]. This tissue differentiation algorithm has yet to be used to model spontaneous repair within an osteochondral defect.

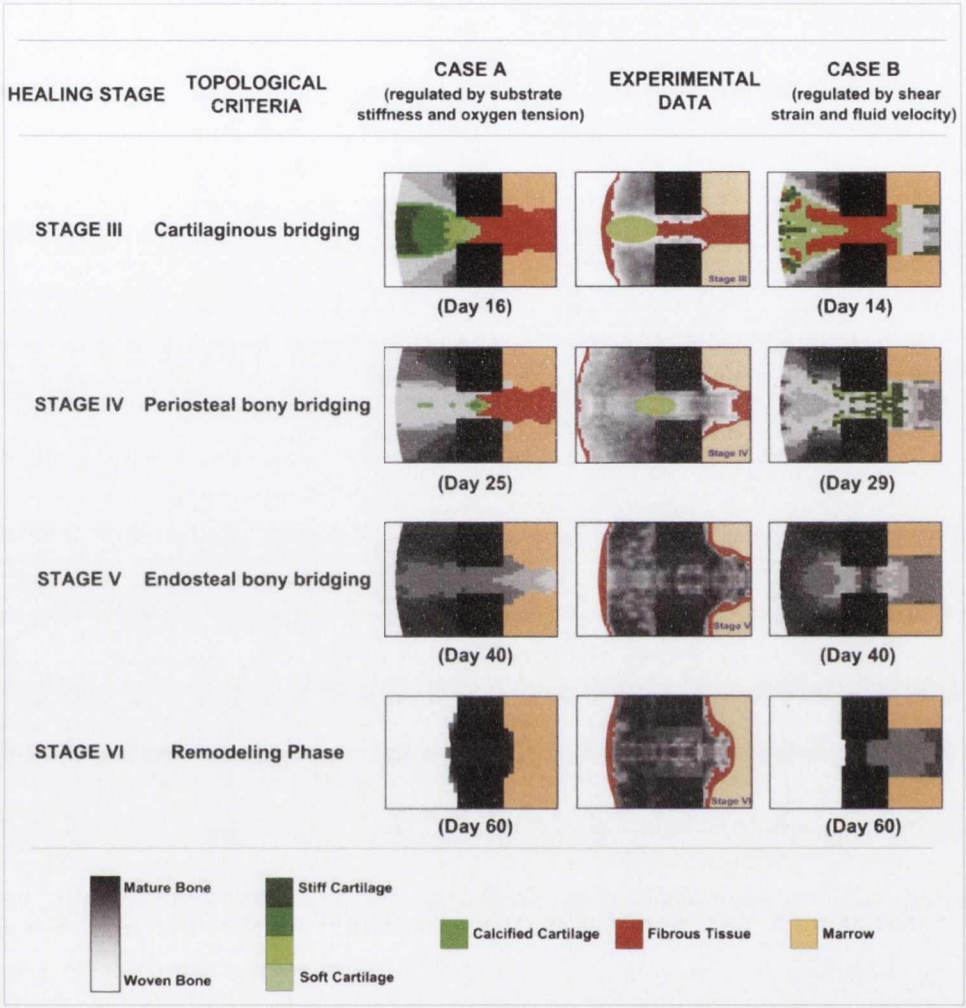

Figure 2-22: Predictions of the course of ovine fracture healing using the tissue differentiation algorithm developed by Burke *et al.* [44] (Case A) and using the algorithm developed by Prendergast *et al.* [22] (Case B). These are compared with experimental observations obtained by Vetter et al [220].

2.5 Conclusion

In vitro studies have provided insights into the factors which affect the lineage commitment of MSCs. However, due to the complex nature of the *in vivo* environment, it becomes less clear which of these factors dictate MSC differentiation and tissue formation within this setting. As MSC differentiation is one of the main processes involved in both fracture healing and osteochondral defect repair, a better understanding of the exact mechanisms controlling stem cell fate will allow for more accurate treatment strategies.

Computational mechanobiology provides a means of elucidating these mechanisms. This approach requires a tissue differentiation algorithm which can accurately predict the lineage commitment of MSCs based on the simulated environmental conditions.

One such tissue differentiation algorithm which has proven capable of predicting MSC lineage commitment *in vivo* was developed by Burke & Kelly [44–46]. This assumes that MSC fate is determined by the substrate stiffness and oxygen tension. Before this model can be applied to osteochondral defect repair however, there are a number of areas where it must be improved. Firstly, cell death is not accounted for [44–46]. This is one of the main processes involved in the latter stages of spontaneous repair of the osteochondral defect [6]. This behaviour was characterised by Kelly *et al.* [209] within their model of the osteochondral defect and was assumed to be caused by high magnitudes of strain. Alternatively, *in vitro* studies have shown this to be caused by the local oxygen concentration (2.2.4 Oxygen Tension). Another deficiency of the model developed by Burke *et al.* [44] is that it does not specifically model the process of endochondral ossification. Instead, chondrocytes are assumed to transdifferentiate into osteoblasts when in the presence of osteogenic conditions (a high oxygen tension and high substrate stiffness). In reality this is a more complex process and the rules governing it need to be elucidated before it may be used within a model of osteochondral defect repair. Finally, the model must be able to differentiate between hyaline cartilage and fibrocartilage, the latter of which is an undesirable phenotype which tends to form during osteochondral defect repair. The commitment of MSCs towards a fibrocartilage phenotype has been shown to be affected by tensile loading and as such, the direct role of mechanics on tissue formation will be considered within the model.

By using this approach to model the spontaneous repair of an osteochondral defect it may be possible to provide insights into the exact mechanisms which control the documented

Chapter 3 A computational model to explore the role of angiogenic impairment on endochondral ossification during fracture healing

The purpose of this chapter is to extend a previously developed tissue differentiation algorithm to include a series of rules whereby chondrocyte hypertrophy and endochondral ossification are regulated by the local oxygen tension. An understanding of the environmental factors regulating these processes is required in order to develop a model of the repair of an osteochondral defect.

The updated tissue differentiation algorithm is developed by using it to simulate the spatial and temporal course of healing experimentally observed during fracture healing of a murine tibia. Support for the model is then provided by using it to predict the pattern of tissue formation observed during fracture healing of a murine tibia under different levels of angiogenic impairment. The results of this chapter provide support for the hypothesis that chondrocyte hypertrophy and endochondral ossification are regulated by the local oxygen tension.

3.1 Introduction

Angiogenesis and oxygen availability are known to be critical regulators of tissue regeneration. Disruption of the blood supply during fracture healing of long bones has been shown to lead to complications such as delayed healing or non-union [221]. Ischemic fractures are typically characterised by an altered temporal and spatial distribution of tissue phenotypes within the callus when compared to non-ischemic fractures [175,181]. In murine models, ischemic fracture healing has been shown to lead to increased cell apoptosis, reduced cell proliferation and a reduction in both cartilage and bone formation when compared to normal fracture healing [175]. Contrary to these findings however, a persistence of cartilaginous tissue has also been reported in a murine model of ischemic fracture healing [181]. Similar results to these have also been observed in knockout mouse models which led to impaired angiogenesis during fracture healing (e.g. GPCR Kinase 2 Interacting Protein-1 (GIT1) knock out mice). In this study a persistence of cartilaginous matrix within the fracture callus was shown to correlate with decreased blood vessel volume, number and connection density [179]. As a result of such conflicting findings, it remains unclear exactly how impaired angiogenesis and the subsequent changes in the microenvironment of the fracture callus regulates MSC fate, and specifically MSC chondrogenesis, chondrocyte hypertrophy and the subsequent process of endochondral ossification.

In silico models of MSC differentiation have long been used to better understand how environmental factors, and in particular mechanical cues, regulate tissue differentiation during fracture healing [222]. While many models have hypothesised that the course of fracture healing is governed solely by the mechanical environment [22–27], more recent *in silico* studies have highlighted the importance of angiogenesis and/or the nutrient supply in directing tissue differentiation within a fracture callus [26,28–32]. Building on these studies, we have developed a tissue differentiation algorithm which assumed that stem cell fate during fracture healing

is governed by the local oxygen concentration and stiffness of the surrounding substrate [44]. This model was tested by using it to simulate the course of fracture healing under both normal and increased angiogenic conditions [45], as well as tissue formation within a mechanically loaded bone chamber [46]. A major limitation of this model, however, is that it does not propose a specific hypothesis to describe how environmental factors regulate the initiation and progression of chondrocyte hypertrophy and endochondral ossification. At present, this model assumes that cartilage is converted directly to bone at the interface between the two tissues. As the conversion of cartilage into bone is central to successful secondary fracture healing and the regeneration of numerous tissue interfaces, an understanding of how environmental factors regulate this process is urgently required. Recently, studies have demonstrated that oxygen plays a role in directing both processes whereby hypoxic conditions have been shown to suppress hypertrophy and endochondral ossification within chondrogenically primed MSCs [37,47–50].

Based on this, the goal of the current study was to use a computational mechanobiological model to test the hypothesis that the local oxygen tension regulates chondrocyte hypertrophy and endochondral ossification of the cartilaginous matrix within the callus of a fractured long bone. Motivated by *in vitro* observations [37,47–50], our previous *in silico* model of MSC differentiation [44] was updated to include specific rules relating oxygen levels to chondrocyte hypertrophy and endochondral ossification. The model was developed by using it to simulate normal fracture healing within a murine tibia, where experimental data was generated to quantify the proportion of hypertrophic cartilage within the callus at specific time-points after the initiation of injury. Following this, in order to provide further support for the model and also to better understand the effect of ischemia on fracture healing, three different models of impaired angiogenesis (mild, moderate and severe) were developed. Model predictions were then compared to experimental

observations of fracture healing in murine ischemic limbs. Each model was constructed based on the hypothesis that ischemia arises as a result of delayed vascular ingrowth from the surrounding tissues.

3.2 Method

3.2.1 Experimental Models of Fracture Healing to be Simulated

Computational mechanobiological models of fracture healing under normal and impaired angiogenesis were developed and compared to experimental murine models of normal and ischemic fracture healing described in detail elsewhere [181,182]. Briefly, for normal fracture healing, closed transverse fractures were created in both the right and left tibiae of 9 to 10 week-old mice. After this, using a hypodermic needle, a hole was bored in the cortex of the medial aspect of the tibial tuberosity through which a sterile 0.009-in-diameter, stainless steel pin was inserted the full length of the tibia until resistance was felt. This pin provided stability to the fracture site while tape "splints" provided initial rotational stability for the first 48 hours. At harvest, right tibias were dissected, intramedullary pins removed and tissues stored for subsequent histological analysis. Histological sections stained with safranin-O were used to differentiate between the total callus area, the cartilaginous area and the woven bone area. For the ischemic case the stabilised fracture was created in the left tibia in the same way as for the normal case. Before this procedure, however, the left femoral artery and its branches between the inguinal ligament and saphenous/popliteal bifurcation were separated and removed.

3.2.2 Iterative Procedure

Tissue differentiation within the fracture callus was simulated via an iterative procedure similar to the one outlined by Burke et al. [44] . Briefly, a finite element (FE) model was used to predict the strain environment within the callus. The results of this were then

used an inputs to a model of angiogenesis which was run in conjunction with models of cell migration, proliferation and death. Both the angiogenesis and cell models then provided inputs to an oxygen diffusion model which determined the oxygen environment within the callus. In this case the angiogenesis model was used to update the oxygen boundary condition while the cell model was used to update the oxygen consumption terms. Following this, cell differentiation was simulated based on the results of the oxygen and cell models. Using the tissue differentiation algorithm the phenotype of each element was calculated. Finally, the results of this were used to update the material parameters of each element of the FE model before the next iteration was run.

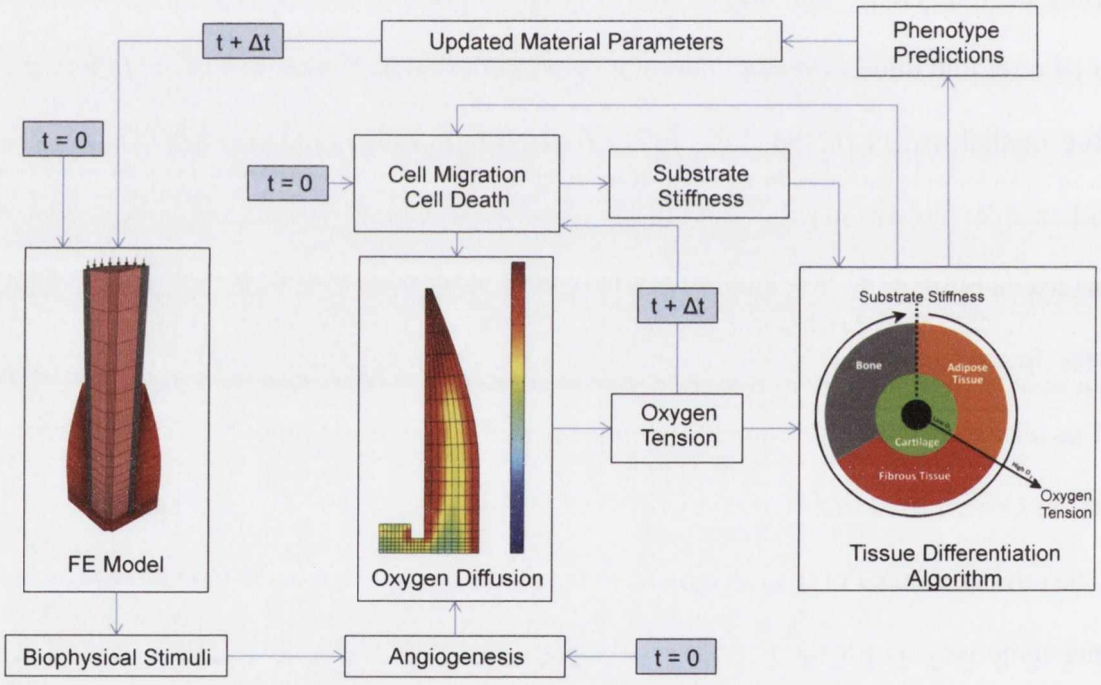

Figure 3-1: Iterative procedure used for the tissue differentiation model.

3.2.3 Finite Element Model

A 3D Finite Element (FE) model of the fracture callus was constructed to determine the biophysical stimuli generated by loading of the callus during gait (Figure 3-2A). Full details of the dimensions and material properties (Table 3-1 and Table 3-2) are available elsewhere [45]. To simulate weight bearing, an axial ramp load was applied over 0.5 s at the

top of the cortical shaft. The maximum applied loading of an intact mouse tibia has been approximated as 1.2 N [223]. It was assumed that the intramedullary pin supported 30 % of this load. It was also assumed that the callus was initially filled only with granulation tissue. At the end of each iteration, the material properties in the FE model were updated based on the results of the cell differentiation algorithm described below. The new parameters were calculated using a rule of mixtures in conjunction with a temporal smoothing procedure [44]. The described model was implemented in the open source finite element package FEBio (version 2.0, University of Utah, Technology Commercialization Office, 615 Arapeen Drive, Suite 310, Salt Lake City).

Table 3-1: Dimensions of Finite Element Model [45]

Dimension	Measurement
Callus Length	6.33 mm
Callus Max Radius	1.365 mm
Cortex Radius	0.68 mm
Cortex Width	0.17 mm
Pin Radius	0.11 mm
Fracture Gap	0.17 mm

Table 3-2: Material Properties

Material Property	Granulation Tissue	Fibrous Tissue	Cartilage	Hypertrophic Cartilage	Marrow	Immature Bone	Cortical Bone	Cell Apoptosis/ Necrotic Tissue
Young's Modulus [MPa]	1[a]	2[a,b]	10[a]	20	0.1	1000[a]	20,000[c]	1
Poisson's Ratio	0.167[a]	0.167[a]	0.167[a]	0.167	0.167[d]	0.3[a]	0.3[a]	0.167
Permeability [$mm^4 Ns^{-1}$]	0.01[a]	0.01[a]	0.001[a]	0.001	0.01[d]	0.001[a]	0.00001[a]	0.01
Solid Volume Fraction	0.2[a]	0.2[a]	0.2[a]	0.2	0.2[d]	0.2[a]	0.2[a]	0.2

a 216

b 224

c 23

d 45

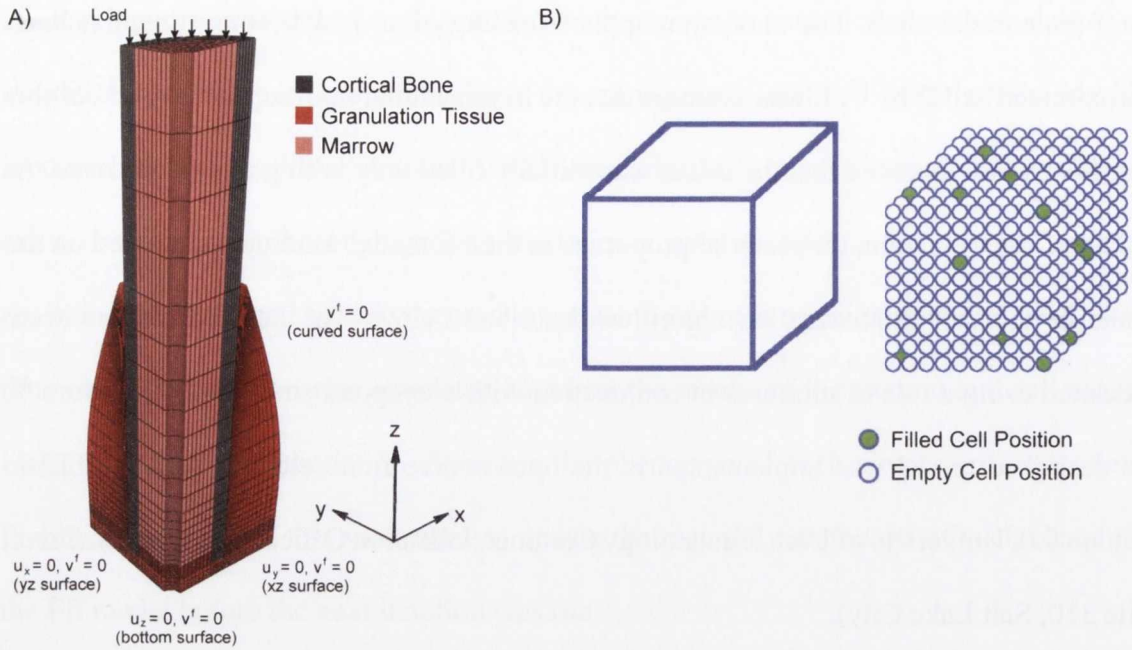

Figure 3-2: (A) FE Model of the fracture callus. Loading is applied at the top of the cortical bone. Displacement and fluid velocity boundary conditions are shown as u and v^f respectively. (B) A 3-dimensional finite element with corresponding lattice. Each lattice point represents a potential location for a cell.

3.2.4 Angiogenesis

Angiogenesis was modelled using a lattice-based approach whereby the elements of the FE model were discretised into a sequence of lattice points, each of which represented a potential cell space (Figure 3-2B) [29]. Each lattice point had a diameter of 10 μm which corresponded to an overall lattice density of 1 x 10^6 lattice points/mm^3. Angiogenesis was then modelled as a sequence of adjoining lattice points, each of which represented an endothelial cell (EC) within a microvessel. Vessels were programmed to stop growing if the octahedral shear strain in the element exceeded a threshold limit (ε^{angio}). If two vessels crossed the same path, anastomosis occurred and the two vessels fused together. Vessels were also able to branch should the vessel length exceed a certain value (L^{min}). The probability of branching then increased linearly until the vessel reached the maximum allowable length (L^{max}), at which point the probability of branching occurring was 1 [29].

Vessels grew at a constant rate (V^{growth}) and could grow into any neighbouring lattice point provided that it was empty. Vessel direction was governed using strain-dependent rules which were developed by simulating [21] the *in vitro* study conducted by Matsumoto *et al.* [219].

In these studies it was shown that, when cultured in 2D, endothelial cell migration was biased in the direction perpendicular to the applied strain. Following from this finding, it was hypothesised that within a 3D environment, EC cells either align themselves in the direction perpendicular to the maximum principal strain or in the direction of the minimum principal strain [21]. In the developed model it was assumed that the latter was case, and there were three potential options which determined the vessel direction: 1) continue growing in the previous direction 2) move in the direction of minimum principal strain or 3) move in a random direction. The probability that a vessel would continue to grow in the same direction as the previous iteration (P^{prev}) was 0.4. The probability that a vessel would grow in the direction of the minimum principal strain (P^{strain}) was dependent upon the absolute magnitude of the strain. This was calculated using a simple linear model where $P^{strain} = 0$ at $\varepsilon^{min} = 0$ up to maximum of $P^{strain} = 0.6$ at $|\varepsilon^{min}| \geq 0.18$. The final case where a vessel grew in a random direction was dictated by the remaining probability ($1 - P^{prev} - P^{strain}$).

Table 3-3: Tissue Differentiation Model Parameters

Model Parameter	Symbol	Source	Unit	Value
Octahedral Shear Strain threshold for inhibition of angiogenesis	ε^{angio}	Estimated	%	9
Blood vessel growth rate	V^{growth}	Estimated	mm day^{-1}	0.02 – 0.1
Density of ECs within an element for it to be considered completely vascularised	$V^{density,max}$	Estimated	-	0.04 – 0.12
Minimum length for branching	L^{min}	[29]	mm	0.2
Maximum length without branching	L^{max}	[29]	mm	0.5
Minimum cell age for differentiation	Age^{diff}	Estimated	days	2.5
Initial oxygen tension	$O_2^{initial}$	[184]	mol mm^{-3}	101.6×10^{-12}
Oxygen limit for cartilage	$O_2^{cartilage}$	[44]	mol mm^{-3}	30.48×10^{-12} – 50.48×10^{-12}
Oxygen limit for cell death	O_2^{death}	[225]	mol mm^{-3}	5.08×10^{-12}
Oxygen limit for differentiation of cartilage to hypertrophic cartilage	$O_2^{hypertrophic}$	Estimated	mol mm^{-3}	30.48×10^{-12}
Oxygen limit for calcification of hypertrophic cartilage	$O_2^{endochondral}$	Estimated	mol mm^{-3}	50.48×10^{-12} – 70.48×10^{-12}
Oxygen limit for inhibition of Proliferation	O_2^{prolif}	[225]	mol mm^{-3}	5.08×10^{-12}

3.2.5 Cell Migration, Cell Proliferation & Cell Death

The migration and proliferation of MSCs, osteoblasts (OBs), adipocytes (ABs), chondrocytes (CCs), hypertrophic chondrocytes (HCs) and fibroblasts (FBs) was also modelled using the lattice approach [20,29]. The migration of cells was implemented using 'random walk' theory where a cell attempted to randomly move into any of its neighbouring lattice points [20]. If the chosen position already contained a cell, however, that cell remained where it was and the migration process terminated for that iteration. Cell proliferation was implemented in a similar fashion provided that there was a vacant position beside the parent cell, i.e. it would proliferate and the newly formed daughter cell would occupy the empty space. If there was no empty space available then the cell did not proliferate (contact inhibition). Proliferation was inhibited should the oxygen concentration fall below a threshold value (O_2^{prolif}), based on *in-vitro* studies examining MSC activity in low-oxygen environments [225]. Proliferation was also inhibited if the cell density within an element

exceeded 1 x 10^5 cells/mm^3 [44]. The migration rate (M) determined the number of attempted migration actions per time step while the doubling time (DT) was the time needed to have elapsed before a cell proliferated (Table 3-4). In accordance with previous studies, 3 % of the lattice points along the assigned boundaries (Figure 3-3B) and 0.05 % of the interior lattice points contained MSCs at the start of the simulation. Finally, if the oxygen concentration fell below O_2^{death} then cell death was initiated where the rate of cell death was governed by the parameter Q^{death} (Table 3-4). Dead cells remained within the lattice for 4 iterations before they were assumed to be removed by immune cells.

Table 3-4: Cell Model Parameters

Model Parameter	MSC	CC	FB	OB	AB	HC
Doubling Time [days]	0.5[a]	1.5[a]	0.5[a]	1[a]	0.5[b]	1.5[a]
Migration Rate [μm hr^{-1}]	26.6[c]	N/A	26.6[c]	N/A	26.6[c]	N/A
Anoxic Death Rate [1/2 day^{-1}]	0.2	0.2	0.2	0.2	0.2	0.2

a 153

b 45

c 226

3.2.6 Oxygen Transport

Oxygen transport was modelled using the FE package COMSOL Multiphysics (version 4.3). The governing equation (Equation 3-1) was updated during each iteration based on the number of each cell type in a specific element. In this case the oxygen consumption term was updated based on the number of MSCs, CCs, OBs, FBs, AB and HCs, while the oxygen production term was determined based on the number of ECs in the element.

$$\frac{dO_2}{dt} = G\nabla^2 O_2 - \sum_{n=1}^{6} \rho^n \frac{Q^{max,n} O_2}{K^{m,n} + O_2} + Q^{vessels}$$

Equation 3-1

The oxygen diffusion coefficient G = 2.2 x 10^{-3} mm^2 s^{-1} [44,227]. Oxygen consumption was modelled for each cell phenotype using Michealas-Menten kinetics [228,229]. In the

equation shown, each phenotype was represented by n, whereby n = 1 represents MSCs; n = 2 represents CCs; n = 3 represents OBs; n = 4 represents FBs; n = 5 represents AB and; n = 6 represents HCs (Table 3-5). For each cell type; ρ^n was the number of cells in the element; $Q^{max,n}$ was the maximum oxygen consumption and; $K^{m,n}$ was the oxygen consumption at half maximum concentration.

The oxygen supply from the blood vessels within each element was modelled with $Q^{vessels}$, which was calculated using the relationship outlined in Equation 3-2.

$$Q^{vessels} = \begin{cases} \dfrac{O_2^{vessels} - O_2}{K^{vessels}}, & \& \quad O_2 < O_2^{vessels} \\ 0, & \& \quad O_2 \geq O_2^{vessels} \end{cases}$$

Equation 3-2

In this equation $K^{vessels}$ is a temporal smoothing term used to prevent irregular jumps in the oxygen concentration ($K^{vessels}$ = 10 s), while $O_2{}^{vessels}$ was the minimum oxygen concentration within the element. In order to ensure that an element was gradually vascularised over time, $O_2{}^{vessels}$ was determined as a function of $v^{density}$, which was the percentage of the lattice points within the element which contained ECs. A linear relationship was used to calculate $O_2{}^{vessels}$ where $O_2{}^{vessels}$ = 0 mol/mm^3 for $v^{density}$ = 0 up to a maximum of $O_2{}^{vessels}$ = 101.6 x 10^{-12} mol/mm^3 at $v^{density,\ max} \geq 8$ %.

Table 3-5: Oxygen consumption parameters of each cell phenotype

Michealas - Menten Coefficients	MSC	CC	OB	FB	AB	HC
Cell type (n)	1	2	3	4	5	6
Max Consumption Rate (Q^{max}) [mol cell^{-1} hr^{-1}]	98 x 10^{-15} a,b	33 x 10^{-15} c,d	98 x 10^{-15} a,b	98 x 10^{-15} a,b	98 x 10^{-15} a,b	33 x 10^{-15} c,d
Oxygen Concentration at half max consumption (K^m) [mol mm^{-3}]	6 x 10^{-12} c,d	6 x 10^{-12} c,d	6 x 10^{-12} c,d	6 x 10^{-12} c,d	6 x 10^{-12} c,d	6 x 10^{-12} c,d

a 45

b 21

c 230

d 228

3.2.7 MSC Differentiation

The rules governing MSC differentiation are outlined in detail elsewhere (Figure 3-3A) [44]. Briefly, in regions of hypoxia ($O_2 \leq O_2^{cartilage}$) MSCs differentiated into chondrocytes. In regions of normoxia ($O_2 > O_2^{cartilage}$) MSCs could differentiate into OBs, ABs or FBs, depending on the substrate stiffness. A high substrate stiffness promoted osteogenesis while low substrate stiffness promoted adipogenesis. If none of these conditions were met then fibrogenesis occurred. FBs also had the capacity to transdifferentiate into OBs provided they met the conditions for osteogenesis i.e. high substrate stiffness and normoxic oxygen tension. Once an element had committed to a particular phenotype any remaining MSCs as well as any FBs in that element differentiated down that phenotypic pathway. An element was said to have committed to a particular phenotype if 50 % of the total allowable lattice points within the element contained cells. Following this, the element was said to belong to the particular phenotype which made up the majority of cells. The model was updated to include a condition whereby MSC differentiation was inhibited in anoxic regions ($O_2 < O_2^{death}$). This was based on experimental studies which have shown that severe hypoxia inhibits differentiation of MSCs [231].

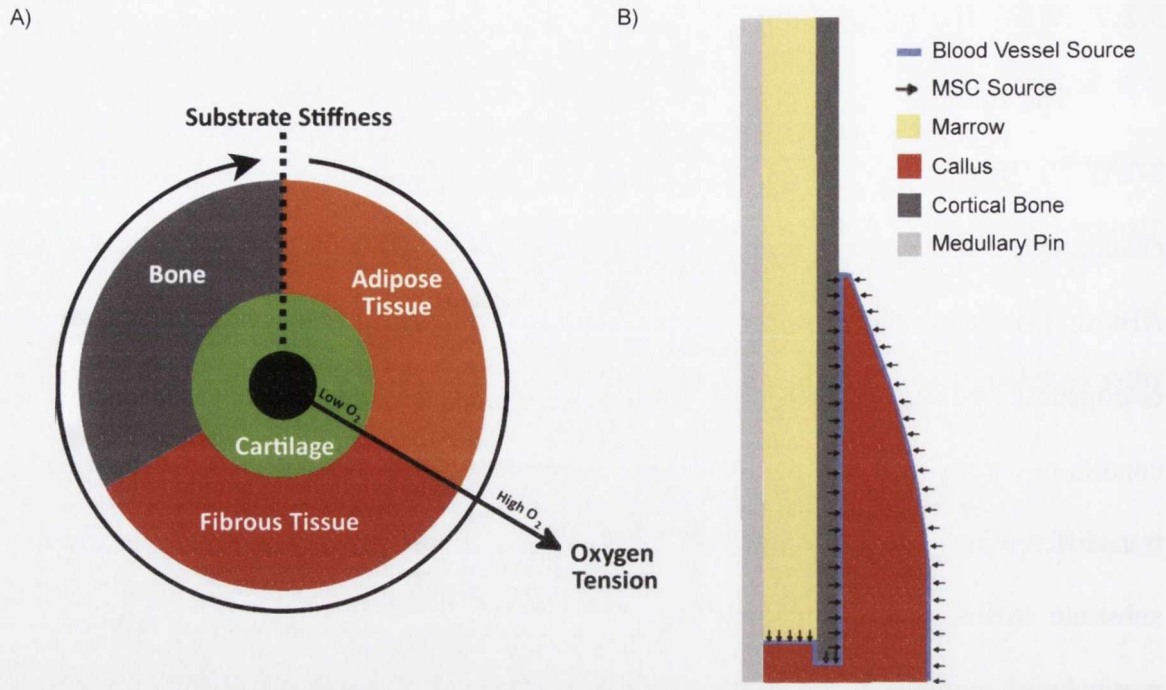

Figure 3-3: (A) Tissue differentiation regulated by substrate stiffness and oxygen availability. The oxygen availability axis extends radially from the centre of the circle with low oxygen in the centre which increases towards the periphery. The substrate stiffness axis extends circumferentially in a clockwise direction from the right side of the dotted line at the top of the circle. (B) Geometry and boundary conditions of the fracture callus

3.2.8 Chondrocyte Hypertrophy and Endochondral Ossification

An updated model of endochondral ossification was implemented as an extension of the developed tissue differentiation algorithm [44]. This split the process into two main steps; initialisation of chondrocyte hypertrophy and subsequent ossification, where it is hypothesised that both process are regulated by local oxygen levels. The initialisation step began when the newly differentiated CCs transformed into HCs. Based on the literature, this was assumed to occur when the local oxygen tension increased beyond a threshold value ($O_2^{hypertrophic}$) [37,232]. The ossification step then characterised the process by which the newly transformed HCs recruit blood vessels and osteoprogenitor cells before undergoing apoptosis [164] or transdifferentiating into OBs [233]. In the model, HCs were assumed to only do the latter and therefore, provided that the following two conditions were met, HCs were converted directly into OBs. The first condition was that they had to be in the vicinity of an OB, while the second condition was that the local oxygen tension had to be greater than a

threshold value ($O_2^{endochondral}$). The rationale for the first condition was to ensure that bone could only form adjacent to bone (i.e. on a stiff substrate).

3.2.9 Simulations

Four different models were developed, one depicting normal fracture healing and three describing impaired vascularity which ranged from mild, to moderate and to severe. For the normal fracture healing model a 3^n parametric study was conducted on the variables V^{growth}, $V^{density,max}$, $O_2^{hypertrophic}$ and $O_2^{endochondral}$. Each parameter was varied between low, medium and high. The vascular growth rate was varied between a minimum value of 0.02 mm day^{-1} up to a maximum value of 0.1 mm day^{-1}, while $V^{density,max}$ was varied between a minimum of 0.04 up to a maximum 0.12. As $O_2^{hypertrophic}$ and $O_2^{endochondral}$ are related, these parameters were varied with respect to one another. In the first instance, $O_2^{hypertrophic} = 30 \times 10^{-12}$ mol mm^{-3} (3 %) and $O_2^{endochondral} = 50.48 \times 10^{-12}$ mol mm^{-3} (5 %). In the second, $O_2^{hypertrophic} = 30 \times 10^{-12}$ mol mm^{-3} (3 %) and $O_2^{endochondral} = 70.48 \times 10^{-12}$ mol mm^{-3} (7 %). In the third $O_2^{hypertrophic} = 50 \times 10^{-12}$ mol mm^{-3} (5 %) and $O_2^{endochondral} = 70.48 \times 10^{-12}$ mol mm^{-3} (5 %). The parameters chosen for the remaining simulations were the ones which accurately predicted the quantity of bone, cartilage and hypertrophic cartilage which was experimentally observed at 10 dpf. These parameters were then fixed for all future simulations of fracture healing with vascular impairment.

The models of vascular impairment were developed based on the findings of Lu *et al.* [175] and Miedel *et al.* [181], who reported different recovery rates of the vascular network following the induction of ischemic fracture healing. Miedel *et al.* [181] reported that, within their model of ischemic fracture healing, blood vessels had invaded the callus by day 10, while Lu *et al.* [175] reported that the ischemic fracture callus remained devoid of vessels until day 14. Based on these studies, the models of impaired vascularity which were developed in this study differed with respect to the boundary conditions used in their respective models

of angiogenesis. In the mild simulation, the angiogenic boundary conditions were assumed to return to the levels used in the normal fracture healing simulation at an earlier time point than they did for the moderate and severe simulations. Similarly, the moderate simulation was restored faster than the severe case.

For all of the simulations it was assumed that vessels could propagate from the periosteum [41,158,183], the endosteum [158], the surrounding soft tissue [234,235] and the marrow within the medullary cavity [236] (Figure 3-3B). Simulations ran over a period of 28 days and, based on previous in silico models [46,237], each iteration represented a time step of 12 hours.

Normal Fracture Healing: In order to model the observed dominant vascular response from the periosteum [41,158], 3 % of the lattice points on this surface were assumed to be vessels which became active at the start of the simulation. The vascular response from the surrounding soft tissue was then modelled by assigning 1 % of the lattice points on this surface to be vessels, which became active at the start of day 3. It has been observed that vessel ingrowth is severely diminished during the early stages of healing on the surfaces at the medullary cavity, [236]. It was therefore assumed that 0.5 % of the lattice points on this surface contained vessels which did not become active until day 7. Finally, it was assumed that all of the surrounding tissues were vascularised and that each surface provided an oxygen supply to the callus. This was modelled by implementing a constant oxygen tension of 50.48E-12 mol mm^{-3} (5 %) at each surface.

Mild Vascular Impairment: On the cortical surface 0.3 % of the lattice points became active vessels at day 0 and from day 5 this value increased linearly to 3 % of the lattice points by day 8. Similarly, on the soft tissue surface 0.2 % of the lattice points became active at day 2

and increased linearly from day 5 to 1 % at day 8. On the marrow surface 0.1 % of the lattice points were active vessels at day 7.5 and this value increased linearly to 1 % by day 10.5.

Moderate Vascular Impairment: Angiogenesis was not initiated in this model until day 6 because it was designed to be a transition between mild and severe ischemia. The number of active vessels then increased linearly with each time step on all the surfaces until it was fully recovered by day 9.

Severe Vascular Impairment: Blood vessel growth into the callus was not initiated until day 10, at which point the number of active vessels on each surface increased linearly from 0 % to 3 % on the periosteum surface, 0 % to 1 % on the soft tissue surface and 0 % to 0.5 % on the marrow surface by day 14.

3.3 Results

3.3.1 Normal Fracture Healing

The model parameters that most accurately predicted the experimentally observed quantity of tissues at 10 dpf during normal fracture healing were chosen for the remainder of the study (Figure 3-4). These were V^{growth} = 0.06 mm day^{-1}, $V^{density,max}$ = 0.04, $O_2^{hypertrophy}$ = 3 % and $O_2^{endochondral}$ = 5 %. The model incorporating these parameters was able to predict quantities of bone and cartilage which were within the experimentally observed range at this time point (Figure 3-5A), as well as the spatial distribution of tissue phenotypes observed after histological staining of the fracture callus (Figure 3-5B). In addition to this, the prediction of the proportion of cartilage that was hypertrophic was within the range observed experimentally at this time point (Figure 3-5C).

(A)

$$d = \sqrt{(C^{exp} - C^{pred})^2 + (B^{exp} - B^{pred})^2 + (HC^{exp} - HC^{pred})^2}$$

C = % callus area made up of cartilage
C^{exp} = 15.60 %

B = % callus area made up of bone
B^{exp} = 27.9 %

HC = % callus area made up of hypertrophic cartilage
HC^{exp} = 26.57 %

(B) $O_2^{hypertrophy}$ = 3 % $O_2^{endochondral}$ = 5 %

$V^{density,max}$	V^{growth} [mm day^{-1}] 0.02	0.06	0.10
0.04	7.78	19.70	24.33
0.08	32.86	2.26	14.24
0.12	44.88	24.48	3.22

(C) $O_2^{hypertrophy}$ = 3 % $O_2^{endochondral}$ = 7 %

$V^{density,max}$	V^{growth} [mm day^{-1}] 0.02	0.06	0.10
0.04	6.89	20.55	24.62
0.08	32.57	3.52	14.12
0.12	45.37	24.03	4.56

(D) $O_2^{hypertrophy}$ = 5 % $O_2^{endochondral}$ = 7 %

$V^{density,max}$	V^{growth} [mm day^{-1}] 0.02	0.06	0.10
0.04	23.61	6.41	18.20
0.08	62.05	24.27	18.04
0.12	83.18	60.95	40.80

Figure 3-4: Results of parametric study. (A) Equation and values used to determine the parameters which best fit the experimental results of normal fracture healing at 10 dpf. The parameters chosen were the ones which produced the minimum value for d. (B) Calculated values for d where $O_2^{hypertrophy}$ = 30 x10^{-12} mol mm^{-3}, $O_2^{endochondral}$ = 50 x10^{-12} mol mm^{-3} and $V^{density,\ max}$ and V^{growth} were varied. (C) Calculated values for d where $O_2^{hypertrophy}$ = 30 x10^{-12} mol mm^{-3}, $O_2^{endochondral}$ = 70 x10^{-12} mol mm^{-3} and $V^{density,\ max}$ and V^{growth} were varied. (B) Calculated values for d where $O_2^{hypertrophy}$ = 50 x10^{-12} mol mm^{-3}, $O_2^{endochondral}$ = 70 x10^{-12} mol mm^{-3} and $V^{density,\ max}$ and V^{growth} were varied. The parameters which produced the smallest value for d were $O_2^{hypertrophy}$ = 30 x10^{-12} mol mm^{-3}, $O_2^{endochondral}$ = 50 x10^{-12} mol mm^{-3}, $V^{density,\ max}$ = 8 % and V^{growth} = 0.06 mm day^{-1}.

At day 5 in the simulation, blood vessels penetrated into the periosteal callus (Figure 3-6A), which led to an increase in the oxygen tension proximal to the cortical bone and the surrounding soft tissue (Figure 3-6B). At this time point osteoblastic differentiation was predicted adjacent to the periosteum of the fractured bone (Figure 3-6C). Cartilage was first observed in the core of the internal callus and by day 8 it had bridged the fracture gap (data not shown). By day 10 only the cores of the external and internal calluses were devoid of

vessels. At this stage, woven bone was predicted to form along the length of the periosteal cortex while fibrous tissue was predicted adjacent to the soft tissue surface of the external callus. In the core of the periosteal callus, cartilage tissue which contained regions of hypertrophic cartilage was predicted. By day 15 only a small region of hypertrophic cartilage remained between the fractured bone ends. By this stage the model predicted that the fracture gap of the external callus was bridged by endochondral bone (Figure 3-6D), and by day 20 over 98 % of the callus was bone.

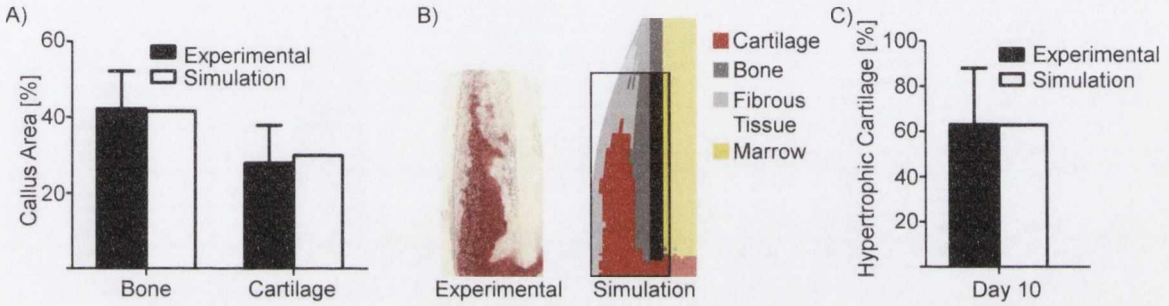

Figure 3-5: (A) Experimental vs. Predicted percentages of callus area made up by cartilage and bone during normal fracture healing. (B) Safranin-O staining 10 days post fracture for normal fracture healing compared to model predictions for cartilage and bone formation. Both cartilage and hypertrophic cartilage are treated as the same material. (C) Experimental vs. Predicted percentage of cartilage tissue area which is hypertrophic in the normal fracture healing model at day 10.

An additional parametric study was also performed which examined the effect that varying the magnitude of the load borne by the intramedullary pin had on the predicted outcome of healing (Appendix I: Parametric Study: Load Supported by Pin (Chapter 3)). When the magnitude of the load applied to the callus was greater than 40 % of the total load, the typical pattern of secondary facture healing was observed (cartilaginous bridging following by hypertrophy and endochondral ossification). When the magnitude of the load borne by the callus was less than 40 %, bone formed initially from the fractured bone ends.

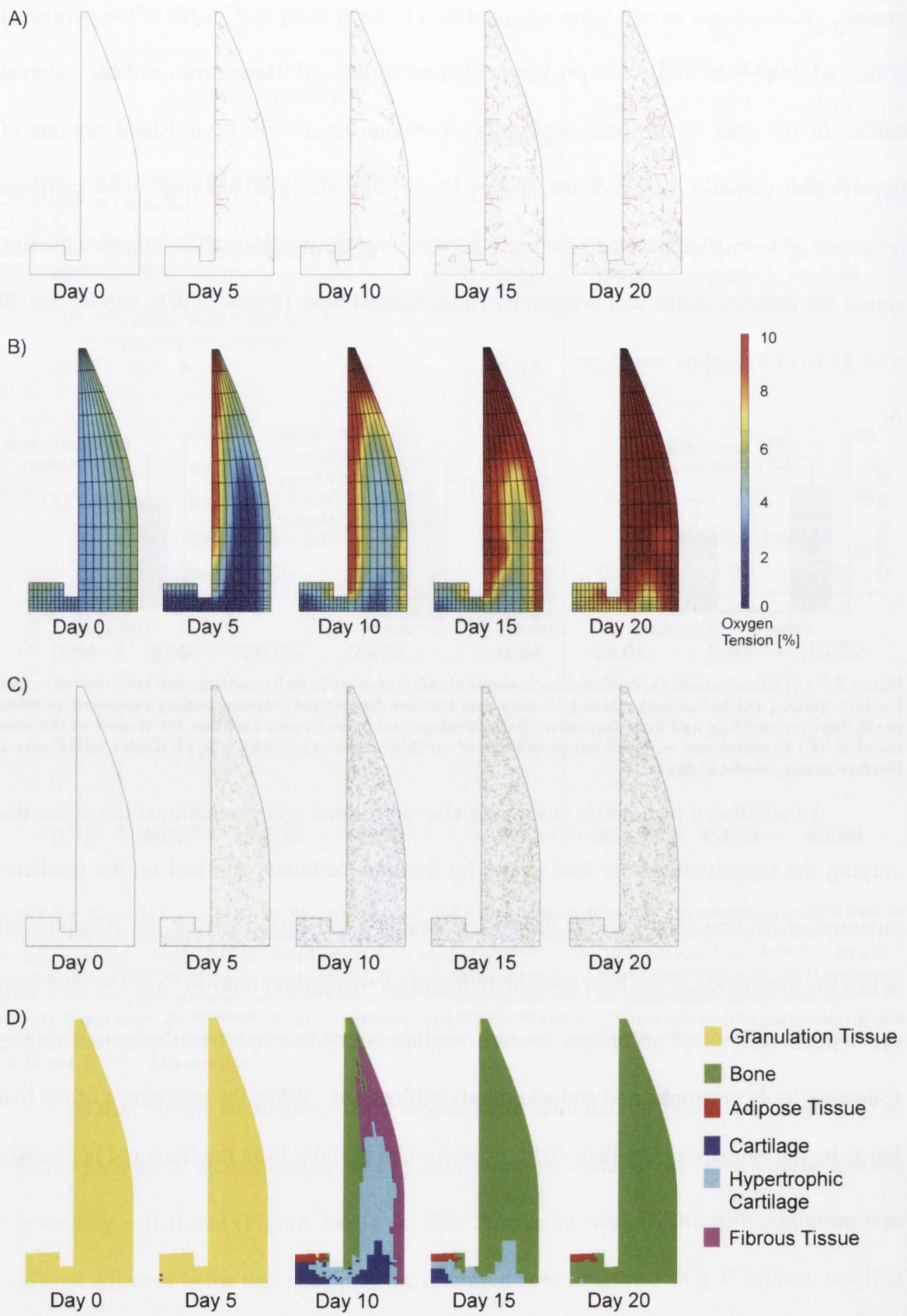

Figure 3-6: Results from normal fracture healing at various time points: (A) Angiogenesis; (B) Oxygen Diffusion; (C) Cell Differentiation; (D) Tissue Phenotypes

3.3.2 Fracture Healing with Impaired Angiogenesis

In the model of mildly impaired angiogenesis, an anoxic environment was predicted throughout the entire callus at the early time points. By day 7, some regions of cell apoptosis were predicted in the medullary cavity. In the external callus the anoxic conditions supressed stem cell differentiation and hence the majority of this region remained as granulation tissue (Figure 3-7A). By day 10, less than 10 % of the callus volume consisted of new bone, while 40 % of the callus consisted of cartilage or hypertrophic cartilage tissue (Figure 3-8A). By day 14, in the external callus, the regions of cell death and any remaining granulation tissue were replaced by cartilage as the blood supply began to recover. As blood vessels penetrated further into the callus, so too did an advancing front of hypertrophic cartilage around the border of the cartilage tissue. In the region proximal to the cortical bone, the hypertrophic cartilage was followed by an osseous front formed via endochondral ossification. By day 28, the callus had bridged and was composed almost entirely of bone.

The model for mildly impaired angiogenesis predicted the quantity of cartilage experimentally observed by Miedel *et al.* [181] at both 10 and 20 dpf (Figure 3-7A). It was also able to predict the quantity of bone observed at 10 dpf. Despite correctly predicting that the callus had bridged at 20 dpf, it over-predicted the quantity of bone observed experimentally at this time point. It was able to predict the proportion of cartilage which was hypertrophic at 10 dpf, but it also over-predicted the proportion which was hypertrophic at 20 dpf (Figure 3-8C). Compared to the model of normal fracture healing, the simulation of mildly impaired angiogenesis predicted a reduction in the proportion of hypertrophic cartilage at 10 dpf; 42 % (Figure 3-8B) vs 62 % (Figure 3-5C). In addition to this, a persistence of cartilage was predicted in the case of mildly impaired angiogenesis, with 15 % of the callus consisting of cartilage at day 20, compared to less than 1 % in the normal callus (data not shown).

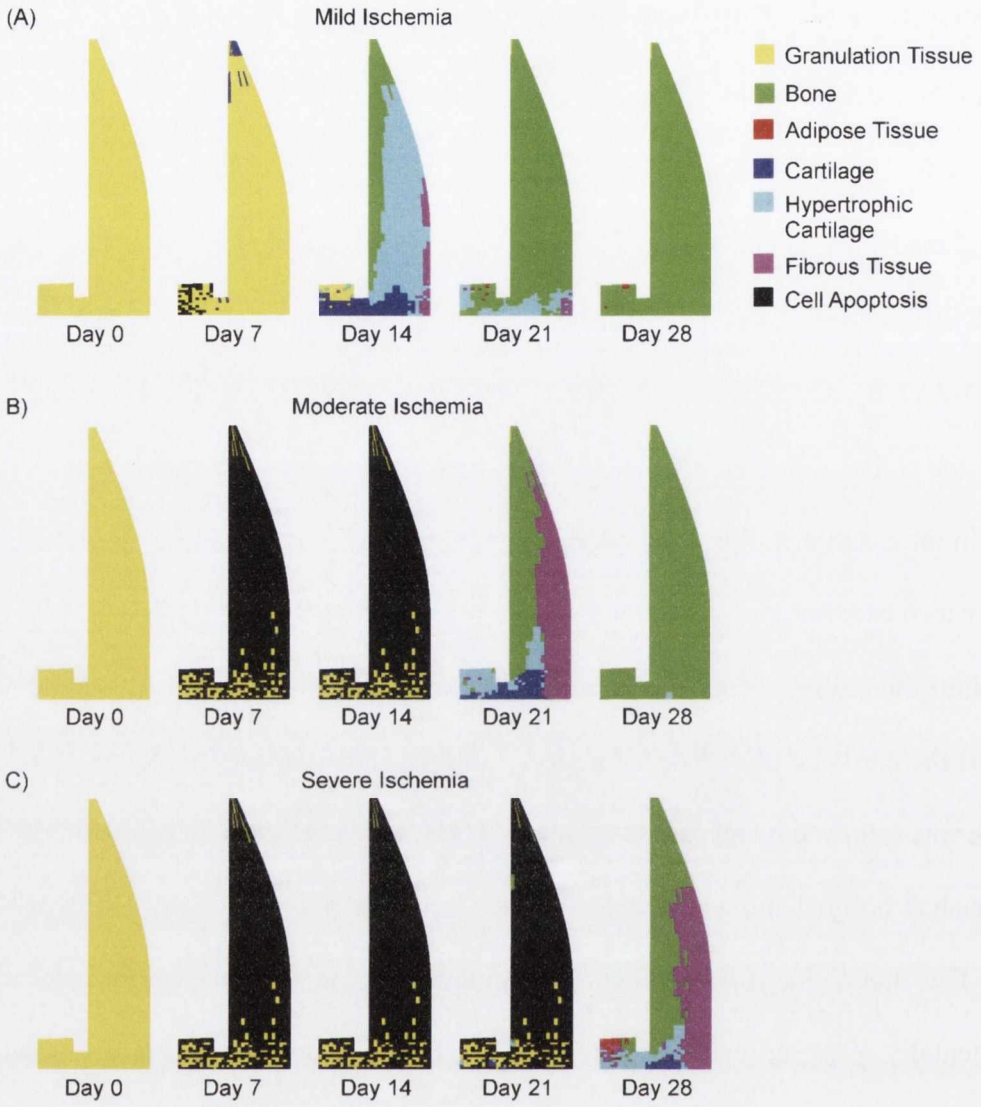

Figure 3-7: Predicted tissue phenotypes from the impaired angiogenic fracture healing models: (A) Fracture healing during mild vascular impairment conditions (B) Fracture healing during moderate vascular impairment conditions (C) Fracture healing during severe vascular impairment conditions.

In the model of moderately impaired angiogenesis, the extended delay in vascularisation was predicted to result in an entirely different pattern of healing. Although blood vessels began to grow into the callus from day 6, it took an additional two weeks before significant amounts of new tissue were predicted to form. By day 21 the internal callus consisted entirely of cartilage and hypertrophic cartilage, while the external callus was composed primarily of fibrous tissue on the soft tissue surface and woven bone which formed from the cortical surface. A cartilage region was also predicted to form in the core of the external callus. By day 28 the fracture gap had been bridged and the majority of the

external callus had been replaced by bone. Throughout the entire healing process the maximum combined quantity of cartilage and hypertrophic cartilage never exceeded 20 % of the total callus area (Figure 3-9).

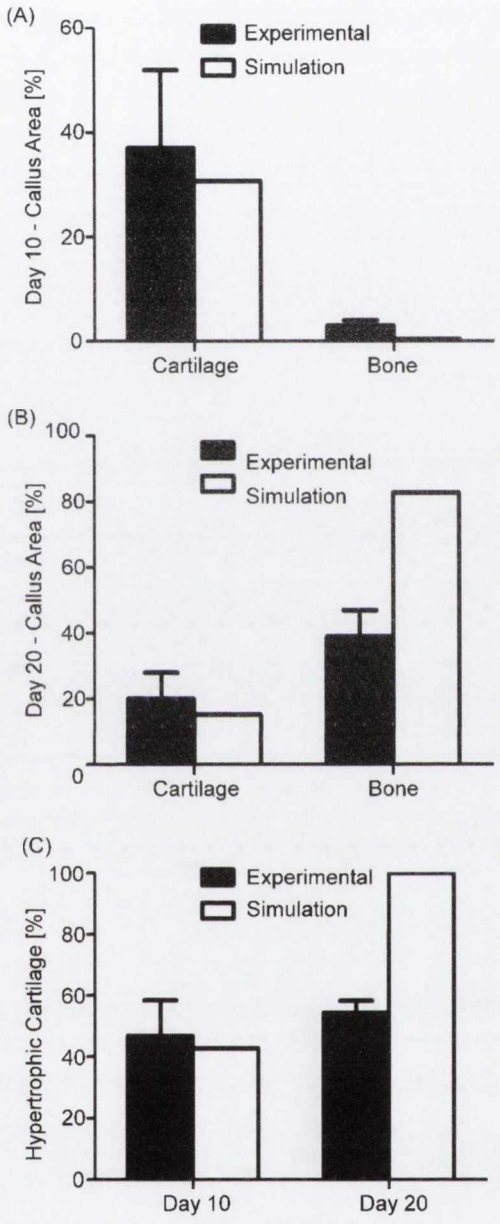

Figure 3-8: (A) Percentages of callus area made up by cartilage and bone observed experimentally by Miedel *et al.* [181] at day 10 in the ischemic fracture healing model compared to the percentages predicted in the computational model of fracture healing during mild vascular impairment. (B) Percentages of callus area made up by cartilage and bone observed experimentally at day 20 by Miedel *et al.* [181] in the ischemic fracture healing model compared to the percentages predicted in the computational model of fracture healing during mild vascular impairment. (C) Percentages of cartilage tissue area which is hypertrophic observed experimentally by Miedel *et al.* [181] in the model of ischemic fracture healing compared to the predicted percentages obtained from the computational model of fracture healing during mild vascular impairment.

A similar pattern of healing was predicted for the case of severely disrupted angiogenesis. For the first three weeks new tissue was not observed within the callus. By

day 10 the number of live cells had decreased to a minimum value of less than 1 % of the day 0 value (data not shown). Following the formation of blood vessels within the callus at day 10, MSCs proliferated and started to differentiate. By day 21 an osseous front of woven bone advanced from the cortical surface while the soft tissue surface consisted mainly of fibrous tissue. Throughout the entire healing process, the combined quantity of cartilage and hypertrophic cartilage did not exceed 10 % of the total callus area. By day 28 the fracture gap had not bridged and cartilage was present in the core of the external callus, the majority of which (> 70 %) was hypertrophic.

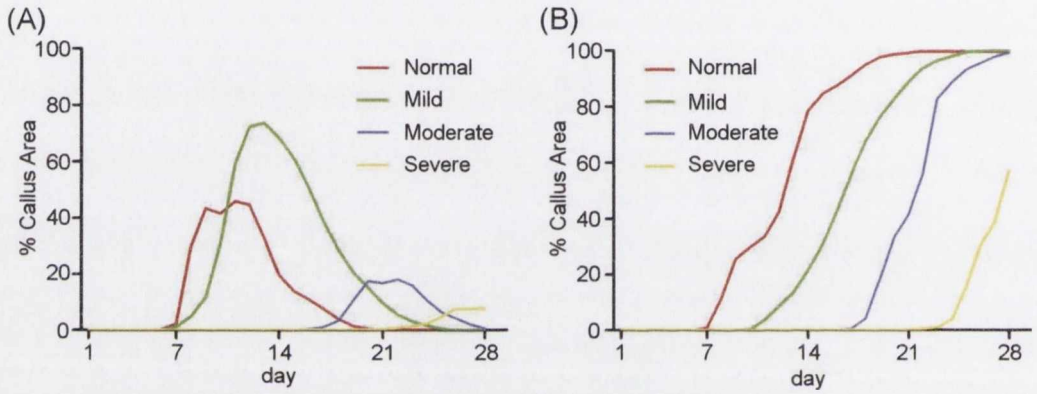

Figure 3-9: Predicted quantity of (A) cartilage and (B) bone at different time points in the simulations of fracture healing under normal, mild angiogenic impairment, moderate angiogenic impairment and severe angiogenic impairment.

3.4 Discussion

The objective of this study was to use a computational mechanobiological model to provide a better understanding for how the altered microenvironment of an angiogenically impaired fracture callus, and in particular the altered levels of oxygen present in such a regenerative scenario, regulates stem cell differentiation and tissue repair. In particular, we sought to test the hypothesis that the local oxygen tension regulates hypertrophy and endochondral ossification of the cartilage which forms in the callus of a fractured long bone. The first part of the study involved updating a previously developed tissue differentiation algorithm [44] to include a condition whereby the local oxygen levels regulate the initiation of chondrocyte hypertrophy and the progression of endochondral ossification. A second

condition was also included to describe cell death and the suppression of MSC differentiation in regions of anoxia. The updated model and the underlying model hypotheses were then tested by simulating the time course of normal fracture healing in a murine tibia. The developed model was able to predict the spatial distribution and the experimentally observed quantity of tissue phenotypes (including the ratio of cartilage to hypertrophic cartilage) which were within the experimentally observed range at 10 and 20 dpf. Following this, the updated tissue differentiation algorithm was then used to simulate fracture healing under conditions of angiogenic impairment. These models were considered to represent different levels of ischemia, whereby it was assumed that ischemia arises as a result of delayed vascular ingrowth from the surrounding tissues. In the simulation of fracture healing under mild vascular impairment, the predicted quantity of cartilage observed at both 10 and 20 dpf increased compared to normal fracture healing, similar to that observed experimentally in a murine model of ischemic fracture healing [181]. In contrast, the models of moderately and severely impaired angiogenesis predicted a reduction in cartilage formation, a behaviour which has also been observed experimentally in different models of ischemic fracture healing [175]. Furthermore, Lu *et al.* [175] also reported a failure to achieve bony union by day 28, a feature which was predicted by the computational model of severe vascular impairment.

Support for the model hypothesis that oxygen levels regulate chondrocyte hypertrophy and endochondral ossification during fracture healing was provided by comparing the model predictions to experimental measurements of different tissue types within the callus. In the case of normal fracture healing, only the day 10 experimental results were available as very little cartilage was observed experimentally by day 20 [182]. At both time points, the model was able to predict the quantity of bone and cartilage as well as the correct ratio of cartilage to hypertrophic cartilage which was experimentally observed at day

10. The simulation of normal fracture healing was also able to predict the general trends of tissue formation experimentally observed within a fractured murine tibia [175]. In this study the authors reported that the quantity of cartilaginous tissue (including hypertrophic cartilage) peaked within the fracture callus by day 10 before decreasing until no cartilage remained by day 20. The authors also reported that the volume of bone increased substantially between days 10 and 20, after which remodelling occurred. Both of these trends were observed in the simulation (Figure 3-9).

Further support for the model hypothesis was provided by comparing the simulation of mild angiogenic impairment with the findings of experimental models of ischemic fracture healing [181]. In the simulation, the percentage of callus cartilage that was hypertrophic was predicted to increase between days 10 and 20. Such an increase was also observed experimentally, although this was not to the same extent as that predicted by the model. It should be noted, however, that at this time point the callus contained significantly less cartilage than that observed at 10 dpf. In absolute terms, at 20 dpf the model predicted that approximately 15 % of the callus consisted of hypertrophic cartilage, compared to an experimental measurement of approximately 10 %.

Additional support for the hypothesis that the local oxygen tension regulates endochondral ossification is provided by comparisons of model predictions of fracture healing under mildly impaired angiogenesis and by the experimental observations of Yin *et al.* [179]. In this study the course of fracture healing within the femur of GPCR kinase 2 interacting protein (GIT1) knock out mice was examined. The authors reported that mice which were deficient in the gene GIT1 presented a reduction in both the density and the size of blood vessels within the fracture callus compared to that observed during normal fracture healing. This reduced vascular response correlated with a higher quantity of cartilage and a reduced quantity of bone observed at the later stages of the healing process. Both of these

behaviours were observed in the simulation of mild angiogenic impairment. It must be noted that the protein GIT1 has been shown to play a role in osteoclast activity [238] (a feature of endochondral ossification), and as such its absence may have directly contributed to the observed reduction in the progression of endochondral ossification. This feature provides an explanation for the fact that, compared to the simulation of mild angiogenic impairment, the rate of bone formation during the later stages of repair was much lower in this experimental model.

The developed models of ischemia also provide a potential explanation for the conflicting results reported by studies examining the pattern of healing within fractured ischemic limbs. Miedel *et al.* [181] observed an increase in the quantity of cartilage while, contrary to their expectations, Lu *et al.* [175] reported that ischemia significantly reduced the formation of cartilage within the fracture callus. Miedel *et al.* [181] reported the presence of vessels within the ischemic callus at 10 dpf while Lu *et al.* [175] did not observe angiogenesis within the callus until 14 dpf. These observations led us to hypothesise that the different levels of cartilage tissue formation arose due to different recovery rates of the vasculature. Support for this hypothesis was provided by the fact that the simulation of fracture healing under mild angiogenic impairment agreed with the findings of Miedel *et al.* [181] (persistence of cartilage), while the simulations of moderate and severe angiogenic impairment agreed more closely with the findings of Lu *et al.* [175] (reduction in cartilage). Interestingly, Duvall *et al.* [239] reported that varying the location where the artery was ligated drastically altered the amount of vasculature which remained following the surgical induction of ischemia, which may explain the different levels of vascular recovery observed experimentally in the literature. Further work is required to test this hypothesis.

There were a number of limitations associated with the computational model which may have limited its predictive capacity. The first of these was that the model did not

consider the increase in tissue volume which occurs as cartilage becomes hypertrophic [240]. In addition to this, in the model of angiogenesis, it was assumed that blood vessels grew at a constant rate. In the parametric study this was shown to have the largest effect on the model predictions. In reality the rate of blood vessel growth may vary both temporally and spatially within the *in vivo* environment due to the presence of different growth factors [241] or the local mechanical environment [41]. These factors have been implemented within a number of different computational models which have successfully predicted the temporal and spatial pattern of tissue formation during different *in vivo* events [29,30,32]. It was also assumed that MSCs only invade the fracture site at the onset of injury. In reality, additional MSCs could be recruited into the callus as the vascular network is restored (particularly in the case of ischemic fracture healing), or indeed progenitor cells could continue to migrate into the facture site from surrounding soft tissues. In addition to this, the developed model may also be sensitive to the length of the time step used as part of the iterative procedure. This was not considered an issue however as all of the values which were dependent upon time were automatically normalised relative to the time step at the start of each simulation.

The model also assumed (with the exception of ABs) that all cell phenotypes could eventually change into an OB when exposed to the appropriate stimuli. This feature meant that, even in the model of severe angiogenic impairment, following the restoration of the vasculature, bony union was eventually predicted (data not shown). In reality this may not be the case as, over time, cells within the fracture callus may lose their osteogenic potential or commit to an alternative phenotype resulting in non-union. This issue will be addressed in future work by establishing conditions whereby cells are unable to transdifferentiate after a period of time. Despite this, it is important to note that, although Lu *et al.* [175] did not observed bony union over 28 days, they could not conclude whether ischemia resulted in a

permanent non-union or if bony healing had been delayed beyond the experimental time period.

Finally, in the development of each model, certain features of ischemic fracture healing were ignored, namely that ischemia tends to result in a smaller fracture callus compared to normal healing [175,181]. This reduction in volume results in an altered mechanical environment in response to loading. The changes to the local strains may in turn lead to changes in the progression of angiogenesis and thus, differences in the local oxygen environment. Despite this, alterations in the callus geometry due to impaired angiogenesis were not considered and the same geometry was used for both the normal and impaired angiogenesis fracture models. In addition to this, ischemia may also affect the migration of stem cells to the fracture site. All of the simulations, however, shared the same conditions regarding the initial quantity of MSCs. The basis of these simplifications was the assumption that delayed vascularity was the main mechanism by which impaired angiogenesis affected progenitor cell fate.

The remaining limitations of the models are the same as the ones previously outlined by Burke *et al.* [45]. These were that: 1) An idealised axisymmetric model of the callus was employed which assumed that the medial and lateral sides of the callus were identical 2) Only axial loading was considered, based on an assumption that the intramedullary pin provided complete lateral stability and the applied splints provided full torsional stability 3) Simplified biphasic material models were used, which ignored the complex viscoelastic nature of the solid constituents of the regenerating soft tissue 4) Simplified representations of complex *in-vivo* processes were used to model cell proliferation and migration, angiogenesis and oxygen transport. In all cases, the effect of each of these simplifications was considered to be sufficiently small so as not to significantly reduce the predictive capacity of the developed models.

In spite of these limitations the updated algorithm used in this study was able to predict the pattern of healing seen in both normal and ischemic fracture repair. Based on the developed models, it was also possible to elucidate a mechanism to potentially explain variations in bone and, in particular, cartilage formation observed in different experimental models of ischemic fracture repair. Furthermore, by being able to predict the different quantities of tissues observed experimentally, the models provided additional evidence in support of the hypothesis that, during *in vivo* regenerative events such as fracture healing, hypertrophy of chondrocytes is regulated by the local oxygen availability. Future work will involve using the updated algorithm to model the spontaneous repair process within an osteochondral defect. In particular, the rules developed in this study will be used to provide an improved understanding of endochondral ossification during osteochondral defect repair. This will allow for further validation and improvement of the developed algorithm. It will also provide a means to better understand how the local microenvironment regulates stem cell fate during tissue regeneration.

Chapter 4 The role of oxygen as a regulator of stem cell fate during the spontaneous repair of osteochondral defects

In the preceding chapter a previously developed tissue differentiation algorithm was updated to include a series of rules whereby chondrocyte hypertrophy and endochondral ossification were regulated by the local oxygen tension. In this chapter the updated algorithm is used to model the spontaneous repair process within an osteochondral defect. In the first part of the study, the temporal and spatial pattern of tissue formation predicted by the model is compared to the results of a number of different *in vivo* studies. A sensitivity analysis is then performed to determine which of the model parameters are the most influential. Following this, a parametric study is conducted to examine how interventions which regulate the rate of angiogenesis, and thus alter the local oxygen environment, influence the progression of healing over a 12 week period. The results from this chapter suggest that osteochondral defect repair can be enhanced by interventions where angiogenesis is promoted but confined to within the subchondral region of the defect.

4.1 Introduction

Osteochondral defects of a certain size have the capacity to spontaneously repair [6]. This process forms the basis of a number of different treatment strategies for both chondral and osteochondral defect repair [10,11]. Repair is initiated after MSCs invade the defect site from the exposed bone marrow and begin to repair the damaged tissue [2,6–9]. In the early stages, bone is synthesised within the subchondral region while a mixture of cartilage, fibrocartilage and fibrous tissue forms above this in the chondral region [6,9]. Over time, however, the newly formed subchondral bone plate progresses into the chondral region, resulting in a thinning of the repair cartilage and the subsequent degradation of the tissue [4,57]. The environmental factors regulating this spontaneous repair process remain poorly understood, with previous computational models suggesting that biomechanical signals may play a key role in directing stem cell fate during osteochondral defect repair [209].

Excessive bone formation during joint regeneration has been linked with vascular invasion of the defect site. Klinger *et al.* [16] examined the effect of inhibiting angiogenesis within a porcine model of cartilage repair by microfracture. In this study, angiogenesis was inhibited by over-expressing the anti-angiogenic factor chondromodulin-1. This resulted in less vascular invasion, an inhibition of chondrocyte hypertrophy and endochondral ossification, as well as more robust hyaline cartilage formation at later time points. Similar results were observed by Nagai *et al.* [15] within a rabbit model of spontaneous osteochondral defect repair, where administration of an anti-vascular endothelial growth factor was used to inhibit angiogenesis. Similar to Klinger *et al.* [16], the authors reported more robust hyaline cartilage at later time points as well as less chondrocyte hypertrophy and endochondral ossification compared to the control group [15]. Both of these studies point to the importance of angiogenesis and associated local oxygen levels in regulating chondrogenesis and endochondral ossification during osteochondral defect repair.

Based on these findings and recent studies which have shown that hypertrophy of chondrocytes is supressed in hypoxic or low oxygen conditions [37,47–49,232], we hypothesised that local oxygen levels are a critical determinant of the success of osteochondral defect repair. It is further hypothesised that limiting angiogenesis within an osteochondral defect improves cartilage repair by inducing a sustained hypoxic environment. To test this hypothesis, we used a previously developed computational model of MSC differentiation to study the spontaneous repair process within an osteochondral defect. In this model, MSC differentiation was predicted using an algorithm which assumed that cell fate is governed by the local oxygen level and surrounding substrate stiffness [44–46]. To test the extent to which angiogenesis and the subsequent oxygen environment regulates tissue formation during osteochondral defect repair, the model was first used to simulate the time-course of healing within an empty defect. Following this, a sensitivity analysis was performed which found that the parameters controlling blood vessel growth and blood vessel branching had the greatest effect on tissue formation within the defect. Finally, a parametric study was conducted to examine how varying these parameters affects tissue formation within an osteochondral defect. In order to test the underlying model hypothesis the results of these simulations were then compared to *in vivo* studies of osteochondral defect repair under altered angiogenic states [15,16].

4.2 Method

4.2.1 Iterative Procedure

Tissue differentiation within the defect region was simulated via an iterative procedure similar to the one outlined in the previous chapter (Section 3.2.2). In all of the simulations each time step modelled a period of 24 hours.

Table 4-1: Material Properties

Material Property	Granulation Tissue	Fibrous Tissue	Cartilage	Hypertrophic Cartilage	Immature Bone	Mature Bone	Cortical Bone	Meniscus
Young's Modulus [MPa]	1[a]	2[a,b]	10[a,b]	20	1000[a]	6000[c]	20,000[c]	50
Poisson's Ratio	0.167	0.167	0.167	0.167	0.3	0.3	0.3	0.3
Permeability [mm^4/ Ns]	0.01[a]	0.01[a,b]	0.005[a,b]	0.005	0.001[a]	0.0037[d]	1e-5[a]	-
Solid Volume Fraction	0.2	0.2	0.2	0.2	0.2	0.2	0.2	-

a 217

b 224

c 23

d 209

4.2.2 Finite Element Model

A simplified 3D Finite Element (FE) model of an osteochondral defect within the femoral condyle was constructed to predict the biophysical stimuli generated within such a defect during gait (Figure 4-1). Similar to previous studies [209,242,243], the condyle was modelled as a flattened semi-sphere of radius 20 mm which consisted of a layer of cortical bone which was 1 mm deep and which overlaid mature cancellous bone. The condyle was covered with a layer of cartilage which was 2 mm thick, and which was supported by the meniscus. The tibial plateau was modelled as a rigid contact layer, the permeability of which was assumed to be the same as cartilage. All materials were modelled as bi-phasic, except for the meniscus which was modelled as a solid elastic material, where a sliding interface was used to model the contact between it and the cartilage layer. At the centre of the FE model, a defect of size φ5 mm x 5 mm was included. This was assumed to be initially filled with granulation tissue. The material properties of each tissue type are listed in Table 4-1. A load of 2400 N was applied over 1 second based on the assumption of five to six times subject weight (80 kg) spread evenly between the lateral and medial compartments [244]. The described model was implemented in the open source finite element package FEBio (version 2.2.2, University of Utah, Technology Commercialization Office, 615 Arapeen Drive, Suite 310, Salt Lake City).

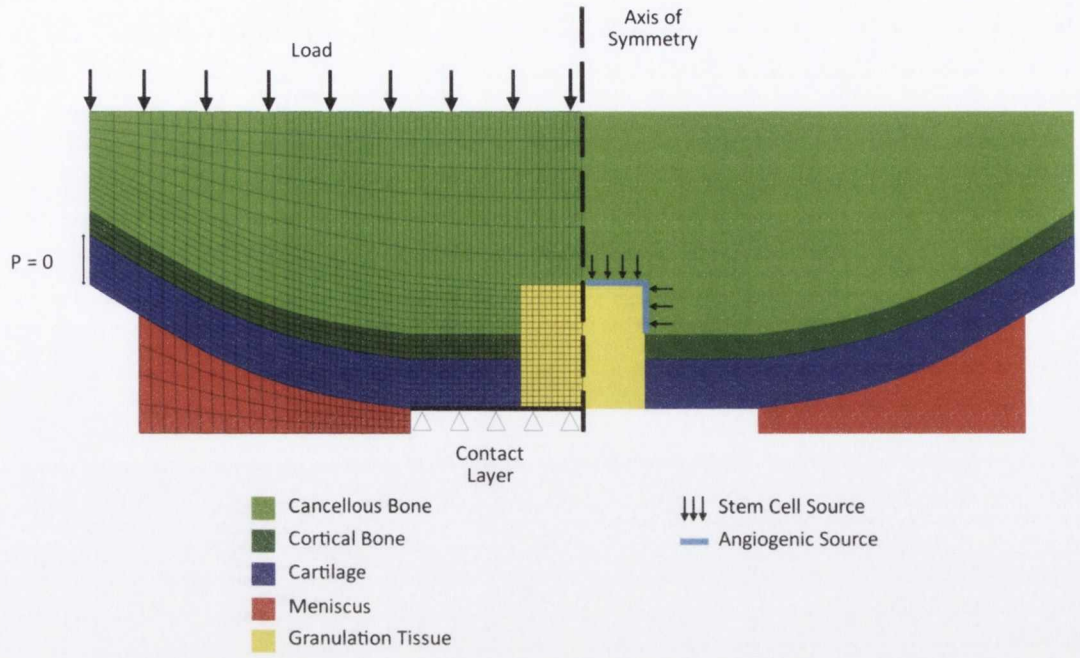

Figure 4-1: Finite Element Model of the knee with an osteochondral defect including boundary conditions.

4.2.3 Angiogenesis

Angiogenesis was modelled using the lattice-based approach described by Checa *et al.* (Figure 4-2B) [29]. Furthermore, the rules governing blood vessel growth and direction were the same as those outlined in the previous chapter (Section 3.2.4). Briefly, vessels stopped growing if the octahedral shear strain exceeded a threshold limit (ε^{angio}) or if anastomosis had occurred. Vessels were also able to branch should their length exceed a certain value (L_{min}). The probability of branching then increased linearly until the vessel reached the maximum allowable length (L_{max}), at which point the probability of branching occurring was 1 [29]. Finally, vessel growth was biased in the direction of the minimum principle strain.

At day 0, it was assumed that vessels grew into the callus from the exposed cancellous bone (Figure 4-1). This assumption was based on the findings that this tissue is highly vascularised and provides a nutrient supply to both itself and the overlaying articular cartilage [11]. The initial number of vessels was governed by the parameter N^{angio} which

denoted the proportion of lattice points on the cancellous bone surfaces which were invading blood vessels.

Table 4-2: Angiogenesis and MSC Differentiation Model Parameters

Model Parameter	Symbol	Source	Unit	Value
Octahedral shear strain threshold for inhibition of angiogenesis	ε^{angio}	Estimated	-	0.1
Blood vessel growth rate	V^{growth}	Estimated	mm day^{-1}	0.1
Minimum length for branching	L_{min}	[29]	mm	0.2
Maximum length without branching	L_{max}	[29]	mm	0.5
Minimum cell age for MSC differentiation	Age^{cell}	Estimated	days	5
Oxygen diffusion coefficient	G	[44,227]	$mm^2\ s^{-1}$	2.2×10^{-3}
Initial oxygen tension	$O_2^{initial}$	[184]	mol mm^{-3}	101.6×10^{-12}
Oxygen tension for inhibition of differentiation	$O_2^{inhibition}$	[129]	mol mm^{-3}	5×10^{-12}
Oxygen limit for cartilage	$O_2^{cartilage}$	[44]	mol mm^{-3}	30.48×10^{-12}
Oxygen limit for differentiation of cartilage to hypertrophic cartilage	$O_2^{hypertrophic}$	Estimated	mol mm^{-3}	30.48×10^{-12}
Oxygen limit for calcification of hypertrophic cartilage	$O_2^{endochondral}$	Estimated	mol mm^{-3}	50.48×10^{-12}

4.2.4 Cell Migration, Cell Proliferation and Cell Death

The migration and proliferation of MSCs, osteoblasts (OBs), chondrocytes (CCs), fibroblasts (FBs) and hypertrophic chondrocytes (HC) was also modelled using a lattice approach [20,29] and is described in detail in the previous chapter (section 3.2.5). The migration of cells was implemented using 'random walk' theory [20]. Cell proliferation was implemented in a similar fashion provided that there was a vacant position beside the parent cell. The maximum number of cells allowed in any element was limited to 1×10^5 cells/mm^3 [44]. The migration rate (M) determined the number of attempted migration actions per time step, while the doubling time (DT) was the age a cell had to be before it proliferated (Table 4-3). Cell proliferation was inhibited in regions where the oxygen concentration fell below a specific threshold value (O_2^{prolif}) (Table 4-3). It was assumed that 5 % of the lattice points on the cancellous surface of the defect (Figure 4-1) and 0.5 % of the interior lattice points

contained MSCs at day 0. If the oxygen concentration fell below a threshold value (O_2^{death}) then cell death was initiated.

Table 4-3: Cell Model Parameters

Model Parameter	MSC	CC	OB	FB	HC
Doubling Time [days]	0.5[a]	1.5[a]	1[a]	0.5[a]	1.5[a]
Migration Rate [$\mu m\ hr^{-1}$]	26.6[b]	N/A	N/A	26.6[b]	N/A
Anoxic Death Rate [% cells day^{-1}]	20	20	20	20	20
Oxygen Concentration for cell proliferation (O_2^{prolif}) [mol mm^{-3}]	40×10^{-12} [c]	10×10^{-12}	80×10^{-12} [c]	20×10^{-12}	30×10^{-12}
Oxygen Concentration for cell death (O_2^{death}) [mol mm^{-3}]	5×10^{-12} [d]	5×10^{-12} [c]	20×10^{-12} [c]	5×10^{-12}	5×10^{-12} [c]

a 153

b 226

c 30

d 47

4.2.5 Oxygen Transport

Oxygen transport was modelled using the same method described in the previous chapter (section 3.2.6). The same mesh used for the defect region in the structural model was used in the model of oxygen transport (Figure 4-1). Cancellous bone is highly vascularised [11], and it was therefore assumed that there was a constant oxygen tension of 10 % at the exposed bone within the defect. In addition to this, a constant oxygen boundary condition of 5 % was applied to the surface of the defect in order to simulate the nutrient supply from the synovial fluid [72,245]. Finally, based on the in silico model developed by Zhou et al.[72], the following three assumptions were made: 1) The synovial fluid was well mixed and as such any gradients within the fluid were negligible. 2) Oxygen transport was steady state, meaning that the effects of mechanical loading and cartilage deformation on oxygen transport were ignored. 3) Gradients from the cell surface to the bulk tissue were negligible.

Table 4-4: Oxygen parameters for each cell phenotype

Michealas - Menten Parameters	MSC	CC	OB	FB	HC
Cell type (n)	1	2	3	4	5
Max Consumption Rate (Q^{max}) [mol $cell^{-1}$ hr^{-1}]	93.2×10^{-15} [a]	1.8×10^{-15} [a, b]	93.2×10^{-15} [a]	93.2×10^{-15} [a]	1.8×10^{-15} [a]
Oxygen Concentration at half max consumption [mol mm^{-3}]	22.5×10^{-12}	22.5×10^{-12}	22.5×10^{-12}	22.5×10^{-12}	22.5×10^{-12}

a 30

b 73

4.2.6 MSC Differentiation

MSC differentiation was dependent upon the local substrate stiffness and oxygen tension (Figure 4-2A). This algorithm is outlined in the previous chapter (3.2.7). As adipogenesis is not observed in the early stages of osteochondral defect repair it was excluded from the model; this was based on the assumption that the stiffness of the granulation tissue is not low enough to facilitate this lineage commitment.

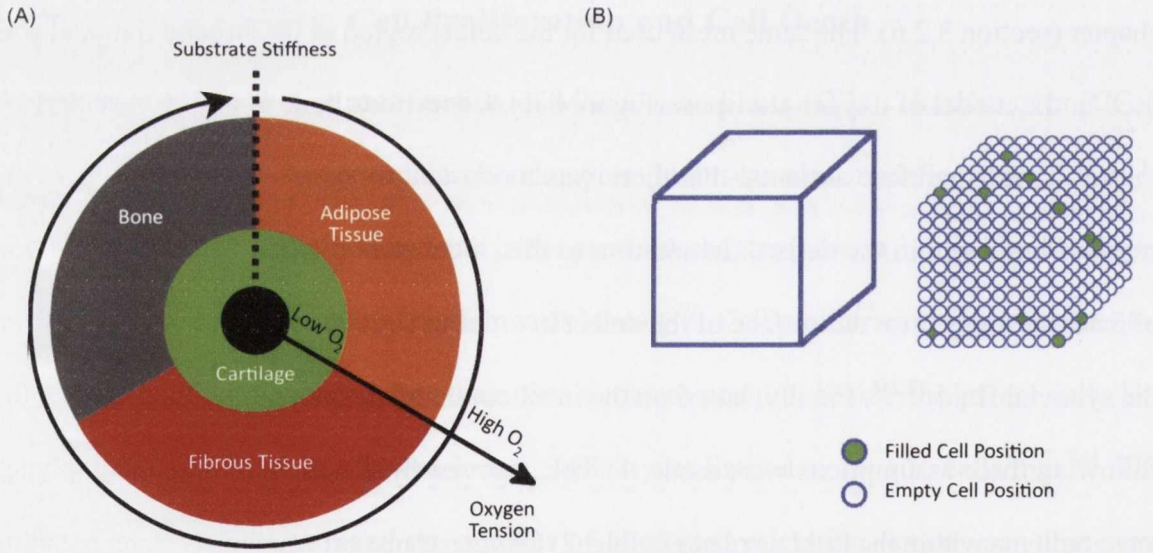

Figure 4-2: (A) Tissue differentiation algorithm as directed by the local oxygen tension and substrate stiffness. (B) A 3-dimensional finite element with corresponding lattice. Each lattice point represents a potential location for a cell.

Endochondral ossification was modelled using the two-step process which was developed in the previous chapter (section 3.2.8). Briefly, in the first step CCs differentiated into HCs in regions where the oxygen tension increased beyond a threshold value ($O_2^{hypertrophic}$). Following this, in the second step HCs transdifferentiated into OBs, provided

that: (1) they were in an element where the oxygen tension was greater than a threshold value ($O_2^{endochondral}$) and (2) they were in the vicinity of an OB.

4.2.7 Simulations

The spontaneous repair process was simulated over a period of 12 weeks, where each iteration represented a time period (T^{step}) of 24 hours. Using the estimated parameters, a model of the spontaneous repair process within an untreated empty defect was simulated. The results of this simulation were then used as the baseline for a sensitivity analysis which was conducted on each of the estimated parameters (Table 4-5). Similar to Carlier *et al.* [30], each parameter was varied between 50 % and 150 % of its estimated value. In addition to this, an analysis of the time step size was also examined whereby the step size was varied between 12 hours and 36 hours. At the end of each simulation the predicted quantity of each tissue type was compared to the baseline model. Following this, the effect of reducing and increasing the rate of angiogenesis within an osteochondral defect was examined by performing a parametric study where the parameters controlling the blood vessel growth rate (V^{growth}) and the branching rate (L^{min} & L^{max}) were varied with respect to the values used in the baseline model.

4.3 Results

4.3.1 Untreated Osteochondral Defect

At day 0, although the defect was predicted to be devoid of vessels (Figure 4-3A), the oxygen tension in the base (Figure 4-3B) was high as a result of the constant oxygen boundary condition at the exposed cancellous bone. Within the first 2 weeks an anoxic environment was predicted in the core of the defect, which resulted in reduced cell viability in this region. Cell proliferation was confined mainly to the base, although some proliferation was observed at the defect surface due to the oxygen supply from the synovial fluid. By day

14, osteogenesis was predicted at the exposed bone. As the majority of the subchondral region was hypoxic, however, most of the MSCs in this region differentiated into chondrocytes (Figure 4-3C). Conversely, at the surface of the defect the more normoxic environment resulted in the formation of fibrous tissue with cartilage directly below it (Figure 4-3D). By day 28, as blood vessels penetrated further into the defect, a normoxic environment formed which resulted in the cartilage in the base becoming hypertrophic. As this was converted to bone by endochondral ossification, the subchondral plate advanced towards the surface of the defect. By day 35 (data not shown), all of the granulation tissue had been replaced. The quantity of cartilage (39%) peaked at this time and steadily decreased as it underwent hypertrophy and was replaced with bone by endochondral ossification. By day 56 the advancing bone formed in an infundibuliform (funnel) shape as it approached the chondral region (Figure 4-3C). At this time point, although some cartilage within the chondral region had undergone hypertrophy, the majority of the tissue within this region remained as cartilage (Figure 4-3D). By day 84, however, the subchondral plate had advanced above the tidemark and all of the cartilage had become hypertrophic (Figure 4-3D).

As an additional part of this study it was shown that the predicted behaviour was largely insensitive to the random elements of the model (i.e. the initial position of the cells and blood vessels, random walk theory and the determination of some elements of blood vessel direction) (Appendix II: Analysis of Random Variation in the Baseline Models (Chapter 4)).

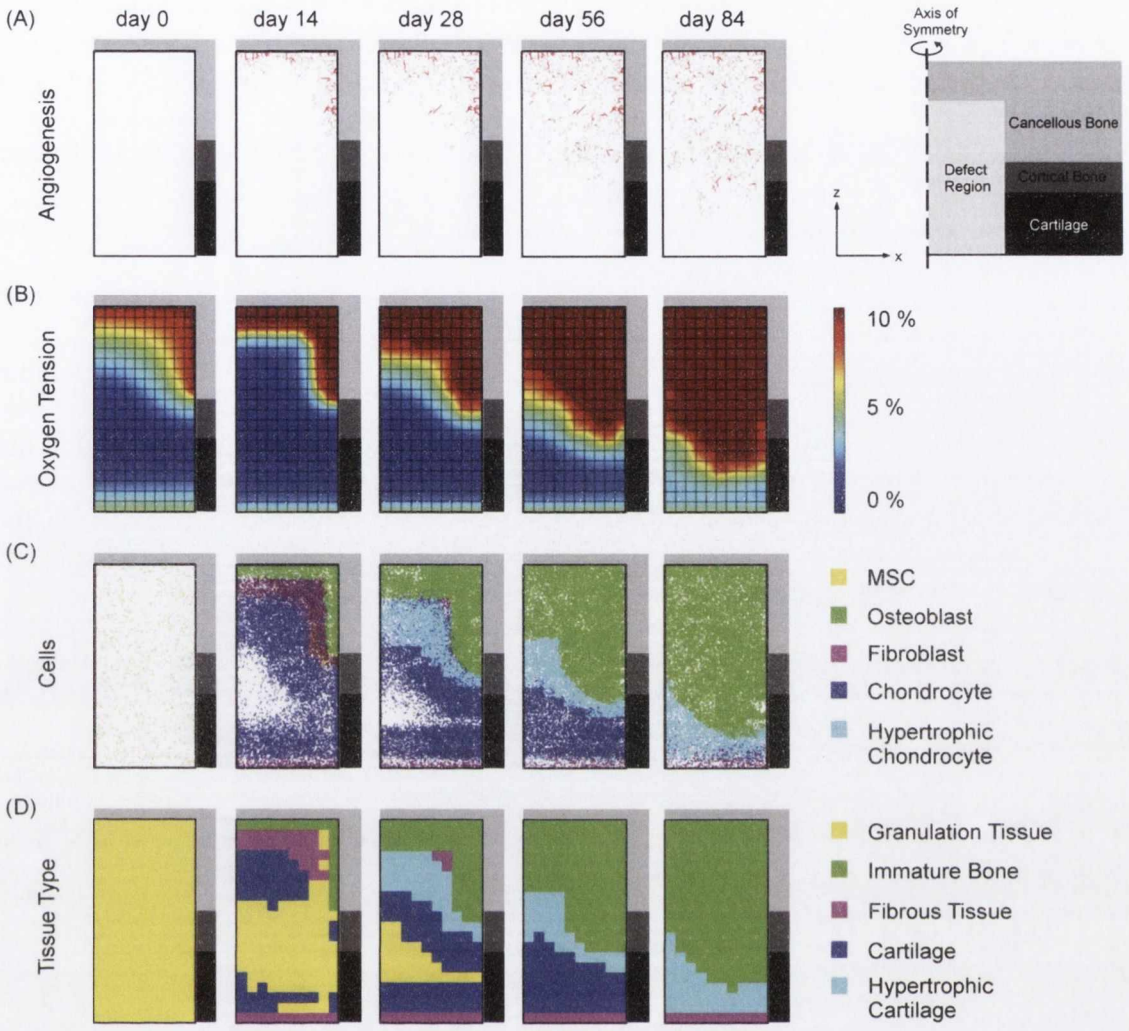

Figure 4-3: Predicted pattern of (A) angiogenesis, (B) oxygen tension, (C) cell differentiation and (D) tissue type during the spontaneous repair of an osteochondral defect at day 28, 56 and 84.

4.3.2 Sensitivity Analysis

The majority of the estimated parameters had very little influence on the final prediction of each tissue type (Table 4-5). Varying each parameter by ± 50 % of its estimated value resulted in a deviation of, at most, ± 10 percentage points from the predicted quantity of each tissue within the baseline simulation. The exceptions to this were the parameters ε^{angio}, $O_2^{Hypertrophy}$, V^{growth} and L^{min} & L^{max}. In the case of the first two, which controlled the octahedral shear strain at which vessels stopped growing and the oxygen tension at which CCs became hypertrophic, altering these parameters affected the amount of cartilage which was hypertrophic at day 84. The latter two parameters controlled the rate of blood vessel

growth and the rate of blood vessel branching respectively. In both cases these parameters influenced the degree of vascularisation within the defect, which in turn regulated the oxygen concentration. Varying these parameters thus affected both the rate at which cartilage became hypertrophic and the rate at which hypertrophic cartilage was converted to bone by endochondral ossification. In this case, either decreasing the blood vessel growth rate, or increasing the branching limits decreased the predicted quantity of bone and hypertrophic cartilage at day 84. Conversely, increasing the blood vessel growth rate, or decreasing the vessel branching limits enhanced the effect of angiogenesis, which in turn increased the predicted quantity of bone at day 84.

Table 4-5: Results of the sensitivity analysis. The percentage of each tissue type is measured at day 84 and the standard condition is indicated in bold. Each parameter is varied between 50 % and 150 % of its respective baseline value.

Parameter	Symbol	Value	Granulation Tissue [%]	Bone [%]	Fibrous Tissue [%]	Cartilage [%]	Hypertrophic Cartilage [%]
Baseline (Untreated Defect)			**0**	**78**	**5**	**0**	**17**
Initial proportion of lattice points which are assigned active blood vessels [%]	N^{angio}	7.5 22.5	0 0	78 77	5 5	0 0	17 18
Proportion of lattice points in an element which must contain vessels for it to be fully vascularised	$V^{density,max}$	0.1 0.3	0 0	83 72	5 5	0 0	12 22
Blood vessel growth rate [mm/day]	V^{growth}	0.06 0.14	1 0	47 84	4 1	38 0	10 15
Strain threshold for inhibition of angiogenesis [%]	ε^{angio}	5 15	0 0	72 78	5 5	12 0	10 17
Oxygen tension required for hypertrophy [%]	$O_2^{hypertrophy}$	1 5	0 0	76 74	5 5	0 14	19 7
Oxygen tension required for endochondral ossification [%]	$O_2^{endochondral}$	3 7	1 0	81 76	5 5	0 0	14 19
Minimum and maximum length for blood vessel branching [mm]	L^{min} & L^{max}	0.1 – 0.3 0.3 – 0.7	0 0	88 58	2 5	0 23	10 14
Young's modulus of the meniscus [MPa]	$E^{meniscus}$	25 75	1 0	76 73	5 5	0 5	19 17
Required age of a cell before it has produced enough matrix to influence the neighbouring cells [days]	$Age^{changed}$	1 5	0 0	79 68	5 5	0 0	16 27
Time step size [hrs]	T^{step}	12 36	1 0	81 71	8 7	0 0	9 22

The model was also reasonably insensitive to the size of the time step used in the iterative process (T^{step}). The reason for this was that, at the start of each simulation, all of the

parameters which were dependent on time were normalised to the size of the time step (i.e. the units of each of these parameter were altered from days to time steps). Despite this, the size of the time step appeared to have an effect on the quantity of hypertrophic cartilage and bone. It may thus be the case that larger time steps ($T^{step} > 36$ hours) will result in an altered prediction of the temporal pattern of bone formation within the defect.

4.3.3 Influence of angiogenesis on osteochondral defect repair

Varying the model parameters controlling the blood vessel growth rate (V^{growth}) and the rate of vessel branching (L^{min} and L^{max}) had different effects on the predicted pattern of angiogenesis (Figure 4-4). Altering the vascular growth rate changed the time it took vessels to progress from the cancellous bone to the surface of the defect. When this parameter was high (relative to the baseline simulation), blood vessels were predicted to have filled the defect by day 56 (Figure 4-4C). When it was low, however, blood vessels had only begun to form within the chondral phase of the defect by day 84 (Figure 4-4E). Conversely, changing the rate of vessel branching affected the density of blood vessels within a vascularised region. They did not, however, affect the distance from the cancellous bone that blood vessel were predicted to have progressed. When these limits were set low (relative to the baseline values) the rate of branching increased. When they were set high, however, the rate of branching decreased.

Changing the parameters controlling angiogenesis in the model also had a large effect on the predicted patterns of MSC differentiation and tissue formation. At day 28 (Figure 4-4B), tissue formation in all of the simulations followed the same general trend, where bone was predicted to form by intramembranous ossification in the base of the defect, with a layer of fibrous tissue predicted at the surface of the defect. Interestingly, regardless of the angiogenic parameters, roughly the same quantity of bone was predicted across all of the simulations at this time point. The simulations differed regarding the type of tissue forming

in the core of the defect. When either the vessel growth or the branching rates were low, a region which was almost devoid of cells was predicted to form in the core of the defect. The size of this core increased when both rates were set low. Conversely, when either of the angiogenic rates was set high, and the other was at its respective baseline value, this hypocellular core region did not form. Instead FBs and HCs were predicted above the bone in the osseous region while the chondral region was almost entirely filled with CCs. When both parameters were set high CCs had started to become hypertrophic in the chondral region of the defect by day 28.

Similar trends were predicted at day 56 (Figure 4-4D) and day 84 (Figure 4-4F) time points. At this stage, in all simulations, it was predicted that bone continued to form in the osseous region while FBs remained at the surface of the defect. In the simulations where either the vascular growth or the branching rates were low, and the other was at its respective baseline value, a hypocellular core remained. This had decreased in size, however, compared to the day 28 simulations. Similar results were apparent when both rates were low. At day 84, bone in these groups did not progress beyond the native subchondral plate and the majority of the chondral region was predicted to be cartilage. Conversely, in the simulations where either of the angiogenic rates was high and the other was at its respective baseline value, or both rates were high, all of the chondrocytes in the defect became hypertrophic. This behaviour continued and by day 84, the majority of the chondral region of the defect was bone.

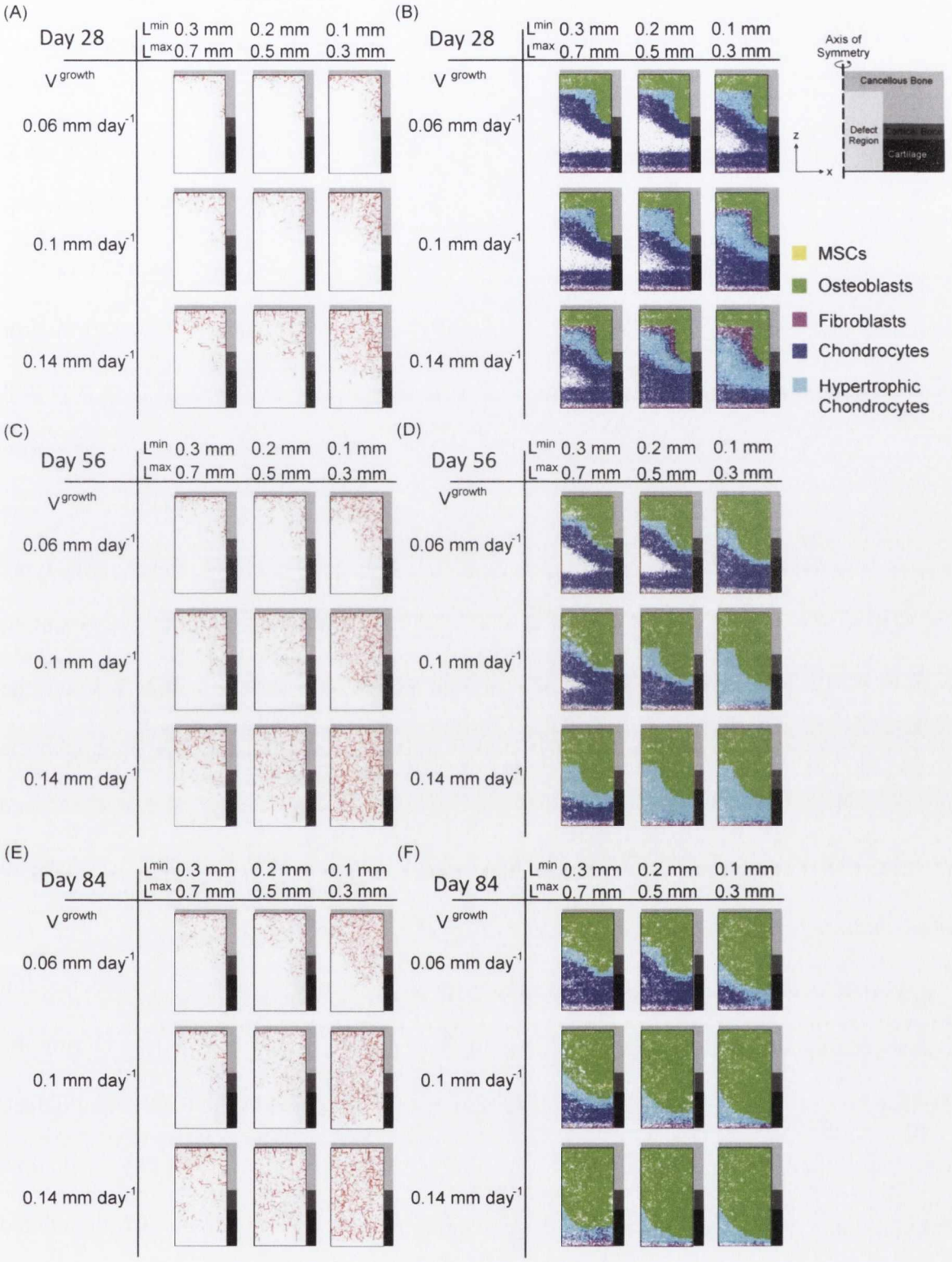

Figure 4-4: Results of the parametric study where V^{growth} and L^{min} & L^{max} are varied with respect to their respective baseline values ($V^{growth,\ baseline}$ = 0.1 mm day^{-1}; $L^{min,\ baseline}$ = 0.2 mm & $L^{max,\ baseline}$ = 0.5 mm). The predicted angiogenesis and cell phenotype within the defect are shown for (A, B) day 28, (C, D) day 56 and (E, F) day 84.

4.4 Discussion

The objective of this study was, firstly, to test if the temporal and spatial patterns of tissue differentiation observed during osteochondral defect repair could be simulated using a computational model where MSC fate was hypothesised to be regulated by local oxygen levels and substrate stiffness. The second objective was to use this computational model to examine how varying the rate of angiogenesis affects the progression of tissue formation during osteochondral defect repair over a 12 week period. A baseline simulation was first performed which used estimated parameters to predict the spontaneous repair process within an untreated osteochondral defect. A sensitivity analysis was then conducted on these parameters in order to examine their influence on the predicted quantities of each tissue type. The results of this study highlighted the extent of the effect that angiogenesis, and in particular the rate of vascular growth and the rate of vessel branching, had on the spontaneous repair process. In the final part of this study, the role played by angiogenesis was further examined by varying the key angiogenic parameters in the model (V^{growth} and L^{min} and L^{max}). These simulations suggest that control of angiogenesis is critical to successful osteochondral defect repair.

The computational model was able to predict the main features of osteochondral defect repair which had been reported in a number of different animal models. During the first two weeks of repair, cell proliferation was mainly confined to the base of the defect, which was similar to that observed experimentally by DePalma *et al.* [187]. By day 14, distinct cellular zones were observed, with OBs predicted in the base of the defect, CCs predicted above these and FBs at the surface. This early spatial pattern of tissue phenotypes has been described in numerous animal models [6,9,188]. As the simulation progressed, it was predicted that the newly formed osseous tissue within the base of the defect began to advance towards the surface as cartilage was converted to bone by endochondral ossification. The

advancement of subchondral bone is one of the main features of osteochondral defect repair [4,6,57,188]. In addition to this, the model was also able to predict the early pattern of bone formation observed by Orth *et al.* [4]. In this case, at 3 weeks, bone formation took on a cylindrical shape where very little immature bone was observed (data not shown) [4]. At day 42, however, bone formation had increased and had started to adopt an infundibuliform shape [4]. Furthermore, as observed in the literature, by day 56, the subchondral plate remained below the native tidemark [4,57]. Finally, by week 12, the subchondral plate was predicted to have progressed above the tidemark while no hyaline cartilage remained within the defect [15].

The model predictions for spontaneous repair where angiogenesis was lowered (by reducing one or both of the parameters controlling the rate of blood vessel growth or blood vessel branching) also agreed with the main findings observed by Nagai *et al.* [15]. In their study, defects which were treated with the anti-angiogenic factor bevacizumab displayed similar patterns of healing to untreated controls at day 28. This behaviour was predicted in the simulations, where similar quantities of tissues were observed at day 28 in both the control and reduced angiogenesis simulations. Furthermore, similar to Nagai *et al.* [15], at this time-point the predominant tissue predicted within the model was cartilage. At week 12 however, Nagai *et al.* [15] reported marked differences in the observed pattern of healing between the untreated control group and the bevacizumab-treated group. In this case, control defects consisted mainly of bone and fibrous tissue with no evidence of cartilage tissue persisting. This was also predicted in the control simulation, where bone penetrated above the native tidemark, while any remaining cartilage had become hypertrophic. In contrast, in the bevacizumab treated group, Nagai *et al.*[15] reported that a large portion of the tissue had retained its chondrogenic phenotype, while bone formation was restricted to the base of the defect. This was also observed within the reduced angiogenesis simulations where the

majority of the chondral region was composed of cartilage and the majority of the subchondral region was composed of bone. These similarities between the model predictions and the *in vivo* results provide support for the underlying model hypotheses regarding the role of oxygen levels in regulating MSC fate during osteochondral defect repair. In particular, the results of this study provide support for the hypothesis that limiting angiogenesis to the osseous region of an osteochondral defect will improve cartilage repair by inducing a sustained hypoxic environment in the chondral region.

In the simulations where angiogenesis was upregulated (by increasing either of the parameters controlling the rate of blood vessel growth or branching), more robust tissue formation was predicted during the first four weeks compared to both the normal and impaired models. In this case, although bone formation was approximately the same in all simulations by week 4, increasing angiogenesis was predicted to lead to greater cell proliferation, as well as an increase in the quantity of cartilage observed within the chondral phase of the defect. As this model progressed, however, the higher rate of angiogenesis resulted in early blood vessel growth into the chondral region. This generated a normoxic environment by day 56, which in turn led to the newly formed cartilage becoming hypertrophic. These results suggest that during osteochondral defect repair, robust tissue formation can be induced by promoting and inhibiting angiogenesis within the subchondral and chondral regions respectively. It is interesting to note that in a rabbit model, osteochondral defects which were treated with a bioabsorbable scaffold that induced regeneration of the cartilage tissue in the superficial layer, the pro-angiogenic factor vascular endothelial growth factor (VEGF) was localised in the subchondral region of the defect [204]. In the same study, in defects which were left untreated, VEGF was localised throughout the entire defect and no cartilage regeneration was observed [204].

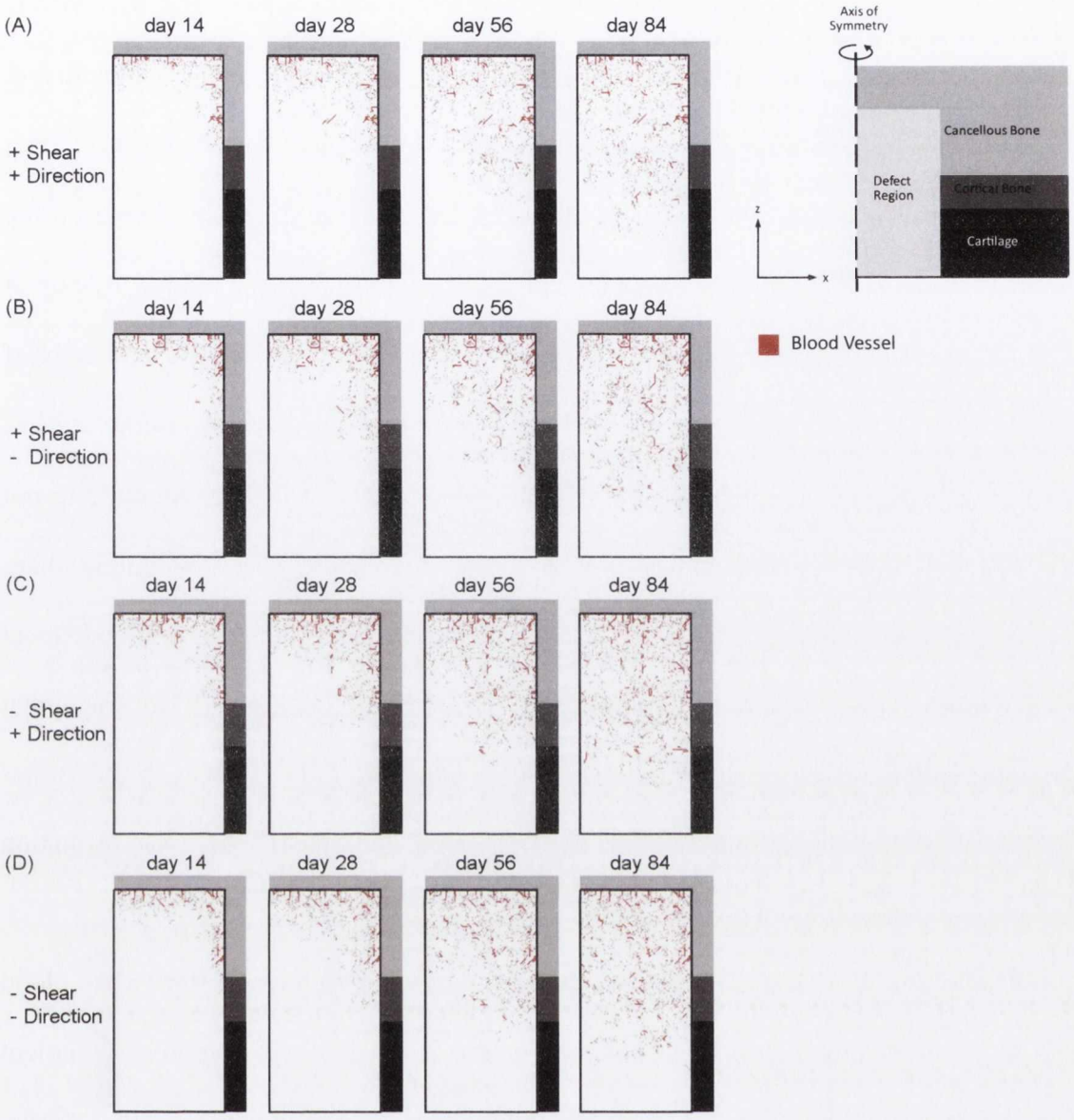

Figure 4-5: Assessment of the effect that the different elements of the mechanically regulated model of angiogenesis had on the predicted vasculature at different time points during the predictions of spontaneous repair within an osteochondral defect. The angiogenesis model was split into two components; inhibition of vessel growth in regions of high octahedral shear strain (shear inhibition), and bias of blood vessel growth in the direction of the minimum principal strain (strain direction). The effects of these components were assessed by running the simulation where: (A) both shear inhibition and strain direction were active (B) shear inhibition was active and strain direction was inactive (C) shear inhibition was inactive and strain direction was active, and (D) shear inhibition and strain direction were inactive.

One of the main issues with the current model was that it was unable to predict the spatial patterns of bone formation observed by Orth *et al.* [4] during the later stages of the spontaneous repair process. Orth *et al.* [4] reported that, as the subchondral plate advances towards the native tidemark, it changes from an infundibuliform shape and becomes plane with the native bone. Following this, as it progresses into the chondral region it adopts a

convex pattern. In all of the developed models, however, it was predicted that the osseous tissue retained this infundibuliform shape as it formed above the native tidemark and progressed into the chondral region. There are a number of potential reasons for this which will be addressed in future work. Firstly, the current model was developed based on the findings of Burke *et al.*[21,44–46] who hypothesised that mechanics plays an indirect role upon tissue formation by affecting the course of blood vessel growth. As an additional feature of this study, the mechanically regulated model of angiogenesis developed by Burke *et al.* [33] was tested by running the model where different components of the algorithm were not active. The two components tested were (1) The inhibition of angiogenesis in regions where the octahedral shear strain exceeded a threshold (ε^{angio}) value and (2) the bias of blood vessel growth in the direction of the minimum principal strain (ε^{min}). In both cases it was found that determining blood vessel direction using a random function, rather than with the strain-dependent algorithm, had only a small effect on the predicted outcome of tissue formation within the simulation (Figure 4-5 and Figure 4-6).

The reason for this was that during the early stages of each simulation, when blood vessel growth was confined to the subchondral region of the defect, the strain environment within the base was low due to stress shielding from the surrounding healthy tissue. Furthermore as the simulation progressed and vessels grew into the chondral region, both cartilage and hypertrophic cartilage were predicted to have formed, which greatly reduced the magnitude of strain within the defect. The result of this was that the magnitude of the strains within the vascularised regions was never high enough to drastically affect the course of angiogenesis. Based on this, we speculate that, within an osteochondral defect, the mechanical environment also has a direct influence on tissue formation by affecting the quality of the cartilage tissue as well as the course of endochondral ossification. This hypothesis is based on a number of *in vivo* studies which have shown that loading of an

osteochondral defect has a large effect on the formation of both cartilage and bone [13,14,188,246], as well as *in vitro* studies which have shown that dynamic compression of MSC-derived chondrocytes inhibits their terminal differentiation [51,52]. In addition to this, the current model did not consider the role that various growth factors (such as VEGF or chondromodulin) released by differentiated cells have on the course of angiogenesis. To address this it may be necessary to include a chemotaxis effect within the model for angiogenesis, similar to that proposed by Carlier *et al.*[30] and Checa *et al.*[29]. A final feature which will be addressed in future work is that that the current model did not differentiate between hyaline cartilage and fibrocartilage. This is necessary as fibrocartilage has been observed to form in the chondral region of the defect [5,8,9,15,16]. Furthermore, it has been hypothesised that the eventual degradation of the repair tissue is caused by differences in the biomechanical properties of these two tissues [247].

There were a number of other limitations associated with the computational model which may have limited its predictive capacity. Firstly, a simplified finite element model of the femoral condyle was developed, and each tissue type was described using as an isotropic elastic material. We are satisfied, however, that the current approach was able to sufficiently describe the mechanical environment within the osteochondral defect. In addition to this, although similar studies to ours have modelled the meniscus as a biphasic, anisotropic material [209,242], in this study it was characterised as an isotropic elastic material. The results of a sensitivity analysis, however, confirm that the final model predictions were reasonably insensitive to the estimated stiffness of the meniscus.

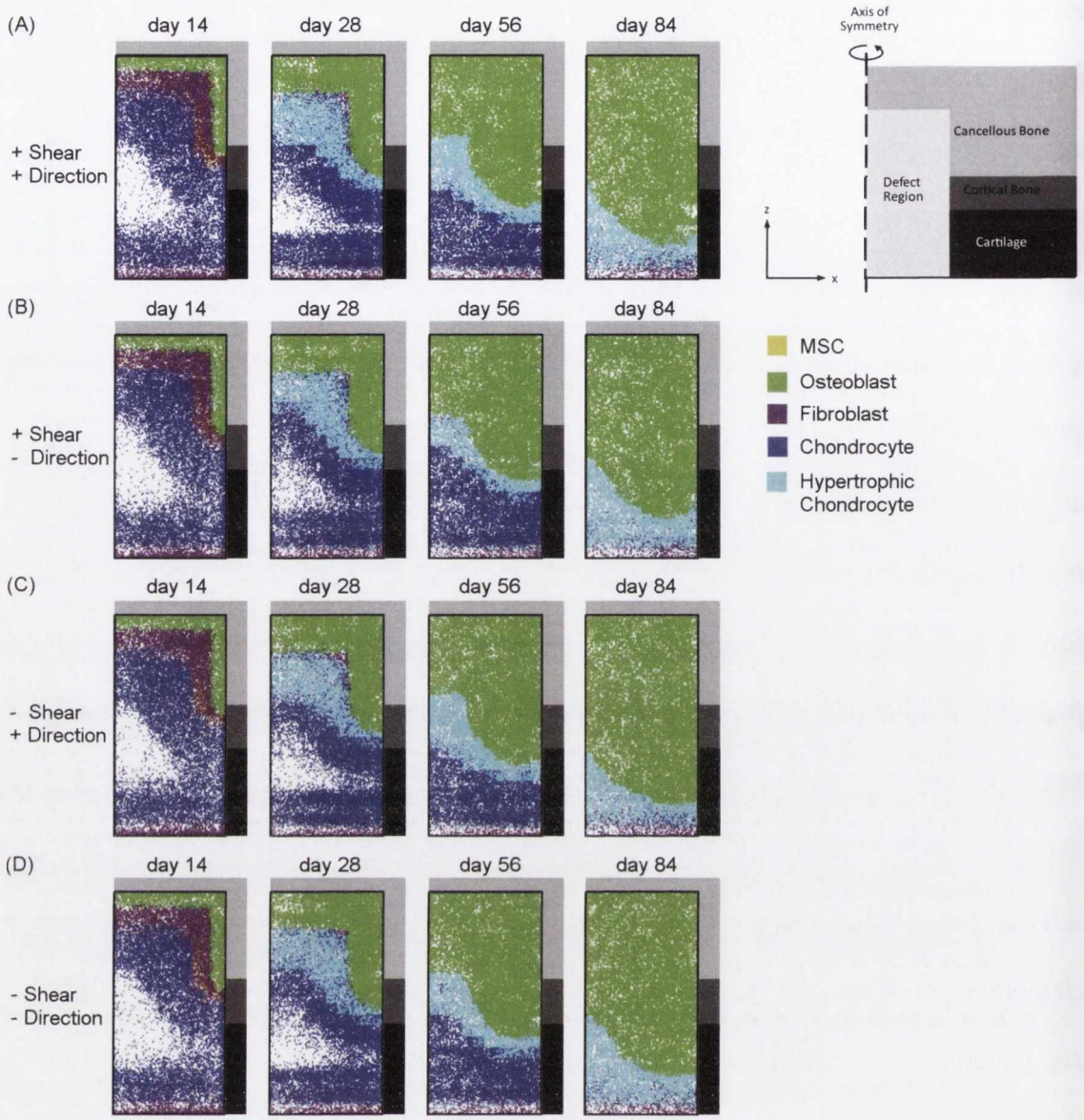

Figure 4-6: Assessment of the effect that the different elements of the mechanically regulated model of angiogenesis had on the predicted pattern of cell differentiation at different time points during the simulation of the spontaneous repair process within an osteochondral defect. The angiogenesis model was split into two components; inhibition of vessel growth in regions of high octahedral shear strain (shear inhibition), and; bias of blood vessel growth towards the direction of the minimum principal strain (strain direction). The effect of these components were assessed by running the simulation where: (A) both shear inhibition and strain direction were active (B) shear inhibition was active and strain direction was inactive (C) shear inhibition was inactive and strain direction was active, and (D) shear inhibition and strain direction were inactive.

In spite of these limitations the current model was able to predict the main features and differences observed during both spontaneous and angiogenically impaired repair within an osteochondral defect. It was therefore possible to determine the mechanism by which limiting blood vessel growth during osteochondral defect repair improves the quality of the repair tissue. In addition to this, the current study provides support for the hypotheses that

MSC differentiation is governed by both the local substrate stiffness and oxygen tension and that chondrocyte hypertrophy is initiated in a normoxic environment. Future work will involve updating the current model to improve its capacity to accurately predict the spatial patterns of tissue formation which were observed during the later stages of the spontaneous repair process.

Chapter 5 An exploration of the role that functional loading of an osteochondral defect plays on tissue formation during the spontaneous repair process

The purpose of this chapter is to investigate the role of tissue strain in regulating the spatial and temporal patterns of stem cell differentiation during the spontaneous repair process within an osteochondral defect. To this end, the tissue differentiation algorithm developed in the previous chapters is updated to include rules which are based on the hypothesis that chondrocyte hypertrophy and endochondral ossification are inhibited in regions of high strain. The model also considers the hypothesis that excessively high magnitudes of local strain result in the formation of mechanically inferior fibrocartilage. These rules are first developed by simulating stem cell differentiation within an *in vitro* bioreactor system which was capable of controlling the levels of oxygen and mechanical cues within MSC laden hydrogels. Following this, the updated model is then used to simulate the pattern of tissue formation experimentally observed during the spontaneous repair process within an osteochondral defect. The results from this chapter lead to the development of an updated version of the tissue differentiation algorithm which was used in chapter 3 and chapter 4. In addition to this, they provide insights into the role which the mechanical environment plays on the spontaneous repair process.

5.1 Introduction

Osteochondral defects of a certain size have the capacity to repair spontaneously [8]. This reparative response is mediated, at least in part, by mesenchymal stem cells (MSCs) which migrate from the bone marrow to the site of injury [6]. This reparative process forms the basis of a number of different surgical strategies designed to treat both osteochondral and chondral defects [10,11]. All of the current options, however, have limited success in the long term, as the repair tissue which initially forms breaks down over time [11]. In order to design novel tissue engineering strategies to overcome these issues, a better understanding of the factors which affect the formation of the repair tissue, as well as its subsequent failure, are required. To this end, we have recently developed a computational model of the spontaneous repair process within an osteochondral defect. The model made use of a previously developed tissue differentiation algorithm where MSC fate was governed by the local oxygen tension and stiffness of the surrounding substrate. While this model provided insight into the role that angiogenesis plays in the repair process, it was unable to predict the spatial formation of bone which has been experimentally observed during the latter stages of repair [4]. In addition to this, it did not account for the putative role that mechanical loading plays in the outcome of osteochondral defect repair. This may explain its inability to accurately predict the patterns of tissue formation observed in the latter stages of the regenerative process whereby cartilage is converted into bone through the process of endochondral ossification.

Mechanical loading has long been implicated in directing tissue formation, and in particular, cartilage formation during osteochondral defect repair [13,14,187,248,249]. Numerous studies have examined the effect that the magnitude and type of loading has on the repair tissue which forms within osteochondral defects [13,14,248,249]. In general it has been shown that active loading applied at an early stage leads to the formation of fibrous tissue and

fibrocartilage, while continuous passive motion has been shown to result in the formation of hyaline cartilage [13,14,250]. A number of *in vitro* studies, where the levels of mechanical stimulation can be carefully controlled using bioreactor systems, have also demonstrated how compressive loading can regulate chondrogenesis of MSCs [52,95,251–253]. For example, Thorpe *et al.* [51] showed that dynamic compressive loading of chondrogenically primed MSCs led to the upregulation of chondrogenic markers and also inhibited terminal differentiation and mineralisation. These findings suggest that mechanics plays a key role in regulating hypertrophy and endochondral ossification of cartilage. In addition, numerous *in vitro* studies have shown that MSCs exposed to high magnitudes of dynamic tensile strain, when maintained in chondrogenic media, display markers of fibrocartilage [55,56,254].

Based on these studies, we sought to improve our previous model of stem cell differentiation by implementing a series of rules whereby the local mechanical environment affects the fate of the cartilaginous tissue formed in damaged bones or joints. In particular we hypothesised that during the spontaneous repair process, tissue level strains regulate chondrocyte hypertrophy and the rate of endochondral ossification, and that excessive local strain promotes the formation of fibrocartilage. In the first part of this study, a rule was implemented into the model whereby chondrocyte hypertrophy and endochondral ossification were inhibited in regions of high (> 5 %) octahedral shear strain. This was developed by modelling the findings of the *in vitro* bioreactor study conducted by Thorpe *et al.* [51], who modulated the levels of strain and oxygen through the depth of MSC-laden hydrogels. We then tested the predictive capacity of this updated model by attempting to simulate the time-course of the spontaneous repair process within an osteochondral defect. In the final part of the study an additional rule was developed whereby high magnitudes of octahedral shear strain (> 10 %), within an otherwise chondrogenic environment, leads to the formation of fibrocartilage.

5.2 Method

5.2.1 *In Vitro* Experiment to be Simulated

The details of this experiment are described in elsewhere [51]. Briefly, porcine MSCs were seeded at a density of 20 x 10^3 cells/mm^3 in cylindrical, 2 % agarose hydrogels of dimensions φ 6 mm x 4 mm. Constructs were cultured in chondrogenic media for 21 days before being split into an unconfined and a confined group which were then cultured for a further 3 weeks. The confined group were press-fitted in a PTFE chamber which served to confine the bottom half of the construct. During this time constructs from both groups either remained under free swelling conditions (FS) or were subjected to dynamic compression (DC) at an amplitude of 10 % strain and a frequency of 1 Hz for 4 hours per day, 5 day per week. Following culture, among other tests, histology and immunohistochemistry were performed to determine the spatial calcific deposition within the MSC-laden hydrogel. This was deemed to be indicative of chondrocyte hypertrophy. In addition to this, the oxygen tension was measured through the depth of the constructs after 4 days of culture in both the confined and unconfined groups, using fibre optic oxygen micro-sensors. The results of this were then used in conjunction with a computational model to determine the Michealas-Menten parameters for the differentiated cells.

5.2.2 Iterative Procedure

Tissue differentiation within the defect region was simulated via an iterative procedure. This was similar to the one outlined in chapter 3 (Section 3.2.2) with the exception that the biophysical stimuli calculated using the finite element (FE) model was also used as an input to the tissue differentiation algorithm. In all of the simulations each time step modelled a period of 24 hours.

5.2.3 Finite Element Models

Three-dimensional Finite Element models were used to determine the biophysical stimuli generated in the cell-seeded constructs which were exposed to DC within the bioreactor system described above, as well as in an osteochondral defect. Both sets of models were implemented in the open source FE package FEBio (version 2.0, University of Utah, Technology Commercialization Office, 615 Arapeen Drive, Suite 310, Salt Lake City). All of the materials used in the models were bi-phasic and the material properties of each tissue type used are listed in Table 5-1.

Table 5-1: Material Parameters

Material Property	Granulation Tissue	Fibrous Tissue	Fibro-Cartilage	Cartilage	Hypertrophic Cartilage	Immature Bone	Mature Bone	Cortical Bone
Young's Modulus [MPa]	1[a]	2[a,b]	5	10[a,b]	20	1000[a]	6000[c]	20,000[c]
Poisson's Ratio	0.167	0.167	0.167	0.167	0.167	0.3	0.3	0.3
Permeability [mm^4/ Ns]	0.01[a]	0.01[a,b]	0.01	0.005[a,b]	0.005	0.001[a]	0.0037[d]	1e-5[a]
Solid Volume Fraction	0.2	0.2	0.2	0.2	0.2	0.2	0.2	0.2

a 217

b 224

c 23

d 209

5.2.3.1 In Vitro Model

Three Dimensional Finite Element models were developed for both the unconfined and the confined groups (Figure 5-1). Both models had a geometry of φ 6 mm x 4 mm and, using symmetry, were simplified to depict a quarter of the construct as it was revolved around the centre axis. For the confined group the confinement chamber was implemented using a sliding contact interface between the construct and the chamber. In both models a 10 % compressive strain was applied to the top surface of the construct over a period of 0.5 s. At the onset of loading, the material parameters for cartilage were used based on the assumption that chondrogenic differentiation had occurred (Table 5-1).

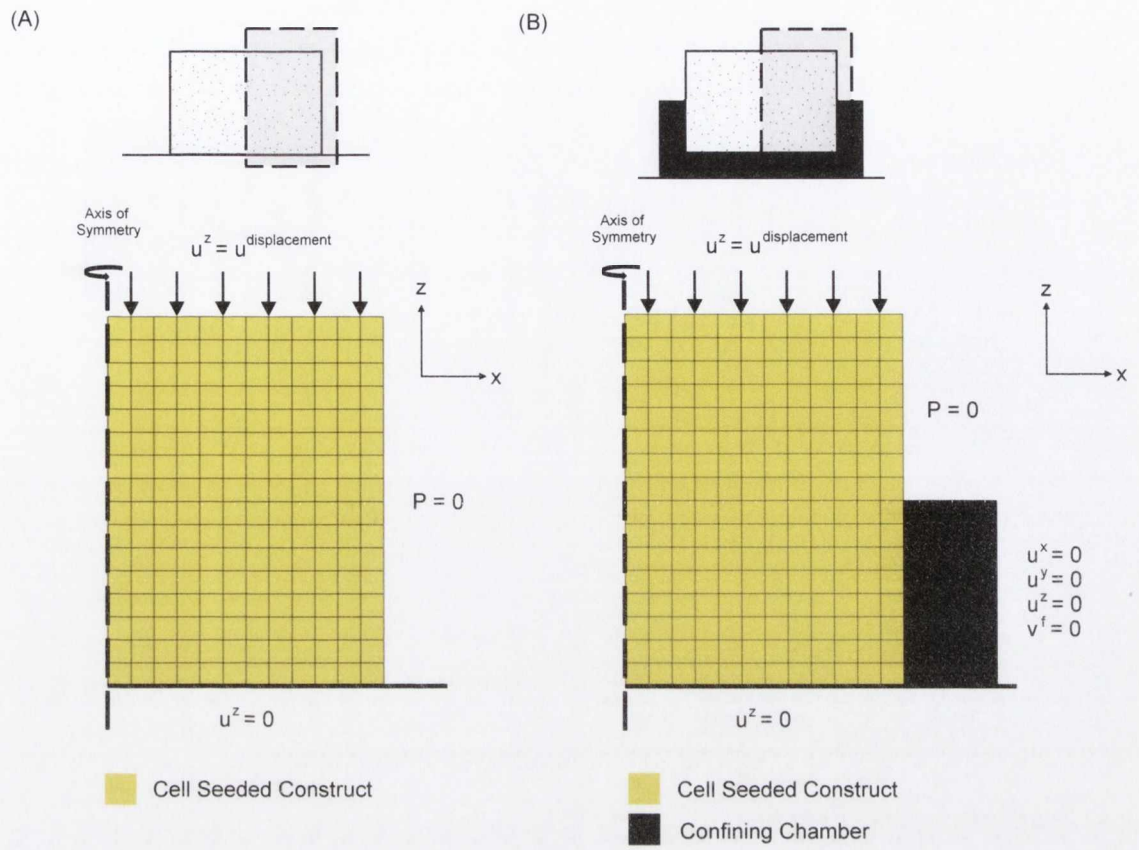

Figure 5-1: FE Model and boundary conditions for the (A) Unconfined and (B) Confined in-vitro simulations. Displacement in the x and z directions, fluid velocity and fluid pressure are shown as u^x, u^z, v^f and P respectively.

5.2.3.2 Osteochondral Defect

A simplified 3D FE model of an osteochondral defect within the femoral condyle was developed using the same geometry as outlined in the chapter 4 (section 4.2.2). Due to convergence issues, the meniscus in the developed model was treated as a solid material whereby a sliding interface was used to model the contact between it and the cartilage layer. This was treated as a transversely isotropic elastic material with a higher stiffness in the circumferential direction ($E^x = E^z = 20$ MPa; $E^y = 140$ MPa; $v^{xy} = 0.2$; $v^{yz} = 0.49$; $G^{xy} = 50$ MPa) [243,255]. At the centre of the FE model, a defect of size φ 5 mm x 5 mm was included (Figure 5-2). This was assumed to be initially filled with granulation tissue.

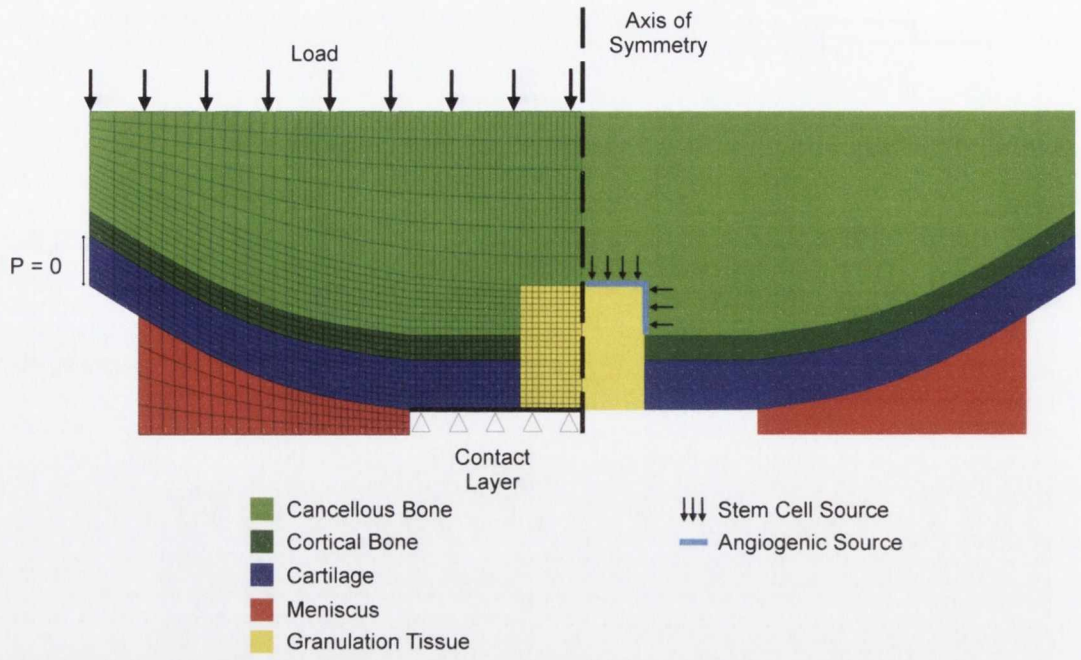

Figure 5-2: FE model and boundary conditions for the osteochondral defect simulations.

5.2.4 Angiogenesis

Angiogenesis was only considered in the osteochondral defect model. This was implemented using the lattice based approach outlined in the previous chapters. As an extension of this model, and similar to the approach described by Carlier *et al.* [30], it was assumed that blood and nutrients could only flow through vessels which had formed a closed loop. Based on this, the ECs which made up a blood vessel were considered inactive until anastomosis had occurred. The implementation of this approach was shown to have only a marginal effect on the model predictions of the spontaneous repair process when compared to the results obtained using the model of angiogenesis outlined in the previous chapters (Appendix III: Comparison of Angiogenesis Models (Chapter 5)).

At day 0, it was assumed that vessels grew into the callus from the exposed cancellous bone (Figure 5-2). This assumption is based on the findings that this tissue is highly vascularised and provides a nutrient supply to both itself and the articular cartilage [11]. The initial number of vessels was governed by the parameter N^{angio} which denoted the

proportion of lattice points on the cancellous bone surfaces which were invading blood vessels.

Table 5-2: Angiogenesis and MSC Differentiation Model Parameters

Model Parameter	Symbol	Source	Unit	Value
Octahedral shear strain threshold for inhibition of angiogenesis	ε^{angio}	Estimated	-	0.1
Blood vessel growth rate	V^{growth}	Estimated	mm day^{-1}	0.1
Minimum length for branching	L_{min}	[29]	mm	0.2
Maximum length without branching	L_{max}	[29]	mm	0.5
Minimum cell age for MSC differentiation	Age^{cell}	Estimated	days	5
Oxygen diffusion coefficient	G	[44,227]	$mm^2\ s^{-1}$	2.2×10^{-3}
Initial oxygen tension	$O_2^{initial}$	[184]	mol mm^{-3}	101.6×10^{-12}
Oxygen tension for inhibition of differentiation	$O_2^{inhibition}$	[129]	mol mm^{-3}	5.48×10^{-12}
Oxygen limit for cartilage	$O_2^{cartilage}$	[44]	mol mm^{-3}	30.48×10^{-12}
Oxygen limit for differentiation of cartilage to hypertrophic cartilage	$O_2^{hypertrophic}$	Estimated	mol mm^{-3}	30.48×10^{-12}
Oxygen limit for calcification of hypertrophic cartilage	$O_2^{endochondral}$	Estimated	mol mm^{-3}	50.48×10^{-12}

5.2.5 Cell Migration, Cell Proliferation and Cell Death

The migration and proliferation of MSCs, osteoblasts (OBs), chondrocytes (CCs), fibroblasts (FBs), hypertrophic chondrocytes (HC) and fibrochondrocytes (FCs) was also modelled using a lattice approach [20,29]. The migration of cells was implemented using 'random walk' theory [20]. Cell proliferation was implemented in a similar fashion, provided that there was a vacant position beside the parent cell. The maximum number of cells allowed in any element was limited to 1×10^5 cells/mm^3 [44]. The migration rate (M) determined the number of attempted migration actions per time step while the doubling time (DT) was the age a cell had to be before it proliferated (Table 5-3). Cell proliferation was inhibited in regions where the oxygen concentration fell below a specific threshold value (O_2^{prolif}) (Table 5-3). If the oxygen concentration fell below a threshold value (O_2^{death}) then cell death was

initiated (Table 5-3). It was assumed that 5 % of the lattice points on the cancellous surface of the defect (Figure 5-2) and 0.5 % of the interior lattice points contained MSCs at day 0.

Table 5-3: Cell Model Parameters

Model Parameter	MSC	CC	OB	FB	HC	FC
Doubling Time [days]	0.5[a]	1.5[a]	1[a]	0.5[a]	1.5[a]	1.5
Migration Rate [μm/hr]	26.6[b]	N/A	N/A	26.6[b]	N/A	N/A
Anoxic Death Rate [% cells day^{-1}]	20	20	20	20	20	20
Oxygen Concentration for cell proliferation (O_2^{prolif}) [mol mm^{-3}]	40×10^{-12} [c]	10×10^{-12}	80×10^{-12} [c]	20×10^{-12}	30×10^{-12}	10×10^{-12}
Oxygen Concentration for cell death (O_2^{death}) [mol mm^{-3}]	5×10^{-12}	5×10^{-12}	20×10^{-12}	5×10^{-12}	5×10^{-12}	5×10^{-12}

a 153

b 226

c 30

5.2.6 Oxygen Transport

Oxygen transport was modelled using the same method as outlined in chapter 3 (Section 3.2.6). Briefly, Michealas-Menten kinetics was used to model the cellular consumption of oxygen (Table 5-4) while (for the osteochondral defect models) a production term was used to model the oxygen supply by the blood vessels.

For the *in vitro* simulations, in accordance with the experimental results of Thorpe *et al.* [51], a constant oxygen boundary condition of 101.6×10^{-12} mol mm^{-3} (10 %) was applied at the exposed surfaces of the gel. Furthermore, based on the experimentally measured values for the Michealas-Menten parameters derived in the same study, in the *in vitro* simulations $q^{max} = 48.6 \times 10^{-15}$ mol $cell^{-1}$ s^{-1} and $K^m = 5 \times 10^{-11}$ mol mm^{-3}.

Table 5-4: Michealas-Menten parameters for each cell phenotype

Michealas - Menten Parameters	MSC	CC	OB	FB	HC	FC
Cell type (n)	1	2	3	4	5	6
Max Consumption Rate (Q^{max}) [mol $cell^{-1}$ hr^{-1}]	93.2×10^{-15} [a]	1.8×10^{-15} [a, b]	93.2×10^{-15} [a]	93.2×10^{-15} [a]	1.8×10^{-15} [a]	1.8×10^{-15} [a, b]
Oxygen Concentration at half max consumption [mol mm^{-3}]	22.5×10^{-12}	22.5×10^{-12}	22.5×10^{-12}	22.5×10^{-12}	22.5×10^{-12}	22.5×10^{-12}

a 30

b 73

5.2.7 MSC Differentiation and Chondrocyte Hypertrophy

MSC differentiation was dependent on the local substrate stiffness and the oxygen tension. This algorithm is outlined in chapter 3 (Section 3.2.7). Adipogenesis was not considered in the osteochondral defect simulations based on the assumption that the stiffness of the granulation tissue was not low enough to facilitate it.

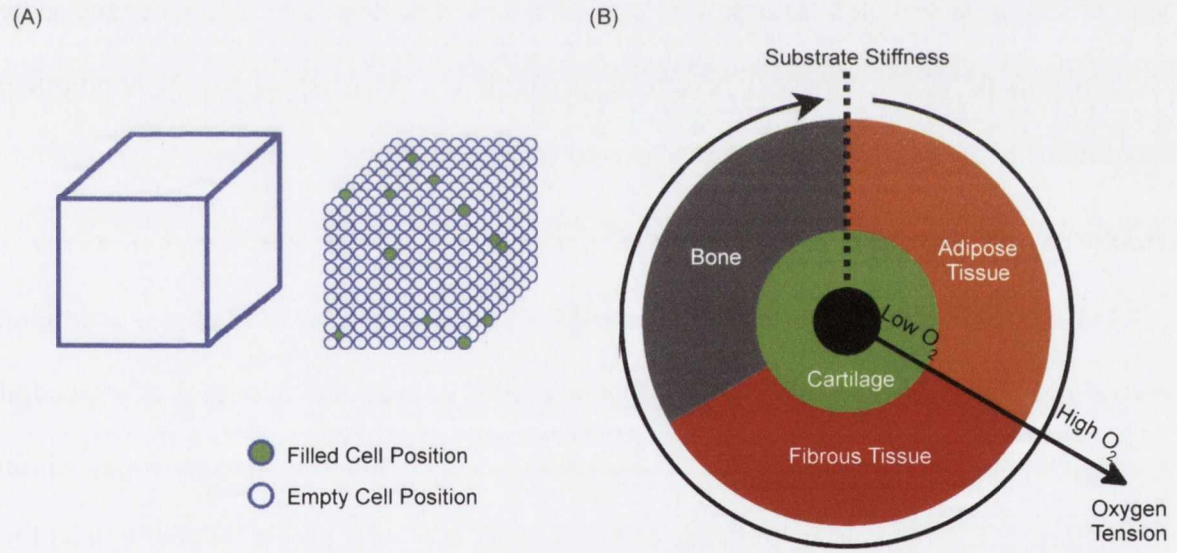

Figure 5-3: (A) A 3-dimensional finite element with corresponding lattice. Each lattice point represents a potential location for a cell. (B) Tissue differentiation algorithm as directed by the local oxygen tension and substrate stiffness.

Endochondral ossification was modelled using the same two-step process developed in the chapter 3 (Section 3.2.8). Briefly, in the first step CCs differentiation in HCs in regions where the oxygen tension increased beyond a threshold value ($O_2^{hypertrophic}$). Following this, in the second step HCs transdifferentiated into OBs provided that (1) they were in an element

where the oxygen tension was greater than a threshold value ($O_2^{endochondral}$) and (2) they were in the vicinity of an OB.

5.2.8 Role of Strain in Cell Differentiation

The tissue differentiation algorithm was updated to include a rule whereby chondrocyte hypertrophy was inhibited in regions where the local octahedral shear strain exceeded a threshold value ($\varepsilon^{oct,\ shear} > \varepsilon^{hypertrophy}$).

Following the development of this rule, an additional cell phenotype was implemented within the model in order to differentiate between cartilage and mechanically inferior fibrocartilage. In this case MSCs differentiated into fibrochondrocytes (FCs) when the oxygen tension was hypoxic ($O_2 \leq O_2^{hypertrophic}$) and the magnitude of the local octahedral shear strain exceeded a threshold value ($\varepsilon^{oct,\ shear} > \varepsilon^{fibrocartilage}$). It was assumed that, when exposed to these stimuli, CCs transdifferentiated into FCs. Finally FCs acted in the same way as chondrocytes and thus, became hypertrophic when exposed to the appropriate conditions.

5.2.9 Study design

The results from the *in vitro* study conducted by Thorpe *et al.* [51] were used to develop the rule whereby chondrocyte hypertrophy is inhibited above a specific level of octahedral shear strain. To achieve this, the model was used to predict chondrocyte hypertrophy within the different construct groups over the 21-day loading period (confined FS, unconfined FS, confined DC and unconfined DC). At the end of each simulation, the model was tested by comparing the predicted spatial arrangement of chondrocyte hypertrophy to histology slides depicting calcific deposition within the respective groups. In this case it was assumed that calcific deposition was indicative of chondrocyte hypertrophy. The simulations of the FS experimental groups were used to further test our previous hypothesis that chondrocyte hypertrophy is regulated by the local oxygen tension. Following this, the DC groups were

then modelled to determine the value of the parameter $\varepsilon^{hypertrophy}$, and hence consider the role of mechanics in regulating hypertrophy in our mechanobiological model. To achieve this, a parametric study was conducted where $\varepsilon^{hypertrophy}$ was varied between 5 % and 15 %, and the results of simulations compared to experimental observations

For each model a number of assumptions were made, based on the experimental findings. Firstly, as the authors did not observe a change in the cell number in any of the experimental groups, cell proliferation and cell death were not included in the simulations. It was also assumed that at the start of each simulation the constructs only contained CCs which could eventually undergo hypertrophy. Each simulation was run iteratively where each iteration represented a time period of 24 hours. Finally, based on studies which have shown that chondrocyte hypertrophy is inhibited by DC [51,52] , the *in vitro* simulations were used to test whether different measurements of strain (e.g. minimum principal strain, hydrostatic strain) could be used to regulate hypertrophy (Appendix IV: Alternative Rules for Strain Regulation of Hypertrophy (Chapter 5)).

In the second part of the study the updated model was used to predict the course of the spontaneous repair process within an osteochondral defect over a time period of 14 weeks. Similar to the *in vitro* simulations each iteration modelled a time period of 24 hours. Following this the models were used to develop and provide support for the rule where fibrocartilage forms instead of cartilage if the octahedral shear strain exceeds a threshold value ($\varepsilon^{fibrocartilage}$). In this case the parameter $\varepsilon^{fibrocartilage}$ was varied between 10 %, 12.5 % and 15 % strain. As an additional part of this study, based on reports that dynamic tensile strain is required to promote fibrocartilage formation [55,56,254], alternative measures of strain were again examined (Appendix V: Alternative Rules for Strain Regulation of Fibrocartilage (Chapter 5)).

5.3 Results

5.3.1 Simulation of In Vitro Models

The tissue differentiation algorithm was able to predict the spatial distribution of chondrocyte hypertrophy (calcification) which was experimentally observed in the confined and unconfined FS groups (Figure 5-4). As previously shown, partial confinement of MSC-laden hydrogels was predicted to lower oxygen levels within the bottom of these constructs (Figure 5-3). In response to these lower levels of oxygen, hypertrophy was predicted to be confined to the exposed surfaces of the MSC-laden hydrogels. In the unconfined group, only the core of the construct did not calcify. These results provide support for the model hypothesis that chondrocyte hypertrophy is regulated by the local oxygen tension.

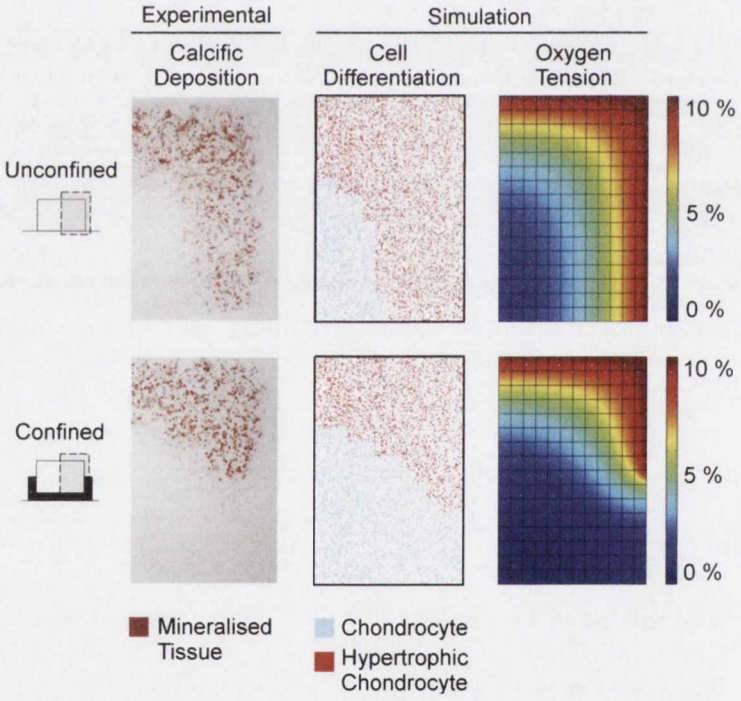

Figure 5-4: Experimental and simulation results for the In vitro FS groups. Alcian red staining was used to determine the spatial arrangement of calcific deposition (and chondrocyte hypertrophy) in the unconfined and confined groups following 21 days of FS culture. These were compared to the predicted spatial distribution of chondrocyte hypertrophy and oxygen tension from the unconfined and confined in silico models of the FS groups.

Following this, the results of the DC experiments were used to develop the rule whereby hypertrophy is inhibited by the local octahedral shear strain. DC resulted in a decrease in hypertrophy and mineralisation. It also resulted, however, in a complex, and

irregular spatial distribution of hypertrophic cartilage (Figure 5-5). In the unconfined DC group, hypertrophy was limited to the top half of the construct, while in the confined group mechanical stimulation nearly completely supressed calcification. The *in silico* models of the unconfined DC group predicted that hypertrophy was completely inhibited when the threshold value $\varepsilon^{hypertrophy}$ was 10 % or less (Figure 5-5B). Similarly, in the confined DC simulations, as the magnitudes of strain were much higher, hypertrophy was completely inhibited within the construct even if the value of $\varepsilon^{hypertrophy}$ was increased to 30 % (data not shown). Based on these results it was hypothesised that for the *in vivo* simulations, the parameter $\varepsilon^{hypertrophy}$ was within the range of 5 % and 10 % strain.

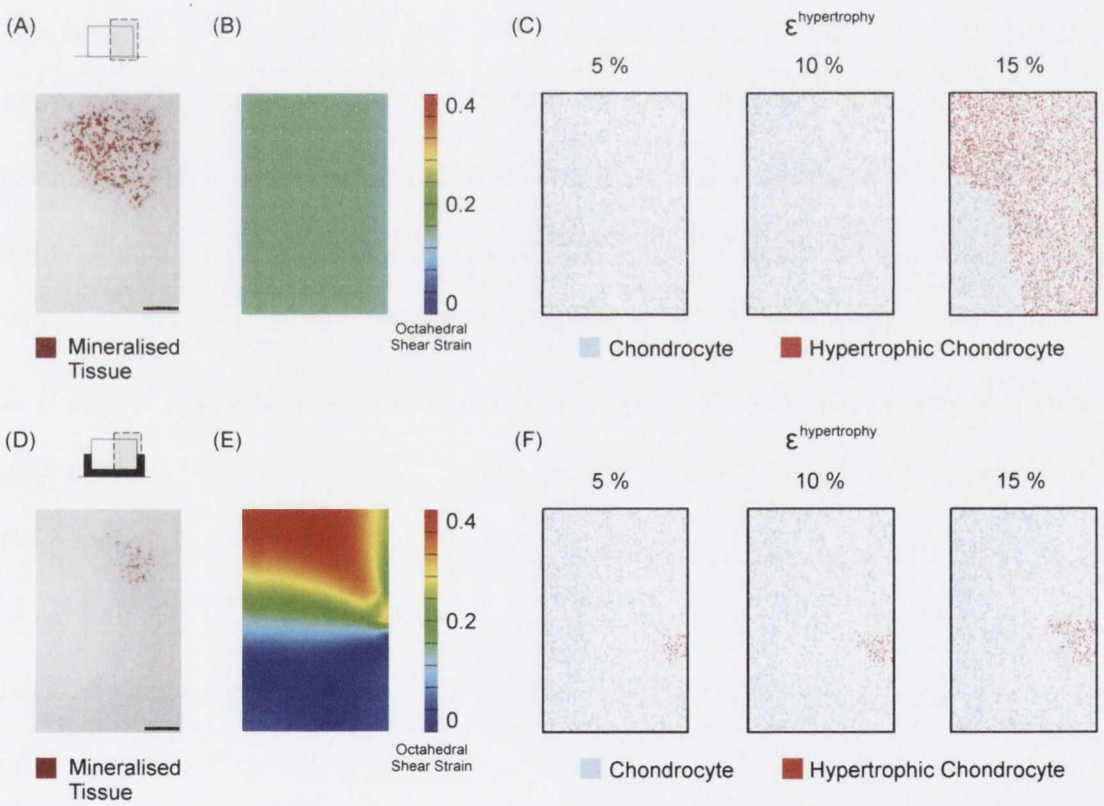

Figure 5-5: Experimental and simulation results for the in vitro DC groups where chondrocyte hypertrophy was inhibited by the octahedral shear strain. (A; D) The spatial arrangement of calcific deposition (and chondrocyte hypertrophy) determined for the unconfined and confined groups after 21 days of DC. (B; E) The octahedral shear strain predicted by the unconfined and confined FE models at the onset of DC. (C; F) The predicted spatial arrangement of chondrocyte hypertrophy for the unconfined and confined in silico models after 21 days of DC for different values of $\varepsilon^{hypertrophy}$.

5.3.2 Simulation of spontaneous repair; inhibition of chondrocyte hypertrophy in response to tissue strain

The spontaneous repair process within an osteochondral defect was first simulated using our original computational model which assumed that mechanics indirectly affects tissue formation by regulating angiogenesis (Figure 5-6A). In the simulation, by week 2, osteogenesis at the exposed cancellous bone was predicted. Due to the limited oxygen supply, however, most of the MSCs in this region differentiated into chondrocytes. At the same time, as a result of the oxygen supplied by the synovial fluid, fibrous tissue was predicted to form above a layer of cartilage at the defect surface. By week 4, as blood vessels penetrated further into the defect, the cartilage in the base became hypertrophic and was converted to bone by endochondral ossification. At this stage, the ossified tissue had formed in a cylindrical shape. By week 8 the advancing bone formed in an infundibuliform (funnel) shape as it approached the chondral region. This infundibuliform shape was retained for the remainder of the simulation. Finally, by week 18 the majority of the tissue in the defect (> 90 %) was predicted to be bone.

The tissue differentiation algorithm was then updated to include the condition whereby hypertrophy was inhibited in regions of high octahedral shear strain (Figure 5-6B – D). The threshold value ($\varepsilon^{hypertrophy}$) was set at either 5 %, 7.5 % or 10 %. Up until week 8, all three models predicted the same spatial and temporal pattern of healing as that predicted using the original tissue differentiation algorithm. Beyond this time point, however, the updated model predicted a different pattern of tissue formation. Firstly, as the subchondral plate advanced towards the chondral region, chondrocyte hypertrophy and endochondral ossification were inhibited at the peripheries of the defect as a result of the high strains in this region. In conjunction with this, stress-shielding from the native tissues ensured that the magnitude of the strain in the core of the defect remained low. The result of this was that

bone advanced towards the surface through the centre of the defect. This ensured that, from week 12 the advancing bone plate began to become plane with the native subchondral bone. Following this, the bone front was predicted to adopt a convex phase as it advanced into the chondral region of the defect. The main effect that the parameter $\varepsilon^{hypertrophy}$ then had on the model predictions was that it determined the distance that the subchondral plate had advanced by week 18. This distance was smallest for $\varepsilon^{hypertrophy} = 5$ % (Figure 5-6B); by week 18 a region of cartilage remained in the chondral phase of the defect when this value was implemented. Conversely, when $\varepsilon^{hypertrophy} = 10$ % (Figure 5-6D), very little cartilage was predicted in the defect by this time point.

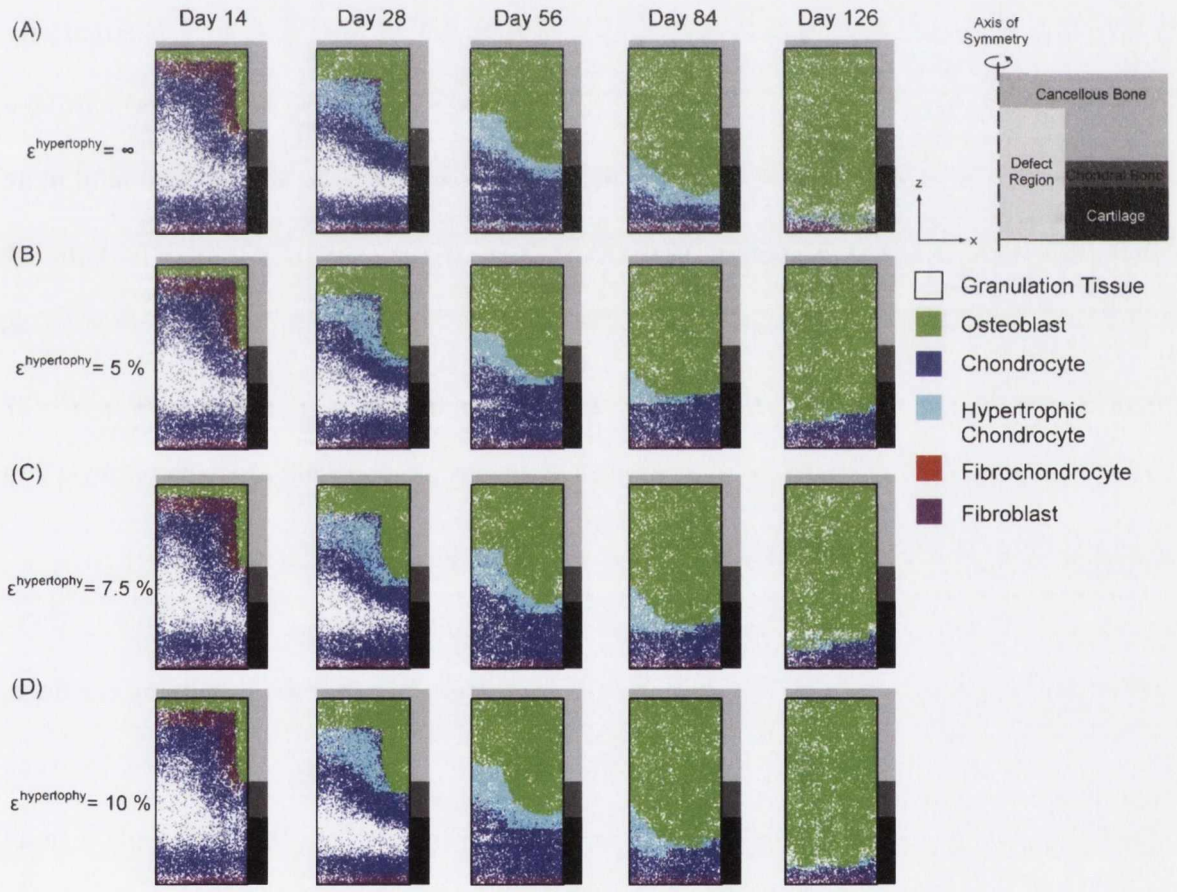

Figure 5-6: Model predictions of cell differentiation at different times during the spontaneous repair of an osteochondral defect using: (A) our previous tissue differentiation algorithm where chondrocyte hypertrophy was regulated solely by the oxygen tension (B – D) an updated algorithm where chondrocyte hypertrophy was regulated by the oxygen tension and the octahedral shear strain. The parameter $\varepsilon^{hypertrophy}$ was varied between (B) 5 %, (C) 7.5 % and (D) 10 %:

5.3.3 Simulation of spontaneous repair; formation of fibrocartilage in response to tissue strain

In the final part of this study the tissue differentiation algorithm was further updated to include the condition whereby fibrocartilage formed, in an otherwise chondrogenic environment, when the octahedral shear strain exceeded a critical value $\varepsilon^{fibrocartilage}$ (Figure 5-7). The parameter $\varepsilon^{hypertrophy}$ was fixed at 5 %, while the parameter $\varepsilon^{fibrocartilage}$ was set at either 10 %, 12.5 % or 15 %. The value of $\varepsilon^{fibrocartilage}$ had a large effect on the model predictions. In the simulation where $\varepsilon^{fibrocartilage}$ = 10 %, a mixture of fibrous tissue and fibrocartilage formed at the surface of the defect as early as week 2 (Figure 5-7A). By week 8, as the vascular network was restored to the subchondral region, bone filled the majority of the osseous phase of the defect and hyaline cartilage formed below the fibrocartilage within the chondral phase of the defect. As the simulation progressed, the subchondral plate advanced above the native tidemark and the hyaline cartilage was replaced with bone by endochondral ossification. Hypertrophy was inhibited within the fibrocartilage, however, as a result of the high strain environment. By week 18 no hyaline cartilage remained in the defect. Instead the chondral phase was composed entirely of osseous tissue covered by a thin layer of fibrocartilage and fibrous tissue.

A different pattern of tissue formation was predicted in the simulation where $\varepsilon^{fibrocartilage}$ = 12.5 % (Figure 5-7B). In this model, by week 2, a mixture of hyaline cartilage, fibrocartilage and fibrous tissue formed at the surface of the defect. Furthermore, by week 8, the majority of the chondral phase was composed of hyaline cartilage with only a small region of fibrocartilage predicted at the surface of the defect. As the bone plate advanced into the chondral phase, however, the magnitude of the strains within this tissue were amplified and the hyaline cartilage was converted into fibrocartilage. By week 18, the spatial distribution of tissues predicted by the model was the same as that predicted in the simulation

where $\varepsilon^{fibrocartilage}$ = 10 %. Finally, in the model where $\varepsilon^{fibrocartilage}$ = 15 %, very little fibrocartilage formed and by week 18, only a small region was predicted at the surface of the defect (Figure 5-7C).

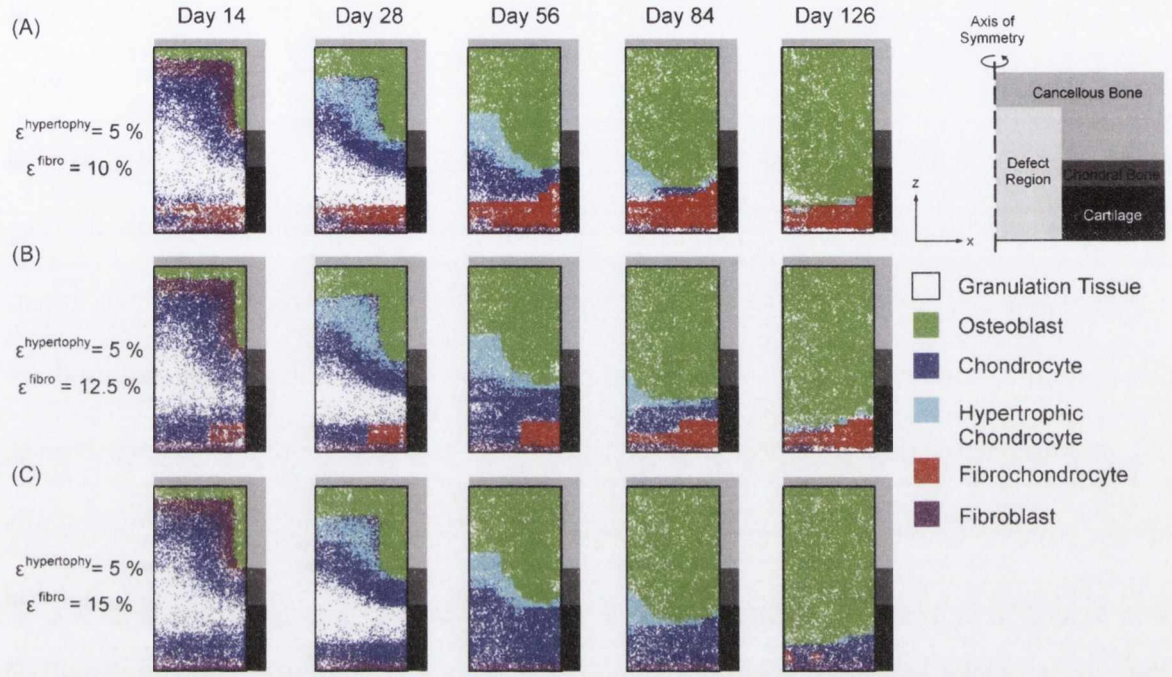

Figure 5-7: Model predictions of cell differentiation at different times during the spontaneous repair of an osteochondral defect using the updated algorithm where chondrocyte hypertrophy was regulated by the oxygen tension and the octahedral shear strain ($\varepsilon^{hypertrophy}$= 5 %) and fibrocartilage could form based on the local octahedral shear strain. The parameter $\varepsilon^{fibrocartilage}$ was varied between (E) 10 %, (F) 12.5 % and (G) 15 %.

5.4 Discussion

In a previous study we developed a computational mechanobiological model which predicted cell fate during the spontaneous repair process within an osteochondral defect. While this model successfully simulated many aspects of the regenerative process, it was unable to predict the spatial pattern of bone formation observed during the latter stages of repair. The objective of this study was thus to improve the predictive capacity of the model by including a series of rules whereby the local mechanical environment affected the fate of cartilage. Based on the findings of a number of *in vitro* studies which have shown that mechanical loading can either prevent hypertrophy and endochondral ossification of cartilage [52,95,251–253], or promote the formation of fibrocartilage [55,56], it was hypothesised that

the fate of the cartilage that forms within an osteochondral defect depends on both oxygen availability and the local mechanical environment. It was postulated that hypertrophy was supressed by appropriate magnitudes of local strain, while fibrocartilage formed in regions where the local strain was excessively high. These rules were developed by first modelling the *in vitro* bioreactor study conducted by Thorpe *et al.* [51]. In this study, dynamic compression of agarose hydrogels which were seeded with MSC-derived chondrocytes led to a reduction in chondrocyte hypertrophy and calcification of the engineered tissue. The updated tissue differentiation algorithm was then used to model the spontaneous repair process within an osteochondral defect. The pattern of tissue formation predicted by these simulations matched the behaviour experimentally observed in a number of *in vivo* models. In addition to this, the models also provide insights into how mechanical loading benefits the spontaneous repair process by inhibiting chondrocyte hypertrophy and endochondral ossification during the latter stages of repair. The models also point to the deleterious effect that loading can have on the process by inducing the formation of fibrocartilage in place of hyaline cartilage.

The first objective in modelling the *in vitro* study conducted by Thorpe *et al.* [51] was to simulate the hypertrophic progression observed within unloaded MSC laden hydrogels, in order to provide additional support for our previous hypothesis that chondrocyte hypertrophy is inhibited by low oxygen availability. In this case, using our original tissue differentiation algorithm, where chondrocyte hypertrophy was regulated solely by the local oxygen tension, the simulations were able to predict the experimentally observed spatial distribution of mineralisation within the confined and unconfined constructs. Following this, the experimental findings that the application of DC supressed mineralization of MSC-laden hydrogels were used to develop the rules whereby chondrocyte hypertrophy is inhibited by the local strain environment. In the developed models chondrocyte hypertrophy was not

predicted in either of the DC groups when the threshold parameter, $\varepsilon^{hypertrophy}$, was below a specific value. The model was therefore unable to predict the spatial pattern of hypertrophy observed in the unconfined group. This was most likely caused by the assumption that the constructs contained a homogeneous distribution of extra cellular matrix (ECM) components at the onset of DC. In reality, histological staining performed prior to the DC loading protocol showed that the ECM was distributed in a heterogeneous arrangement (data not shown) [51]. In addition to this, as a result of the high oxygen tension within the top half of the construct, prior to the application of DC, cells within this region may have undergone hypertrophy and begun mineralising their surrounding tissue. These factors may then have resulted in the upper section of the construct being stiffer than the bottom section of the construct at the onset of loading. This strain shielding effect would have reduced the strains in the top half of the construct (where chondrocyte hypertrophy was experimentally observed) and amplified the strains in the bottom half of the construct (where chondrocyte hypertrophy was not observed). Despite these simplifications, however, the developed models were able to predict the general trends observed by Thorpe *et al.*[51] whereby the application of DC led to a reduction in chondrocyte hypertrophy.

In addition to the octahedral shear strain, the third principal strain and the hydrostatic strain were examined as inhibiters of chondrocyte hypertrophy (Appendix IV: Alternative Rules for Strain Regulation of Hypertrophy (Chapter 5) and Appendix V: Alternative Rules for Strain Regulation of Fibrocartilage (Chapter 5)). In the case of the latter approach, hypertrophy was inhibited in regions where the magnitude of the 3rd principal strain exceeded a threshold value ($\varepsilon^{min} \geq \varepsilon^{hypertrophy}$). The predicted results from these simulations followed the same trends as the models where the octahedral shear strain was used to inhibit hypertrophy. Conversely, in the case of hydrostatic strain, hypertrophy was inhibited in regions where the deformation was compressive ($\varepsilon^{hydrostatic} < 0$) and appropriately high

($\varepsilon^{oct,shear} \geq \varepsilon^{hypertrophy}$). These simulations were unable to predict the experimentally observed behaviour because the calculated hydrostatic strain was approximately zero in all of the models. This arose due to the assumptions that the fluid phase was incompressible and that the constructs had the same material parameters as native cartilage (i.e. low permeability). Based on these findings, the octahedral shear strain was considered as an appropriate measure of strain for use in the updated tissue differentiation algorithm where tissue strain directly influenced chondrocyte fate.

Following the development of the *in vitro* simulations, the updated tissue differentiation algorithm was then used to model the spontaneous repair process within an osteochondral defect. The purpose of this was, firstly, to determine a value for the parameter $\varepsilon^{hypertrophy}$ and, secondly, to develop an additional rule whereby excessive magnitudes of strain, coupled with chondrogenic conditions, resulted in the formation of fibrocartilage. By performing a series of parametric studies it was determined that the model where $\varepsilon^{hypertrophy}$ = 5 % and $\varepsilon^{fibrocartilage}$ = 12.5 % was most representative of the experimentally observed behaviour (Figure 5-8). The efficacy of this model was examined by comparing the spatial patterns of bone formation predicted in the simulation with those experimentally observed during the different stages of the spontaneous repair process [4]. In this *in vivo* study it was reported that the osseous tissue first forms in a cylindrical arrangement, then an infundibuliform shape, before becoming plane with the native bone and eventually advancing into the chondral phase in a convex arrangement (Figure 5-8E). These different arrangements were predicted at various time points within the updated model.

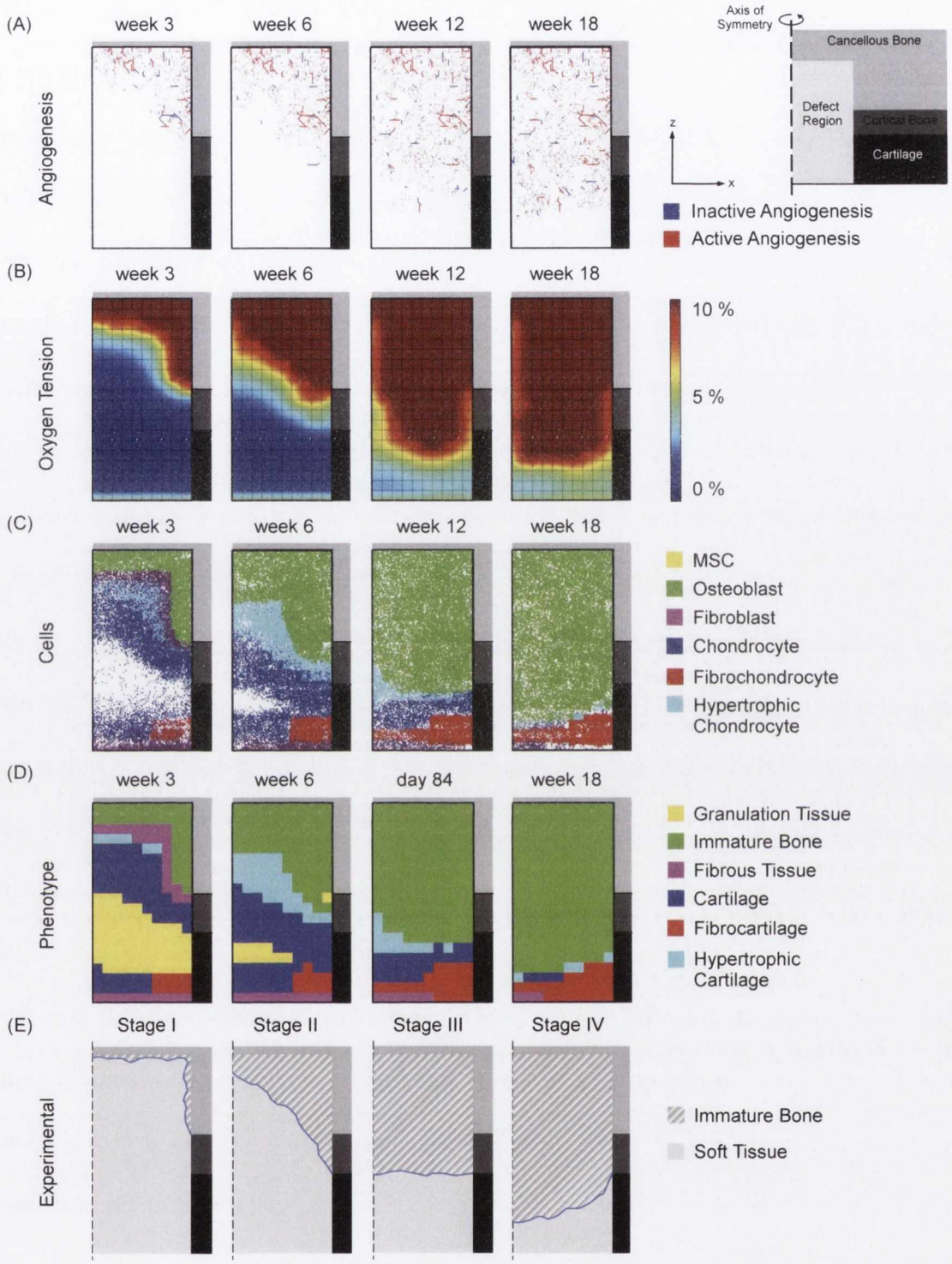

Figure 5-8: Model Predictions vs experimental observations for the simulations where $\varepsilon^{hypertrophy} = 5$ % and $\varepsilon^{fibrocartilage} = 12.5$ %. (A – D) The model predictions of the spatial pattern of (A) blood vessel growth, (B) oxygen tension, (C) cell differentiation and (D) tissue formation at different stages of the spontaneous repair process within an osteochondral defect. (E) The spatial pattern of bone formation within an osteochondral defect observed at different stages of the spontaneous repair process by Orth et al. [4].

The developed model also provides insights into the effect that the changing environment within the osteochondral defect has on the spontaneous repair process. Firstly, during the initial stages of the repair process (< 8 weeks), as a result of stress shielding from

the surrounding tissues, bone formation was controlled largely by oxygen. As the subchondral plate advanced into the chondral phase, however, the mechanical environment began to play a much larger role in directing endochondral ossification, most notably by inhibiting chondrocyte hypertrophy in the peripheries of the defect. These results imply that an appropriate loading regime may improve the treatment of osteochondral defects by inhibiting terminal differentiation and endochondral ossification within the chondral phase. This feature has been explored in a number of *in vivo* studies which have examined the effect that both the magnitude [13,14,250] and the timing of loading [246] has on the outcome of the spontaneous repair process. In all of these studies it was reported that an appropriate loading regime benefited the repair process by promoting the formation of stable hyaline cartilage.

The altering environment also affected the formation of fibrocartilage during the repair process. In the first 8 weeks of the simulation only a small region of fibrocartilage was predicted to form within the chondral phase of the defect. As the subchondral plate advanced above the native tidemark, however, the magnitude of the strains within this phase increased and the remaining hyaline cartilage was converted to fibrocartilage. These results agree with a number of long term *in vivo* studies which have reported that the hyaline cartilage which initially forms in the chondral phase of the defect eventually breaks down [4,57]. It may thus be the case that, the magnitude of the strains within the newly formed chondral tissue increases, as the bone front advances towards the surface of the defect, as observed in the simulations. This may in turn lead to the formation of mechanically inferior fibrocartilage which is unable to withstand the loading environment of the knee joint.

The main limitation of the current study was the FE models which were used to determine the local mechanical environment within the *in vitro* and the *in vivo* cases. These models were simplified by assuming that all of the tissues involved could be characterised as biphasic where the solid phase was isotropic elastic. In reality, however, biological tissues

are much more complex and require sophisticated mathematical models to accurately predict their behaviour. As a result of this simplification, it was only possible to predict the general behaviour rather than the exact magnitudes of the strain within the deforming tissue. For this reason, the threshold values $\varepsilon^{hypertrophy}$ and $\varepsilon^{fibrocartilage}$ are exclusive to the models in which they were developed and as a result may change as the model is used to simulate different regenerative events within the *in vivo* setting.

A final simplification which may limit the predictive capacity of the developed model arises in relation to the algorithm which was used to predict angiogenesis within the defect. As part of this study, our previous model of angiogenesis was updated to include a feature whereby blood vessels had to form a closed loop before they were considered active [30]. The benefit of this updated algorithm was that it made the model more physiologically relevant. Despite this feature however, angiogenesis was still considered to be governed largely by the mechanical environment and the contribution of growth factors was, therefore not considered. Studies have shown that during regenerative events there exists a 'cross-talk' between the differentiating cells and the forming blood vessels which may affect tissue formation [53,54,204,256]. Such a relationship has been explored as a potential mechanism which may be used to direct the course of endochondral ossification during the repair of osteochondral defects in a number of tissue engineering studies [15,186,257]. Future work will involve updating the current model to include this behaviour in order to better understand the mechanisms involved in such approaches.

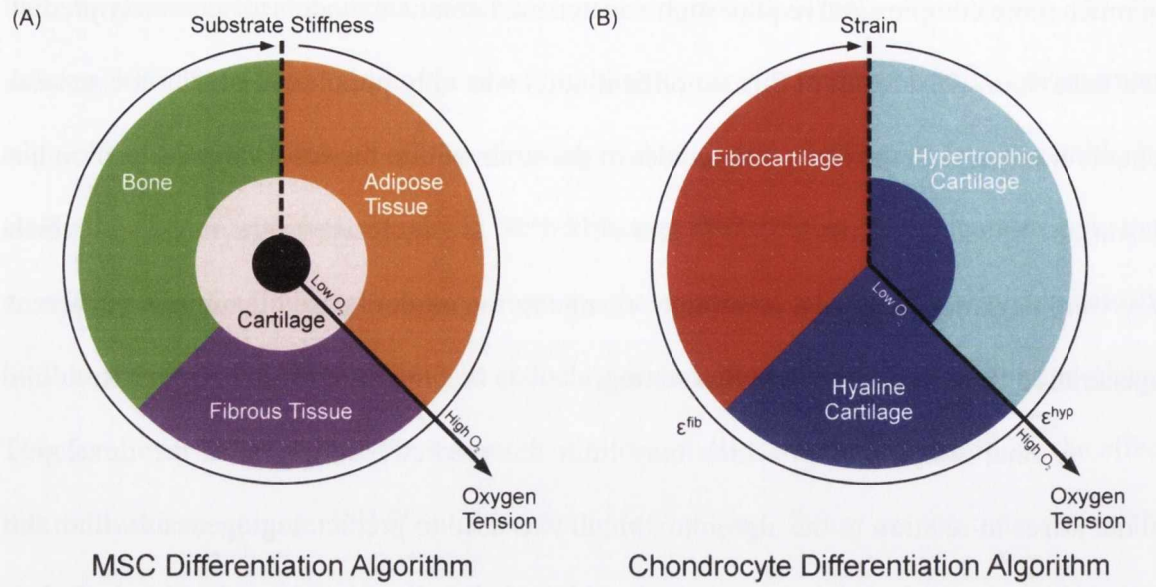

Figure 5-9: Tissue differentiation algorithm where (A) MSC fate is governed by a combination of the substrate stiffness and local oxygen tension and (B) chondrocyte fate is governed by the octahedral shear strain and the local oxygen tension.

Despite these limitations, the developed model was able to predict the pattern of tissue formation which has been experimentally observed during the spontaneous repair process within an osteochondral defect. Based on these results we propose an updated version of the tissue differentiation algorithm developed by Burke *et al.*[44] where MSC fate is governed by the substrate stiffness and the local oxygen tension while the chondrogenic phenotype is affected by the magnitude of the local octahedral shear strain and the local oxygen tension (Figure 5-9). This model was able to account for the role that mechanical loading plays on the quality of the repair tissue which forms during osteochondral defect repair. In particular, it provides insights into how an appropriate loading regime can improve the repair process by promoting the formation of stable hyaline cartilage. Future work will involve using this model to better understand the mechanisms involved in successful and unsuccessful tissue engineering strategies designed to treat osteochondral defect.

Chapter 6 A Computational Model of Osteochondral Defect Repair Using a Tissue Engineered Scaffold.

The objective of this chapter is to develop a computational model in order to better understand the potential mechanisms which may be utilised by tissue engineering strategies to regenerate the damaged tissues during osteochondral defect repair. To this end, the *in silico* model developed in the previous chapter is updated to include a condition whereby mature cartilage is resistant to both terminal differentiation and vascularisation. The updated model is then tested by using it to predict tissue formation during the spontaneous repair process within an osteochondral defect. Following this, the model is used to simulate an osteochondral defect treated with different variations of a multiphasic scaffold. By comparing the results of the different simulations we are able to highlight the importance of controlling angiogenesis when designing TE strategies for the treatment of osteochondral defects.

6.1 Introduction

In recent years tissue engineering (TE) has emerged as a viable strategy for the treatment of osteochondral defects [11]. The goal of these strategies is to use cells, scaffolds and growth factors to regenerate the damaged tissue and thus provide long term relief to the patient [258]. While numerous advances have been made in the design of multiphasic scaffolds [197,205,259], cell culture protocols [260,261] and growth-factor releasing materials [262,263], a number of issues still exist which limit the widespread implementation of these techniques. One of the most prominent of these is promoting the formation of stable bone and stable cartilage within the osseous and chondral regions of the defect respectively. In particular, the cartilage that forms within the chondral region of an osteochondral defect must be resistant to terminal differentiation in order to prevent the upward migration of the bone plate [264], a phenomenon which has been hypothesised to contribute to the eventual break down of the repair tissue [57].

In an effort to better understand the factors which promote a stable cartilage phenotype, a number of studies have explored the influence of various environmental and culture conditions on chondrogenesis and hypertrophy of adult stem cells [260,265–267]. Liu *et al.* [265] explored the relationship between the length of time in chondrogenic conditions *in vitro* and the extent of hypertrophy and endochondral ossification *in vivo*. The authors demonstrated that mesenchymal stem cell (MSC) derived chondrocytes were resistant to both mineralisation and vascularisation if maintained *in vitro* for 12 weeks prior to implantation. Furthermore, it has been demonstrated that MSCs maintained *in vitro* in hypoxic conditions remained cartilaginous *in vivo*, demonstrating that oxygen tension is a key regulator of the chondrogenic phenotype [50]. Recognising such a relationship between vascularisation, oxygen and chondrocyte hypertrophy [53,54], a number of studies have reported improved cartilage formation in an osteochondral defect following the application of anti-angiogenic factors [15,16,257,268]. Other studies have attempted to alter the physical

characteristics of scaffolds to mimic the calcified layer that separates cartilage and bone in the osteochondral unit [58], thereby creating unique oxygen and nutrient environments in each region of a regenerating osteochondral defect.

While these studies have improved our understanding of how environmental factors regulate MSC fate, and have led to the development of better treatment options, we still lack tools to systemically explore how the design of scaffolds and engineered constructs regulates osteochondral defect regeneration. The objective of this study was to provide a mechanistic explanation for why design changes to scaffolds might either enhance or impair osteochondral defect regeneration. To this end, we utilised a previously developed computational model of angiogenesis and MSC differentiation in which cell fate was regulated by the local oxygen tension and the mechanical environment (substrate stiffness and tissue strain). In the first part of this study, motivated by the findings of Liu *et al.* [265] and the well documented finding that articular cartilage releases factors that supress angiogenesis [269–272], the model of angiogenesis was extended to include a rule whereby blood vessel growth into regions of mature cartilage was inhibited. This model was developed by using it to predict the observed course of tissue formation during the spontaneous repair process within an osteochondral defect. In order to demonstrate the utility of the model, it was then used to simulate osteochondral defect repair following the implantation of different variations of the scaffold developed by Da *et al.* [58]. As previously discussed, this study explored the implantation of an MSC-laden trilayer scaffold incorporating a compact layer. In addition to this it also examined the implantation of a bilayered scaffold which did not contain the compact region. We hypothesised that, during the early stages of healing, the compact layer would serve to limit angiogenesis to the osseous phase of the defect. This confinement of angiogenesis would then allow the seeded MSCs in the chondral phase to

form stable cartilage which, following the absorption of the compact layer, would be resistant to both vascularisation and mineralisation.

6.2 Method

6.2.1 Iterative Procedure

Tissue differentiation within the defect region was simulated via an iterative procedure. This was similar to the one outlined in chapter 3 (Section 3.2.2) with the exception that the biophysical stimuli calculated using the finite element (FE) model was also used as an input to the tissue differentiation algorithm. All of the simulations in this study depicted a time period of 24 weeks where each time step modelled a period of 24 hours.

6.2.2 Finite Element Models

A simplified 3D FE model of an osteochondral defect within the femoral condyle was constructed using the FE package FEBio (version 2.2.2, University of Utah, Technology Commercialization Office, 615 Arapeen Drive, Suite 310, Salt Lake City). This model had the same geometry as the one outlined in the chapter 4 (Section 4.2.2). A defect of size φ5 mm x 5 mm was included at the centre of the condyle and, depending on the model, this was assumed to be filled with either granulation tissue or a tissue-engineered scaffold (Figure 6-1). The material properties of each biological tissue are listed in Table 6-1. A load of 2400 N was applied over 1 second, based on the assumption of five to six times subject weight (80 kg) spread evenly between the lateral and medial compartments [244].

Table 6-1: Material Parameters

Material Property	Granulation Tissue	Fibrous Tissue	Fibro-Cartilage	Cartilage	Hypertrophic Cartilage	Immature Bone	Mature Bone	Cortical Bone
Young's Modulus [MPa]	1[a]	2[a,b]	5	10[a,b]	20	1000[a]	6000[c]	20,000[c]
Poisson's Ratio	0.167	0.167	0.167	0.167	0.167	0.3	0.3	0.3
Permeability [mm^4/ Ns]	0.01[a]	0.01[a,b]	0.01	0.005[a,b]	0.005	0.001[a]	0.0037[d]	1e-5[a]
Solid Volume Fraction	0.2	0.2	0.2	0.2	0.2	0.2	0.2	0.2

a 217

b 224

c 23

d 209

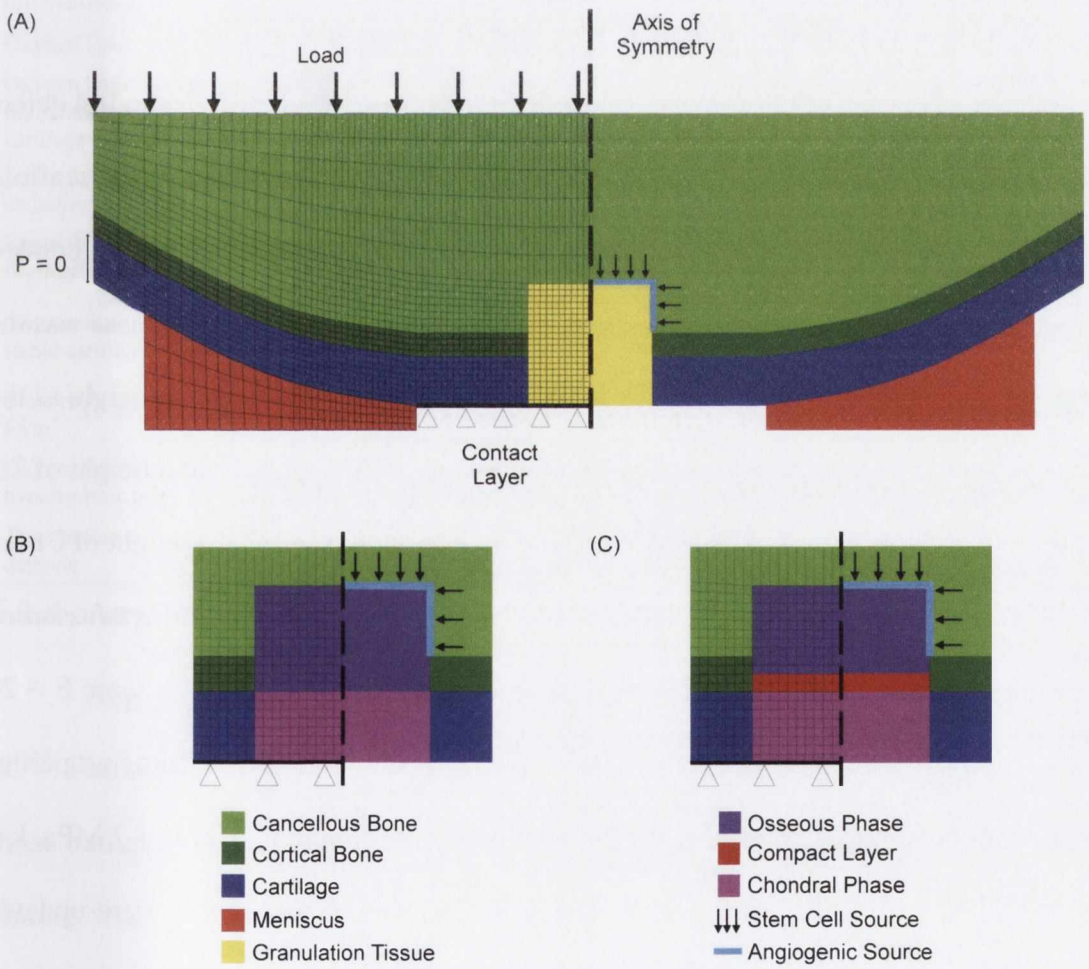

Figure 6-1: FE model and boundary conditions of an osteochondral defect for the simulations of (A) the spontaneous repair process and tissue formation following the implantation of the (B) bilayer scaffold and (C) trilayer scaffold , similar to that developed by Da et al. [58].

6.2.3 Finite Element Models of Scaffold Treated Defects

The study to be modelled is discussed in greater detail elsewhere [58]. Briefly, two different TE scaffolds were developed and tested. The first was a bilayer scaffold composed of an osseous layer and a chondral layer bonded directly to each other. The second was a trilayer scaffold composed of an osseous and a chondral layer separated by an impermeable compact layer. In both scaffolds the osseous layer was formed from a composite scaffold fabricated from PLGA/TCP skeleton wrapped in type I collagen [273], while the chondral layer was manufactured from bovine cartilage extra-cellular matrix [274]. The compact layer was formed from dense PLGA/TCP and was shown to be impermeable [58]. The material properties of the different scaffold phases had been assessed in earlier studies [273,274].

As part of this study, FE models were constructed depicting an osteochondral defect treated with either of the developed scaffolds (Figure 6-1B & C). In both cases the scaffold had the same dimensions as the defect and it was assumed that the repair tissue bonded directly to the native tissue. For the model of the bilayer scaffold, the osseous phase was the same height as the native bone (3 mm) while the chondral phase was the same height as the native cartilage (2 mm). In the trilayer scaffold model the osseous phase had a height of 2.5 mm, the compact layer had a height of 0.5 mm and the chondral phase had a height of 2 mm. All of the scaffold materials were modelled as bi-phasic where the solid phase was assumed to be isotropic elastic. At day 0, the material parameters for the osseous phase were $E = 20$ MPa, $k = 1\ mm^4 N^{-1} s^{-1}$, $\nu = 0.167$ and $\varphi = 0.9$ [273]. The compact layer had the same properties except $k = 0.00001\ mm^4 N^{-1} s^{-1}$ and $\varphi = 0.99$. Finally, for the chondral layer $E = 2$ MPa, $k = 1\ mm^4 N^{-1} s^{-1}$, $\nu = 0.167$ and $\varphi = 0.9$ [274]. The scaffold material parameters were updated iteratively in the same way as for the spontaneous repair model. Regarding the FE model of the trilayer scaffold group, the material parameters of the compact layer remained constant for a period of time ($T^{degrade}$). After this point the material in the compact layer was assumed

to start resorbing and cells were therefore able to migrate into the vacant space. The material parameters in these elements were then updated accordingly.

Table 6-2: Angiogenesis and MSC Differentiation Model Parameters

Model Parameter	Symbol	Source	Unit	Value
Octahedral shear strain threshold for inhibition of angiogenesis	ε^{angio}	Estimated	-	0.1
Blood vessel growth rate	V^{growth}	Estimated	mm day^{-1}	0.1
Minimum length for branching	L_{min}	[29]	mm	0.2
Maximum length without branching	L_{max}	[29]	mm	0.5
Minimum cell age for MSC differentiation	Age^{cell}	Estimated	days	5
Oxygen diffusion coefficient	G	[44,227]	$mm^2\ s^{-1}$	2.2×10^{-3}
Initial oxygen tension	$O_2^{initial}$	[184]	mol mm^{-3}	101.6×10^{-12}
Oxygen tension for inhibition of differentiation	$O_2^{inhibition}$	[129]	mol mm^{-3}	5.48×10^{-12}
Oxygen limit for cartilage	$O_2^{cartilage}$	[44]	mol mm^{-3}	30.48×10^{-12}
Oxygen limit for differentiation of immature cartilage to hypertrophic cartilage	$O_2^{hypertrophic}$	Estimated	mol mm^{-3}	30.48×10^{-12}
Strain threshold above which chondrocyte hypertrophy was inhibited	$\varepsilon^{hypertrophic}$	Estimated	%	5
Strain threshold above which fibrocartilage formed	$\varepsilon^{fibrocartilage}$	Estimated	%	12.5
Oxygen limit for differentiation of stable cartilage to hypertrophic cartilage	$O_2^{hyp,\ stable}$	Estimated	mol mm^{-3}	50.48×10^{-12}
Time required for stable cartilage to form	T^{stable}	[260,265–267]	weeks	8 – 12
Oxygen limit for calcification of hypertrophic cartilage	$O_2^{endochondral}$	Estimated	mol mm^{-3}	50.48×10^{-12}
Time before the compact layer starts to degrade	$T^{degrade}$		weeks	4 - 12

6.2.4 Angiogenesis

Angiogenesis was modelled using the lattice-based approach described by Checa *et al.* [29]. Furthermore, the rules governing blood vessel growth and direction were the same as those outlined in the previous chapter 5 (Section 5.2.4). As part of this study an additional feature was added to the model whereby blood vessel growth was inhibited by stable cartilage [269–272]. It was thus assumed that blood vessels stopped growing if they entered an element which had been classified as cartilage for a sustained period of time (T^{stable}).

6.2.5 Cell Migration, Cell Proliferation and Cell Death

The migration and proliferation of MSCs, osteoblasts (OBs), chondrocytes (CCs), fibroblasts (FBs), hypertrophic chondrocytes (HC) and fibrochondrocytes (FCs) was also modelled using a lattice approach [20,29]. The migration of cells was implemented using 'random walk' theory [20]. Cell proliferation was implemented in a similar fashion provided that there was a vacant position beside the parent cell. The maximum number of cells allowed in any element was limited to 1×10^5 cells/mm^3 [44]. The migration rate (M) determined the number of attempted migration actions per time step while the doubling time (DT) was the age a cell had to be before it proliferated (Table 6-3). Cell proliferation was inhibited in regions where the oxygen concentration fell below a specific threshold value (O_2^{prolif}) (Table 6-3). If the oxygen concentration fell below a threshold value (O_2^{death}) then cell death was initiated (Table 6-3).

Table 6-3: Cell Model Parameters

Model Parameter	MSC	CC	OB	FB	HC	FC
Doubling Time [days]	0.5[a]	1.5[a]	1[a]	0.5[a]	1.5[a]	1.5
Migration Rate [μm/hr]	26.6[b]	N/A	N/A	26.6[b]	N/A	N/A
Anoxic Death Rate [% cells day^{-1}]	20	20	20	20	20	20
Oxygen Concentration for cell proliferation (O_2^{prolif}) [mol mm^{-3}]	40 x10^{-12} [c]	10 x10^{-12}	80 x10^{-12} [c]	20 x10^{-12}	30 x10^{-12}	10 x10^{-12}
Oxygen Concentration for cell death (O_2^{death}) [mol mm^{-3}]	5 x10^{-12}	5 x10^{-12}	20 x10^{-12}	5 x10^{-12}	5 x10^{-12}	5 x10^{-12}

a153

b226

c30

6.2.6 Oxygen Transport

Oxygen transport was modelled using the same method outlined in the chapter 3 (Section 3.2.6). Briefly, the cellular consumption of oxygen was modelled using Michealas-Menten kinetics (Table 6-4) while the oxygen supply from the vascular network was determined using a production term which was updated based on the number of ECs within an element.

Table 6-4: Michealas-Menten parameters for each cell phenotype

Michealas - Menten Parameters	MSC	CC	OB	FB	HC	FC
Cell type (n)	1	2	3	4	5	6
Max Consumption Rate (Q^{max}) [mol $cell^{-1}$ hr^{-1}]	93.2×10^{-15} [a]	1.8×10^{-15} [a, b]	93.2×10^{-15} [a]	93.2×10^{-15} [a]	1.8×10^{-15} [a]	1.8×10^{-15} [a, b]
Oxygen Concentration at half max consumption (K^m) [mol mm^{-3}]	22.5×10^{-12}	22.5×10^{-12}	22.5×10^{-12}	22.5×10^{-12}	22.5×10^{-12}	22.5×10^{-12}

a 30

b 73

6.2.7 MSC Differentiation and Chondrocyte Hypertrophy

MSC differentiation was determined using the updated tissue differentiation algorithm developed in the chapter 5 (Section 5.2.8). Briefly, MSC fate was governed by the substrate stiffness and the local oxygen tension while the chondrogenic phenotype was affected by the magnitude of the local octahedral shear strain and the local oxygen tension (Figure 6-2). Regarding cartilage fate, in regions where the octahedral shear strain exceeded a threshold value ($\varepsilon^{fibrocartilage}$), fibrocartilage formed irrespective of the oxygen tension. Below this strain threshold CCs became hypertrophic when the oxygen tension exceeded a specific value ($O_2^{hypertrophic}$). This process was inhibited, however, by sufficiently large magnitudes of strain ($\varepsilon^{hypertropicy} < \varepsilon^{oct,\ shear} < \varepsilon^{fibrocartilage}$).

This model was updated to include a condition whereby a higher oxygen tension was required to induce hypertrophy in stable cartilage. Motivated by the findings of Liu *et al.* [265] and Leijten *et al.* [50], a region of phenotypically stable cartilage was considered to have formed after stable cartilage was predicted within a specific region for a sufficiently long period of time (T^{stable}). Following this, a higher oxygen tension ($O_2^{hyp,\ stable}$) was required to induce hypertrophy. In addition to this, it was also assumed that stable cartilage was unable to transdifferentiate into fibrocartilage.

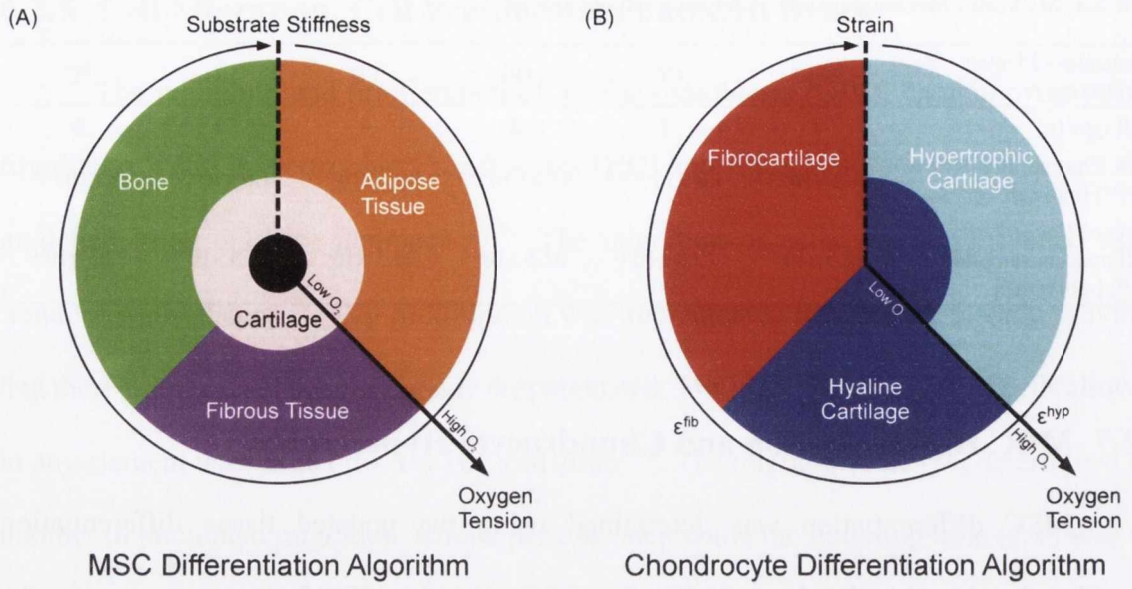

Figure 6-2: Tissue differentiation algorithm where (A) MSC fate is governed by a combination of the substrate stiffness and local oxygen tension and (B) chondrocyte fate is governed by the octahedral shear strain and the local oxygen tension.

6.2.8 Bilayer and Trilayer Models

In the experimental study being modelled, bone marrow-derived MSCs were seeded onto the different phases of the scaffold (5×10^5 cells on the osseous phase and 2×10^5 cells on the chondral phase) [58]. Prior to implantation, by using a custom made bioreactor, the cells were then cultured in either osteogenic or chondrogenic media for a period of 21 days depending on whether they were in the osseous or the chondral phase respectively. This was modelled in both the bilayer and trilayer scaffold simulations by initialising 2×10^5 of the lattice points in the chondral phase as CCs and 5×10^5 lattice points in the osseous phase as OBs. It was assumed that there was a homogeneous distribution of cells throughout the construct. Furthermore, in the simulations, MSCs from the native tissue were able to migrate into the scaffold at day 0. This was implemented by assigning 5 % of the lattice points on the cancellous bone surface to MSCs. In the trilayer layer model, cells and blood vessels were unable to pass through the compact layer until it had been completely absorbed. This absorption process was considered to have finished at the time $T = T^{degrade}$, at which point the compact layer was no longer present in the model. In each simulation the compact layer

was absorbed over a period of 4 weeks ($\Delta T^{degrade}$ = 4 weeks). As a result, the absorption process was initiated at the time point ($T = T^{degrade} - \Delta T^{degrade}$). In addition to this, it was assumed that the compact layer inhibited the diffusion of oxygen between the osseous and chondral phases. To model this, a lower diffusion coefficient ($G^{compact} = G_0/5$) was initially applied to this region. In order to characterise the absorption of this layer, the diffusion coefficient was updated using a linear model where $G = G^{compact}$ at $T \leq T^{degrade} - \Delta T^{degrade}$ up to $G = G_0$ at $T \geq T^{degrade}$.

6.2.9 Study Design

In the first part of this study, the updated model was used to simulate the time-course of tissue differentiation observed during the spontaneous repair process within an osteochondral defect (i.e. no scaffold was included in the model). In this case, motivated by the *in vivo* study conducted by Liu et al. [265], the parameter T^{stable} was varied between 2 weeks and 12 weeks. The results of these simulations were compared to the results obtained using our previously developed model where blood vessel growth was independent of the tissue phenotype ($T^{stable} = \infty$).

In the second part of this study the updated model was used to predict the course of healing in an osteochondral defect treated with different types of scaffolds, similar to that developed by Da *et al.* [58]. Firstly, the model predicted the course of healing in a defect treated with the bilayer (compact layer free) scaffold (Figure 6-1B). In these simulations the parameter T^{stable} was varied between 8, 10 and 12 weeks in order to examine the effect that the maturation time of cartilage has on the predicted pattern of healing. Following this, the model was used to predict the course of healing observed in a defect treated with a trilayer (compact layer) scaffold (Figure 6-1C). The purpose of this part of the study was to examine the effect the absorption time of the compact layer has on the predicted course of healing. In this simulation, T^{stable} = 10 weeks and the parameter $T^{degrade}$ was varied between 4, 6, 8, 6,

10 and 12 weeks. This was based on the results of the *in vivo* model, where it was reported that all of the scaffold materials had been completely absorbed by three months [58]. In the final part of this study, models were developed which simulated the course of healing in an osteochondral defect following treatment with either a cell-free bilayer scaffold or a cell-free trilayer scaffold. It was assumed that in these models the healing response was initiated by MSCs which migrated into the scaffold from the exposed cancellous bone at day 0. In both models the parameter T^{stable} = 10 weeks and in the trilayer simulation $T^{degrade}$ = 10 weeks. The purpose of this section was to examine the influence that the seeded cells have on tissue formation within the developed scaffold.

6.3 Results

6.3.1 Spontaneous repair within an empty osteochondral defect

The length of time required for MSC-derived cartilage to become phenotypically stable (T^{stable}) was predicted to impact on the patterns of tissue differentiation within the defect during the later stages of the repair process (Figure 6-3). In all of the models there was very little difference in the predicted behaviours for the first 8 weeks of the simulations. During this period, blood vessel growth was confined to the subchondral region of the defect (data not shown). For the opening 2 weeks of each simulation, bone formed in the base of the defect via intramembranous ossification. Cartilage tissue was predicted above this new bone, although this soon underwent endochondral ossification as blood vessels grew further into defect. From week 4 onwards, bone formed mainly by further endochondral ossification. As the simulations progressed, the osseous front advanced towards the chondral phase of the defect until by week 8 it had reached the native subchondral bone.

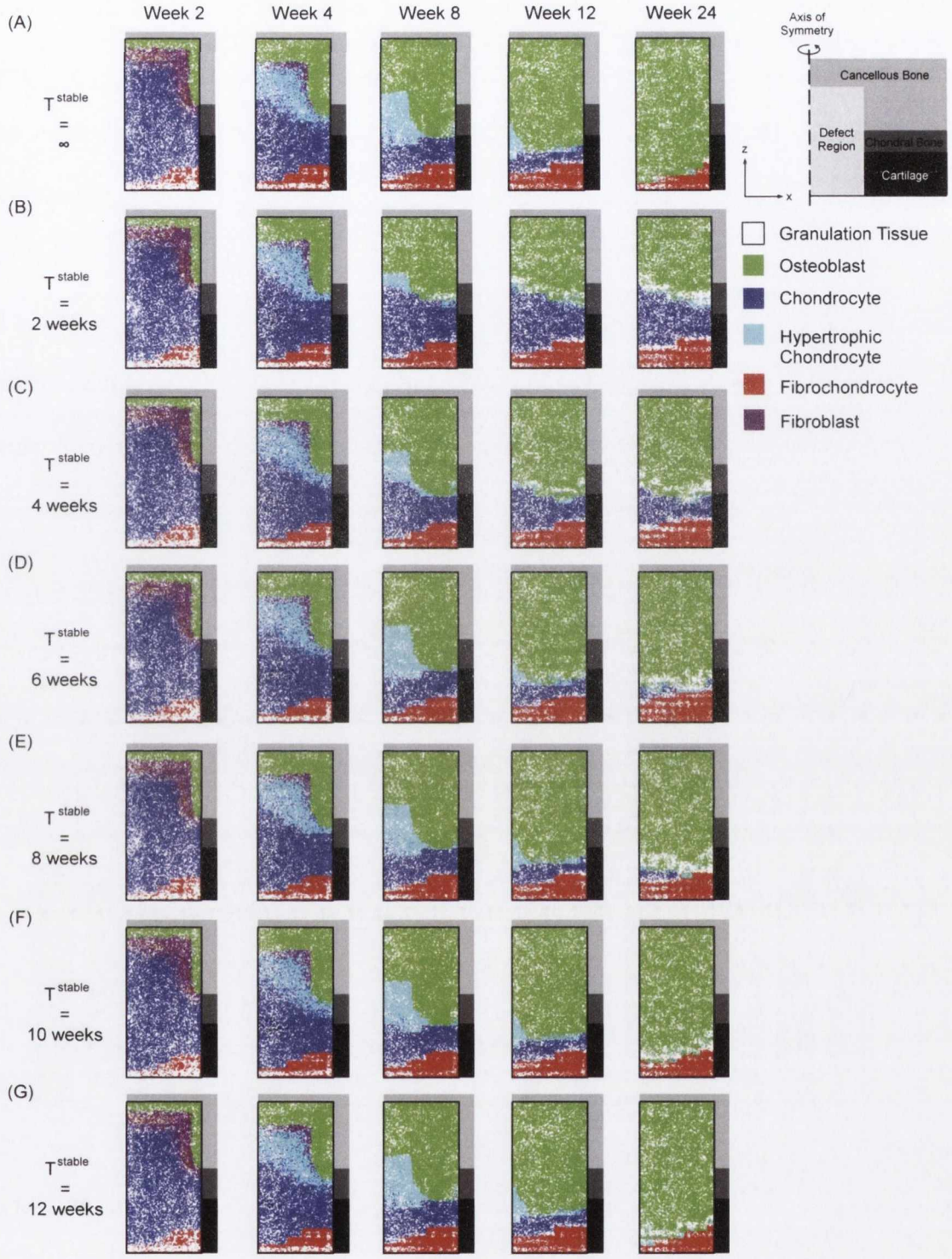

Figure 6-3: Model predictions of cell differentiation at different times during the spontaneous repair of an osteochondral defect using: (A) our previous tissue differentiation algorithm where angiogenesis was independent of the tissue phenotype and (B - G) the updated model where the parameter T^{stable} was varied between (B) 2 weeks (C) 4 weeks (D) 6 weeks (E) 8 weeks (F) 10 weeks and (G) 12 weeks.

By week 12, the spatial patterns of tissue differentiation predicted by the various models had begun to differ. In the original model ($T^{stable} = \infty$), the subchondral plate continued to advance until by week 24 the majority of the defect was composed of bone. In

the updated models, the general trend was that the parameter T^{stable} governed the quantity of stable cartilage which was present in the chondral phase at weeks 12 and 24 (Figure 6-4). When this value was low (i.e. when stable cartilage was assumed to form after a relatively short period of time), stable cartilage formed at an earlier time point. This in turn meant that the advancing vascular network and subchondral plate were halted closer to the base of the defect. As T^{stable} increased, the quantity of bone predicted in the chondral phase at weeks 12 and 24 increased as the volume of cartilage decreased. Finally, in the simulations where $T^{stable} \geq 10$ the pattern of healing was the same as the pattern predicted by the model where $T^{stable} = \infty$.

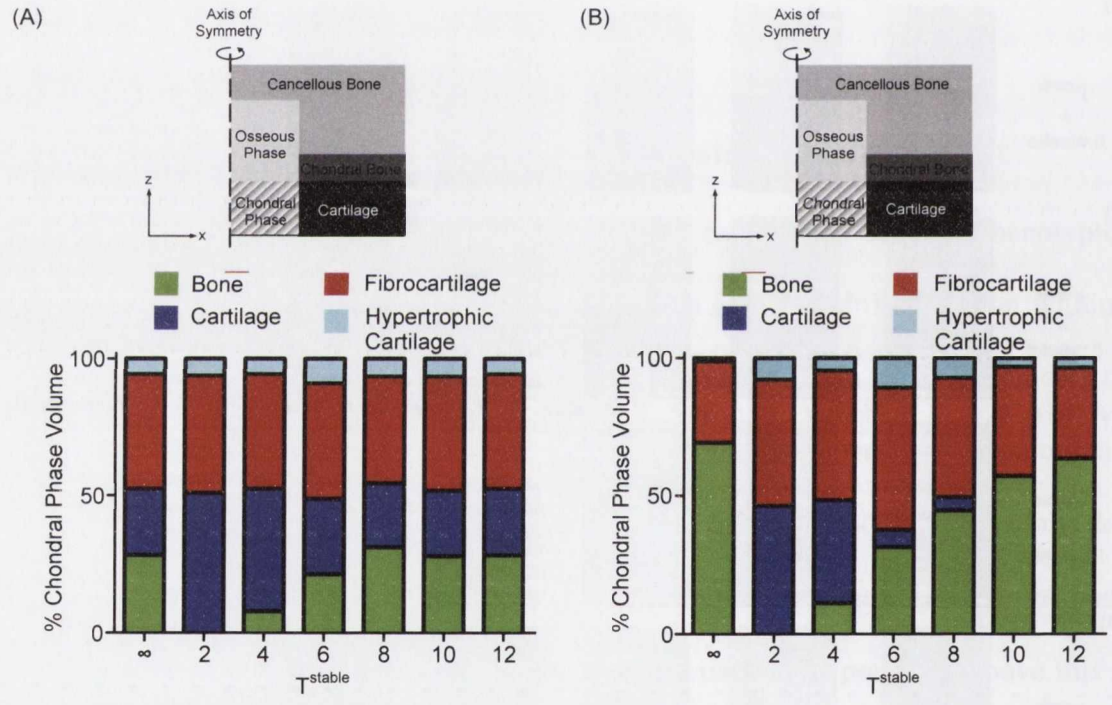

Figure 6-4: The relative volume of the different tissue phenotypes predicted within the chondral phase of the osteochondral defect at the (A) 12 week and (B) 24 week time points for different values of T^{stable}.

6.3.2 Osteochondral defect treated with a bilayer scaffold

The updated tissue differentiation algorithm was then used to predict the pattern of healing within an osteochondral defect treated with the bilayered scaffold (Figure 6-5). For the first 6 weeks of the simulations this parameter had no effect on the predicted pattern of healing. Over this period, cartilage and a small region of fibrocartilage formed in the

chondral layer of the defect while bone formed in the osseous phase. This mineralised tissue formed through a mixture of intramembranous and endochondral ossification. Regarding the latter process, regions of cartilage initially formed in the osseous phase as the invading MSCs differentiated into CCs. This occurred as a result of the low oxygen environment which was present in the core of the bilayer scaffold at the early stages of the simulations. This was eventually converted to bone, however, as blood vessels grew further into the osseous phase as the simulation continued.

From week 12 onwards, the parameter T^{stable} began to have an effect on the predicted pattern of healing. Similar to the models of the spontaneous repair process, this parameter affected the quantity of stable cartilage which was predicted in the chondral phase of the defect by weeks 12 and 24 (Figure 6-5B & C). In the simulation where T^{stable} = 8 weeks the subchondral plate had become plane with the native bone by week 12. By the end of the simulation, only a small portion of this tissue had advanced into the chondral phase, the majority of which was stable cartilage. Conversely, in the simulations where either T^{stable} = 10 weeks or T^{stable} = 12 weeks, mineralised tissue had begun to form in the chondral phase of the defect by week 12. At this point the advance of the bone front had stopped and there was very little difference in the spatial pattern of bone predicted at 12 weeks and the pattern predicted at 24 weeks. Over this period the presence of the subchondral plate in the chondral phase increased the magnitude of the local strains at the surface of the defect, this in turn resulted in an increase in the quantity of fibrocartilage present in the subchondral phase.

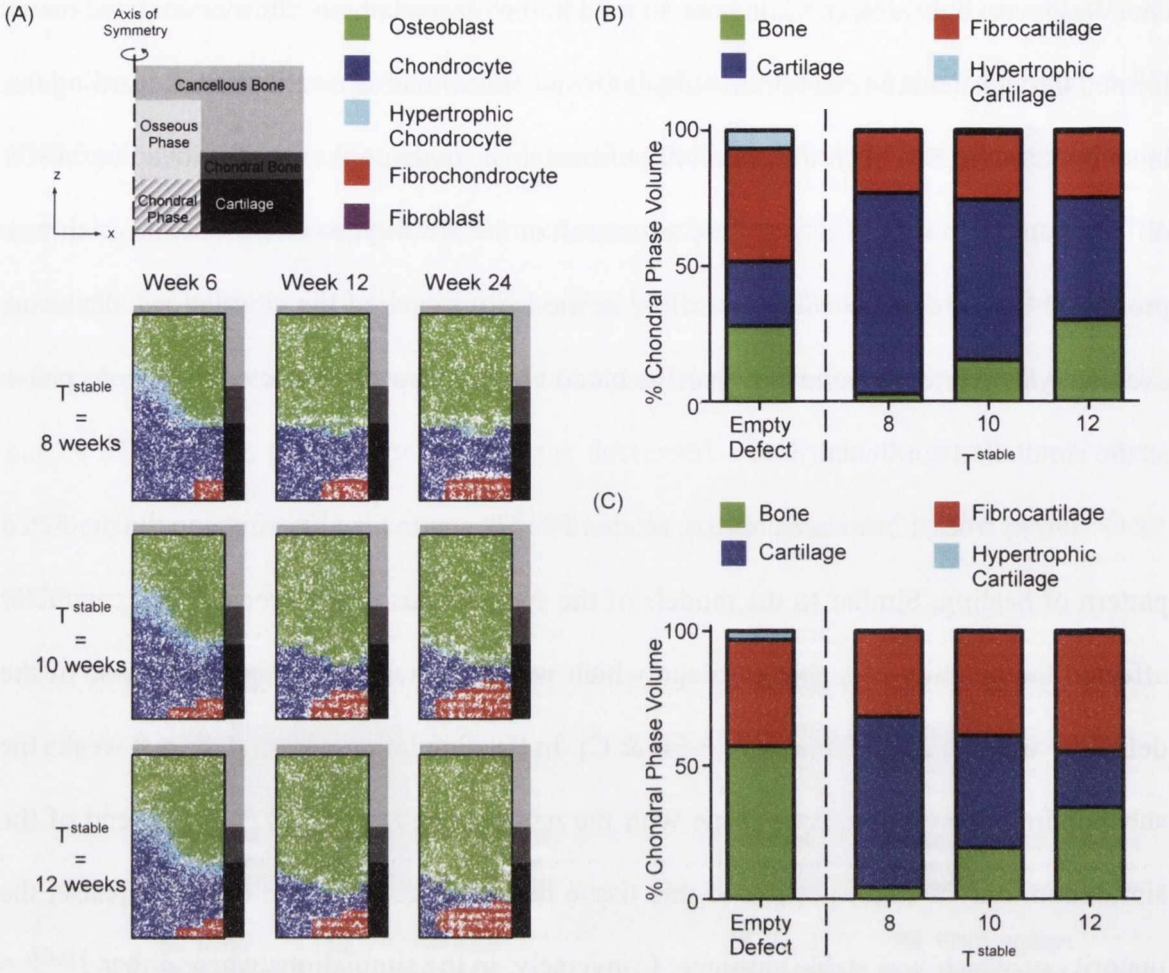

Figure 6-5: Results of the simulations of an osteochondral defect treated with the bilayer scaffold developed by Da et al. [58]. (A) Model predictions of cell differentiation for different values of the parameter T^{stable}. (B; C)The relative volume of the different tissue phenotypes predicted within the chondral phase of an empty defect (T^{stable} = 10 weeks) and a defect treated with the bilayer scaffold at the (B) 12 week and (C) 24 week time points for different values of T^{stable}.

6.3.3 Osteochondral defect treated with a trilayer scaffold

The developed models of an osteochondral defect treated with the trilayer scaffold all followed the same general pattern of repair (Figure 6-6). In the same way as predicted in the bilayer scaffold simulations, bone formed in the osseous region through a combination of intramembranous and endochondral ossification. At the same time, cartilage formed in the chondral layer of the scaffold. As the models progressed blood vessel growth was restricted to the osseous phase by the compact layer (Figure 6-7). In all simulations, by week 12 this layer had been absorbed and the osseous phase was composed entirely of bone while the chondral phase was composed mainly of stable cartilage with a small region of

fibrocartilage present at the surface of the defect. At this time point the parameter $T^{degrade}$ had a small effect on the volume of bone predicted in the chondral phase (Figure 6-6B).

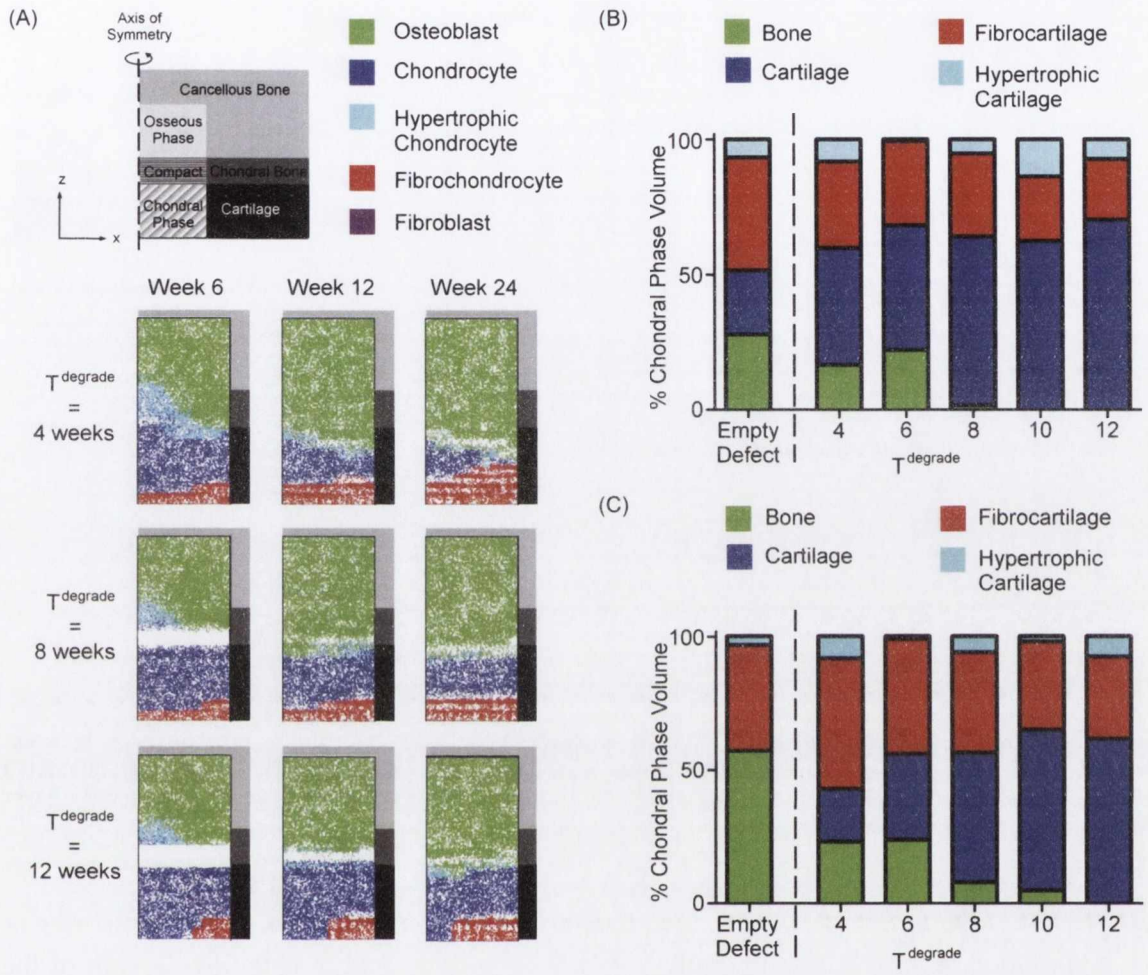

Figure 6-6: Results of the simulations of an osteochondral defect treated with the trilayer scaffold developed by Da et al. [58]. (A) Model predictions of cell differentiation for different values of the parameter $T^{degrade}$. (B; C)The relative volume of the different tissue phenotypes predicted within the chondral phase of an empty defect (T^{stable} = 10 weeks) and a defect treated with the trilayer scaffold at the (B) 12 week and (C) 24 week time points for different values of $T^{degrade}$.

By week 24, the influence that the parameter $T^{degrade}$ had on the volume of bone in the chondral phase became more apparent (Figure 6-6C). In general, the volume of bone was higher for smaller values of $T^{degrade}$. This resulted in there being a lower quantity of cartilage and, in the case where $T^{degrade}$ = 4 weeks, a higher quantity of fibrocartilage. In the simulations where $T^{degrade}$ < 8 weeks, the pattern of healing was similar to the pattern predicted in the bilayer simulations. Conversely, in the simulations where $T^{degrade} \geq 8$ weeks, the models predicted that there was a higher quantity of stable cartilage and a lower quantity

of fibrocartilage compared to the equivalent bilayer simulation. Finally, in the model where $T^{degrade}$ = 12 weeks, no bone was predicted in the chondral phase of the defect.

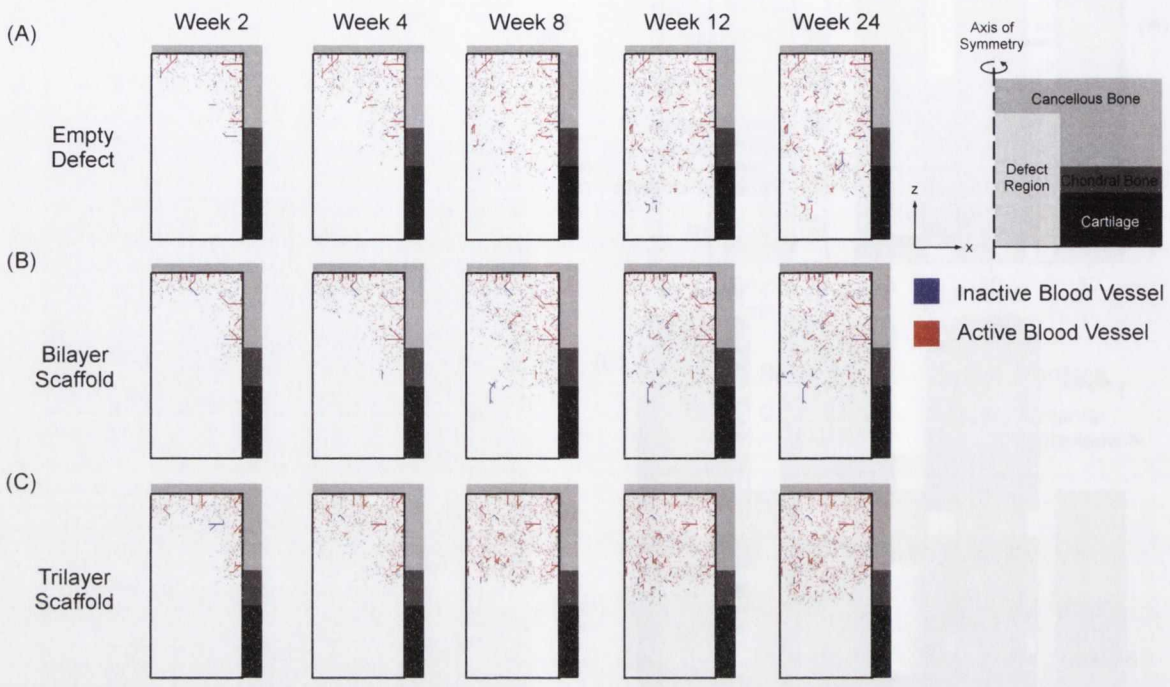

Figure 6-7: Comparison of the predicted spatial pattern of blood vessel formation at different time points between: (A) the model of the spontaneous repair process (B) the model of a defect treated with the bilayer scaffold and (C) the model of the defect treated with the trilayer scaffold. In all simulations T^{stable} = 10 weeks and for the trilayer simulation $T^{degrade}$ = 10 weeks.

6.3.4 Osteochondral defects treated with cell-free scaffolds

In the simulation of an osteochondral defect treated with a cell-free version of the bilayer scaffold, the pattern of healing resembled the pattern predicted by the models of the spontaneous repair process (Figure 6-8). Bone initially formed in the base of the defect by means of intramembranous ossification while a region of cartilage formed above this in the core of the defect. In contrast to the models of the spontaneous repair process, the surface of the defect was relatively devoid of cells for the opening 4 weeks of the simulations. The result of this was that fibrocartilage was not observed in this region until week 8. By this stage, the bone front had begun to advance towards the surface of the defect as the cartilage in the core was ossified via endochondral ossification. Similar to the spontaneous repair process, stable cartilage did not have sufficient time to form before it was vascularised. As

a result, the subchondral plate continued to advance until by week 24 the majority of the chondral region was composed of bone. By this stage, the only other tissue which remained in the defect was fibrocartilage.

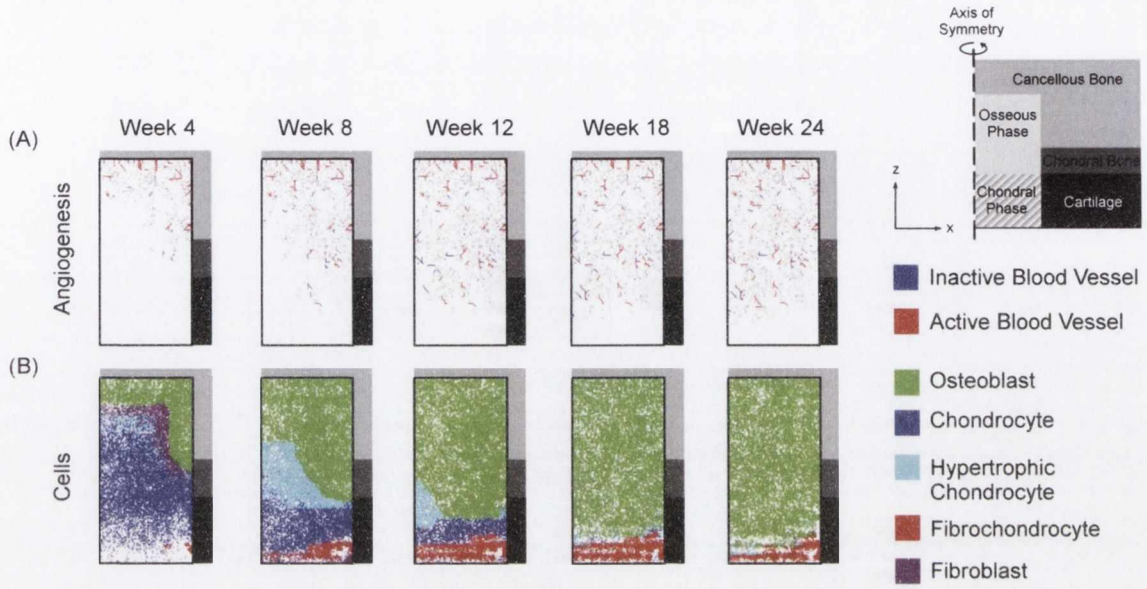

Figure 6-8: Model predictions of the spatial and temporal pattern of (A) angiogenesis and (B) cell differentiation in the simulation of an osteochondral defect treated with a cell-free bilayer scaffold developed by Da et al.[58] .

Stable cartilage also failed to form in the model of an osteochondral defect treated with a cell-free trilayer scaffold (Figure 6-9). For the opening 10 weeks of this simulation, the compact layer confined blood vessel growth, as well as cell proliferation and migration to within the osseous phase of the defect. As a result, this layer was absorbed, and the pattern of healing resembled that of a chondral defect i.e. no healing response was predicted within the chondral phase. Following the absorption of the scaffold, blood vessels began to form within the chondral phase. This in turn allowed cells to proliferate and to form new tissue within this region. For the first few weeks, this new tissue was composed of a mixture of fibrocartilage and fibrous tissue. As the simulation progressed, the fibrous tissue was replaced with bone which in turn caused the upwards migration of the bone plate. Finally, by week 24, the chondral region was composed of a mixture of bone and fibrocartilage similar to the model of the defect treated with a bilayer scaffold.

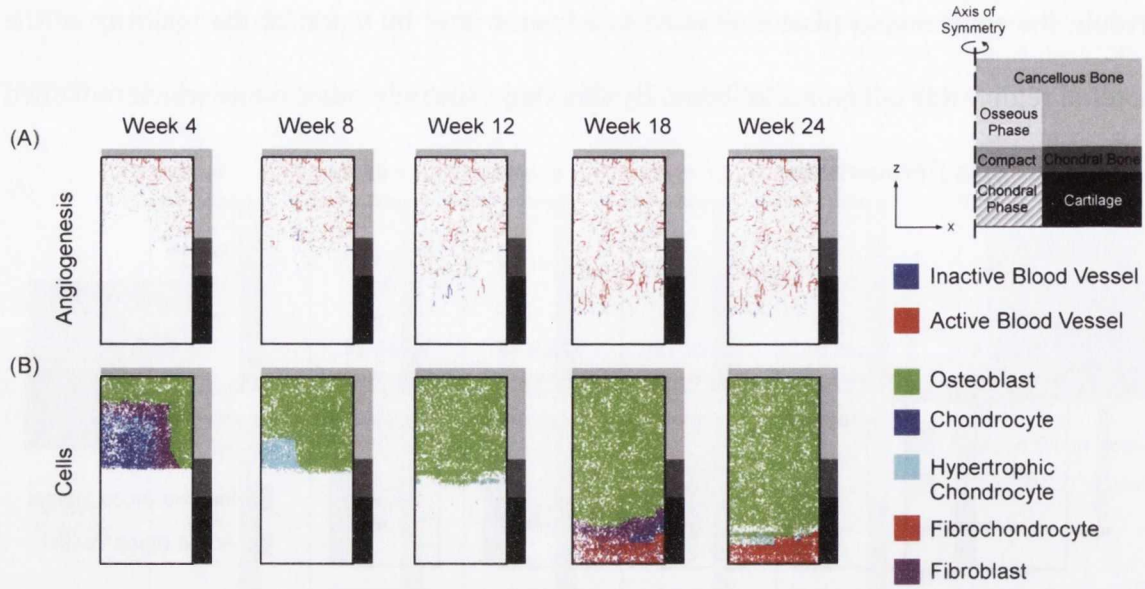

Figure 6-9: Model predictions of the spatial and temporal pattern of (A) angiogenesis and (B) cell differentiation in the simulation of an osteochondral defect treated with a cell-free trilayer scaffold developed by Da et al.[58]

6.4 Discussion

The objective of this study was to develop a computational model in order to better understand the potential mechanisms which may be utilised by TE strategies to regenerate the damaged tissues during osteochondral defect repair. The overall goal was to develop a computational model of the experimental study conducted by Da *et al.* [58] in which the authors reported successful cartilage and bone formation within an osteochondral defect following treatment with a novel multiphasic scaffold. As part of this, a previous *in silico* model of the spontaneous repair process within an osteochondral defect was updated to include a condition whereby mature cartilage was resistant to both terminal differentiation and vascularisation. This rule was developed, based on studies which have shown that chondrocytes release anti-angiogenic factors such as chondromodulin-I [269,270] and troponin-I [271,272]. Furthermore, recent studies have shown that, prior to subcutaneous implantation within a murine model, the time of *in vitro* culture of chondrogenically-primed MSCs affects the cells' ability to resist terminal differentiation and vascularisation. The updated model was tested by using it to predict tissue formation during the spontaneous repair process

within an osteochondral defect. Following this, the model was used to simulate an osteochondral defect treated with different variations of the trilayer scaffold developed by Da *et al.* [58]. By comparing the results of these different simulations we were able to provide support for the study hypothesis that the success of the scaffold can be attributed to the compact layer which provided a functional barrier to angiogenesis until stable cartilage had formed. These results suggest the importance of controlling angiogenesis when designing TE strategies for the treatment of osteochondral defects.

A previously developed model of the spontaneous repair process within an osteochondral defect was used to develop the rules whereby stable cartilage was resistant to hypertrophy and inhibited blood vessel formation. In this previous study, the model was shown to be able to predict the main stages of the repair process which had been experimentally observed in a number of different *in vivo* models. For this reason the temporal and spatial pattern of healing predicted by the updated models were compared to the results of this simulation. The parameter T^{stable} was varied between 2 weeks and 12 weeks with the purpose of examining its influence on the spontaneous repair process. In the simulations where $T^{stable} < 10$ weeks, an altered pattern of healing was observed, whereby stable cartilage was predicted in the chondral phase of the defect by week 24. Conversely, in the simulations where $T^{stable} \geq 10$ weeks, the updated model had very little effect on the predicted course of the spontaneous repair process. Interestingly, Liu *et al.* [265] reported that in order to induce MSCs to form stable cartilage, an *in vitro* culture time of greater than 8 weeks in chondrogenic media was required prior to subcutaneous implantation. For this reason, the models where $T^{stable} \geq 10$ weeks are considered most representative of the actual behaviour which has been experimentally observed during the spontaneous repair process. These results provide support for the hypothesis that, during the spontaneous repair process, stable

cartilage does not have sufficient time to form before it is vascularised and converted to bone via endochondral ossification.

Further support for the updated model was provided by the results of the simulations of an osteochondral defect treated with either the bilayer or trilayer scaffold which was developed by Da *et al.* [58]. Both of these models were able to predict the features of healing which had been experimentally observed within this *in vivo* study. Regarding this, Da *et al.* [58] reported that, by 24 weeks, defects treated with either scaffold had formed cartilage and bone within the chondral and osseous phases respectively. This healing was more robust in the trilayer scaffold group, where thicker cartilage was observed after 24 weeks, a feature which was also observed within the simulations. In addition to this, the authors also reported that the cartilage which formed in the trilayer scaffold group was histologically superior to the cartilage which formed in the bilayer scaffold group. This was also observed in the models in which there was a higher volume of stable cartilage predicted in the trilayer scaffold simulations ($T^{degrade} \geq 8$ weeks), compared to the bilayer scaffold simulations ($T^{stable} \geq 10$ weeks).

The developed models also provide support for the hypothesis that the success of the trilayer scaffold can be attributed to the compact layer which served to confine angiogenesis to the osseous region until stable cartilage had formed in the chondral phase. In the simulations where the parameter $T^{degrade} \leq 6$ weeks, the predicted pattern of healing was similar to the pattern predicted in the bilayer scaffold models i.e. the compact layer had no effect on the pattern of healing. Conversely in the simulations where $T^{degrade} \geq 8$ weeks, a higher quantity of stable cartilage was predicted in the chondral phase of the defect by week 24. These findings suggest that our model hypothesis is correct on the condition that the compact layer remained within the defect for a minimum period of 8 weeks. Although no

study has to our knowledge examined the absorption rate of PLGA/TCP *in vivo*, it has been shown *in vitro* that when left in a buffer saline solution, this material did not start degrading until approximately 8 weeks [275,276]. After this point, the tested material then degraded rapidly and, depending on the culture conditions (static vs. dynamic), took between 4 and 8 weeks to lose between 30 % and 70 % of its mass [275,276]. While it has been shown that scaffold materials tend to have a higher absorption rate *in vivo* [277], these studies suggest that the compact layer is present within the defect for a sufficient amount of time to support our hypothesis.

In the final part of this study, the benefit of the cell seeding and pre-culture steps were shown through the simulation of an osteochondral defect which was treated with cell-free versions of either the bilayer or trilayer scaffolds. In both models the scaffold alone was not sufficient to promote regeneration of the damaged tissues. This is in agreement with TE studies which have examined the efficacy of cell-free scaffolds as a means with which to treat osteochondral defects [278,279]. In the case of the bilayer model, the predicted pattern of healing was similar to that observed in the model of the spontaneous repair process. The scaffold served to improve healing by a small degree as by both week 12 and week 24 there was a lower volume of fibrocartilage predicted in the chondral phase when compared to the quantity predicted in the equivalent model of spontaneous repair (i.e. $T^{stable} = 10$ weeks) (data not shown). This can be attributed to the increased stiffness of the scaffold compared to granulation tissue. In the case of the trilayer model, the scaffold had an adverse effect on healing when compared to spontaneous repair. The reason for this was that the compact layer served to inhibit the passage of cells from the exposed cancellous bone into the chondral phase. The result of this was that, although bone was able to form in the osseous phase of the defect, no tissue formed in the chondral phase for the opening 12 weeks. It is important to note that in the cell-free trilayer model, the elements in the chondral phase were replaced

with granulation tissue as the scaffold was absorbed. In reality however this could not happen because there were no cells present in this phase at the time of absorption. For this reason, the latter 12 weeks of the simulation are not considered representative of what would happen if a cell-free trilayer scaffold was inserted into an osteochondral defect.

There are a number of limitations associated with this study which limit the predictive capacity of the developed models. Firstly, a simplified mechanism was used to model the behaviour whereby stable cartilage inhibits vascularisation by releasing anti-angiogenic factors. While this behaviour is well established experimentally [269–272], in the current approach the release of these factors was not explicitly modelled. Instead it was assumed that angiogenesis was inhibited after blood vessels formed in an element which contained stable cartilage. By not considering the diffusion of these factors mature cartilage was unable to influence the surrounding tissues. This 'crosstalk' has been postulated to affect bone and cartilage formation [280] and is one of the mechanisms by which the compact layer in the trilayer scaffold was hypothesised to improve the regeneration of the damaged tissues [58]. Another simplification was that stable cartilage had a binary effect on angiogenesis i.e. blood vessels either grew at a constant rate or were completely inhibited by stable cartilage. In reality, as a result of the growth factors released by the different cells phenotypes, the rate of blood vessels growth may vary both temporally and spatially within an osteochondral defect. We have previously hypothesised that this may explain the reduced rate of bone formation which was observed during the latter stages of the spontaneous repair process within an osteochondral defect. In the case of this study, this may explain the reduced rate of bone formation experimentally observed at 12 weeks in defects treated with the bilayer scaffold (a feature not predicted within the developed *in silico* models). Regarding this mechanism, anti-angiogenic factors released by the chondrogenically-primed MSCs in the chondral phase may have diffused into the osseous phase of the bilayer scaffold. This would

have resulting in a reduced rate of angiogenesis and in turn, a slower rate of bone formation within this phase.

Despite these limitations the developed model was able to predict the main features of healing experimentally observed in osteochondral defects treated with the scaffolds designed by Da *et al.*[58]. These simulations provided support for our hypothesis that the compact layer improved cartilage formation by confining angiogenesis to the osseous phase of the defect. This in turn provides support for the hypothesis which we suggested in a previous study; that osteochondral defect repair could be enhanced by interventions where angiogenesis is promoted but confined to within the subchondral region of the defect. Regarding the design of such treatments, based on the findings of this study we suggest that, in order to promote the formation of stable cartilage, angiogenesis should be actively confined to the osseous phase for a period of 10 weeks. The length of this time period can be reduced however by pre-culturing MSCs under chondrogenic conditions prior to implantation within the defect.

Chapter 7 Discussion

7.1 Main Findings of this Thesis

The overall objective of this thesis was to develop a computational model of an osteochondral defect in order to better understand the factors which promote the successful regeneration of the spatial configuration of cartilage and bone within such defects. This objective was achieved through a sequence of four successive studies (a list of the parameters used in each study is available in Appendix VI: Model Parameters). As part of our approach, stem cell fate was predicted using the tissue differentiation algorithm developed by Burke *et al.* [33] in which it was assumed that tissue formation was dependent upon the stiffness of the surrounding substrate and the local oxygen tension. A major limitation of this algorithm was that it did not contain rules to explain how the local environment regulates chondrocyte hypertrophy and endochondral ossification. As both of these processes account for a large portion of the osseous tissue which forms within osteochondral defects [4,6,9,187], knowledge of the factors which affect them was required prior to the implementation of the algorithm into the computational framework.

The objective of Chapter 3 was, therefore, to update the algorithm developed by Burke *et al.* [33] to include a series of rules to explain how the local environment directs chondrocyte hypertrophy and endochondral ossification. Based on the findings of a number of *in vitro* studies [37,47–49,232], it was hypothesised that these processes were directed by the local oxygen tension. The tissue differentiation algorithm was then developed and tested by using it to predict cell fate during fracture healing. This regenerative event was chosen as it has been studied extensively and has a repeatable temporal and spatial pattern of tissue formation [26,27,163,218,220]. The rules were first developed by using them to predict the course of healing observed within a murine fracture callus. In this case the developed model was

able to predict the quantity and spatial distribution of tissue phenotypes within the fracture callus at 10 dpf. Following this, the efficacy of the updated model was determined by using it to predict the experimentally observed pattern of tissue formation within a murine fracture callus where the local blood supply had been compromised [175,182]. In this instance, although the developed models were unable to predict the quantity of bone and hypertrophic cartilage experimentally observed at 20 dpf, they predicted the different quantities observed at 10 dpf as well as the general behaviour observed throughout the healing process [175,181]. In addition to providing support for the updated algorithm, this study also highlighted the relationship between angiogenesis and bone formation during tissue regenerative events.

In Chapter 4 the updated model was further tested by using it to predict the course of tissue formation which had been experimentally observed during the spontaneous repair process within an osteochondral defect [4,6–9,57]. In the first part of Chapter 4, a sensitivity analysis was conducted which determined the model parameters which had the greatest effect on the course of healing. The results of this highlighted angiogenesis as one of the main factors influencing cell fate within an osteochondral defect. This provided further support for the finding from Chapter 3; that there was a relationship between blood vessel growth and bone formation. Following this, a parametric study was conducted to better understand the dramatic impact on osteochondral healing reported in experimental studies where the rate of angiogenesis was altered [15,270]. The main finding from chapter 4 was that when angiogenesis was reduced, bone formation was limited to the osseous phase of the defect while the chondral region was composed entirely of cartilage and fibrous tissue. Conversely, in the simulations where angiogenesis was increased, more robust cell proliferation and cartilage formation were observed during the opening stages of the repair process. By the end of these simulations, however, the subchondral plate had advanced above the native tidemark and any of the non-ossified tissue within the chondral phase was

either hypertrophic cartilage or fibrous tissue. These results led us to hypothesise that osteochondral defect repair can be enhanced by interventions where angiogenesis was promoted but confined to within the subchondral region of the defect.

While the model developed in Chapter 4 was able to predict many aspects of the regenerative process, there were two major limitations associated with it. The first of these was that it was unable to account for the experimentally observed role that mechanical loading has been shown to play on the spontaneous repair process [13,14,248,249]. The original tissue differentiation algorithm developed by Burke *et al.* [33] suggested that mechanical strain acts indirectly on cell fate by controlling blood vessel direction. In the developed model, however, there was very little difference between the predicted pattern of healing which was obtained using a model where blood vessel direction was random and the model proposed by Burke *et al.* [33] (where vessel direction was biased towards the minimum principal strain). The other limitation associated with Chapter 4 was that the model was unable to predict the spatial pattern of bone formation which had been experimentally observed by Orth *et al.* [4] during the latter stages of the repair process.

The objective of Chapter 5 was to address these issues by investigating the role of tissue strain in regulating the spatial and temporal patterns of stem cell differentiation during the spontaneous repair process within an osteochondral defect. Motivated by the findings of a number of *in vitro* studies [51,52,251–253,281], the tissue differentiation algorithm was updated to include rules which were based on the hypothesis that chondrocyte hypertrophy and endochondral ossification were inhibited in regions of high strain. The model also considered the hypothesis that excessively high magnitudes of local strain result in the formation of mechanically inferior fibrocartilage. These rules were first developed by simulating stem cell differentiation within an *in vitro* bioreactor system which was capable of controlling the levels of oxygen and mechanical cues within MSC laden hydrogels [51]. Although the final

model was not able predict the spatial arrangement of chondrocyte hypertrophy observed in all of the experimental groups, it was able to predict the general behaviour reported in the *in vitro* study [51]. Following this, the efficacy of the updated model was examined by using it to predict tissue formation during the spontaneous osteochondral defect repair process. As well as correctly predicting the spatial pattern of bone formation, the updated model also provided insights into the role which the mechanical environment plays on the spontaneous repair process; namely that oxygen regulates endochondral ossification during the early phases of repair while mechanics plays a key role in directing this process during the latter stages.

In Chapter 6 the updated tissue differentiation algorithm was used to better understand the potential mechanisms which may be utilised by TE strategies to regenerate the native configuration of cartilage and bone within an osteochondral defect. To this end, based on a number of subcutaneous studies [260,265–267], the model developed in Chapter 5 was updated to include a condition whereby mature cartilage formed when chondrocytes were exposed to low oxygen conditions for a sufficient period of time. This tissue was then resistant to both terminal differentiation and vascularisation. The updated model was developed by using it to predict tissue formation during the spontaneous repair process. It was further hypothesised that, during the spontaneous repair process, the chondral phase of the defect is eventually converted to bone because the neo-cartilage is vascularised before it has time to reach a mature phenotype. The updated model was then used to simulate an osteochondral defect which was treated with different variations of a previously developed tissue-engineered scaffold [58]. By comparing the results of these different simulations we were able to suggest a potential mechanism to explain the success of the scaffold. These findings also provided evidence for the hypothesis presented at the end of Chapter 4; that osteochondral defect repair can be enhanced by interventions where angiogenesis is promoted but confined to the subchondral region of the defect. The findings of this study

also suggested that, in order to promote the formation of stable cartilage within the chondral phase of an osteochondral defect, angiogenesis should be actively confined to the osseous phase for a period of 10 weeks.

7.2 Updated Tissue Differentiation Algorithm

An additional aim of this thesis was to update and refine the tissue differentiation algorithm developed by Burke *et al.* [33] in which it was assumed that MSC fate could be predicted based on the substrate stiffness and the local oxygen tension. Prior to this thesis, corroboration for the algorithm had been provided by using it to predict the temporal and spatial pattern of tissue formation during normal fracture healing [44], fracture healing under accelerated angiogenic conditions [45] and within a mechanically loaded bone chamber [46]. The model was also shown to be more effective at predicting the main features of normal fracture healing than an alternative tissue differentiation algorithm which assumed that cell fate was governed by the octahedral shear strain and the fluid velocity [44].

As part of this thesis the tissue differentiation algorithm was expanded upon to include a number of conditions to explain how the local environment affects the fate of cartilage. In particular, the updated model now accounts for the effects which oxygen tension and the mechanical environment have on the regulation of hypertrophy and the formation of fibrocartilage. Furthermore, the model of angiogenesis was also updated to account for the observed relationship between cartilage tissue and the inhibition of blood vessel growth. While support for this updated model is provided in Chapter 3 – 6, the hypothesis that oxygen tension and mechanical strain regulate chondrocyte fate requires further corroboration in the future.

7.3 General Limitations

In general, all of the studies presented in this thesis were limited by simplifications which were made regarding the algorithms used to predict complex cellular behaviours. This is an issue which is not exclusive to this thesis, but is a problem which is associated with *in silico* studies in general. The main simplification was that, in all of the developed simulations, simplified biphasic material models were used. These ignored the complex viscoelastic nature of the solid constituents of the regenerating soft tissue. While the finite element models employed in this thesis were able to predict the general behaviour within the deforming tissues, the implementation of more complex material models would allow for more accurate predictions.

Another simplification associated with the developed models was that they did not take into account the effect that the local environment has on the cellular production of extra cellular matrix (ECM). In all of the models it was assumed that once a cell had committed to a particular phenotype it automatically started synthesising ECM, independent of the local environment. The result of this was that, while the developed models were able to correctly determine the lineage commitment of the cells, they were unable to determine whether the differentiated cells were provided with the appropriate stimuli to regenerate the native tissue. This is most pertinent in the models examining the regeneration of articular cartilage as it is known that this tissue has a complex spatial arrangement of different matrix components. In addition to this, it is well established in the literature that the synthesis and organisation of these components is dependent on the external environment [103,282,283]. While future work is required to address this limitation, the current model provides an appropriate framework upon which to implement such a feature. This would greatly improve the predictive capacity of the model as, to our knowledge, no current tissue differentiation algorithm within the literature has been extended to include this relationship.

7.4 Summary

Despite these limitations, in this thesis we developed a model which predicted the spatial pattern of tissue formation during the spontaneous repair process within an osteochondral defect, as well as following the implantation of a TE scaffold within an osteochondral defect. This model improved the understanding of the factors affecting cell fate within such defects as, to our knowledge, only one other *in silico* model has been developed in the same field. While this earlier model examined the influence that the mechanical environment has on the determination of cell fate [209], it did not account for the role that angiogenesis and the corresponding oxygen tension has on this process. In response, the models developed in this thesis provided a better understanding of the relationship between blood vessel growth and tissue formation during regenerative events *in vivo*. As part of this, we developed and provided support for the hypothesis that tissue engineering strategies should actively promote angiogenesis, but confine it to the osseous phase of the defect in order to induce robust bone and cartilage formation.

In addition to this, the studies conducted as part of this thesis built upon the tissue differentiation algorithm developed by Burke *et al.* [33] by extending it to include a series of rules to explain how the local environment affects the fate of cartilage. While future research is required to further corroborate this model, such work will provide an improved understanding which will allow us to exploit the full potential of tissue engineering in the field of regenerative medicine.

Chapter 8 Conclusions and Future Directions

8.1 Conclusions

The primary objective of this thesis was to develop a computational model of MSC differentiation and tissue formation within an osteochondral defect. The purpose of this was to assist in the design of tissue engineering strategies by providing insights into the factors which promote successful regeneration of the native tissues within such defects. Based on the results of this thesis the following conclusions can be drawn:

- A computational model of the spontaneous repair process within an osteochondral defect was developed which predicted the experimentally observed temporal and spatial pattern of tissue formation.
- Support was provided for the hypothesis that limiting blood vessel growth during osteochondral defect repair improves the quality of the repair tissue by inducing a sustained hypoxic environment within the chondral phase.
- Functional loading of an osteochondral defect can assist in the repair process by inhibiting chondrocyte hypertrophy and endochondral ossification.
- Excessive loading of an osteochondral defect is detrimental to the healing process as it leads to the formation of fibrocartilage in place of hyaline cartilage.
- During osteochondral defect repair, MSC-derived chondrocytes require a period of 10 weeks under chondrogenic conditions in order to form stable cartilage which is resistant to vascularisation and chondrocyte hypertrophy.
- During osteochondral defect repair, actively confining angiogenesis to the osseous phase of the defect for a period of 10 weeks promotes the formation of robust bone and cartilage formation in the osseous and chondral phases respectively.

In addition to these findings, a number of other conclusions may be drawn based on the results of the studies conducted as part of this thesis:

- Support was provided for the hypothesis that MSC differentiation is regulated by the substrate stiffness and oxygen availability.
- Support was provided for the hypothesis that chondrocyte hypertrophy and endochondral ossification are regulated by the local oxygen tension and local mechanical environment.
- Support was provided for the updated model of angiogenesis whereby blood vessel formation is inhibited in the presence of mature cartilage.
- Support was provided for the hypothesis that the variations in bone and cartilage formation observed in different experimental models of ischemic fracture healing may be explained by there being different rates of vascular recovery between the different studies.

8.2 Future Directions

The modelling framework developed in this thesis allowed for an improved understanding of the factors which affect osteochondral defect repair. Future work will improve the predictive capacity of this model, and this in turn will allow for its use in the design of more robust strategies for the treatment of these defects. This can be achieved in the following ways:

- In order to further corroborate the tissue differentiation algorithm developed as part of this thesis, the model should be used to predict tissue formation in different bio-regenerative scenarios. Potential scenarios include distraction osteogenesis [284,285] and fracture healing under altered conditions (i.e. increased gap size [286], altered loading conditions [171] and oblique fractures [287]). The

application of the existing model to such regenerative events will provide further insights into its predictive capacity.

- The computational framework can be enhanced to include a more detailed model which describes the relationship between tissue phenotype and blood vessel growth. This could involve explicitly modelling the release and diffusion of anti-angiogenic factors (such as chondromodulin-1) by mature cartilage [269,270] and pro-angiogenic factors (such as VEGF) by hypertrophic cartilage [288,289]. The presence of these factors could then influence the blood vessel growth rate or the blood vessel directionality.
- The predictive capacity of the finite element models can be improved by including more complex material models into the computational framework. In particular, multiphasic material models which explicitly model the different extra cellular matrix (ECM) components of soft tissue [290–292], will greatly improve the model predictions of the mechanical strain environment. This in turn will allow for further corroboration of the hypothesis developed in this thesis that mechanical strain can inhibit chondrocyte hypertrophy.
    - The implementation of material models which explicitly model the different ECM components will also allow for the development of an algorithm to explain how the local environment regulates the synthesis of these ECM components. In particular, such an algorithm will allow for an understanding of the factors which enable MSC-derived chondrocytes to regenerate the zonal architecture of hyaline cartilage.

Bibliography

1. Prakash, D. & Learmonth, D. Natural progression of osteo-chondral defect in the femoral condyle. *Knee* **9,** 7–10 (2002).
2. Mankin, H. J. The Response of Articular Cartilage to Mechanical Injury. *J. Bone Jt. Surg.* **64-A,** 460–6 (1982).
3. Chu, C. R., Szczodry, M. & Bruno, S. Animal models for cartilage regeneration and repair. *Tissue Eng Part B Rev* **16,** 105–115 (2010).
4. Orth, P. *et al.* Temporal and spatial migration pattern of the subchondral bone plate in a rabbit osteochondral defect model. *Osteoarthr. Cartil.* **20,** 1161–1169 (2012).
5. Jackson, D. W., Lalor, P. A., Aberman, H. M. & Simon, T. M. Spontaneous Repair of Full- Thickness Defects of Articular Cartilage in a Goat Model. *J. Bone Jt. Surg.* **83-A,** 53–64 (2001).
6. Shapiro, F., Koide, S. & Glimcher, M. J. Cell Origin and Differentiation in the Repair of Full-Thickness Defects of Articular Cartilage. *J. Bone Jt. Surg.* **75-A,** 532–53 (1993).
7. Shahgaldi, B. F. Repair of large osteochondral defects : load-bearing and structural properties of osteochondral repair tissue. *Knee* **5,** 111–117 (1998).
8. Gotterbarm, T., Breusch, S. J., Schneider, U. & Jung, M. The minipig model for experimental chondral and osteochondral defect repair in tissue engineering: retrospective analysis of 180 defects. *Lab. Anim.* **42,** 71–82 (2008).
9. Metsaranta, M. *et al.* Evidence for Insufficient Chondrocytic Differentiation During Repair of Full-Thickness Defects of Articular Cartilage. *Matrix Biol.* **15,** 39–47 (1996).
10. Panseri, S. *et al.* Osteochondral tissue engineering approaches for articular cartilage and subchondral bone regeneration. *Knee Surg. Sports Traumatol. Arthrosc.* **20,** 1182–91 (2012).
11. Nukavarapu, S. P. & Dorcemus, D. L. Osteochondral tissue engineering: current strategies and challenges. *Biotechnol. Adv.* **31,** 706–21 (2013).
12. Pittenger, M. F. Multilineage Potential of Adult Human Mesenchymal Stem Cells. *Science (80-.).* **284,** 143–147 (1999).
13. Salter, R. B. *et al.* The Biological Effect of Continuous Passive Motion on the Healing of Full-Thickness Defects in Articular Cartilage. An Experimental Investigation. *J. Bone Jt. Surg.* **62,** 1232–1251 (1980).
14. Kim, H. K., Moran, M. E. & Salter, R. B. The potential for regeneration of articular cartilage in defects created by chondral shaving and subchondral abrasion. An experimental investigation in rabbits. *J. Bone Jt. Surg.* **73,** 1301–1315 (1991).
15. Nagai, T. *et al.* Intravenous administration of anti-vascular endothelial growth factor humanized monoclonal antibody bevacizumab improves articular cartilage repair. *Arthritis Res. Ther.* **12,** R178 (2010).
16. Klinger, P. *et al.* Chondromodulin 1 stabilizes the chondrocyte phenotype and inhibits endochondral ossification of porcine cartilage repair tissue. *Arthritis Rheum.* **63,** 2721–2731 (2011).
17. Isaksson, H. Recent advances in mechanobiological modeling of bone regeneration.

Mech. Res. Commun. **42,** 22–31 (2012).

18. Nowlan, N. C., Murphy, P. & Prendergast, P. J. Mechanobiology of embryonic limb development. *Ann. N. Y. Acad. Sci.* **1101,** 389–411 (2007).
19. Wren, T. a L. A computational model for the adaptation of muscle and tendon length to average muscle length and minimum tendon strain. *J. Biomech.* **36,** 1117–1124 (2003).
20. Pérez, M. a & Prendergast, P. J. Random-walk models of cell dispersal included in mechanobiological simulations of tissue differentiation. *J. Biomech.* **40,** 2244–53 (2007).
21. Burke, D. P. & Kelly, D. J. A mechanobiological model of endothelial cell migration and proliferation. *Comput. Methods Biomech. Biomed. Engin.* **19,** 74 – 83 (2016).
22. Prendergast, P. J., Huiskes, R. & Soballe, K. Biophysical stimuli on cells during tissue differentiation at implant interfaces. *J. Biomech.* **30,** 539–548 (1997).
23. Claes, L. E. *et al.* Effects of mechanical factors on the fracture healing process. *Clin. Orthop. Relat. Res.* S132–47 (1998). at <http://www.ncbi.nlm.nih.gov/pubmed/9917634>
24. Alierta, J. a., Pérez, M. a. & García-Aznar, J. M. An interface finite element model can be used to predict healing outcome of bone fractures. *J. Mech. Behav. Biomed. Mater.* **29,** 328–338 (2014).
25. Carter, D. R., Blenman, P. R. & Beaupré, G. S. Correlations between mechanical stress history and tissue differentiation in initial fracture healing. *J. Orthop. Res.* **6,** 736–748 (1988).
26. Carter, D. R., Beaupre, G., Giori, N. & Helms, J. Mechanobiology of skeletal regeneration. *Clin. Orthop. Relat. Res.* **355 Suppl,** S41–55 (1998).
27. Vetter, a., Witt, F., Sander, O., Duda, G. N. & Weinkamer, R. The spatio-temporal arrangement of different tissues during bone healing as a result of simple mechanobiological rules. *Biomech. Model. Mechanobiol.* **11,** 147–160 (2012).
28. Chen, G. *et al.* Simulation of the nutrient supply in fracture healing. *J. Biomech.* **42,** 2575–83 (2009).
29. Checa, S. & Prendergast, P. J. A mechanobiological model for tissue differentiation that includes angiogenesis: a lattice-based modeling approach. *Ann. Biomed. Eng.* **37,** 129–45 (2009).
30. Carlier, A., Geris, L., Gastel, N. Van, Carmeliet, G. & Oosterwyck, H. Van. Oxygen as a critical determinant of bone fracture healing — A multiscale model. *J. Theor. Biol.* **365,** 247–264 (2015).
31. Geris, L., Sloten, J. Vander & Van Oosterwyck, H. Connecting biology and mechanics in fracture healing: an integrated mathematical modeling framework for the study of nonunions. *Biomech. Model. Mechanobiol.* **9,** 713–24 (2010).
32. Shefelbine, S. J., Augat, P., Claes, L. & Simon, U. Trabecular bone fracture healing simulation with finite element analysis and fuzzy logic. *J. Biomech.* **38,** 2440–50 (2005).
33. Burke, D. P. An investigation into the role of substrate stiffness and oxygen availability in the regulation of stem cell differentiation during tissue regeneration. (Trinity College Dublin, 2013).

34. Engler, A. J., Sen, S., Sweeney, H. L. & Discher, D. E. Matrix elasticity directs stem cell lineage specification. *Cell* **126,** 677–89 (2006).

35. Park, J. S. *et al.* The effect of matrix stiffness on the differentiation of mesenchymal stem cells in response to TGF-β. *Biomaterials* **32,** 3921–30 (2011).

36. Young, D. A., Choi, Y. S., Engler, A. J. & Christman, K. L. Stimulation of adipogenesis of adult adipose-derived stem cells using substrates that mimic the stiffness of adipose tissue. *Biomaterials* **34,** 8581–8 (2013).

37. Sheehy, E. J., Buckley, C. T. & Kelly, D. J. Oxygen tension regulates the osteogenic, chondrogenic and endochondral phenotype of bone marrow derived mesenchymal stem cells. *Biochem. Biophys. Res. Commun.* **417,** 305–10 (2012).

38. Munir, S. *et al.* Hypoxia enhances chondrogenic differentiation of human adipose tissue-derived stromal cells in scaffold-free and scaffold systems. *Cell Tissue Res.* **355,** 89–102 (2014).

39. Markway, B. D. *et al.* Enhanced chondrogenic differentiation of human bone marrow-derived mesenchymal stem cells in low oxygen environment micropellet cultures. *Cell Transplant.* **19,** 29–42 (2010).

40. Wagegg, M. *et al.* Hypoxia promotes osteogenesis but suppresses adipogenesis of human mesenchymal stromal cells in a hypoxia-inducible factor-1 dependent manner. *PLoS One* **7,** e46483 (2012).

41. Boerckel, J. D., Uhrig, B. a, Willett, N. J., Huebsch, N. & Guldberg, R. E. Mechanical regulation of vascular growth and tissue regeneration in vivo. *Proc. Natl. Acad. Sci. U. S. A.* **108,** E674–80 (2011).

42. Krishnan, L. *et al.* Effect of mechanical boundary conditions on orientation of angiogenic microvessels. *Cardiovasc. Res.* **78,** 324–32 (2008).

43. Lienau, J. *et al.* Initial vascularization and tissue differentiation are influenced by fixation stability. *J. Orthop. Res.* **23,** 639–45 (2005).

44. Burke, D. P. & Kelly, D. J. Substrate stiffness and oxygen as regulators of stem cell differentiation during skeletal tissue regeneration: a mechanobiological model. *PLoS One* **7,** e40737 (2012).

45. Burke, D. *et al.* The role of oxygen as a regulator of stem cell fate during fracture repair in TSP2-null mice. *J. Orthop. Res.* **31,** 1585–96 (2013).

46. Burke, D. P., Khayyeri, H. & Kelly, D. J. Substrate stiffness and oxygen availability as regulators of mesenchymal stem cell differentiation within a mechanically loaded bone chamber. *Biomech. Model. Mechanobiol.* (2014). doi:10.1007/s10237-014-0591-7

47. Zhu, M., Feng, Q. & Bian, L. Differential effect of hypoxia on human mesenchymal stem cell chondrogenesis and hypertrophy in hyaluronic acid hydrogels. *Acta Biomater.* **10,** 1333–40 (2014).

48. Gawlitta, D., van Rijen, M. H. P., Schrijver, E. J. M., Alblas, J. & Dhert, W. J. A. Hypoxia Impedes Hypertrophic Chondrogenesis of Human Multipotent Stromal Cells. *Tissue Eng. Part A.* **18,** 1957–1966 (2012).

49. Leijten, J. C. H., Moreira Teixeira, L. S., Landman, E. B. M., van Blitterswijk, C. a & Karperien, M. Hypoxia inhibits hypertrophic differentiation and endochondral ossification in explanted tibiae. *PLoS One* **7,** e49896 (2012).

50. Leijten, J. *et al.* Metabolic programming of mesenchymal stromal cells by oxygen tension directs chondrogenic cell fate. *Proc. Natl. Acad. Sci. U. S. A.* (2014). doi:10.1073/pnas.1410977111

51. Thorpe, S. D., Nagel, T., Carroll, S. F. & Kelly, D. J. Modulating Gradients in Regulatory Signals within Mesenchymal Stem Cell Seeded Hydrogels: A Novel Strategy to Engineer Zonal Articular Cartilage. *PLoS One* **8,** e60764 (2013).

52. Bian, L., Zhai, D. Y., Zhang, E. C., Mauck, R. L. & Burdick, J. a. Dynamic Compressive Loading Enhances Cartilage Matrix Synthesis and Distribution and Suppresses Hypertrophy in hMSC-Laden Hyaluronic Acid Hydrogels. *Tissue Eng. Part A* **18,** 715–724 (2012).

53. Gerber, H.-P. *et al.* VEGF couples hypertrophic cartilage remodeling , ossification and angiogenesis during endochondral bone formation. *Nat. Med.* **5,** 623–628 (1999).

54. Gerber, H. P. & Ferrara, N. Angiogenesis and bone growth. *Trends Cardiovasc. Med.* **10,** 223–228 (2000).

55. Thomopoulos, S. *et al.* Fibrocartilage tissue engineering: the role of the stress environment on cell morphology and matrix expression. *Tissue Eng. Part A* **17,** 1039–1053 (2011).

56. Connelly, J. T., Vanderploeg, E. J., Mouw, J. K., Wilson, C. G. & Levenston, M. E. Tensile loading modulates bone marrow stromal cell differentiation and the development of engineered fibrocartilage constructs. *Tissue Eng. Part A* **16,** 1913–1923 (2010).

57. Qui, Y. S., Shahgaldi, B. F., Revell, W. J. & Heatley, F. W. Observations of subchondral plate advancement during osteochondral repair: A histomorphometric and mechanical study in the rabbit femoral condyle. *Osteoarthr. Cartil.* **11,** 810–820 (2003).

58. Da, H. *et al.* The impact of compact layer in biphasic scaffold on osteochondral tissue engineering. *PLoS One* **8,** e54838 (2013).

59. Friedenstein, A., Gorskaja, J. & Kulagina, N. Fibroblast precursors in normal and irradiated mouse hematopoietic organs. *Exp. Hematol.* **4,** 267–274 (1976).

60. da Silva Meirelles, L., Chagastelles, P. C. & Nardi, N. B. Mesenchymal stem cells reside in virtually all post-natal organs and tissues. *J. Cell Sci.* **119,** 2204–13 (2006).

61. Uccelli, A., Moretta, L. & Pistoia, V. Mesenchymal stem cells in health and disease. *Nat. Rev. Immunol.* **8,** 726–36 (2008).

62. Chamberlain, G., Fox, J., Ashton, B. & Middleton, J. Concise review: mesenchymal stem cells: their phenotype, differentiation capacity, immunological features, and potential for homing. *Stem Cells* **25,** 2739–49 (2007).

63. Steinert, A. F., Rackwitz, L., Gilbert, F., Nöth, U. & Tuan, R. S. Concise review: the clinical application of mesenchymal stem cells for musculoskeletal regeneration: current status and perspectives. *Stem Cells Transl. Med.* **1,** 237–47 (2012).

64. Caplan, A. The Mesengenic Process. *Clin. Plast. Surg.* **21,** 429 – 435 (1994).

65. Pennock, R. *et al.* Human cell dedifferentiation in mesenchymal condensates through controlled autophagy. *Sci. Rep.* **5,** 13113 (2015).

66. Huebsch, N. *et al.* Harnessing traction-mediated manipulation of the cell/matrix interface to control stem-cell fate. *Nat. Mater.* **9,** 518–26 (2010).

67. Guvendiren, M. & Burdick, J. a. Stiffening hydrogels to probe short- and long-term cellular responses to dynamic mechanics. *Nat. Commun.* **3,** 792 (2012).

68. McBeath, R., Pirone, D. M., Nelson, C. M., Bhadriraju, K. & Chen, C. S. Cell shape, cytoskeletal tension, and RhoA regulate stem cell lineage commitment. *Dev. Cell* **6,** 483–95 (2004).

69. Gao, L., McBeath, R. & Chen, C. S. Stem cell shape regulates a chondrogenic versus myogenic fate through Rac1 and N-cadherin. *Stem Cells* **28,** 564–72 (2010).

70. Kelly, D. J. & Jacobs, C. R. The role of mechanical signals in regulating chondrogenesis and osteogenesis of mesenchymal stem cells. *Birth Defects Res.* **90,** 75–85 (2010).

71. DuFort, C. C., Paszek, M. J. & Weaver, V. M. Balancing forces: architectural control of mechanotransduction. *Nat. Rev. Mol. Cell Biol.* **12,** 308–19 (2011).

72. Zhou, S., Cui, Z. & Urban, J. P. G. Factors influencing the oxygen concentration gradient from the synovial surface of articular cartilage to the cartilage-bone interface: a modeling study. *Arthritis Rheum.* **50,** 3915–24 (2004).

73. Malda, J. *et al.* Oxygen gradients in tissue-engineered PEGT/PBT cartilaginous constructs: measurement and modeling. *Biotechnol. Bioeng.* **86,** 9–18 (2004).

74. Oshimori, N. & Fuchs, E. The harmonies played by TGF-β in stem cell biology. *Cell Stem Cell* **11,** 751–64 (2012).

75. Sakaki-Yumoto, M., Katsuno, Y. & Derynck, R. TGF-β family signaling in stem cells. *Biochim. Biophys. Acta* **1830,** 2280–96 (2013).

76. Crane, J. L. & Cao, X. Bone marrow mesenchymal stem cells and TGF-β signaling in bone remodeling. *J. Clin. Invest.* **124,** 466–72 (2014).

77. Caplan, a. I. Mesenchymal Stem Cells: The Past, the Present, the Future. *Cartilage* **1,** 6–9 (2009).

78. Pauwels, F. Grundriß einer Biomechanik der Frakturheilung. *34th Kongress der Dtsch. Orthopädischen Gesellschaft, Ferdinand Enke Verlag, Stuttgart* 62–108 (1941).

79. Pauwels, F. A new theory on the influence of mechanical stimuli on the differentiation of supporting tissue. The tenth contribution to the functional anatomy and causal morphology of the supporting structure. *Z. Anat. Entwicklungsgesch.* **121,** 478–515 (1960).

80. Li, Y. J. *et al.* Oscillatory fluid flow affects human marrow stromal cell proliferation and differentia tion. *J. Orthop. Res.* **22,** 1283–1289 (2004).

81. Arnsdorf, E. J., Tummala, P., Kwon, R. Y. & Jacobs, C. R. Mechanically induced osteogenic differentiation--the role of RhoA, ROCKII and cytoskeletal dynamics. *J. Cell Sci.* **122,** 546–53 (2009).

82. Arnsdorf, E. J., Tummala, P. & Jacobs, C. R. Non-canonical Wnt signaling and N-cadherin related beta-catenin signaling play a role in mechanically induced osteogenic cell fate. *PLoS One* **4,** e5388 (2009).

83. Baksh, D., Boland, G. M. & Tuan, R. S. Cross-talk between Wnt signaling pathways in human mesenchymal stem cells leads to functional antagonism during osteogenic differentiation. *J. Cell. Biochem.* **101,** 1109–24 (2007).

84. Haudenschild, A. K., Hsieh, A. H., Kapila, S. & Lotz, J. C. Pressure and distortion

regulate human mesenchymal stem cell gene expression. *Ann. Biomed. Eng.* **37,** 492–502 (2009).

85. Sumanasinghe, R., Bernacki, S. & Loboa, E. Osteogenic Differentiation of Human Mesenchymal Stem Cells in Collagen Matrices: Effect of Uniaxial Cyclic Tensile Strain on Bone Morphogenetic Protein (BMP-2) mRNA Expression. *Tissue Eng.* **12,** 3459 – 3465 (2006).

86. Subramony, S. D. *et al.* The guidance of stem cell differentiation by substrate alignment and mechanical stimulation. *Biomaterials* **34,** 1942–53 (2013).

87. Qiu, Y., Lei, J., Koob, J. K. & Temenoff, J. S. Cyclic tension promotes fibroblastic differentiation of human MSCs cultured on collagen-fibre scaffolds. *J. Tissue Eng. Regen. Med.* (2014).

88. Sen, B. *et al.* Mechanical strain inhibits adipogenesis in mesenchymal stem cells by stimulating a durable beta-catenin signal. *Endocrinology* **149,** 6065–75 (2008).

89. Mouw, J. K., Connelly, J. T., Wilson, C. G., Michael, K. E. & Levenston, M. E. Dynamic compression regulates the expression and synthesis of chondrocyte-specific matrix molecules in bone marrow stromal cells. *Stem Cells* **25,** 655–63 (2007).

90. Bais, M. V *et al.* BMP2 is essential for post natal osteogenesis but not for recruitment of osteogenic stem cells. *Bone* **45,** 254–66 (2009).

91. Koike, M., Shimokawa, H., Kanno, Z., Ohya, K. & Soma, K. Effects of mechanical strain on proliferation and differentiation of bone marrow stromal cell line ST2. *J. Bone Miner. Metab.* **23,** 219–225 (2005).

92. Chen, Y.-J. *et al.* Effects of cyclic mechanical stretching on the mRNA expression of tendon/ligament-related and osteoblast-specific genes in human mesenchymal stem cells. *Connect. Tissue Res.* **49,** 7–14 (2008).

93. Castillo, A. B. & Jacobs, C. R. Mesenchymal stem cell mechanobiology. *Curr. Osteoporos. Rep.* **8,** 98–104 (2010).

94. Takahashi, I. *et al.* Compressive force promotes Sox9 , type II collagen and aggrecan and inhibits IL-1 β expression resulting in chondrogenesis in mouse embryonic limb bud mesenchymal cells. *J. Cell Sci.* **2076,** 2067–2076 (1998).

95. Huang, A. H., Farrell, M. J., Kim, M. & Mauck, R. L. LONG-TERM DYNAMIC LOADING IMPROVES THE MECHANICAL PROPERTIES OF CHONDROGENIC MESENCHYMAL STEM CELL-LADEN HYDROGELS. *Eur. Cells Mater.* **19,** 72 – 85 (2010).

96. Huang, C. Y., Hagar, K. L., Frost, L. E., Sun, Y. & Cheung, H. S. Effects of Cyclic Compressive Loading on Chondrogenesis of Rabbit Bone-Marrow Derived Mesenchymal Stem Cells. *Stem Cells* **22,** 313–323 (2004).

97. Zahedmanesh, H. *et al.* Deciphering mechanical regulation of chondrogenesis in fibrin-polyurethane composite scaffolds enriched with human mesenchymal stem cells; a dual computational and experimental approach. *Tissue Eng. Part A.* **20,** 1197–1212 (2014).

98. Li, Z., Kupcsik, L., Yao, S.-J., Alini, M. & Stoddart, M. J. Mechanical load modulates chondrogenesis of human mesenchymal stem cells through the TGF-beta pathway. *J. Cell. Mol. Med.* **14,** 1338–46 (2010).

99. Wagner, D. R. *et al.* Hydrostatic pressure enhances chondrogenic differentiation of human bone marrow stromal cells in osteochondrogenic medium. *Ann. Biomed. Eng.*

36, 813–20 (2008).

100. Carroll, S. F., Buckley, C. T. & Kelly, D. J. Cyclic hydrostatic pressure promotes a stable cartilage phenotype and enhances the functional development of cartilaginous grafts engineered using multipotent stromal cells isolated from bone marrow and infrapatellar fat pad. *J. Biomech.* **47,** 2115–21 (2014).

101. Wong, M., Siegrist, M. & Goodwin, K. Cyclic tensile strain and cyclic hydrostatic pressure differentially regulate expression of hypertrophic markers in primary chondrocytes. *Bone* **33,** 685–693 (2003).

102. Steward, a J. *et al.* Cell-matrix interactions regulate mesenchymal stem cell response to hydrostatic pressure. *Acta Biomater.* **8,** 2153–9 (2012).

103. Meyer, E. G., Buckley, C. T., Steward, a J. & Kelly, D. J. The effect of cyclic hydrostatic pressure on the functional development of cartilaginous tissues engineered using bone marrow derived mesenchymal stem cells. *J. Mech. Behav. Biomed. Mater.* **4,** 1257–65 (2011).

104. Alenghat, F. J. & Ingber, D. E. Mechanotransduction: all signals point to cytoskeleton, matrix, and integrins. *Sci. STKE* **2002,** pe6 (2002).

105. Ingber, D. E. Cellular mechanotransduction : putting all the pieces together again. *J. Fed. Am. Soc. Exp. Biol.* **20,** 811–827 (2006).

106. Geiger, B., Spatz, J. P. & Bershadsky, A. D. Environmental sensing through focal adhesions. *Nat. Rev. Mol. Cell Biol.* **10,** 21–33 (2009).

107. Donahue, H. J. Gap junctions and biophysical regulation of bone cell differentiation. *Bone* **26,** 417–22 (2000).

108. Batra, N., Kar, R. & Jiang, J. X. Gap junctions and hemichannels in signal transmission, function and development of bone. *Biochim. Biophys. Acta* **1818,** 1909–18 (2012).

109. Muhammad, H., Rais, Y., Miosge, N. & Ornan, E. M. The primary cilium as a dual sensor of mechanochemical signals in chondrocytes. *Cell. Mol. Life Sci.* **69,** 2101–7 (2012).

110. Hoey, D. a, Tormey, S., Ramcharan, S., O'Brien, F. J. & Jacobs, C. R. Primary cilia-mediated mechanotransduction in human mesenchymal stem cells. *Stem Cells* **30,** 2561–70 (2012).

111. Wann, A. K. T. *et al.* Primary cilia mediate mechanotransduction through control of ATP-induced Ca2+ signaling in compressed chondrocytes. *FASEB J.* **26,** 1663–1671 (2012).

112. Kopan, R. & Ilagan, M. X. G. The canonical Notch signaling pathway: unfolding the activation mechanism. *Cell* **137,** 216–33 (2009).

113. Bhadriraju, K. *et al.* Activation of ROCK by RhoA is regulated by cell adhesion, shape, and cytoskeletal tension. *Exp. Cell Res.* **313,** 3616–23 (2007).

114. Parfitt, A. M. Age-related structural changes in trabecular and cortical bone: Cellular mechanisms and biomechanical consequences. *Calcif. Tissue Int.* **36,** S123–S128 (1984).

115. Caplan, a I. Mesenchymal stem cells. *J. Orthop. Res.* **9,** 641–50 (1991).

116. Erickson, G. R. *et al.* Chondrogenic potential of adipose tissue-derived stromal cells in vitro and in vivo. *Biochem. Biophys. Res. Commun.* **290,** 763–9 (2002).

117. Hoben, G. M., Koay, E. J. & Athanasiou, K. a. Fibrochondrogenesis in two embryonic stem cell lines: effects of differentiation timelines. *Stem Cells* **26,** 422–30 (2008).

118. Yin, Z. *et al.* Electrospun scaffolds for multiple tissues regeneration in vivo through topography dependent induction of lineage specific differentiation. *Biomaterials* **44,** 173–185 (2015).

119. Zhang, Z., Messana, J., Hwang, N. S. H. & Elisseeff, J. H. Reorganization of actin filaments enhances chondrogenic differentiation of cells derived from murine embryonic stem cells. *Biochem. Biophys. Res. Commun.* **348,** 421–7 (2006).

120. Discher, D. E., Janmey, P. & Wang, Y.-L. Tissue cells feel and respond to the stiffness of their substrate. *Science* **310,** 1139–43 (2005).

121. Engler, A. J. *et al.* Myotubes differentiate optimally on substrates with tissue-like stiffness: pathological implications for soft or stiff microenvironments. *J. Cell Biol.* **166,** 877–87 (2004).

122. Bershadsky, A. D., Balaban, N. Q. & Geiger, B. Adhesion-dependent cell mechanosensitivity. *Annu. Rev. Cell Dev. Biol.* **19,** 677–95 (2003).

123. Even-Ram, S., Artym, V. & Yamada, K. M. Matrix control of stem cell fate. *Cell* **126,** 645–7 (2006).

124. Pek, Y. S., Wan, A. C. a & Ying, J. Y. The effect of matrix stiffness on mesenchymal stem cell differentiation in a 3D thixotropic gel. *Biomaterials* **31,** 385–91 (2010).

125. Dupont, S. *et al.* Role of YAP/TAZ in mechanotransduction. *Nature* **474,** 179–83 (2011).

126. Chaudhuri, O. *et al.* Substrate stress relaxation regulates cell spreading. *Nat. Commun.* **6,** 1–10 (2015).

127. Valorani, M. G. *et al.* Pre-culturing human adipose tissue mesenchymal stem cells under hypoxia increases their adipogenic and osteogenic differentiation potentials. *Cell Prolif.* **45,** 225–38 (2012).

128. Meyer, E. G., Buckley, C. T., Thorpe, S. D. & Kelly, D. J. Low oxygen tension is a more potent promoter of chondrogenic differentiation than dynamic compression. *J. Biomech.* **43,** 2516–23 (2010).

129. Holzwarth, C. *et al.* Low physiologic oxygen tensions reduce proliferation and differentiation of human multipotent mesenchymal stromal cells. *BMC Cell Biol.* **11,** (2010).

130. Merceron, C. *et al.* Differential effects of hypoxia on osteochondrogenic potential of human adipose-derived stem cells. *Am. J. Physiol. Physiol.* **298,** 355–364 (2010).

131. Malladi, P., Xu, Y., Chiou, M., Giaccia, A. J. & Longaker, M. T. Effect of reduced oxygen tension on chondrogenesis and osteogenesis in adipose-derived mesenchymal cells. *Am. J. Physiol. Cell Physiol.* **290,** C1139–46 (2006).

132. Semenza, G. L. HIF-1: mediator of physiological and pathophysiological responses to hypoxia. *J. Appl. Physiol.* **88,** 1474–1480 (2000).

133. Duval, E. *et al.* Hypoxia-inducible factor 1alpha inhibits the fibroblast-like markers type I and type III collagen during hypoxia-induced chondrocyte redifferentiation: hypoxia not only induces type II collagen and aggrecan, but it also inhibits type I and type III collag. *Arthritis Rheum.* **60,** 3038–48 (2009).

134. Kanichai, M., Ferguson, D., Prendergast, P. J. & Campbell, V. a. Hypoxia promotes

chondrogenesis in rat mesenchymal stem cells: a role for AKT and hypoxia-inducible factor (HIF)-1alpha. *J. Cell. Physiol.* **216,** 708–15 (2008).

135. Schaffer, D. V. Physical and Engineering Principles in Stem Cell Research. *Stem Cell Eng.* 21–43 (2014).
136. Danisovic, L. *et al.* Chondrogenic differentiation of human bone marrow and adipose tissue-derived mesenchymal stem cells. *J. Appl. Biomed.* **5,** 139–150 (2007).
137. Danišovič, L., Varga, I. & Polák, S. Growth factors and chondrogenic differentiation of mesenchymal stem cells. *Tissue Cell* **44,** 69–73 (2012).
138. Tang, Y. *et al.* TGF-beta1-induced migration of bone mesenchymal stem cells couples bone resorption with formation. *Nat. Med.* **15,** 757–65 (2009).
139. Worster, A. A., Nixon, A. J., Brower-Toland, B. D. & Williams, J. Effect of transforming growth factor β1 on chondrogenic differentiation of cultured equine mesenchymal stem cells. *Am. J. Vet. Res.* **61,** 1003–1010 (2000).
140. Havas, V. *et al.* Comparison of chondrogenic differentiation of adipose tissue-derived mesenchymal stem cells with cultured chondrocytes and bone marrow mesenchymal stem cells. *Acta Chir Orthop Traumatol Cech* **78,** 138–144 (2011).
141. Thorpe, S. D. *et al.* The response of bone marrow-derived mesenchymal stem cells to dynamic compression following TGF-beta3 induced chondrogenic differentiation. *Ann. Biomed. Eng.* **38,** 2896–909 (2010).
142. Mohan, N., Nair, P. D. & Tabata, Y. A 3D biodegradable protein based matrix for cartilage tissue engineering and stem cell differentiation to cartilage. *J. Mater. Sci. Mater. Med.* **20 Suppl 1,** S49–60 (2009).
143. Barry, F., Boynton, R. E., Liu, B. & Murphy, J. M. Chondrogenic differentiation of mesenchymal stem cells from bone marrow: differentiation-dependent gene expression of matrix components. *Exp. Cell Res.* **268,** 189–200 (2001).
144. Chen, D., Zhao, M. & Mundy, G. R. Bone morphogenetic proteins. *Growth Factors* **22,** 233–41 (2004).
145. Winnier, G., Blessing, M., Labosky, P. a & Hogan, B. L. Bone morphogenetic protein-4 is required for mesoderm formation and patterning in the mouse. *Genes Dev.* **9,** 2105–2116 (1995).
146. Zhang, H. & Bradley, a. Mice deficient for BMP2 are nonviable and have defects in amnion/chorion and cardiac development. *Development* **122,** 2977–86 (1996).
147. Yoshida, Y. *et al.* Negative Regulation of BMP / Smad Signaling by Tob in Osteoblasts. *Cell* **103,** 1085–1097 (2000).
148. Chang, S. C.-N. *et al.* Ex vivo gene therapy in autologous bone marrow stromal stem cells for tissue-engineered maxillofacial bone regeneration. *Gene Ther.* **10,** 2013–9 (2003).
149. Simmons, D. J. Fracture healing review.pdf. *Clin. Orthop. Relat. Res.* **200,** 100–113 (1985).
150. Marsell, R. & Einhorn, T. a. The biology of fracture healing. *Injury* **42,** 551–5 (2011).
151. Jahagirdar, R. & Scammell, B. E. Principles of fracture healing and disorders of bone union. *Surg.* **27,** 63–69 (2009).
152. Mckibbin, B. The biology of fracture healing in long bones. *J. Bone Jt. Surg.* **60-B,** 150–62 (1978).

153. Isaksson, H., van Donkelaar, C. C., Huiskes, R. & Ito, K. A mechano-regulatory bone-healing model incorporating cell-phenotype specific activity. *J. Theor. Biol.* **252,** 230–46 (2008).

154. Kalfas, I. H. Principles of bone healing. *Neurosurg. Focus* **10,** E1 (2001).

155. Kon, T. *et al.* Expression of Osteoprotegerin, Receptor Activator of NF- KB Ligand (Osteoprotegerin Ligand) and Related. *J. Bon* **16,** 1004–1014 (2001).

156. Wan, C. *et al.* Activation of the hypoxia-inducible factor-1a pathway accelerates bone regeneration. *Proc. Natl. Acad. Sci. U. S. A.* **105,** 686–91 (2008).

157. Nakahara, H. *et al.* Bone and cartilage formation in diffusion chambers by subcultured cells derived from the periosteum. *Bone* **11,** 181–8 (1990).

158. Gerstenfeld, L. C., Cullinane, D. M., Barnes, G. L., Graves, D. T. & Einhorn, T. a. Fracture healing as a post-natal developmental process: molecular, spatial, and temporal aspects of its regulation. *J. Cell. Biochem.* **88,** 873–84 (2003).

159. Granero-Moltó, F. *et al.* Regenerative effects of transplanted mesenchymal stem cells in fracture healing. *Stem Cells* **27,** 1887–98 (2009).

160. Kitaori, T. *et al.* Stromal cell-derived factor 1/CXCR4 signaling is critical for the recruitment of mesenchymal stem cells to the fracture site during skeletal repair in a mouse model. *Arthritis Rheum.* **60,** 813–23 (2009).

161. Frost, H. M. The biology of fracture healing. An overview for clinicians. Part I. *Clin. Orthop. Relat. Res.* **248,** 283–93 (1989).

162. Einhorn, T. A. Enhancement of fracture-healing. *J. Bone Jt. Surg.* **77,** 940–56 (1995).

163. Claes, L. E. & Heigele, C. a. Magnitudes of local stress and strain along bony surfaces predict the course and type of fracture healing. *J. Biomech.* **32,** 255–66 (1999).

164. Mackie, E. J., Ahmed, Y. a, Tatarczuch, L., Chen, K.-S. & Mirams, M. Endochondral ossification: how cartilage is converted into bone in the developing skeleton. *Int. J. Biochem. Cell Biol.* **40,** 46–62 (2008).

165. Kronenberg, H. M. Developmental regulation of the growth plate. *Nature* **423,** 332–6 (2003).

166. Giannoudis, P. V, Einhorn, T. a & Marsh, D. Fracture healing: the diamond concept. *Injury* **38 Suppl 4,** S3–6 (2007).

167. Steiner, M., Claes, L., Ignatius, A., Simon, U. & Wehner, T. Disadvantages of interfragmentary shear on fracture healing--mechanical insights through numerical simulation. *J. Orthop. Res.* **32,** 865–72 (2014).

168. Claes, L. E., Recknagel, S. & Ignatius, A. Fracture healing under healthy and inflammatory conditions. *Nat. Rev. Rheumatol.* **8,** 133–143 (2012).

169. Goodship, A. . & Kenwright, J. The influence of induced micromovement upon the healing of experiemtnal tibial fractures. *J. Bone Jt. Surg.* **67,** 650–655 (1985).

170. Claes, L., Eckert-Hübner, K. & Augat, P. The effect of mechanical stability on local vascularization and tissue differentiation in callus healing. *J. Orthop. Res.* **20,** 1099–105 (2002).

171. Epari, D. R., Schell, H., Bail, H. J. & Duda, G. N. Instability prolongs the chondral phase during bone healing in sheep. *Bone* **38,** 864–70 (2006).

172. Augat, P. *et al.* Shear movement at the fracture site delays healing in a diaphyseal

fracture model. *J. Orthop. Res.* **21,** 1011–7 (2003).

173. Park, S. H., O'Connor, K., McKellop, H. & Sarmiento, a. The influence of active shear or compressive motion on fracture-healing. *J. Bone Joint Surg. Am.* **80,** 868–78 (1998).

174. Epari, D. R., Duda, G. N. & Thompson, M. S. Mechanobiology of bone healing and regeneration: in vivo models. *Proc. Inst. Mech. Eng. Part H* **224,** 1543–53 (2010).

175. Lu, C., Miclau, T., Hu, D., Marcucio, R. S. & Al, L. U. E. T. Ischemia Leads to Delayed Union during Fracture Healing : A Mouse Model. *J. Orthop. Res.* **25,** 51–61 (2007).

176. Cenni, E. ANGIOGENESIS AND BONE REGENERATION. *J. Bone Jt. Surg.* **87-B,** 58 (2005).

177. Hulth, A. & Olerud, S. Early fracture callus in normal and cortisone treated rats. A study by a combination of tetracycline labelling, microangiography and microradiography. *Acta Orthop. Scand.* **34,** 1–23 (1964).

178. Hausman, M. R., Schaffler, M. B. & Majeska, R. J. Prevention of fracture healing in rats by an inhibitor of angiogenesis. *Bone* **29,** 560–4 (2001).

179. Yin, G. *et al.* Impaired angiogenesis during fracture healing in GPCR kinase 2 interacting protein-1 (GIT1) knock out mice. *PLoS One* **9,** e89127 (2014).

180. Murata, K. *et al.* Inhibition of miR-92a Enhances Fracture Healing via Promoting Angiogenesis in a model of Stabilized Fracture in Young Mice. *J. Bone Miner. Res.* **29,** 316–326 (2014).

181. Miedel, E. *et al.* Disruption of thrombospondin-2 accelerates ischemic fracture healing. *J. Orthop. Res.* **31,** 935–43 (2013).

182. Taylor, D. K. *et al.* Thrombospondin-2 Influences the Proportion of Cartilage and Bone During Fracture Healing. *J. Bone Miner. Res.* **24,** 1043–1054 (2009).

183. Wallace, A. L., Draper, E. R. C., Strachan, R. K., Mccarthy, I. D. & Hughes, S. P. F. THE EFFECT OF DEVASCULARISATION UPON EARLY BONE HEALING IN DYNAMIC EXTERNAL FIXATION. *J. Bone Jt. Surg.* **73,** 819–25 (1991).

184. Epari, D. R., Lienau, J., Schell, H., Witt, F. & Duda, G. N. Pressure, oxygen tension and temperature in the periosteal callus during bone healing--an in vivo study in sheep. *Bone* **43,** 734–9 (2008).

185. Lu, C. *et al.* The role of oxygen during fracture healing. *Bone* **52,** 220–9 (2013).

186. Hunziker, E. B. Articular cartilage repair: basic science and clinical progress. A review of the current status and prospects. *Osteoarthritis Cartilage* **10,** 432–63 (2002).

187. DePalma, A. F., McKeever, C. D. & Subin, D. K. Process of Repair of Articular Cartilage Demonstrated by Histology and Autoradiography with Tritiated Thymidine. *Clin. Orthop. Relat. Res.* **48,** 229–42 (1966).

188. Harada, Y., Tomita, N., Nakajima, M., Ikeuchi, K. & Wakitani, S. Effect of low loading and joint immobilization for spontaneous repair of osteochondral defect in the knees of weightless (tail suspension) rats. *J. Orthop. Sci.* **10,** 508–514 (2005).

189. Rautiainen, J. *et al.* Osteochondral Repair: Evaluation with Sweep Imaging with Fourier Transform in an Equine Model. *Radiology* **269,** 113–21 (2013).

190. Convery, R. F., Akeson, W. H. & Keown, G. . The repair of large osteochondral

defects: An experimental study in horses. *Clin. Orthop. Relat. Res.* **82,** 253–262 (1972).

191. Gobbi, A. *et al.* Patellofemoral full-thickness chondral defects treated with second-generation autologous chondrocyte implantation: results at 5 years' follow-up. *Am. J. Sports Med.* **37,** 1083–92 (2009).

192. Kon, E. *et al.* Matrix-assisted autologous chondrocyte transplantation for the repair of cartilage defects of the knee: systematic clinical data review and study quality analysis. *Am. J. Sports Med.* **37 Suppl 1,** 156S–66S (2009).

193. Capito, R. M. & Spector, M. Scaffold-Based Articular Cartilage Repair. *IEEE Eng. Med. Biol. Mag.* **22,** 42–50 (2003).

194. Getgood, a, Brooks, R., Fortier, L. & Rushton, N. Articular cartilage tissue engineering: today's research, tomorrow's practice? *J. Bone Joint Surg. Br.* **91,** 565–76 (2009).

195. Coburn, J. M., Gibson, M., Monagle, S., Patterson, Z. & Elisseeff, J. H. Bioinspired nanofibers support chondrogenesis for articular cartilage repair. *Proc. Natl. Acad. Sci. U. S. A.* **109,** 10012–10017 (2012).

196. Keeney, M. & Pandit, M. The osteochondral junction and its repair via bi-phasic tissue engineering scaffolds. *Tissue Eng. Part B. Rev.* **15,** 55–73 (2009).

197. Deng, T., Jing, L., Pang, J., Liu, B. & Ke, J. Construction of tissue-engineered osteochondral composites and repair of large joint defects in rabbit. *J. Tissue Eng. Regen. Med.* **8,** 546–556 (2012).

198. Shao, X., Goh, J. C. ., Hutmacher, D. W., Lee, E. H. & Zigang, G. Repair of large articular osteochondral defects using hybrid scaffolds and bone marrow derived mesenchymal stem cells in a rabbit model. *Tissue Eng.* **12,** 1539 – 1551 (2006).

199. Angele, P. *et al.* Engineering of Osteochondral Tissue with Bone Marrow Mesenchymal Progenitor Cells in a Derivatized Hyaluronan-Gelatin Composite Sponge. *Tissue Eng.* **5,** 545–553 (1999).

200. Wang, X. *et al.* Growth Factor Gradients via Microsphere Delivery in Biopolymer Scaffolds for Osteochondral Tissue Engineering. *J. Control. Release* **134,** 617–627 (2010).

201. Pei, Y., Fan, J., Zhang, X., Zhang, Z. & Yu, M. Repairing the osteochondral defect in goat with the tissue-engineered osteochondral graft preconstructed in a double-chamber stirring bioreactor. *Biomed Res. Int.* **2014,** 219–203 (2014).

202. Vunjak-Novakovic, G., Meinel, L., Altman, G. & Kaplan, D. Bioreactor cultivation of osteochondral grafts. *Orthod. Craniofac. Res.* **8,** 209–18 (2005).

203. Martin, I., Miot, S., Barbero, A., Jakob, M. & Wendt, D. Osteochondral tissue engineering. *J. Biomech.* **40,** 750–65 (2007).

204. Sakata, R. *et al.* Localization of vascular endothelial growth factor during the early stages of osteochondral regeneration using a bioabsorbable synthetic polymer scaffold. *J. Orthop. Res.* **30,** 252–259 (2012).

205. Jiang, J. *et al.* Bioactive stratified polymer ceramic-hydrogel scaffold for integrative osteochondral repair. *Ann. Biomed. Eng.* **38,** 2183–96 (2010).

206. Connelly, J. T., Wilson, C. G. & Levenston, M. E. Characterization of Proteoglycan Production and Processing by Chondrocytes and BMSCs in Tissue Engineered

Constructs. *Osteoarthritus Cartil.* **16,** 1092–1100 (2008).

207. Csaki, C., Schneider, P. R. a & Shakibaei, M. Mesenchymal stem cells as a potential pool for cartilage tissue engineering. *Ann. Anat.* **190,** 395–412 (2008).

208. Byrne, D. P., Lacroix, D., Planell, J. a, Kelly, D. J. & Prendergast, P. J. Simulation of tissue differentiation in a scaffold as a function of porosity, Young's modulus and dissolution rate: application of mechanobiological models in tissue engineering. *Biomaterials* **28,** 5544–54 (2007).

209. Kelly, D. J. & Prendergast, P. J. Mechano-regulation of stem cell differentiation and tissue regeneration in osteochondral defects. *J. Biomech.* **38,** 1413–22 (2005).

210. Prendergast, P. J. Review Paper Finite element models in tissue mechanics and orthopaedic implant design. *Clin. Biomech.* **12,** 343–366 (1997).

211. van der Meulen, M. C. H. & Huiskes, R. Why mechanobiology? A survey article. *J. Biomech.* **35,** 401–14 (2002).

212. Giori, N. J., Ryd, L. & Carter, D. R. Mechanical influences on tissue differentiation at bone-cement interfaces. *J. Arthroplasty* **10,** 514–22 (1995).

213. Gardner, T. N., Mishra, S. & Marks, L. The role of osteogenic index, octahedral shear stress and dilatational stress in the ossification of a fracture callus. *Med. Eng. Phys.* **26,** 493–501 (2004).

214. Morgan, E. F., Longbaker, M. T. & Carter, D. R. Relationships between tissue dilatation and differentiation in distraction osteogenesis. *Matrix Biol.* **25,** 94–103 (2006).

215. Mow, V. C., Kuei, S. C., Lai, W. M. & C.G., A. Biphasic Creep and Stress Relaxation of Articular Cartilage in Compression: Theory and Experiments. *J. Biomech. Eng.* **102,** 73–84 (1980).

216. Lacroix, D., Prendergast, P. J., Li, G. & Marsh, D. Biomechanical model to simulate tissue differentiation and bone regeneration: application to fracture healing. *Med. Biol. Eng. Comput.* **40,** 14–21 (2002).

217. Lacroix, D. & Prendergast, P. J. A mechano-regulation model for tissue differentiation during fracture healing: analysis of gap size and loading. *J. Biomech.* **35,** 1163–71 (2002).

218. Isaksson, H., van Donkelaar, C. C., Huiskes, R. & Ito, K. Corroboration of mechanoregulatory algorithms for tissue differentiation during fracture healing: Comparison with in vivo results. *J. Orthop. Res.* **24,** 898–907 (2006).

219. Matsumoto, T. *et al.* Mechanical strain regulates endothelial cell patterning in-vitro. *Tissue Eng.* **13,** 207–217 (2007).

220. Vetter, A. *et al.* Temporal tissue patterns in bone healing of sheep. *J. Orthop. Res.* **28,** 1440–7 (2010).

221. Brinker, Mark R., M. & Bailey, Daniel E. Jr, M. Fracture Healing in Tibia Fractures with an Associated Vascular Injury . Fracture Healing in Tibia Fractures with an Associated Vascular Injury Ovid : Fracture Healing in Tibia Fractures with an Associated Vascular Injury . *J. Trauma Inj. Infect. Crit. Care* **42,** 11–19 (1997).

222. Betts, D. C. & MÃller, R. Mechanical Regulation of Bone Regeneration: Theories, Models, and Experiments. *Front. Endocrinol. (Lausanne).* **5,** 1–14 (2014).

223. Prasad, J., Wiater, B. P., Nork, S. E., Bain, S. D. & Gross, T. S. Characterizing gait

induced normal strains in a murine tibia cortical bone defect model. *J. Biomech.* **43,** 2765–70 (2010).

224. Hori, R. Y. & Lewis, J. L. Mechanical properties of the fibrous tissue found at the bone-cement interface following total joint replacement. *J. Biomed. Mater. Res.* **16,** 911–27 (1982).
225. Zhu, W., Chen, J., Cong, Xiangfeng, M. D., Hu, S. & Chen, Xi, P. D. Hypoxia and Serum Deprivation-Induced Apoptosis in Mesenchymal Stem Cells. *Stem Cells* **24,** 416–425 (2006).
226. Appeddu, P. A. & Shur, B. D. Molecular analysis of cell surface fi-1 , 4-galactosyltransferase function during cell migration. *Proc. Natl. Acad. Sci. U. S. A.* **91,** 2095–2099 (1994).
227. Hershey, D. & Karhan, T. Diffusion Coefficients for Oxygen Transport in Whole Blood. *AIChE* **14,** 969–972 (1968).
228. Sengers, B. G., van Donkelaar, C. C., Oomens, C. W. J. & Baaijens, F. P. T. Computational study of culture conditions and nutrient supply in cartilage tissue engineering. *Biotechnol. Prog.* **21,** 1252–61 (2005).
229. Heywood, H. K., Knight, M. M. & Lee, D. a. Both superficial and deep zone articular chondrocyte subpopulations exhibit the Crabtree effect but have different basal oxygen consumption rates. *J. Cell. Physiol.* **223,** 630–9 (2010).
230. Pattappa, G., Heywood, H. K., de Bruijn, J. D. & Lee, D. a. The metabolism of human mesenchymal stem cells during proliferation and differentiation. *J. Cell. Physiol.* **226,** 2562–70 (2011).
231. Cicione, C. *et al.* Effects of severe hypoxia on bone marrow mesenchymal stem cells differentiation potential. *Stem Cells Int.* **2013,** 232896 (2013).
232. Leijten, J. *et al.* Metabolic programming of mesenchymal stromal cells by oxygen tension directs chondrogenic cell fate. *Proc. Natl. Acad. Sci. U. S. A.* **111,** 13954 – 13959 (2014).
233. Bahney, C. *et al.* Transdifferentiation of hypertrophic chondrocytes during endochondral bone repair by activation of pluripotent stem cell programs (216.1). *J. Fed. Am. Soc. Exp. Biol.* **28,** 216.1 (2014).
234. Holden, C. E. . The role of blood supply to soft tissue in the healing of diaphyseal fractures. An experimental study. *J. Bone Jt. Surg. Am.* **54,** 993 – 1000 (1972).
235. Mosheiff, R., Cordey, J., Rahn, B. a, Perren, S. M. & Stein, H. The vascular supply to bone in distraction osteoneogenesis: an experimental study. *J. Bone Joint Surg. Br.* **78,** 497–498 (1996).
236. Brueton, R. N., Brookes, M. & Heatley, F. W. The vascular repair of an experimental osteotomy held in an external fixator. *Clin. Orthop. Relat. Res.* **257,** 286 – 304 (1990).
237. Khayyeri, H., Checa, S., Tägil, M., Aspenberg, P. & Prendergast, P. J. Variability observed in mechano-regulated in vivo tissue differentiation can be explained by variation in cell mechano-sensitivity. *J. Biomech.* **44,** 1051–8 (2011).
238. Menon, P. *et al.* GPCR kinase 2 interacting protein 1 (GIT1) regulates osteoclast function and bone mass. *J. Cell. Physiol.* **225,** 777–785 (2010).
239. Duvall, C. L., Taylor, W. R., Weiss, D. & Guldberg, R. E. Quantitative microcomputed tomography analysis of collateral vessel development after ischemic

injury. *Am. J. Physiol. Heart Circ. Physiol.* **287,** H302–H310 (2004).

240. Cooper, K. L. *et al.* Multiple phases of chondrocyte enlargement underlie differences in skeletal proportions. *Nature* **495,** 375–378 (2013).

241. Keramaris, N. C., Calori, G. M., Nikolaou, V. S., Schemitsch, E. H. & Giannoudis, P. V. Fracture vascularity and bone healing: a systematic review of the role of VEGF. *Injury* **39 Suppl 2,** S45–57 (2008).

242. Wilson, W., Van Rietbergen, B., Van Donkelaar, C. C. & Huiskes, R. Pathways of load-induced cartilage damage causing cartilage degeneration in the knee after meniscectomy. *J. Biomech.* **36,** 845–851 (2003).

243. Vaziri, A., Nayeb-Hashemi, H., Singh, A. & Tafti, B. a. Influence of meniscectomy and meniscus replacement on the stress distribution in human knee joint. *Ann. Biomed. Eng.* **36,** 1335–1344 (2008).

244. Shirazi, R. & Shirazi-Adl, a. Computational biomechanics of articular cartilage of human knee joint: Effect of osteochondral defects. *J. Biomech.* **42,** 2458–2465 (2009).

245. Lund-Olesen, K. Oxygen tension in synovial fluids. *Arthritis Rheum.* **13,** 769–776 (1970).

246. Song, J. Q. *et al.* Effect of treadmill exercise timing on repair of full-thickness defects of articular cartilage by bone-derived mesenchymal stem cells: An experimental investigation in rats. *PLoS One* **9,** 1–10 (2014).

247. Ochi, M., Uchio, Y., Tobita, M. & Kuriwaka, M. Current concepts in tissue engineering technique for repair of cartilage defect. *Artif. Organs* **25,** 172–179 (2001).

248. Chang, N. J. *et al.* The combined effects of continuous passive motion treatment and acellular PLGA implants on osteochondral regeneration in the rabbit. *Biomaterials* **33,** 3153–3163 (2012).

249. Arakaki, K. *et al.* Joint immobilization inhibits spontaneous hyaline cartilage regeneration induced by a novel double-network gel implantation. *J. Mater. Sci. Mater. Med.* **22,** 417–425 (2011).

250. O'Driscoll, S. W., Keeley, F. W. & Salter, R. B. The chondrogenic potential of free autogenous periosteal grafts for biological resurfacing of major full-thickness defects in joint surfaces under the influence of continous passive motion. *J. Bone Jt. Surg.* **68,** 1017–35 (1986).

251. Thorpe, S. D., Buckley, C. T., Steward, A. J. & Kelly, D. J. European Society of Biomechanics S.M. Perren Award 2012: The external mechanical environment can override the influence of local substrate in determining stem cell fate. *J. Biomech.* **45,** 2483–2492 (2012).

252. Mauck, R. L., Byers, B. a., Yuan, X. & Tuan, R. S. Regulation of cartilaginous ECM gene transcription by chondrocytes and MSCs in 3D culture in response to dynamic loading. *Biomech. Model. Mechanobiol.* **6,** 113–125 (2007).

253. Kisiday, J. D., Frisbie, D. D., McIlwraith, C. W. & Grodzinsky, A. J. Dynamic compression stimulates proteoglycan synthesis by mesenchymal stem cells in the absence of chondrogenic cytokines. *Tissue Eng. Part A* **15,** 2817–2824 (2009).

254. Baker, B. M., Shah, R. P., Huang, A. H. & Mauck, R. L. Dynamic tensile loading improves the functional properties of mesenchymal stem cell-laden nanofiber-based fibrocartilage. *Tissue Eng. Part A* **17,** 1445–1455 (2011).

255. Yao, J., Salo, A. D., Barbau-McInnis, M. & Lerner, A. L. Finite Element Modeling of Knee Joint Contact Pressures and Comparison to Magnetic Resonance Imaging of the Loaded Knee. in *ASME International Mechanical Engineering Congress and Exposition* (2003).

256. Orth, P., Cucchiarini, M., Kohn, D. & Madry, H. Alterations of the subchondral bone in osteochondral repair--translational data and clinical evidence. *Eur. Cell. Mater.* **25,** 299–316; discussion 314–6 (2013).

257. Hunziker, E. B. & Driesang, I. M. K. Functional barrier principle for growth-factor-based articular cartilage repair. *Osteoarthr. Cartil.* **11,** 320–327 (2003).

258. Vacanti, J. P. & Langer, R. Tissue engineering: the design and fabrication of living replacement devices for surgical reconstruction and transplantation. *Lancet* **354 Suppl ,** SI32–I34 (1999).

259. Getgood, A. M. J. *et al.* Evaluation of early-stage osteochondral defect repair using a biphasic scaffold based on a collagen-glycosaminoglycan biopolymer in a caprine model. *Knee* **19,** 422–430 (2012).

260. Sheehy, E. J., Vinardell, T., Buckley, C. T. & Kelly, D. J. Engineering osteochondral constructs through spatial regulation of endochondral ossification. *Acta Biomater.* **9,** 5484–5492 (2013).

261. Miot, S. *et al.* Influence of in vitro maturation of engineered cartilage on the outcome of osteochondral repair in a goat model. *Eur. Cells Mater.* **23,** 222–236 (2012).

262. Re'Em, T., Witte, F., Willbold, E., Ruvinov, E. & Cohen, S. Simultaneous regeneration of articular cartilage and subchondral bone induced by spatially presented TGF-beta and BMP-4 in a bilayer affinity binding system. *Acta Biomater.* **8,** 3283–3293 (2012).

263. Dormer, N. H. *et al.* Osteochondral interface regeneration of the rabbit knee with macroscopic gradients of bioactive signals. *J. Biomed. Mater. Res.* **100,** 162 – 170 (2012).

264. Dickhut, A. *et al.* Calcification or dedifferentiation: Requirement to lock mesenchymal stem cells in a desired differentiation stage. *J. Cell. Physiol.* **219,** 219–226 (2009).

265. Liu, K. *et al.* The dependence of in vivo stable ectopic chondrogenesis by human mesenchymal stem cells on chondrogenic differentiation in vitro. *Biomaterials* **29,** 2183–2192 (2008).

266. Pelttari, K. *et al.* Premature induction of hypertrophy during in vitro chondrogenesis of human mesenchymal stem cells correlates with calcification and vascular invasion after ectopic transplantation in SCID mice. *Arthritis Rheum.* **54,** 3254–3266 (2006).

267. Vinardell, T., Sheehy, E. J., Buckley, C. T. & Kelly, D. J. A comparison of the functionality and in vivo phenotypic stability of cartilaginous tissues engineered from different stem cell sources. *Tissue Eng. Part A* **18,** 1161 – 1170 (2012).

268. Hunziker, E. B., Driesang, I. M. K. & Saager, C. Structural barriar principal for growth factor based articular cartilage repair. *Clin. Orthop. Relat. Res.* **391,** S182 – S189 (2001).

269. Shukunami, C. & Hiraki, Y. Role of cartilage derived anti-angiogenic factor, chondromodulin-1 during endochondral bone formation. *Osteoarthr. Cartil.* **9,** S91–S101 (2001).

270. Hayami, T. *et al.* Expression of the cartilage derived anti-angiogenic factor chondromodulin-I decreases in the early stage of experimental osteoarthritis. *J. Rheumatol.* **30,** 2207–2217 (2003).

271. Moses, M. a *et al.* Troponin I is present in human cartilage and inhibits angiogenesis. *Proc. Natl. Acad. Sci. U. S. A.* **96,** 2645–2650 (1999).

272. Kern, B. E., Balcom IV, J. H., Antoniu, B. a., Warshaw, A. L. & Fernández-del Castillo, C. Troponin I peptide (Glu94-Leu123), a cartilage-derived angiogenesis inhibitor: In vitro and in vivo effects on human endothelial cells and on pancreatic cancer. *J. Gastrointest. Surg.* **7,** 961–969 (2003).

273. Wang, C., Meng, G., Zhang, L., Xiong, Z. & Liu, J. Physical properties and biocompatibility of a core-sheath structure composite scaffold for bone tissue engineering in vitro. *J. Biomed. Biotechnol.* **2012,** (2012).

274. Jia, S. *et al.* Oriented cartilage extracellular matrix-derived scaffold for cartilage tissue engineering. *J. Biosci. Bioeng.* **113,** 647–653 (2012).

275. Wu, L. & Ding, J. In vitro degradation of three-dimensional porous poly(D,L-lactide-co-glycolide) scaffolds for tissue engineering. *Biomaterials* **25,** 5821–5830 (2004).

276. Yang, Y. *et al.* In vitro degradation of porous poly(l-lactide-co-glycolide)/β-tricalcium phosphate (PLGA/β-TCP) scaffolds under dynamic and static conditions. *Polym. Degrad. Stab.* **93,** 1838–1845 (2008).

277. Sung, H.-J., Meredith, C., Johnson, C. & Galis, Z. S. The effect of scaffold degradation rate on three-dimensional cell growth and angiogenesis. *Biomaterials* **25,** 5735–5742 (2004).

278. Reyes, R. *et al.* Comparative, osteochondral defect repair: Stem cells versus chondrocytes versus bone morphogenetic protein-2, solely or in combination. *Eur. Cells Mater.* **25,** 351–365 (2012).

279. Dahlin, R. L. *et al.* Articular chondrocytes and mesenchymal stem cells seeded on biodegradable scaffolds for the repair of cartilage in a rat osteochondral defect model. *Biomaterials* **35,** 7460–7469 (2014).

280. Funck-Brentano, T. & Cohen-Solal, M. Crosstalk between cartilage and bone: When bone cytokines matter. *Cytokine Growth Factor Rev.* **22,** 91–97 (2011).

281. Huang, A. H., Farrell, M. J., Kim, M. & Mauck, R. L. Long-term dynamic loading improves the mechanical properties of chondrogenic mesenchymal stem cell-laden hydrogels. *Eur. Cells Mater.* **19,** 72–85 (2010).

282. Nagel, T. & Kelly, D. J. Mechanically induced structural changes during dynamic compression of engineered cartilaginous constructs can potentially explain increases in bulk mechanical properties. *J. R. Soc. Interface* **9,** 777–89 (2012).

283. Murphy, C. L. & Sambanis, a. Effect of oxygen tension on chondrocyte extracellular matrix accumulation. *Connect. Tissue Res.* **42,** 87–96 (2001).

284. Isaksson, H. *et al.* Bone regeneration during distraction osteogenesis: Mechano-regulation by shear strain and fluid velocity. *J. Biomech.* **40,** 2002–2011 (2007).

285. Reina-Romo, E., Gómez-Benito, M. J., García-Aznar, J. M., Domínguez, J. & Doblaré, M. Modeling distraction osteogenesis: Analysis of the distraction rate. *Biomech. Model. Mechanobiol.* **8,** 323–335 (2009).

286. Claes, L., Augat, P., Suger, G. & Wilke, H. J. Influence of size and stability of the

osteotomy gap on the success of fracture healing. *J. Orthop. Res.* **15,** 577–584 (1997).

287. Loboa, E. G., Beaupré, G. S. & Carter, D. R. Mechanobiology of initial pseudoarthrosis formation with oblique fracture. *J. Orthop. Res.* **19,** 1067–1072 (2001).

288. Colnot, C., Thompson, Z., Miclau, T., Werb, Z. & Helms, J. a. Altered fracture repair in the absence of MMP9. *Development* **130,** 4123–4133 (2003).

289. Maes, C. *et al.* Impaired angiogenesis and endochondral bone formation in mice lacking the vascular endothelial growth factor isoforms VEGF164 and VEGF188. *Mech. Dev.* **111,** 61–73 (2002).

290. Nagel, T. & Kelly, D. J. Apparent behaviour of charged and neutral materials with ellipsoidal fibre distributions and cross-validation of finite element implementations. *J. Mech. Behav. Biomed. Mater.* **9,** 122–9 (2012).

291. Wilson, W., Huyghe, J. M. & van Donkelaar, C. C. Depth-dependent compressive equilibrium properties of articular cartilage explained by its composition. *Biomech. Model. Mechanobiol.* **6,** 43–53 (2007).

292. Ateshian, G. a, Ellis, B. J. & Weiss, J. a. Equivalence between short-time biphasic and incompressible elastic material responses. *J. Biomech. Eng.* **129,** 405–12 (2007).

293. Bian, L., Mauck, R. L. & Burdick, J. a. Dynamic Compressive Loading and Crosslinking Density Influence the. in *Proceedings of the ASME 2012 Summer Bioengineering Conference.* 23–24 (2012).

Appendices

Appendix I: Parametric Study: Load Supported by Pin (Chapter 3)

The objective of this section was to examine the effect that the magnitude of the load borne by the pin had on the predicted pattern of tissue formation in the normal fracture healing model. The value of the load applied to the callus was varied between 0.12 N (90 % of the load supported by the pin) and 0.84 N (30 % of the load supported by the pin).

The main finding of this section was that when the magnitude of the load supported by the pin was less than 60 % of the total load, the predicted pattern of bone and cartilage formation resembled that observed in the literature (a bony bridge formed in the external callus) (Figure S1). When the magnitude of the load supported by the pin was greater than 60 % however, the spatial prediction of bone formation differed from the behaviour observed in the literature (bone formed initially from the fractured bone ends). The reason for this behaviour was that, when the load was sufficiently high, the octahedral shear strain was high at the fractured bone ends and thus, blood vessels were initially unable to form in this region. After the callus had bridged however, the octahedral shear strain decreased and blood vessels were able to propagate which in turn allowed bone to form.

Based on these results it can be said that the developed model was able to predict the spatial pattern of fracture healing provided that the intramedullary pin supported less than 60 % of the total load applied to the tibia during gait. It is difficult to determine whether this is correct (the intramedullary pin may support > 60 % of the load in the *in vivo* setting), however, for the developed model this assumption is sufficient as it produces the experimentally observed behaviour. Any errors regarding the predictive capacity of the FE model can be attributed to the simplified material models (all materials were modelled as

biphasic where the solid phase was isotropic elastic), simplified geometry (the tibia was modelled as a cylinder) and the boundary conditions (an axial load was applied at the top of the tibia).

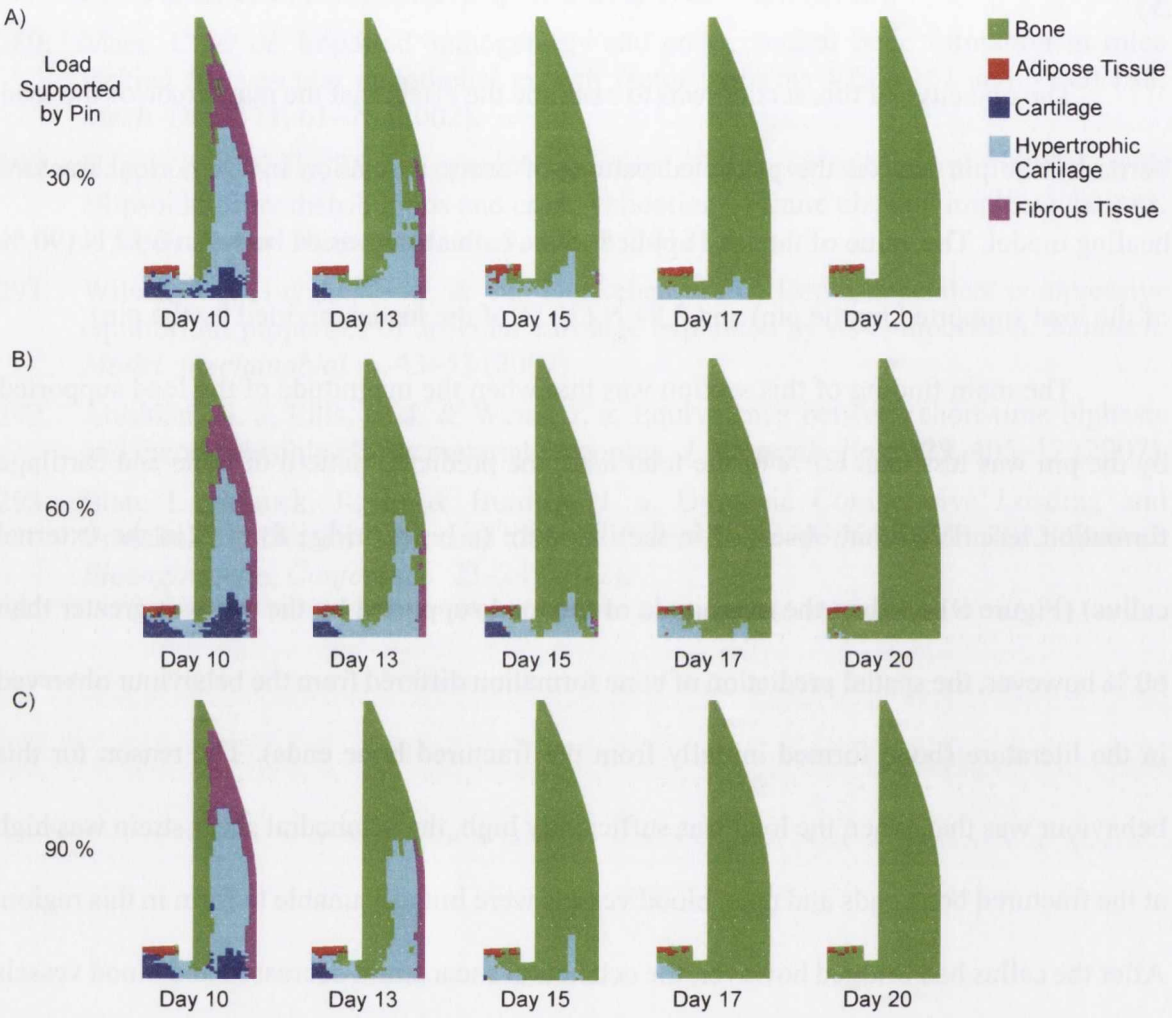

Figure S1: Results of the parametric study examining the effect of loading on the predicted pattern of tissue formation in the model of normal fracture healing. The spatial arrangement of tissue formation was predicted for simulations where the magnitude of the load supported by the pin was varied between (A) 30 %, (B) 60 % and (C) 90 % of the maximum load applied to the tibia during gait (1.2 N).

Appendix II: Analysis of Random Variation in the Baseline Models (Chapter 4)

The objective of this section was to determine whether the predicted results from the baseline model were influenced by the random elements of the model. These random elements included the initial position of the cells and blood vessels, the predicted directions of cell migration and proliferation (random walk) and the determination of blood vessel direction (blood vessels could grow in a random direction). In order to assess whether these elements had an effect on the final predictions of the tissue phenotype, the model was run 3 times using a different random number generator.

The final results show that altering the random number generator had very little effect on the final model predictions of angiogenesis and cell differentiation (Figure S2).

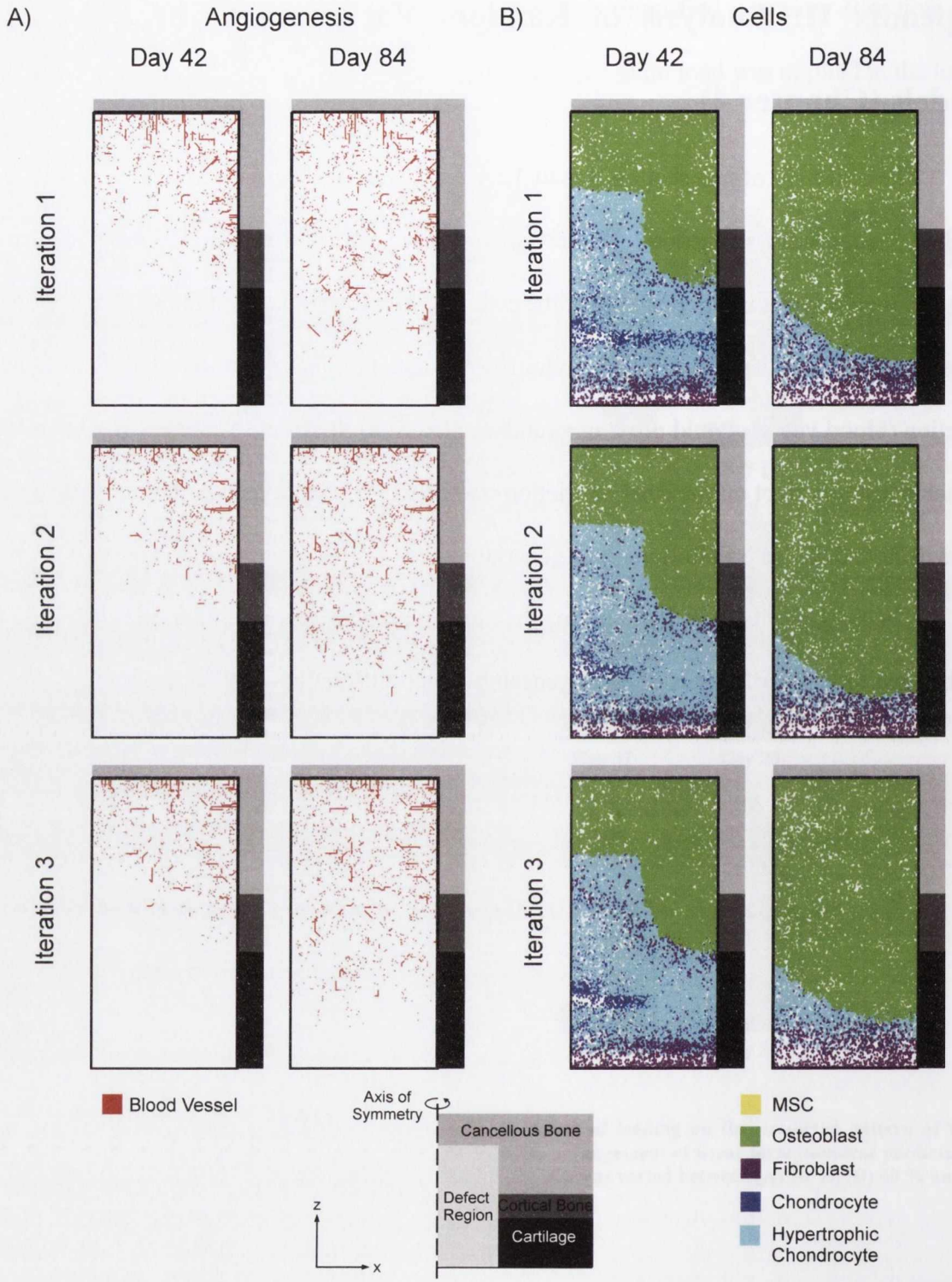

Figure S2: Analysis of the influence that the random elements of the models have on the predicted spatial and temporal patterns of (A) Angiogenesis and (B) Cell differentiation during the spontaneous repair process within an osteochondral defect. For each iteration a different random number generator was used.

Appendix III: Comparison of Angiogenesis Models (Chapter 5)

The objective of this section was to determine whether the model of angiogenesis used in chapter 5 resulted in a different prediction for the spontaneous repair process within an osteochondral defect when compared to the results obtained using the model of angiogenesis from chapter 3. In the model from chapter 3, blood vessels were considered active (capable of providing oxygen) regardless of whether they had formed a closed loop or not (Section 3.2.4). In the model from chapter 5, blood vessels were only considered active once they had formed a closed loop (Section 5.2.4).

The two models were used to predict the course of tissue differentiation at different time points during the spontaneous repair process within an osteochondral defect (Figure S3). Both models predicted that blood vessels had penetrated the same distance within the defect at Days 14, 28, 56, 84 and 126. Despite this, in the updated model, as vessels penetrated further into the chondral phase the number of active vessels began to decrease as the rate of vessel fusion exceeded the rate of vessel branching. The result of this was that, although both models predicted the same pattern of stem cell differentiation up until day 56, beyond this time point the spatial distribution of the cellular phenotypes began to differ between the two models. By day 84 the original model had predicted that all of the remaining cartilage had become hypertrophic while in the updated model a region of cartilage remained above the advancing hypertrophic cartilage. Finally, by day 126, the original model had predicted that the entire defect had become bone while in the updated model a small region of fibrous tissue (< 5 % defect volume) remained at the surface of the defect.

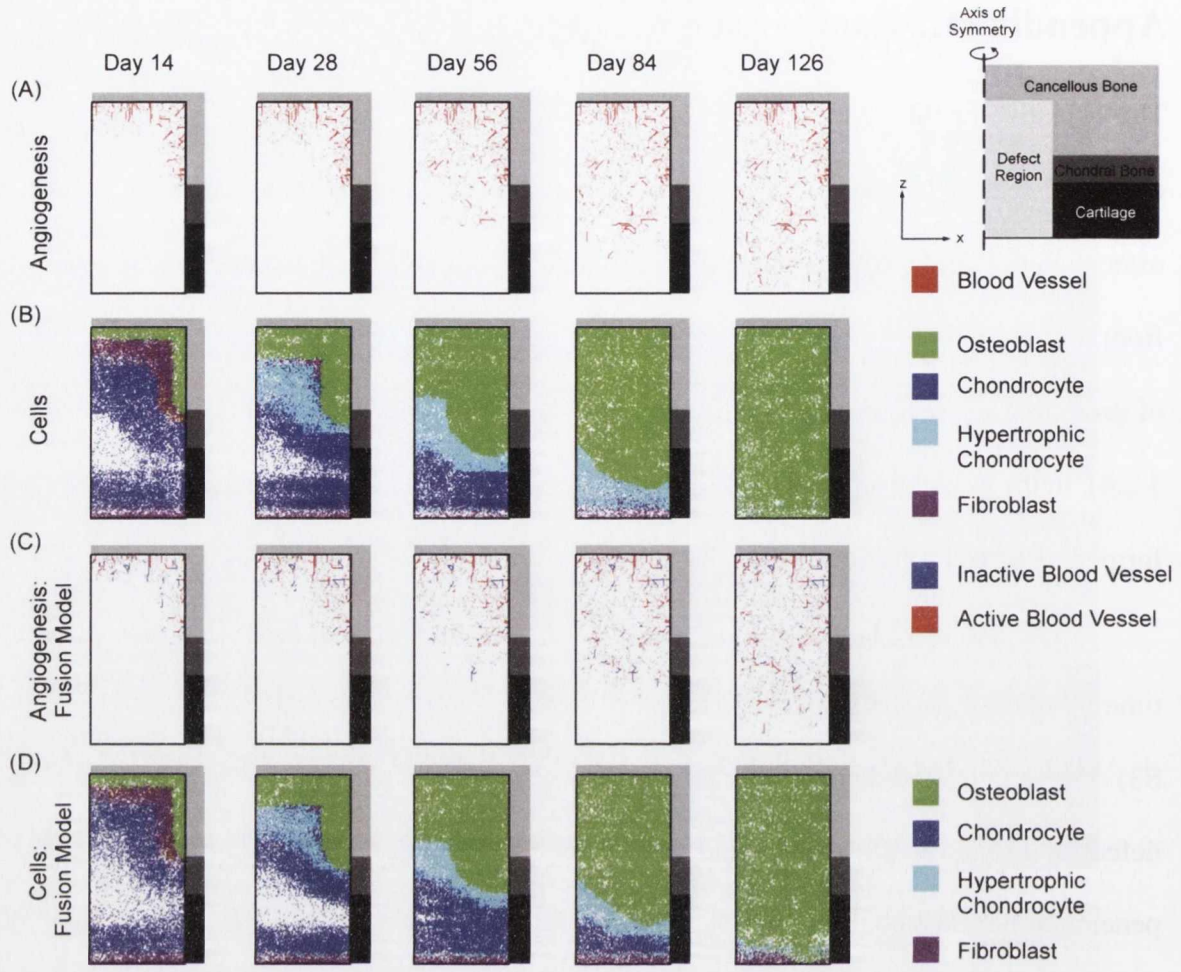

Figure S3: Comparison of the vascular network and course of cell differentiation predicted at Days 14, 28, 56, 84 and 126, obtained using the early model of angiogenesis where all vessels were considered active (A, B), and the updated model of angiogenesis where vessels had to form a closed loop before they were considered active (C, D).

Overall, implementing the fusion model of angiogenesis had a small effect on the predicted course of tissue formation during the spontaneous repair process. Despite this, the fusion model was more physiologically relevant, as it ensured that the advancing bone was preceded by a thin region of hypertrophic cartilage. In contrast to this, in the original model, the preceding front of hypertrophic cartilage was much thicker and resulted in the entire chondral phase becoming hypertrophic prior to the advancement of the subchondral plate beyond the native bone.

Appendix IV: Alternative Rules for Strain Regulation of Hypertrophy (Chapter 5)

Alternative rules for the strain regulation of hypertrophy were examined based on the results of *in vitro* studies which have reported that dynamic compressive loading inhibits chondrocyte hypertrophy [51,293]. In the first of these, hypertrophy was inhibited in regions where the local third principal strain was less than a threshold value ($\varepsilon^{min} < \varepsilon^{hypertrophy}$) (Note: the third principal strain is negative and therefore had to be less than the threshold value). The second rule which was examined was that hypertrophy was inhibited in regions where the hydrostatic strain was negative ($\varepsilon^{hydrostatic} < 0$) and the octahedral shear strain exceeded a threshold value ($\varepsilon^{octahedral} > \varepsilon^{hypertrophy}$).

These rules were tested by using them to model the results of the *in vitro* bioreactor study conducted by Thorpe *et al.* [51] (Figure S4 and Figure S5) and the spontaneous repair process within an osteochondral defect (Figure S6 and Figure S7). For the *in vitro* models the value of third principal strain threshold ($\varepsilon^{hypertrophy}$) was varied between -5 %, -10 % and -15 %. For the osteochondral defect simulations these values were varied between -2.5 %, -5 % and -7.5 %. For the hydrostatic strain rule, in the *in vitro* model the threshold value ($\varepsilon^{hypertrophy}$) was varied between 5 %, 10 % and 15 % while for the osteochondral defect model this parameter was varied between 5 %, 7.5 % and 10 %.

In the simulations of the *in vitro* bioreactor study, in the case of the third principal strain, the general results were similar to those obtained using the octahedral shear strain rule (i.e. for both groups hypertrophy was inhibited below a threshold value) (Figure S4). In the simulations where a combination of the hydrostatic strain and the octahedral shear strain were used to inhibit hypertrophy, the models were unable to predict the experimental behaviour (hypertrophy was not inhibited by DC) (Figure S5). The reason for this was that

the finite element models predicted that the hydrostatic strain was approximately zero due to the assumption that the fluid phase was incompressible.

In the simulations of the spontaneous repair process, in the case where the 3rd principal strain was used, the spatial pattern of bone first adopted a cylindrical shape, then infundibuliform, then planer and finally, a convex arrangement as the subchondral plate advanced towards the surface of the defect (Figure S6). Furthermore, the threshold value ($\varepsilon^{hypertrophy}$) determined the distance that the subchondral plate had advanced by week 18. This behaviour was also observed in the simulations where a combination of the hydrostatic strain and the octahedral shear strain were used to inhibit hypertrophy (Figure S7). In these simulations however, unlike in the models where hypertrophy was inhibited by either the octahedral shear strain or the 3rd principal strain, the advancing bone front adopted a jagged appearance.

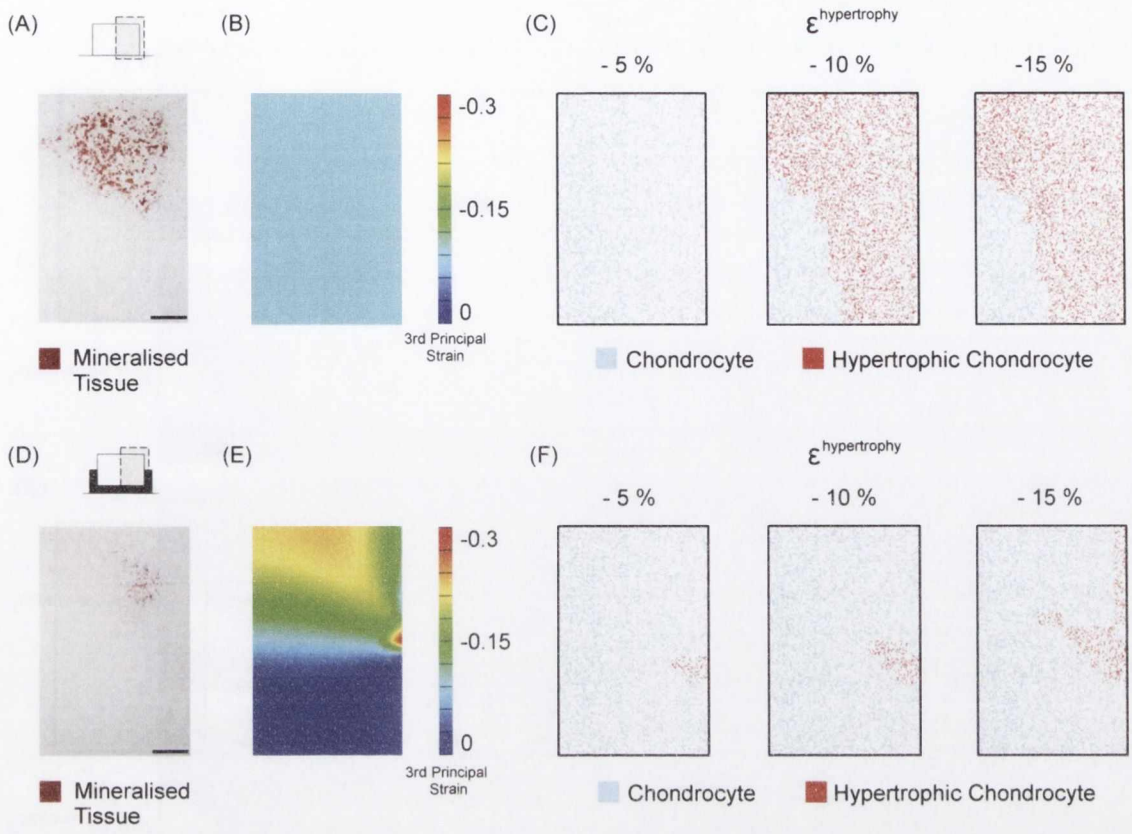

Figure S4: Experimental and simulation results of the In vitro DC groups. Alcian red staining was used to determine the spatial arrangement of calcific deposition (and chondrocyte hypertrophy) in the (A) unconfined and (C) confined groups following 28 days of DC. These were compared to the predicted spatial distribution of chondrocyte hypertrophy from the (B) unconfined and (D) confined in silico models of the DC groups for different values of $\varepsilon^{hypertrophy}$ where hypertrophy was inhibited by the 3rd principal strain.

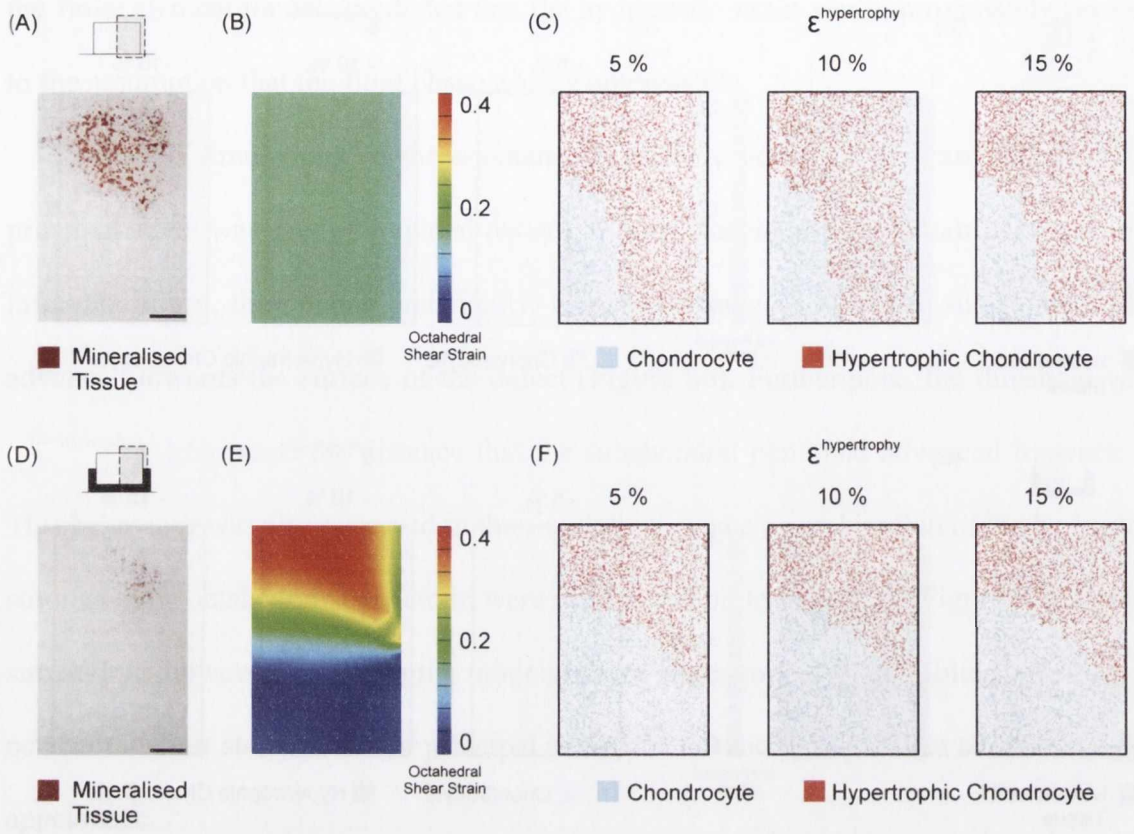

Figure S5: Experimental and simulation results of the In vitro DC groups. Alcian red staining was used to determine the spatial arrangement of calcific deposition (and chondrocyte hypertrophy) in the (A) unconfined and (C) confined groups following 28 days of DC; These were compared to the predicted spatial distribution of chondrocyte hypertrophy from the (B) unconfined and (D) confined in silico models of the DC groups for different values of $\varepsilon^{hypertrophy}$ where hypertrophy was inhibited by a combination of the hydrostatic strain and the octahedral shear strain.

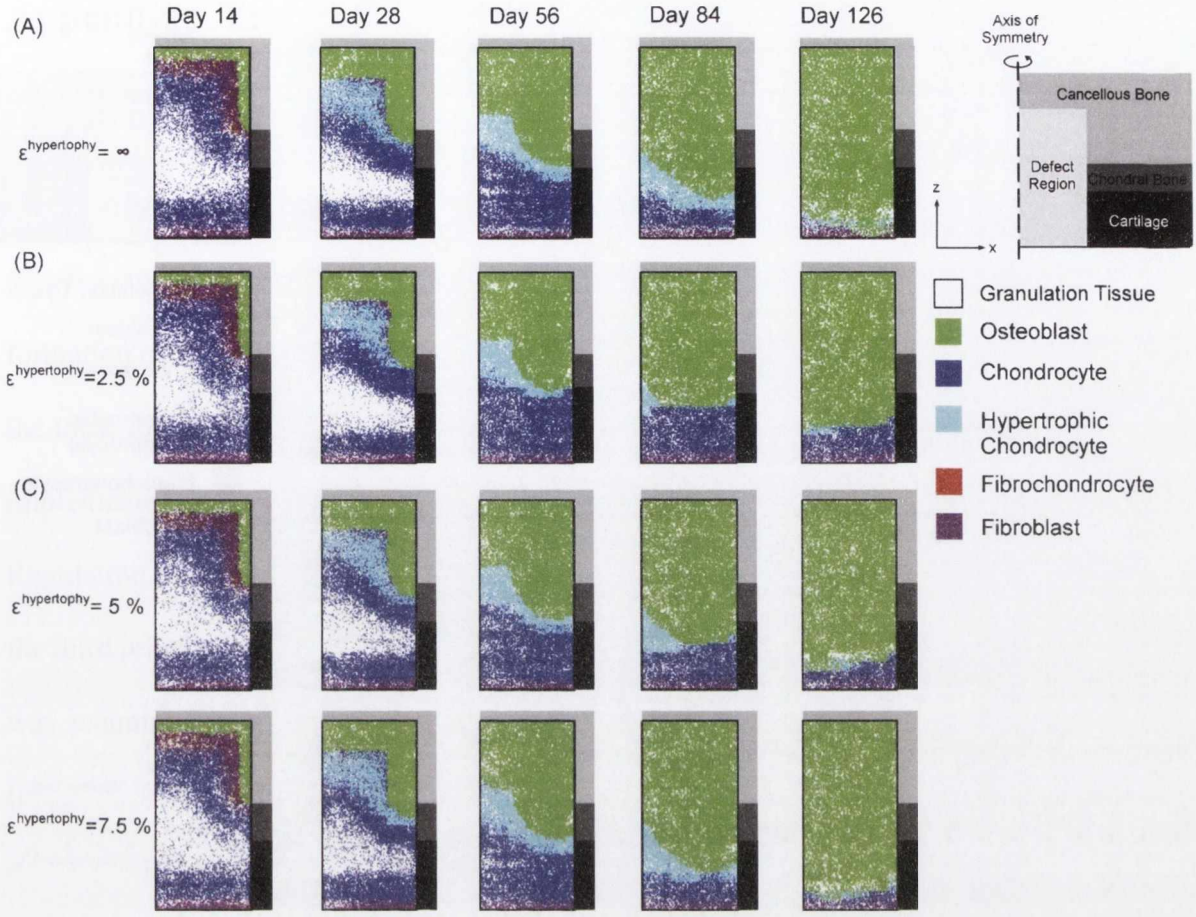

Figure S6: Model predictions of cell differentiation at different times during the spontaneous repair of an osteochondral defect using the: (A) previous tissue differentiation algorithm where chondrocyte hypertrophy was regulated solely by the oxygen tension (B – D) The updated algorithm where chondrocyte hypertrophy was regulated by the oxygen tension and the 3rd principal strain. The parameter $\varepsilon^{hypertrophy}$ was varied between (B) 2.5 %, (C) 5 % and (D) 7.5 %.

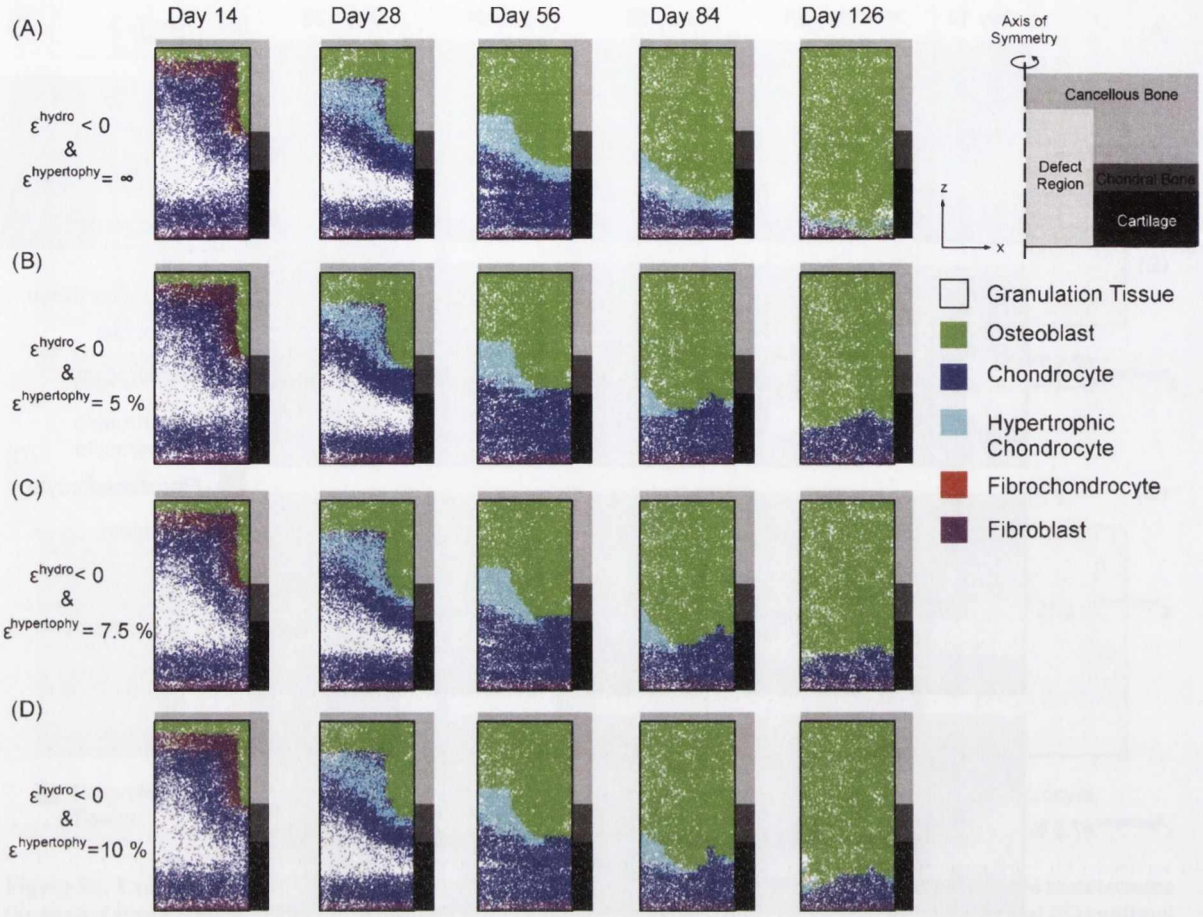

Figure S7: Model predictions of cell differentiation at different times during the spontaneous repair of an osteochondral defect using: (A) our previous tissue differentiation algorithm where chondrocyte hypertrophy was regulated solely by the oxygen tension (B – D) an updated algorithm where chondrocyte hypertrophy was regulated by the oxygen tension, the hydrostatic strain and the octahedral shear strain. The parameter $\varepsilon^{hypertrophy}$ was varied between (B) 5 %, (C) 7.5 % and (D) 10 %.

Appendix V: Alternative Rules for Strain Regulation of Fibrocartilage (Chapter 5)

Alternative rules for the strain regulation of fibrocartilage were examined based on *in vitro* studies which reported that dynamic tensile loading was required to promote the formation of fibrocartilage [55,56]. In the first of these, fibrocartilage formed in regions where the local first principal strain exceeded a threshold value ($\varepsilon^{max} > \varepsilon^{fibrocartilage}$). This rule was implemented in conjunction with the rule from Appendix IV: Alternative Rules for Strain Regulation of Hypertrophy (Chapter 5) where hypertrophy was inhibited in regions where the third principal strain was less than a threshold value ($\varepsilon^{min} < -5$ %). The second rule which was examined was that fibrocartilage formed when the hydrostatic strain was positive ($\varepsilon^{hydrostatic} > 0$) and the octahedral shear strain exceeded a threshold value ($\varepsilon^{octahedral} > \varepsilon^{fibrocartilage}$). This rule was implemented in conjunction with the rule from Appendix IV: Alternative Rules for Strain Regulation of Hypertrophy (Chapter 5) where hypertrophy was inhibited in regions where the hydrostatic strain was negative ($\varepsilon^{hydrostatic} < 0$) and the octahedral shear strain exceeded a threshold value ($\varepsilon^{min} < -5$ %)

These rules were tested by using them to model both the spontaneous repair process within an osteochondral defect (Figure S8 and Figure S9). The value of first principal strain threshold ($\varepsilon^{hypertrophy}$) was varied between 2.5 %, 5 % and 7.5 % while for the hydrostatic strain rule, the threshold value ($\varepsilon^{hypertrophy}$) was varied between 5 %, 7.5 % and 10 %. Both of these conditions produced similar results to the simulations where fibrocartilage was regulated by the octahedral shear strain. When the threshold value was sufficiently low the majority of fibrocartilage formed prior to week 8. When it was sufficiently high, the majority of fibrocartilage formed after the subchondral plate had advanced beyond the native tissue, and when it was too high no fibrocartilage formed within the defect.

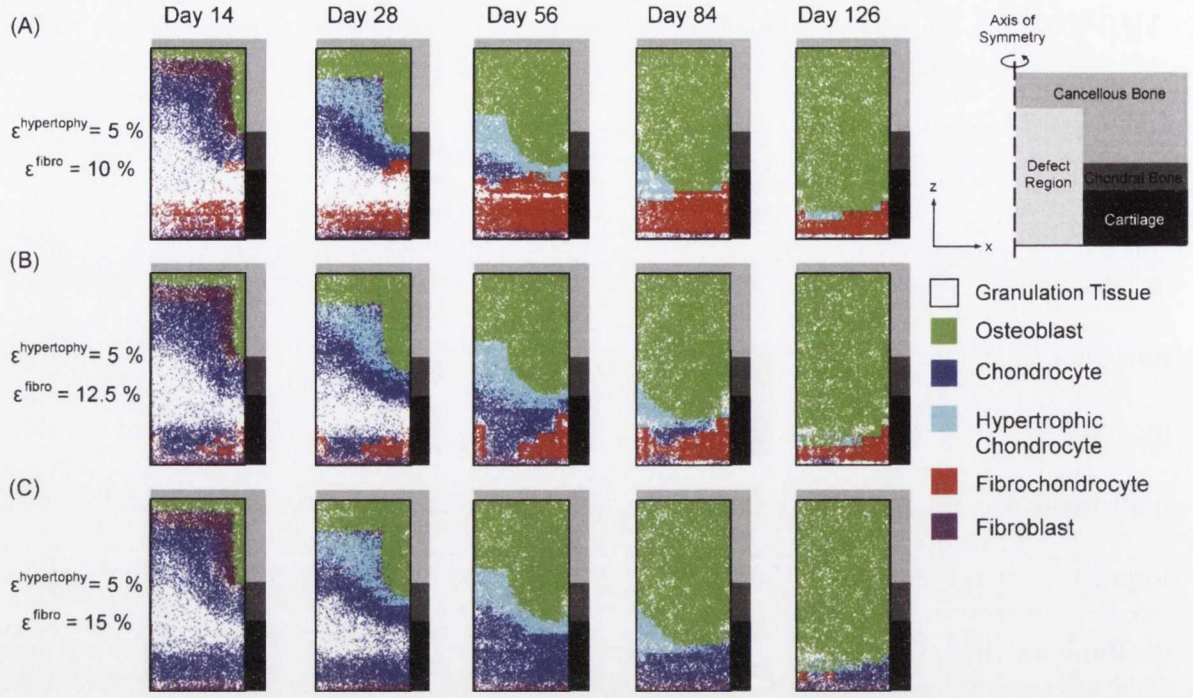

Figure S8: Model predictions of cell differentiation at different times during the spontaneous repair of an osteochondral defect using an updated algorithm where chondrocyte hypertrophy was regulated by the oxygen tension and the octahedral shear strain ($\varepsilon^{hypertrophy}$= 5 %) and fibrocartilage could form based on the local 1st principal strain. The parameter $\varepsilon^{fibrocartilage}$ was varied between (E) 2.5 %, (F) 5 % and (G) 7.5 %.

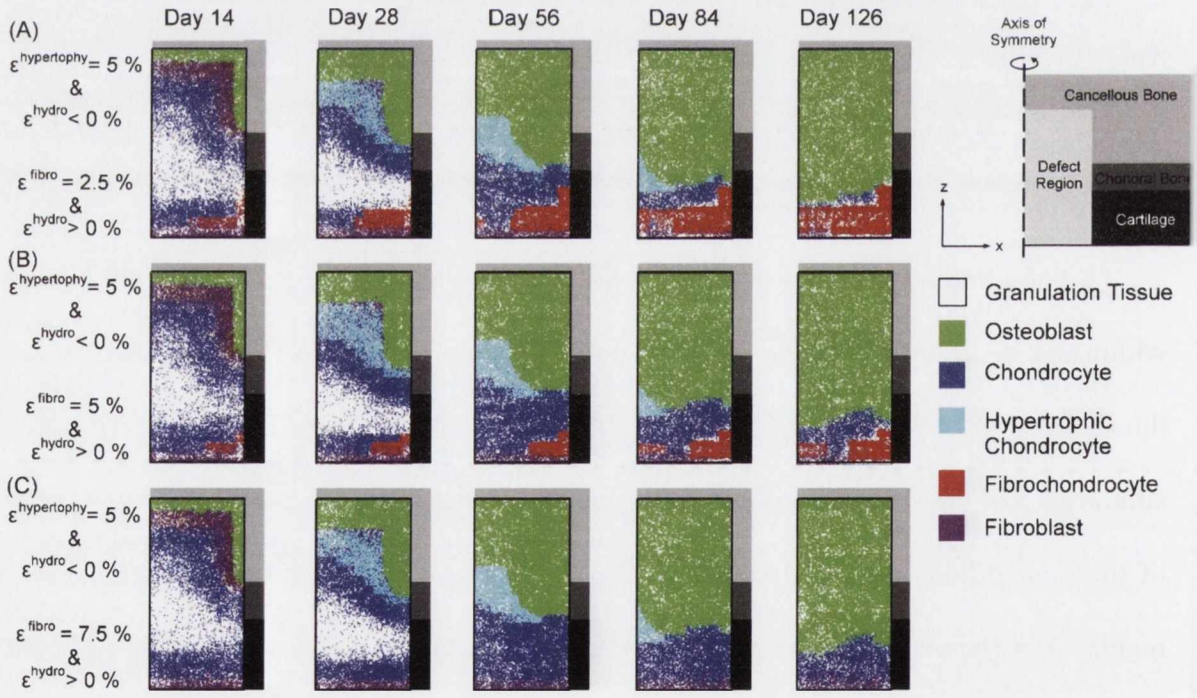

Figure S9: Model predictions of cell differentiation at different times during the spontaneous repair of an osteochondral defect using an updated algorithm where chondrocyte hypertrophy was regulated by the oxygen tension, the hydrostatic strain and the octahedral shear strain ($\varepsilon^{hypertrophy}$= 5 %) and fibrocartilage could form based on a combination of the local hydrostatic strain and octahedral shear strain. The parameter $\varepsilon^{fibrocartilage}$ was varied between (E) 10 %, (F) 12.5 % and (G) 15 %.

Appendix VI: Model Parameters

Table S-1: Parameters used in different finite element models.

Parameter	Description	Chapter 3	Chapter 4	Chapter 5	Chapter 6
$E^{granulation}$	Young's Modulus of granulation tissue [MPa]	1	1	1	1
$E^{fibrous}$	Young's Modulus of fibrous tissue [MPa]	2	2	2	2
$E^{cartilage}$	Young's Modulus of cartilage [MPa]	10	10	10	10
$E^{hypertrophic}$	Young's Modulus of hypertrophic cartilage [MPa]	20	20	20	20
$E^{adipose}$	Young's Modulus of adipose tissue [MPa]	0.1	N/A	N/A	N/A
$E^{bone,immature}$	Young's Modulus of immature bone [MPa]	1000	1000	1000	1000
$E^{bone,mature}$	Young's Modulus of mature bone [MPa]	-	6000	6000	6000
$E^{cortical}$	Young's Modulus of cortical bone [MPa]	20,000	20,000	20,000	20,000
$E^{cell\ death}$	Young's Modulus of necrotic tissue [MPa]	1	1	1	1
$E^{fibrocartilage}$	Young's Modulus of fibrocartilage [MPa]	N/A	N/A	5	5
$v^{granulation}$	Poisson's ratio of granulation tissue	0.167	0.167	0.167	0.167
$v^{fibrous}$	Poisson's ratio of fibrous tissue	0.167	0.167	0.167	0.167
$v^{cartilage}$	Poisson's ratio of cartilage	0.167	0.167	0.167	0.167
$v^{hypertrophic}$	Poisson's ratio of hypertrophic cartilage	0.167	0.167	0.167	0.167
$v^{adipose}$	Poisson's ratio of adipose tissue	0.167	N/A	N/A	N/A
$v^{bone,immature}$	Poisson's ratio of immature bone	0.3	0.3	0.3	0.3
$v^{bone,mature}$	Poisson's ratio of mature bone	N/A	0.3	0.3	0.3
$v^{cortical}$	Poisson's ratio of cortical bone	0.3	0.3	0.3	0.3
$v^{cell\ death}$	Poisson's ratio of necrotic tissue	0.167	0.167	0.167	0.167
$v^{fibrocartilage}$	Poisson's ratio of fibrocartilage	-	-	0.167	0.167
$k^{granulation}$	Permeability coefficient of granulation tissue [mm4/Ns]	0.01	0.01	0.01	0.01
$k^{fibrous}$	Permeability coefficient of fibrous tissue [mm4/Ns]	0.01	0.01	0.01	0.01
$k^{cartilage}$	Permeability coefficient of cartilage [mm4/Ns]	0.001	0.005	0.005	0.005
$k^{hypertrophic}$	Permeability coefficient of hypertrophic cartilage [mm4/Ns]	0.001	0.005	0.005	0.005
$k^{adipose}$	Permeability coefficient of adipose tissue [mm4/Ns]	0.01	N/A	N/A	N/A
$k^{bone,immature}$	Permeability coefficient of immature bone [mm4/Ns]	0.001	0.001	0.001	0.001
$k^{bone,mature}$	Permeability coefficient of mature bone [mm4/Ns]	N/A	0.0037	0.0037	0.0037
$k^{cortical}$	Permeability coefficient of cortical bone [mm^4/Ns]	0.00001	0.00001	0.00001	0.00001
$k^{cell\ death}$	Permeability coefficient of necrotic tissue [mm4/Ns]	0.01	0.01	0.01	0.01
$k^{fibrocartilage}$	Permeability coefficient of fibrocartilage [mm4/Ns]	N/A	N/A	0.01	0.01
φ	Solid volume fraction of all tissue phenotypes	0.2	0.2	0.2	0.2

Table S-2: Parameters used in the different models of angiogenesis.

Parameter	Description	Chapter 3	Chapter 4	Chapter 5	Chapter 6
ε^{angio}	Octahedral shear strain threshold for inhibition of angiogenesis	0.09	0.1	0.1	0.1
L^{min}	Minimum length for branching [mm]	0.2	0.2	0.2	0.2
L^{max}	Maximum length without branching [mm]	0.5	0.5	0.5	0.5
V^{growth}	Blood vessel growth rate [mm day-1]	0.06	0.1	0.1	0.1
P^{prev}	Probability of a vessel continuing in the same direction	0.4	0.4	0.4	0.4
T^{stable}	Time required for mature cartilage inhibition of angiogenesis [days]	N/A	N/A	N/A	70

Table S-3: Parameters used in the different models of cell migration, proliferation and death.

Parameter	Description	Chapter 3	Chapter 4	Chapter 5	Chapter 6
DT^{MSC}	Doubling time for MSCs [days]	0.5	0.5	0.5	0.5
DT^{CC}	Doubling time for chondrocytes [days]	1.5	1.5	1.5	1.5
DT^{OB}	Doubling time for osteoblasts [days]	1	1	1	1
DT^{FB}	Doubling time for fibroblasts [days]	0.5	0.5	0.5	0.5
DT^{HC}	Doubling time for hypertrophic chondrocytes [days]	1.5	1.5	1.5	1.5
DT^{AB}	Doubling time for adipocytes [days]	0.5	N/A	N/A	N/A
DT^{FC}	Doubling time for fibrochondrocytes [days]	N/A	N/A	1000	1000
MR^{MSC}	Migration rate for MSCs [μm hr^{-1}]	26.6	26.6	26.6	26.6
MR^{FB}	Migration rate for fibroblasts [μm hr^{-1}]	26.6	26.6	26.6	26.6
MR^{AB}	Migration rate for adipocytes [μm hr^{-1}]	26.6	N/A	N/A	N/A
$O_2^{prolif,MSC}$	Oxygen limit for inhibition of MSC proliferation [mol mm^{-3}]	5.08 x 10^{-12}	40 x 10^{-12}	40 x 10^{-12}	40 x 10^{-12}
$O_2^{prolif,CC}$	Oxygen limit for inhibition of chondrocyte proliferation [mol mm^{-3}]	5.08 x 10^{-12}	10 x 10^{-12}	10 x 10^{-12}	10 x 10^{-12}
$O_2^{prolif,OB}$	Oxygen limit for inhibition of osteoblast proliferation [mol mm^{-3}]	5.08 x 10^{-12}	80 x 10^{-12}	80 x 10^{-12}	80 x 10^{-12}
$O_2^{prolif,FB}$	Oxygen limit for inhibition of fibroblast proliferation [mol mm^{-3}]	5.08 x 10^{-12}	20 x 10^{-12}	20 x 10^{-12}	20 x 10^{-12}
$O_2^{prolif,HC}$	Oxygen limit for inhibition of hypertrophic chondrocyte proliferation [mol mm^{-3}]	5.08 x 10^{-12}	30 x 10^{-12}	30 x 10^{-12}	30 x 10^{-12}
$O_2^{prolif,FC}$	Oxygen limit for inhibition of fibrochondrocyte proliferation [mol mm^{-3}]	N/A	N/A	10 x 10^{-12}	10 x 10^{-12}
O_2^{death}	Oxygen limit below which cell death is initiated [mol mm^{-3}]	5.08 x 10^{-12}	5.08 x 10^{-12}	5.08 x 10^{-12}	5.08 x 10^{-12}
Death Rate	Proportion of cells which die in an anoxic environment [% cells day^{-1}]	20	20	20	20

Table S-4: Parameters used in the different oxygen transport models.

Parameter	Description	Chapter 3	Chapter 4	Chapter 5	Chapter 6
$Q^{max,MSC}$	Maximum oxygen consumption rate by MSCs [mol $cell^{-1}$ hr^{-1}]	98 x 10^{-15}	93.2 x 10^{-15}	93.2 x 10^{-15}	93.2 x 10^{-15}
$Q^{max,CC}$	Maximum oxygen consumption rate by chondrocytes [mol $cell^{-1}$ hr^{-1}]	33 x 10^{-15}	1.8 x 10^{-15}	1.8 x 10^{-15}	1.8 x 10^{-15}
$Q^{max,OB}$	Maximum oxygen consumption rate by osteoblasts [mol $cell^{-1}$ hr^{-1}]	98 x 10^{-15}	93.2 x 10^{-15}	93.2 x 10^{-15}	93.2 x 10^{-15}
$Q^{max,FB}$	Maximum oxygen consumption rate by fibroblasts [mol $cell^{-1}$ hr^{-1}]	98 x 10^{-15}	93.2 x 10^{-15}	93.2 x 10^{-15}	93.2 x 10^{-15}
$Q^{max,HC}$	Maximum oxygen consumption rate by hypertrophic chondrocytes [mol $cell^{-1}$ hr^{-1}]	33 x 10^{-15}	1.8 x 10^{-15}	1.8 x 10^{-15}	1.8 x 10^{-15}
$Q^{max,AB}$	Maximum oxygen consumption rate by adipocytes [mol $cell^{-1}$ hr^{-1}]	98 x 10^{-15}	N/A	N/A	N/A
$Q^{max,FC}$	Maximum oxygen consumption rate by fibrochondrocytes [mol $cell^{-1}$ hr^{-1}]	N/A	N/A	1.8 x 10^{-15}	1.8 x 10^{-15}
$K^{m,MSC}$	Oxygen concentration at half max consumption by MSCs [mol mm^{-3}]	6 x 10^{-12}	22.5 x 10^{-12}	22.5 x 10^{-12}	22.5 x 10^{-12}
$K^{m,CC}$	Oxygen concentration at half max consumption by chondrocytes [mol mm^{-3}]	6 x 10^{-12}	22.5 x 10^{-12}	22.5 x 10^{-12}	22.5 x 10^{-12}
$K^{m,OB}$	Oxygen concentration at half max consumption by osteoblasts [mol mm^{-3}]	6 x 10^{-12}	22.5 x 10^{-12}	22.5 x 10^{-12}	22.5 x 10^{-12}
$K^{m,FB}$	Oxygen concentration at half max consumption by fibroblasts[mol mm^{-3}]	6 x 10^{-12}	22.5 x 10^{-12}	22.5 x 10^{-12}	22.5 x 10^{-12}
$K^{m,HC}$	Oxygen concentration at half max consumption by hypertrophic chondrocytes [mol mm^{-3}]	6 x 10^{-12}	22.5 x 10^{-12}	22.5 x 10^{-12}	22.5 x 10^{-12}
$K^{m,AB}$	Oxygen concentration at half max consumption by adipocytes [mol mm^{-3}]	6 x 10^{-12}	22.5 x 10^{-12}	22.5 x 10^{-12}	22.5 x 10^{-12}
$K^{m,FC}$	Oxygen concentration at half max consumption by fibrochondrocytes [mol mm^{-3}]	N/A	N/A	22.5 x 10^{-12}	22.5 x 10^{-12}
G	Oxygen diffusion coefficient [mm^2 s^{-1}]	2.2 x 10^{-3}	2.2 x 10^{-3}	2.2 x 10^{-3}	2.2 x 10^{-3}
$V^{density}$	Proportion of ECs within an element for it to be considered completely vascularised	0.08	0.2	0.2	0.2

Table S- 5: Parameters used in the tissue differentiation algorithm.

Parameter	Description	Chapter 3	Chapter 4	Chapter 5	Chapter 6
$O_2^{cartilage}$	Oxygen tension for chondrogenic differentiation of MSCs [mol mm-3]	30.48 x 10^{-12}	30.48 x 10^{-12}	30.48 x 10^{-12}	30.48 x 10^{-12}
$O_2^{hypertrophic}$	Oxygen tension for chondrocyte hypertrophy [mol mm-3]	30.48 x 10^{-12}	30.48 x 10^{-12}	30.48 x 10^{-12}	30.48 x 10^{-12}
$O_2^{endochondral}$	Oxygen tension for ossification of chondrocyte hypertrophy [mol mm-3]	50.48 x 10^{-12}	50.48 x 10^{-12}	50.48 x 10^{-12}	50.48 x 10^{-12}
Age^{cell}	Minimum cell age for MSC differentiation [days]	5	5	5	5
$O_2^{inhibition}$	Oxygen tension for inhibition of differentiation	5 x 10^{-12}	5 x 10^{-12}	5 x 10^{-12}	5 x 10^{-12}
$\varepsilon^{oct,hypertrophy}$	Octahedral shear strain above which chondrocyte hypertrophy is inhibited [%]	N/A	N/A	5	12.5
$\varepsilon^{oct,fibrochondrocyte}$	Octahedral shear strain above which chondrocytes become fibrochondrocytes [%]	N/A	N/A	5	12.5